UNIVERSITY OF CATANIA

PH.D. IN CHEMICAL SCIENCES

XXXVIII CYCLE

PH.D. THESIS

Benjamin CLÉPOINT

"Green" Synthetic Methodologies for the Fabrication of Gold Nanostructures with Photothermal Properties for Multi-Responsive Therapies

---

Ph.D. Supervisor:

Prof.ssa Aurore Fraix

Ph.D. Coordinator:

Prof. Salvatore Scirè

Pour mes parents et grands-parents,

pour mes enseignants et professeurs,

et pour mon chien.

Abstract

The low turnover rate of new drugs, coupled with the multiple drug resistance of cancer cells and bacteria, necessitates the exploration of novel therapeutic approaches. Photothermal (PTT) and photodynamic (PDT) therapies, based on a photo-controlled single-wavelength release of heat and singlet oxygen, offer the benefit of treatment control with an enhanced or synergistic action. This work develops two principal research axes: 1) the preparation of anisotropic gold nanoparticles (AuNPs) via green synthetic procedures for an application in PTT with a particular focus on the development of multimodal therapies to observe additive or synergistic effects; and 2) the preparation of an all-in-one innovative cyclodextrin-based platform that will not only contribute to the formation AuNPs but will be able to report the photothermal activity of the system acting as a fluorescent ratiometric thermometer. Regarding the first approach, two biocompatible reducing agents, curcumin and indigo carmine, were used in association with a β-cyclodextrin (βCD) polymer to initiate the nucleation, to stabilize, and to template the resulting anisotropic AuNPs. Both systems demonstrated satisfactory heat generation, and gold particles obtained their shape characterization in collaborations with the University of Padova (Italy) and the University of West Brittany (Brest, France). *In vitro* studies on *E. coli*, *P. aeruginosa*, and ovarian cancer cells were conducted at UMR INSERM 1078 (Brest, France) and demonstrated the photo-induced cytotoxicity of gold nanoparticles obtained from curcumin- and indigo carmine-based syntheses. Moreover, these systems can enhance the solubility of additional molecules of interest, such as photosensitizers for PDT. For instance, the THPP, a Foscan analogue, has demonstrated the production of singlet oxygen in the presence of synthesized gold nanoparticles. In the second approach, investigations were conducted into the design of original fluorescent βCD polymer systems for use as a ratiometric fluorescent thermometer. First, these studies demonstrated the feasibility of the concept using two separate polymers modified with fluorescein and rhodamine B fluorophores. Furthermore, along this polymer mix, we achieved the *in situ* production of AuNPs using nitric oxide radicals generated from an *ad hoc* design photoreactive molecule as a reducing agent. Finally, in collaboration with CarboHyde (Budapest, Hungary), labeled monofluorescent βCD monomers and original polyfluorescent polymers were synthesized to adapt fluorescent thermometers for different perspectives of use.

Keywords: Multiple drug resistance, gold nanoparticles, green synthesis, photothermia, multimodal therapy, cyclodextrin polymer, fluorescent thermometer, photochemistry, nanomedicine.

Abbreviation list

Abbreviation/ Symbol	Meaning
A	Absorbance
a.u.	Arbitrary Units
Ad	Adamantane
AFM	Atomic Force Microscopy
AgNP	Silver Nanoparticle
AuNP	Gold Nanoparticle
$\vec{B}$	Magnetic wave vector
CD	Cyclodextrin
CT	X-ray Computed Tomography
CTAB	Hexadecyltrimethylammonium bromide
CTAC	Hexadecyltrimethylammonium chloride
DCM	Dichloromethane
DFT	Density Functional Theory
DLS	Dynamic Light Scattering
DLVO	Derjaguin–Landau–Verwey–Overbeek
DMF	Dimethylformamide
DMSO	Dimethyl Sulfoxide
DNA	Deoxyribonucleic acid
DNSA	Dansyl amine
$\vec{E}$	Electric wave vector
E_f	Fermi level
ESPT	Excited State Proton Transfer
EPR	Enhanced Permeability and Retention effect
F	Fluorescence
FITC	Fluorescein Isothiocyanate
FRET	Fluorescence Resonance Energy Transfer
GSH	L-Glutathione reduced
GSNO	S-Nitrosoglutathione
hν	Photon Energy
Hb	Hemoglobin
HbO_2	Oxy hemoglobin
HOMO	Highest Occupied Molecular Orbital
HSQC	Heteronuclear Single Quantum Coherence
I	Intensity
I_{max}	Intensity maximum
IC	Internal Conversion
IndC	Indigo Carmine

IR	Infrared
ISC	Intersystem Crossing
$\vec{k}$	Wave vector
LSPR	Localized Surface Plasmon Resonance
LUMO	Lowest Unoccupied Molecular Orbital
MDR	Multiple Drug Resistance effect
M-NP	Metallic Nanoparticle
MRI	Magnetic Resonance Imaging
MS	Mass Spectroscopy
NA-Ad	Nitroaniline-Adamantane
NHE	Normal Hydrogen Electrode
NIR	Near-Infrared Region
NIR-I	First biological window
NIR-II	Second biological window
NMR	Nuclear Magnetic Resonance
NOPD	Nitric Oxide Photodonor
NP	Nanoparticle
NTA	Nanoparticle Tracking Analysis
P	Phosphorescence
p	Product
PBS	Phosphate-Buffered Saline
PDI	Polydispersity Index
PDT	Photodynamic Therapy
PEG	Polyethylene Glycol
PET	Positron Emission Tomography
pH	Potential Hydrogen
PS	Photosensitizer
PSS	Poly(styrenesulfonate)
PTA	Photothermal Agent
PtNP	Platinum Nanoparticle
PTT	Photothermal Therapy
PVP	Polyvinylpyrrolidone
Py	Pyridine
Q	Intensity of fluorescence
QAβCDPS	Quaternary Ammonium β-Cyclodextrin Polymer Soluble
R	Thermometric parameter
RhB	Rhodamine B
RhBITC	Rhodamine B Isothiocyanate
RNS	Reactive Nitrogen Species
ROS	Reactive Oxygen Species
RT	Room Temperature
s	Substrate
SBβCDPS	Sulfobutylated β-Cyclodextrin Polymer Soluble

SEM	Scanning Electron Microscopy
SHE	Standard Hydrogen Electrode
S_N2	Bimolecular Nucleophilic Substitution
SPR	Surface Plasmon Resonance
S_r	Relative Sensitivity
S_0	Ground Singlet State
S_1	First Excited Singlet State
T	Temperature
TEM	Transmission Electron Microscopy
TGMS	Thermal Gravimetric Mass Spectroscopy
TLC	Thin-Layer Chromatography
THPP	5,10,15,20-Tetrakis(4-hydroxyphenyl)-21H23H-porphine
T_1	First Excited Triplet State
UV	Ultraviolet
UV-Vis	Ultraviolet-Visible spectroscopy
VP	Verteporfin
VR	Vibrational Relaxation
ZP	Zeta Potential
ZnPc	Zinc Phthalocyanine
Δ	Heat
σ_{abs}	Absorbance Cross-Section
σ_{ext}	Extinction Cross-Section
σ_{scat}	Scattering Cross-Section
Φ	Quantum Yield

TABLE OF CONTENTS

Aim of the project

The low turnover of new anticancer drugs and the Multiple Drug Resistance (MDR) phenomenon emerging for conventional drugs call for an urgent shift of attention to other "unconventional" therapeutic modalities. Photothermal (PTT) and photodynamic therapies (PDT) are two recently developed strategies based on the controlled release of unconventional therapeutic agents: heat and reactive oxygen species (ROS), respectively. These agents share desirable properties: they are transient, which restricts their activity to the area near their site of generation; they are versatile, able to interact with several biological targets (DNA, lipids, proteins); and they typically do not suffer from the MDR phenomenon. Moreover, both can be generated under light stimulation, enabling excellent control of the treatment in terms of location, timing, and dosage.

This project aims to develop a biocompatible nanosystem for photothermal bio-applications, with a particular interest in multimodal platforms for cancer and bacterial disease treatment. Even if PTT is already, by itself, a promising treatment, the development of nanosystems capable of displaying multiple properties of interest is highly desirable for the development of new therapeutic strategies. Therefore, we will pay particular attention to the development of possible multimodal systems exhibiting more than one photo-activable property. Thus, the goal is to develop synthetic routes involving the principles of green chemistry for the formation, in a single step, of highly anisotropic gold nanoparticles (AuNPs) as a biocompatible photothermal agent (PTA) and vector for a drug of interest. Light in this context offers unique advantages: it is a clean reagent that can be easily controlled in terms of intensity and energy, allowing the production of heat and highly reactive oxygen species starting from appropriate photo-precursors. The system will imply the use of a highly biocompatible and water-soluble branched βCD polymer to be used as: a templating and stabilizing agent for the AuNPs, as a fluorescent thermometer to monitor the temperature variation for PTT applications, and finally as an enhancer of the solubility of the green reducing agent, a photosensitizer, or an additional drug. The reducing agent (i.e., curcumin, indigo carmine, or a NOPD), once irradiated, initiates the reduction of the gold precursor, the tetrachloroauric(III) trihydrate acid ($HAuCl_4 \cdot 3H_2O$), and consequently nucleates gold nanoparticles. The reduction of Au(III) to Au(0) will naturally occur both in solution and within the compartments of the polymer because of its capping properties, and the polymer will prevent the aggregation of the AuNPs formed. Different syntheses will be settled, compared, and optimized (Figure 1).

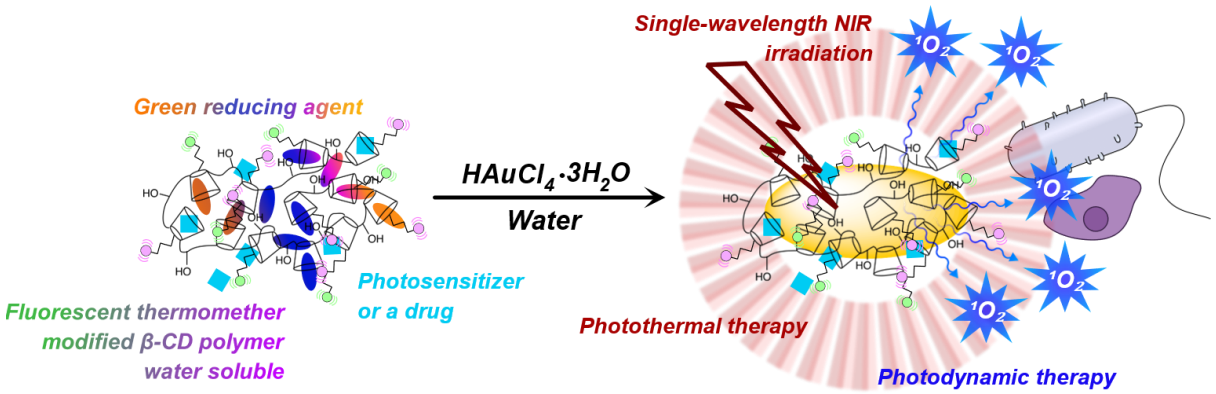

Figure 1: Overall strategy illustration: green synthesis of gold nanoparticles from the reduction of the tetrachloroauric(III) acid trihydrate ($HAuCl_4 \bullet 3H_2O$) by a green reducing agent. After a single-wavelength near-infrared irradiation of both anisotropic gold nanoparticles and a photosensitizer (PS), a possible multimodal biological application in photothermal and photodynamic therapies will be possible. We aim to incorporate a fluorescent thermometer to monitor the temperature for bio-applications. Orange: curcumin; purple: indigo carmine; yellow: nitroaniline-adamantane; green: fluorescein; pink: rhodamine B; light blue: photosensitizer or a drug.

1. Introduction

Classical cancer therapeutic strategies generally involve chemotherapy, radiotherapy, or surgery. By 2040, chemotherapy will treat about 15 million cancer patients as the optimal therapeutic strategy.[1] However, because of 1) the high toxicity of anticancer drugs to healthy as well as their targets, 2) an insufficient turnover of active molecules, 3) the rise of drug resistance, and 4) the reduced solubility of anticancer drugs in water, traditional chemotherapy becomes more and more unsuitable as a single therapeutic procedure. A new approach is needed to overcome these limitations.[2] Additionally, Gram-positive and Gram-negative bacteria are also developing multiple drug resistance effect (MDR), which can be due to the presence of efflux pumps to pump out multiple drug types, and genes coding for resistance to therapeutic agents.[3] Moreover, planktonic bacteria are not the only entities that manage to develop resistance to antibiotics; there are also biofilms, the main form of growth of microorganisms. Due to the biofilm's distinct properties, it exhibits significantly better resistance to antimicrobial drugs than free-living bacteria.[4] To respond correctly to the problem of the MDR effect, which bacterial resistance toward specific modes of action causes, we urgently need to design new antimicrobial drugs with a multiple-targeting system.

Photothermal (PTT) and photodynamic (PDT) therapies are two strategies based on the controlled release of unconventional therapeutic agents: heat and reactive oxygen species (ROS), respectively. They share desirable properties: they can restrict their activities in the vicinity of their generation area, they are versatile agents able to interact with several biological targets (DNA, lipids, proteins), and they typically do not suffer from MDR phenomena. Moreover, both can be generated under the same light irradiation, allowing for excellent control of the treatment in terms of location, time, and dosage. We can utilize gold nanoparticles to combine both photothermal and photodynamic therapies for applications in cancer and antimicrobial treatment, serving as both a photothermal agent and a vector for photosensitive molecules. The objective of this work is to develop various synthesis methodologies that adhere to the twelve principles of green chemistry (they intend to make a framework for designing a sustainable chemistry in environmental, economic and industrial fields),[5] to form gold nanoparticles for PTT, and to potentially incorporate a photosensitizer, ultimately resulting in a multimodal system for use in photothermal and photodynamic therapies against cancer and bacteria.

2. State of the Art

2.1. Photothermal therapy

2.1.1. Definition

Photothermal therapy is a non-invasive and non-selective therapeutic technique that utilizes hyperthermia (heat) induced by external light irradiation of a photothermal agent as a therapeutic tool.

The hyperthermia phenomenon is characterized by an increase in body temperature (between 41 and 48°C), which may occur at a specific site or throughout the entire body. Most times, hyperthermia is a non-controlled and non-desirable phenomenon; however, it can be used in a therapeutic perspective by increasing susceptibility to chemotherapy and radiotherapy.[6] The temperature rise has consequences for biological material, including the unfolding, aggregation, and denaturation of proteins, as well as the degradation of chromatin and the inhibition of DNA repair and replication.[7,8] Interestingly, the control of the heat rise using an appropriate trigger offers therapeutic perspectives.

We can utilize PTT in both cancer therapy and in the fight against antimicrobial resistance. The temperature reached will determine the biological effect induced by the irradiated photothermal agent. Without active targeting, its capacity to damage only cancer cells is due to the enhanced permeability and retention (EPR) effect, where the photothermal agent tends to accumulate in tumors. Two factors induce this effect: 1) the malformed vascular structure of cancerous cells,[9] and 2) the structure or functionalization of the PTA, which can facilitate binding to targeted tumors,[10] thereby offering a higher retention time than traditional drugs before clearance from the body (Figure 2).

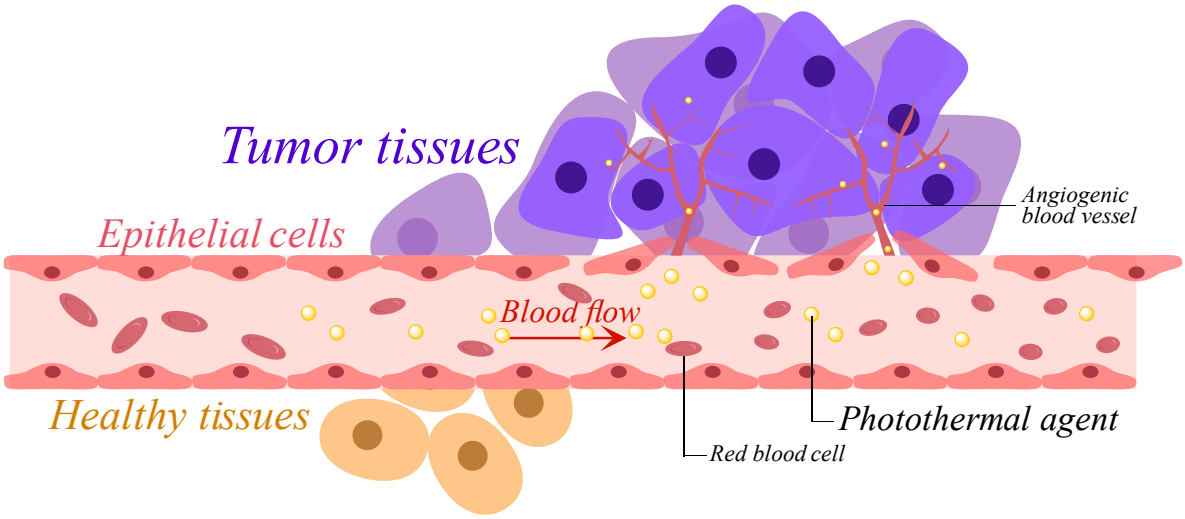

Figure 2: Schematic representation of the EPR effect. The photothermal agent travels through the blood vessels until it reaches an angiogenic blood vessel, slips into it, and accumulates in tumor tissues.

For a cancer therapy application, the temperature must be within the hyperthermia range (i.e., 41 – 48 °C) and trigger the apoptosis mechanism. PTT yields best results at 41 – 42 °C: these temperatures are sufficient to trigger the apoptotic cell death mechanism, overcoming the target's heat resistance induced by slightly lower temperatures (i.e., 38 – 41 °C), while preventing damage to healthy cells and enhancing blood flow.[11] Furthermore, the aimed temperatures are even easier to reach for cancer cells as the tumor's cooling properties are worse due to the presence of permeable blood vasculature, metabolic heat generation, or worse blood flow.[12,13,14]

If the temperature is below 41 °C (diathermia range), the heat resistance is higher. Unfortunately, this moderate temperature elevation increases blood flow in the surrounding area, thereby increasing the oxygen supply to the tumor. On the other hand, if the temperature exceeds 42 °C, damage to healthy cells can occur, and a decrease in blood flow or destruction of the surrounding microvasculature can also occur.[6] Finally, beyond 48 °C, irreversible degradation of DNA and proteins arises, and both healthy and cancerous cells are irreversibly damaged and killed by necrosis; no selectivity can arise.,[15,16]

Regardless of the range, cells' reaction to the applied heat is also dependent on the duration and magnitude of the heat exposure.[17] In soft tissues, the thermal diffusion radius induced by irradiation of the photothermal agent is generally between 1 and 2 millimeters.[18] Up to 44 °C, the damaged cells are killed by apoptosis, and from 46 °C, by the necrosis mechanism. At 45 °C, both processes occur.[19]

We can also utilize PTT for its bactericidal effect. As in cancer therapy, its effectiveness against antimicrobial resistance depends on the same temperature range (i.e., 41–48°C) applied. However, this range is not optimal for killing bacteria, as it is just enough to cause membrane degradation in Gram-positive or Gram-negative bacteria. If no higher temperature is applied, the bacteria's growth will restart. Only higher temperatures (i.e., 50–80 °C) can destroy the double cell wall and trigger bacterial necrosis.[20,21] Furthermore, it appears that low to moderate temperatures (i.e., 37 – 42 °C) can induce a drug resistance effect. In contrast, temperatures higher than 42 °C tend to reduce it.[22] Besides its use to overcome the MDR effect, PTT offers different advantages over the classic use of antibiotics: a broad spectrum activity and a shorter treatment time needed to observe bacterial necrosis.[23]

Figure 3 summarizes and represents the temperatures aimed for against cancer and bacterial multiple drug resistance:

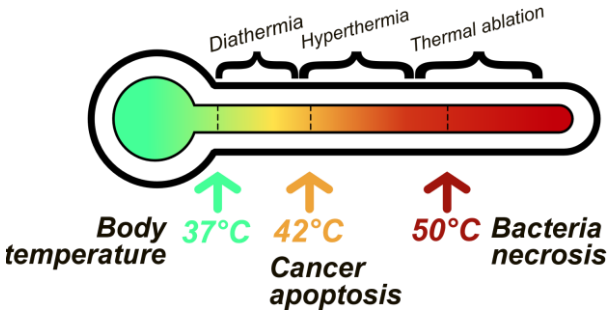

Figure 3: Temperature ranges of diathermia, hyperthermia, and thermal ablation, as well as target temperatures for cancer and bacterial elimination.

Despite the multiple advantages and the clinical positive results the photothermal therapy provides,[24,25] at mild heat (targeted temperature inferior to 42 °C), this technique is not enough for an efficient application by itself, but we can improve results if we combine PTT with another treatment.[26]

2.1.2. Irradiation parameters & photothermal agent

To control the temperature applied, and consequently to prevent the overheating from the photothermal agent and the degradation of the healthy cells, three leading factors need to be adjusted: 1) PTA photothermal properties, 2) the concentration of the PTA, and 3) the irradiation's parameters (emission regime, wavelength, irradiation area, and time).[27]

Regarding the last point, a continuous light irradiation is preferred for PTT as it allows a proper heat dissipation from the photothermal agent to its environment. A pulsed laser can produce a rapid and large quantity of heat and can degrade and melt the photothermal agent.[28]

For the irradiation time, the results demonstrated irreversible damage to cancer cells at 41 °C after 60 minutes or at 46 °C after only 5 – 10 minutes.[29]

Furthermore, for targets beneath the skin or deep within tissues, the wavelength used for PTT cannot be freely chosen. Due to the inhomogeneous composition of the skin tissue, photons are reflected and scattered in all directions before reaching deep targets. In light of this, selecting the correct wavelength in the near-infrared region (NIR) (between 750 and 1400 nm) will enable the incident photons to penetrate the superficial biological material and reach the target up to a few centimeters.[30] And by comparison with UV and visible light, this range also allows a low photo-damage to biological material, and by employing non-ionizing radiations, the risk of developing a secondary cancer is low.[31,32] The exact choice of the wavelength must be comprised inside two biological windows where the reflection and the scattering of the tissues become irrelevant: 1) the first biological window (NIR-I), delimited from 650 nm by the hemoglobin absorbance to the water absorbance at 950 nm, or 2) the second window (NIR-II), from 1000 to 1400 nm, with boundaries also due to water absorption bands.[17] The main difference between the ranges is the length of the radiation penetration in the tissues, with a scattering inversely proportional to the wavelength. NIR-I region irradiation can reach targets up to 1 cm, while in NIR-II, the tissue penetration depth can reach 3 cm.[33] The limiting penetration depth of the laser is suitable for small and well-localized tumors. In contrast, for unreachable ones, an optical fiber can be used instead to deliver the photons.[34] *In fine*, an “optimal” wavelength for irradiation may be close to 800 nm: it lies within the NIR-I, where the absorption of light by water and tissues (mainly by melanin) is absent, and it is the isosbestic point between the absorbance of oxygenated and deoxygenated hemoglobin and allowing a deeper photon penetration and consequently deeper photothermal applications (Figure 4).[35]

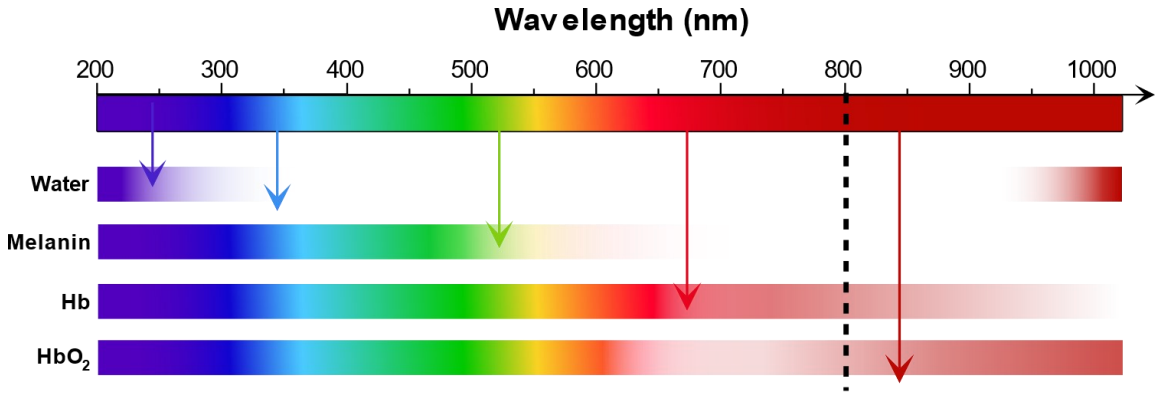

Figure 4: Biological windows and absorbance ranges of different obstacle molecules. Data is from Vogel and Venugopalan.[36] Hb: hemoglobin; HbO_2: oxyhemoglobin.

Additionally, due to the lower absorption of HbO_2 compared to hemoglobin in the near-infrared region, the concentration of dioxygen and pH affect light penetration through tissues in the tumor area. The acidic environment of cancerous cells reduces the HbO_2/Hb ratio. In contrast, the rise in O_2 concentration increases oxyhemoglobin concentration, thereby raising the HbO_2/Hb ratio.[37] Thus, the higher this ratio is, the better the absorption in the 585 – 805 nm window will be.

Furthermore, to accurately monitor the temperature rise caused by photothermal agent irradiation, various techniques have been employed in biological applications, including: Magnetic Resonance Imaging (MRI),[38] photoluminescence,[39] photoacoustic imaging, ultrasound,[40] X-ray computed tomography (CT),[41] thermal imaging, and positron emission tomography (PET).

2.2. Nanoparticles as a photothermal agent

Photothermal agents can be divided into two different categories: organic or inorganic materials. Light does not interact the same way depending on the PTA used. For organic agents, such as cyanines, pyrrole derivatives, porphyrins, and polymers, they afford efficient targeting of cancer cells, and heat is generated from the relaxation of the excited PTA through a non-radiative vibrational relaxation process (Figure 5). However, these organic PTAs are highly photobleachable and exhibit low photothermal conversion efficiency.[42] However, inorganic agents like carbon nanotubes, graphene, quantum dots, iron oxide NPs, or gold nanoparticles demonstrated excellent photothermal properties, photostability, and appealing absorbance properties. When photons reach an inorganic photothermal agent, the absorbed

light energy is converted into kinetic energy via the vibrational motion of electrons (lattice/phonon vibrations). Then this energy is released from the system into heat.[12] The generation of heat from an inorganic photothermal agent is presented and described below (see part 2.2.1.).

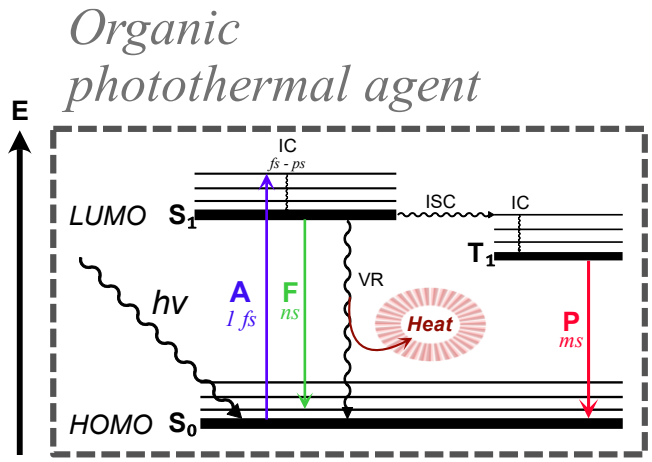

Figure 5: Simplified Jablonski Diagram of a single photon absorption by an organic PTA and its vibrational relaxation leading to heat generation; HOMO: highest occupied molecular orbital; LUMO: lowest unoccupied molecular orbital; S_n: singlet spin multiplicity; hν: photon energy; T_n: triplet spin multiplicity; A: absorbance; F: fluorescence; P: phosphorescence; IC: internal conversion; ISC: intersystem crossing; s: substrate; p: product.

Organic or inorganic particles in the nanometer range have strong potential for a multimodal therapeutic approach to counteract the MDR effect.

In cancer therapy, due to their dimensions and ease of functionalization, nanoparticles (NPs) can leverage the EPR effect as described previously (part 2.1.1.).

Both Gram-positive and Gram-negative bacteria have defense mechanisms that are ineffective against nanoparticles, as nanoparticles can target multiple vital parts of the bacteria (proteins and DNA). A high concentration of NPs (i.e., like TiO_2, ZnO, Ag NPs, or AuNPs, etc.) can lead to a concomitant increase in ROS generation and free radical formation, both of which can disrupt the plasma membrane, inducing cell damage and inhibiting the cell's antioxidant defense system.[43,44] Furthermore, some NPs can be found helpful as a vector agent for photosensitizers or drugs with antibacterial properties, offering great additive and synergistic effects to the photothermal properties of NPs.[44]

It is also worth noting that some nanoparticles can face antibacterial resistance.[45]

The application of NPs for PTT allows a remote and localized heating by laser source,[17] while for photodynamic therapy, the nanoparticles with a high surface-to-volume ratio allow a great functionalization with other photosensitizers to access PDT efficiency.[46]

Furthermore, for an application in PTT and PDT, nanoparticles need to possess important prerequisites for an optimal use:[17] 1) they need a suitable size (inferior to 100 nm) to enter in cancerous cells or to stay the longest time possible in the blood vessels, 2) NPs need to have a good dispersity in aqueous solvent (hydrophilic surface), 3) since the targeting of cancerous cells or bacteria is sought, a minimal interaction with healthy cells is also an important feature, and 4) obviously, a good heat production is needed for applications in photothermal therapy.

2.2.1. Metallic nanoparticles under the electromagnetic wave

However, the nanoparticles' nature is an important parameter. Metallic inorganic nanoparticles (M-NPs) exhibit distinct light behavior and consequently possess inherent properties for photothermal therapy applications that their organic counterparts do not have. Through their 1) light absorption in the visible-near infrared region, 2) high molar extinction coefficient, 3) high light-to-heat conversion, and 4) excellent photostability and biocompatibility, their use is optimum for PTT and for an association with a photosensitizer.

These differences between organic NPs and bulk materials in their interactions with light can be explained on a physical basis at the nanoscale level. When irradiated, the electrons in the conduction band of the M-NPs are excited and enter a surface plasmon resonance (SPR) state, initiating electron-electron scattering and transferring their energy to nearby electrons, thereby forming hot electrons. Hot electrons are excited electrons with high temperature and kinetic energy above the Fermi level. The relaxation of these hot electrons increases the temperature of the particle's immediate environment (Figure 6).

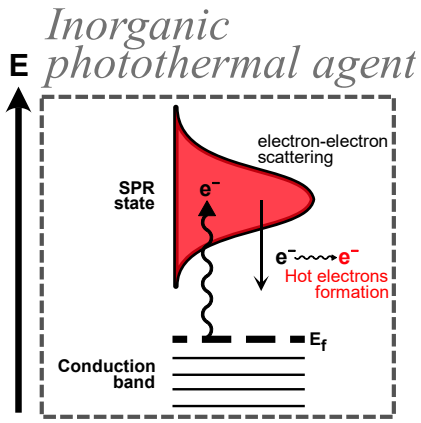

Figure 6: Radiative excitation of the phonon from the conduction band to the SPR state, followed by its non-radiative relaxation and disintegration into hot electrons. E_f: Fermi level.

Concretely, for M-NPs, the localized surface plasmon resonance (LSPR), firstly reported by Mie in 1908,[47] refers to a physical phenomenon where the electron cloud (i.e., the free electrons of the metals), mainly at the surface of the M-NPs, is driven by an enhanced polarization (i.e., in resonance) from the electric field of an electromagnetic wave to produce heat. After being polarized, the cloud is restored to the nucleus due to Coulomb attraction and continues to oscillate coherently, in resonance, in response to the incoming light (Figures 7 and 8A).[48] The perturbation of the electron cloud is called the plasmon. The LSPR phenomenon induces three events: 1) near-field enhancement; 2) generation of hot electrons, and lastly 3) the thermal conversion of the light. During the oscillation of the electrons, both potential and kinetic energies of the plasmon are transferred towards other conduction electrons to form hot electrons. They are transitioning from filled to vacant energy states, leading to a non-thermal charge distribution. After, these hot electrons release their energy either by light emission or by transferring it to the neighboring electrons of the lattice, leading to an increase in the number of excited electrons within the phonon, raising the temperature to five thousand Kelvin degrees in about 10 ps throughout the lattice (Figure 8B).[49] After this electron-phonon process, another one takes place: the phonon-phonon process. Here, the vibrational energy of one lattice is redistributed by close interaction between phonons of adjacent metallic atoms (by diffusion, division, or combination of phonons) (Figure 8C). This dispersal of the energy between the excited lattices induces a rise in the temperature of the NPs in about 100 ps.[21] Finally, the dispersion of the heat in the close environment induces the cooling of metallic nanoparticles (Figure 8D).[26]

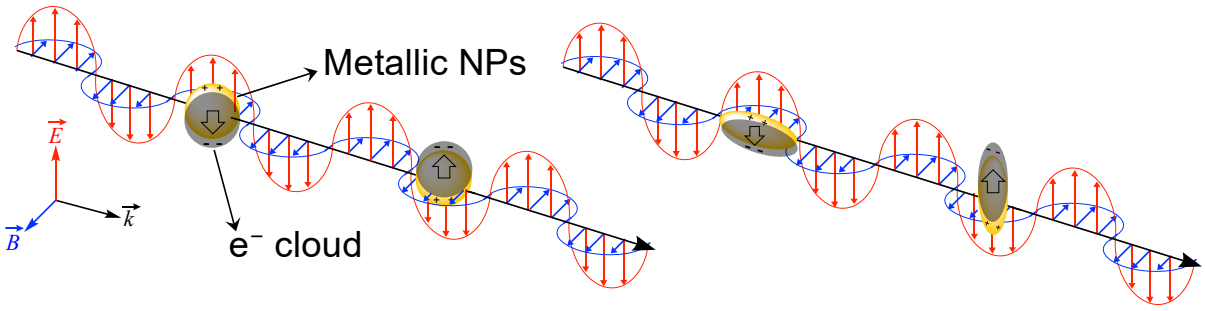

Figure 7: Schematic representation of the theory of the plasmonic effect for isotropic (left) and anisotropic (right) metallic NPs. The electric and magnetic fields of the electromagnetic radiation are represented in red and blue, respectively. $\vec{k}$: wave vector; $\vec{E}$: electric wave vector; $\vec{B}$: magnetic wave vector.

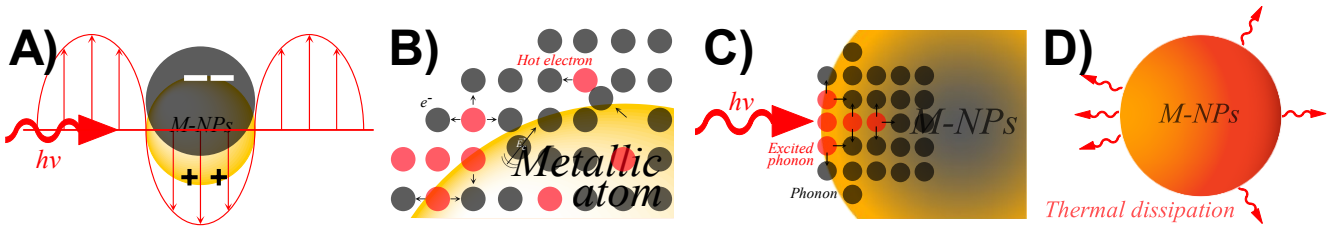

Figure 8: Schematic representation of the LSPR phenomenon step-by-step: A) oscillation of the lattice under light irradiation; B) kinetic energy of the electrons are transferred to other conductive electrons leading to hot electrons; hot electrons are diffusing their energy through the electron lattice; C) phonon-phonon process, the energy is spread all over inside the nanoparticle; and D) dissipation of the heat in the proximity of the M-NPs.

The LSPR is a necessary phenomenon for PTT applications. It can only be possible when the frequency of the light applied is the same as the frequency of the oscillating cloud.[50] At the same frequency, the oscillation scope of the plasmon reaches its maximum, resulting in an antenna effect that redirects a larger light to the particle area than its size can usually capture (Figure 9).[51] Consequently, the absorption of the light by the NPs, the electric field in their surroundings, and their energy released as heat are enhanced.[52] This light-absorption enhancement is more pronounced for metals with d-orbital electrons, such as silver or gold, which can travel freely within the particle and influence the frequency of the plasmon, making them ideal for optical applications.[48,53]

However, not all photons are absorbed by the nanoparticle; scattering is still present, and they are released at the same frequency and in all directions.[54]

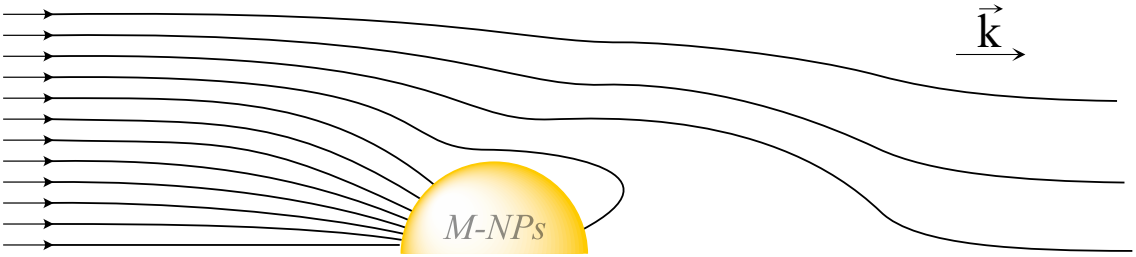

Figure 9: Schematic representation of the M-NPs antenna effect of the electromagnetic wave during the LSPR phenomenon. $\vec{k}$: wave vector.

Four different parameters determine the oscillation frequency of the cloud of electrons: 1) the density of electrons, 2) the effective electron mass, 3) the shape of the electron cloud, and 4) the size of the electron cloud. *In fine*, because the LSPR can be modified by the shape and the size of the M-NPs (resulting from a modification of the surface geometry of the electron cloud, causing a shift of the electric field density and ending in a modification of the frequency of the plasmon), these nanoscale objects can see their absorption band tuned in function of these physical properties. Nevertheless, for M-NPs, the introduction of an anisotropy to spherical particles is generally necessary to observe a characteristic band red-shift (especially to reach the NIR) of the LSPR band in the visible region. As the aspect ratio of the M-NPs increases (length divided by width), the longitudinal plasmon oscillation rises, ending in a split of the absorption band into two other ones. The first is characteristic of the transversal size, and the second is characteristic of the longitudinal size of the anisotropic particle; furthermore, the apparition of the anisotropy is followed by the augmentation of the intensity and of bathochromic shift of the second absorption band.[53]

Besides the formation of an LSPR band in the NIR, these non-isotropic particles offer other advantages: they provide better tumor penetration than spherical particles due to improved transport through cancerous cells' pores.[55] Their high volume-surface ratio delivers an excellent opportunity for the addition of targeting ligands, thereby improving the cellular binding, the cellular uptake, and the therapeutic efficacy.[56] Anisotropic particles, like gold nanoflower or gold nanostars, also offer a superior prevention to biofilms than their isotropic analogues because of the presence of the high aspect ratio of the sparks, leading to membrane rupture of the bacterial cell wall.[57]

2.2.2. Gold nanoparticles

Because of its bacteriostatic effect,[58] its lack of surface oxidation, its photostability, its high light-to-heat quantum yield,[28] its LSPR band, and its simple preparation in the laboratory, gold nanoparticles have been intensely studied and applied for medical applications, and their reported first uses date back to 400 BC in India and China.[59,60]

AuNPs are great candidates for a multimodal PTT and PDT system to overcome the MDR effect in cancer and bacteria. In photothermal therapy, AuNPs can release heat at the picosecond order under irradiation due to the electron-phonon and phonon-phonon processes described above.[61] In terms of photothermal efficiency, other M-NPs are not strong candidates; indeed, silver nanoparticles (AgNPs) are prone to oxidation and toxicity in the dark,[62,63] while palladium nanoparticles also pose some toxicity concerns.[64]

For PDT, instead of releasing heat, AuNPs can transfer their absorbed energy to a close photosensitizer (functionalized on the particle surface or via a surfactant) or molecular oxygen. As a photosensitizer, their quantum yield ($\Phi(^1O_2) = 0.037$) is not as good when compared to other M-NPs like AgNPs ($\Phi(^1O_2) = 0.155$) or PtNPs ($\Phi(^1O_2) = 0.085$), nor as great as classic organic PS (Rose Bengal ($\Phi(^1O_2) = 0.76$)). Still, the use of M-NPs is less prone to photodegradation and has a higher extinction coefficient than organic PS (4 – 6 orders of magnitude).[65,66] Consequently, gold nanoparticles appear to be more commonly used as a vector to deliver PS to the target via the EPR effect than as a photosensitizer on its own. With a near photosensitive agent, the formation of ROS appears to increase under light irradiation via energy transfer from the AuNPs to the PS, driven by the localized plasmonic effect of AuNPs.[67] However, this enhancement was not observed for gold particles coupled with zinc phthalocyanine.[68,69]

Unfunctionalized and spherical particles are ideal for cancer therapy, as they can easily travel to tumor cells' location through the tumor vasculature.[70] Unfortunately, spherical gold nanoparticles (between 10 and 100 nm) only absorb in the visible spectrum (in the 500 – 550 nm region), making them incompatible for deep PTT applications.[71] To allow gold nanoparticles to absorb at higher wavelengths, non-spherical gold particles like nanorods, nanostars, or nanoprisms are required as they can allow the formation of a second absorption band in the near-infrared region (Figure 10). Due to the strong absorption of anisotropic AuNPs in the near-

infrared region, an easy modulation of their size and shape makes them great candidates as therapeutic agents that can absorb in the biological windows of the NIR.[17]

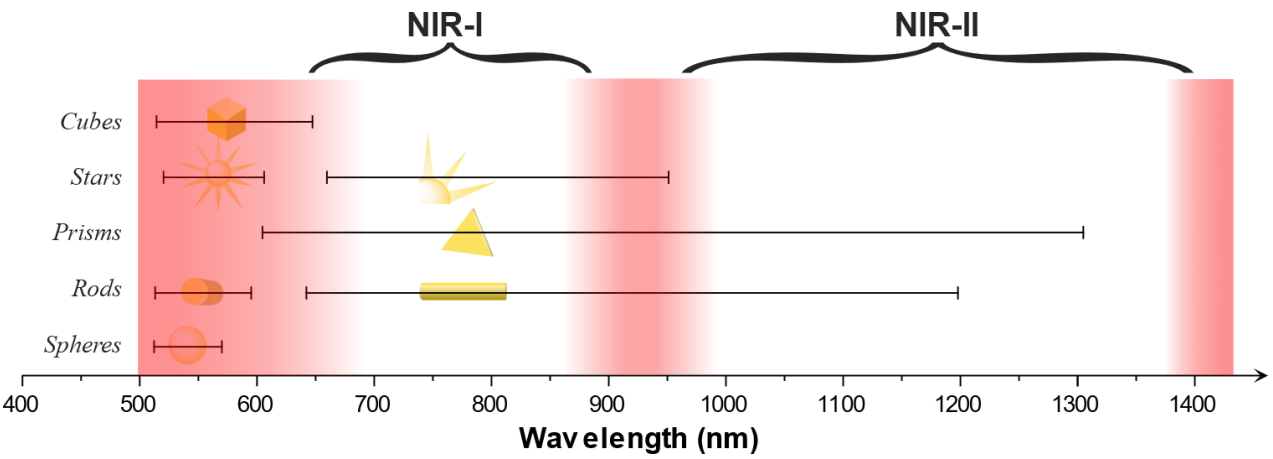

Figure 10: LSPR bands range of selected basic AuNPs shapes. Both biological windows are located between 650 – 950 nm (NIR-I) and 1000 – 1400 nm (NIR-II). Ranges data are from Yu et al.[72]

Another advantage of anisotropic structures, such as nanorods over nanospheres, is their ability to generate heat differently due to their morphology. Gold nanorods are better photothermal agents than gold spheres for PTT. This enhancement is due to greater involvement of the entire structure in the heating process. The generation of the heat is directly performed from the central part of the rod instead of the light-faced outer part of spheres, due to a closer proximity of the core to the surface of the rod.[73]

At the same volume, with gold nanorods of an aspect ratio of 1:3, a 60% improvement in heat generation is expected compared to nanospheres. This improved performance is due to the absence of a shield effect for small particles, nanorods, or nanotriangles, allowing the electric field to pass through these gold nanostructures more easily and to oscillate the entire plasmon.[73] Furthermore, this absence of shield effect leads also to a heterogeneous heat generation within the particle; however, their temperature is quasi-uniform due to the fast heat propagation throughout the NPs.[73]

Moreover, not all incident photons absorbed by the gold nanoparticle will be converted into heat; some of the incoming energy is scattered in all directions.[74] The photothermal efficiency (μ), is defined by a ratio of the absorbance cross-section (probability of the absorption phenomenon) over the extinction cross-section (sum of the probability of the absorption and the probability of the scattering phenomena) of the light by the photothermal agent (Equation 1):

$$\mu = \frac{\sigma_{abs}}{\sigma_{ext}} = \frac{\sigma_{abs}}{\sigma_{abs} + \sigma_{scat}}$$

Equation 1: Formula for the photothermal efficiency. μ: Photothermal efficiency; σ_{abs}: absorbance cross-section; σ_{ext}: extinction cross-section; σ_{scat}: scattering cross-section.

Besides, for concentrated AuNPs colloidal suspension (i.e., [AuNPs] = 10^9 - 10^{10} particles per mL), the scattering of the light from adjacent AuNPs can induce an increase in the absorption of photons and so of the heat generated by the photothermal agent.[75]

For PTT applications, the particle size should be approximately 50 nm. Indeed, the size of the particle influences the heat generation/scattering ratio: heat generation is the primary energy release for particles with sizes between 10 and 50 nm, whereas for larger spherical AuNPs, scattering becomes more significant.[54] The EPR effect generally concerns particles with sizes between 50 and 200 nm. Above 200 nm, the NPs are held outside of the target, while under 50 nm, they can easily leave the cancerous cell. And as mentioned before, the performances for PTT applications are optimal up to 100 nm.[70]

Experimentally, the formation of small particles is induced by short reaction time (i.e., 24 hours), low H^+ concentration (i.e., pH = 5), low gold salt concentration (i.e., [$HAuCl_4$] = 250 $mg.L^{-1}$),[76] and the amount of reducing agent (i.e., 3 % extract concentration).[77] In synthetic conditions, the narrowness of the size distribution is favored at room temperature, as elevated temperatures can induce aggregation of the particles and thus a larger size population.[78]

Isotropic nanoparticles are thermodynamically favored because the sphere is the lowest energy shape that the reduced metallic salts can result in.[79] Thus, to prepare anisotropic particles, precise and suitable experimental parameters are needed. The choice of the reducing agent seems to have a substantial effect on the obtention of the anisotropy. Reducing agents can promote the preferential growth of one direction of a particle by acting as a stabilizing agent, by being adsorbed on one of their surfaces, and also by their interactions with gold precursors and the particles.[80,81] Furthermore, the use of cationic surfactants like CTAB (hexadecyltrimethylammonium bromide) can induce the differential growth of the particle in one direction by binding themselves to one preferential face of the nanoparticle, allowing the development on bare sides without cationic surfactants.[82]

For anisotropic gold nanoparticles with cylindrical shapes, such as nanorods, the first absorbance band at approximately 520 nm is characteristic of the transverse ratio, while the

band in the near-infrared region is due to the longitudinal resonance of the electron cloud. As longitudinal resonance increases, the wavelength increases, shifting the LSPR band into the infrared.[53] For other anisotropic gold nanoparticles, like gold nanotriangles, their aspect ratio is also essential for the presence of an LSPR band in the biological window. It can be tuned by increasing the particle edge length, its thickness, or changing its geometry. For gold nanostars, the length of the spikes significantly influences their red-light absorption properties. The longer the spikes are, the better the particle will absorb in the NIR.[72]

According to DLVO (Derjaguin-Landau-Verwey-Overbeek) theory, the absence of electrostatic repulsion between metallic nanoparticles due to van der Waals forces necessitates the use of capping and stabilizing agents to prevent particle aggregation during synthesis.[83,84] Since the goal is to synthesize stable AuNPs, the stability of the nanostructures is important for optimal biological applications. In aqueous solution, the charge surface value, or the Zeta potential, must be farther from 0 with a value above +40 mV or under -40 mV, characteristic of very stable particles. Furthermore, the closer the Zeta potential is to 0 mV, the more unstable the particles are as they tend to aggregate.[85] However, for *in vivo* applications, a neutral surface or slightly negative surface can enhance the retention time, while cationic surfaces allow a better penetration of the nanoparticles inside cancerous cells.[86]

2.2.3. Classic chemical synthesis of anisotropic gold nanoparticles

Michael Faraday reported the first synthesis of colloidal gold nanoparticles in 1857.[87] Generally, nanoparticle synthesis relies on two opposing strategies. In a top-down approach, a bulk material is divided into small nanoparticles. In contrast, a bottom-up synthesis involves assembling atoms or salts to form a larger entity, typically achieved through chemical reactions (such as reduction or oxidation),[88] or biological synthesis.[89] In the bottom-up approach, the nanoscale particle can be formed either by:[90] 1) an *in situ* method done by the reduction of a cationic metal and the stabilization of the particle formed, or 2) a seed-growth method that will expand the particle gradually with reduced metallic atoms. For AuNPs and M-NPs, the most widely used synthetic route is a chemical “bottom-up” *in situ* strategy involving a metallic salt and a reducing agent, most commonly sodium borohydride ($NaBH_4$) or sodium citrate.[91] Indeed, the bottom-up approach is usually used for the synthesis of AuNPs because the opposite technique is generally more expensive and offers a generally mixed shapes and sizes distributions.[92] In 1950, LaMer and Dinegar studied the synthesis of uniform sulfur colloids (i.e.,

nanoparticles). After describing their theory, the authors detailed the formation mechanism of the sulfur hydrosols.[93] They described what is now called the LaMer diagram, the latter defining the general and widely accepted formation and growth of nanoparticles from a bottom-up approach. Accordingly, a classic synthesis is divided into three parts: 1) the reduction of the metallic gold salt into gold atoms, 2) the nucleation of the AuNPs, and 3) the growth of the particles (Figure 11).

At the beginning of the reaction at the reduction step, the concentration in solution of the insoluble monomer Au(0) is increasing as the reduction of Au(III), generally in solution as $AuCl_4^-$, is going forward. When the concentration of Au(0) reaches a minimum for nucleation, the second part begins, and the number of nuclei of AuNPs starts to rise. The number of AuNPs' nuclei reaches a maximum and then decreases due to particle aggregation (Ostwald ripening). Nucleation of the NPs is a rapid process, leading to a significant decrease in the gold atom concentration in solution. Consequently, the concentration will drop under the nucleation limit, and the gold atoms in solution will now be used to grow and to increase the size of the particles already formed. Then, their concentration decreases over time until it reaches the solubility limit of solubility [Au]. Over this limit, gold atoms are no longer a colloidal suspension.

The kinetics of the nucleation phase influence the nuclei concentration, and consequently, the final concentration of AuNPs, while the kinetics of the growth phase influence the AuNPs' size. Since the speed of the nucleation step has consequences on the concentration of gold atoms left in solution for the growth of the particles, the kinetics of the nucleation phase is ultimately the most important parameter during the synthesis because it has a direct influence on the growth phase and so, on the size of the final AuNPs formed.

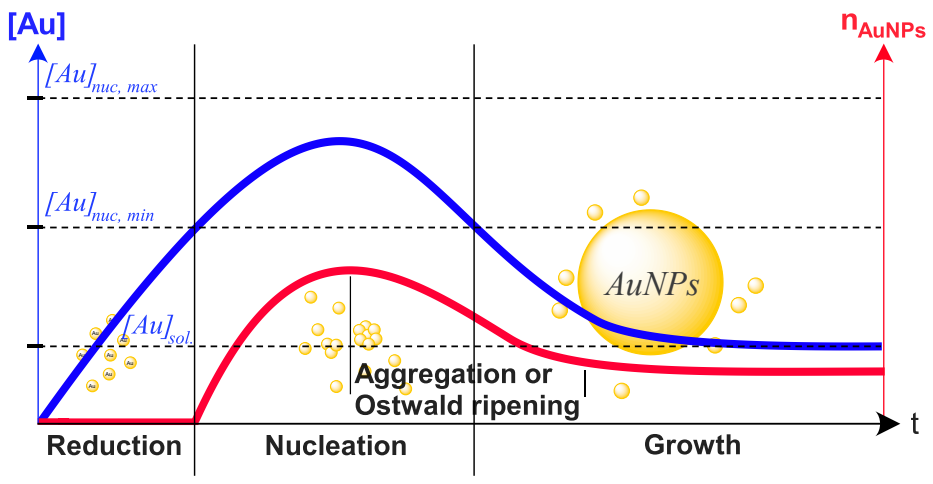

Figure 11: LaMer diagram illustrating the three stages of classical AuNPs formation: reduction, nucleation, and growth. The concentration of gold atoms in solution as a function of time of reaction is represented in blue, while the number of gold nanoparticles in solution is represented in red.

Anisotropy is likely to form during the growth step via Ostwald ripening. Initially described in 1900,[94] it is based on the solubilization of small metallic nanoparticles, leading to their aggregation into larger nanoparticles with or without the formation of a particular shape. Some faces of the particle will be more stable than others, and the aggregation will be preferred on one face, leading to the shape change of the M-NPs.

Like other materials, AuNPs can still be toxic at high concentrations, approaching the $\mu g.mL^{-1}$ range.[95] Some factors can reduce their toxicity, like a suitable coating for the targeted medium (citrate, cysteine, PEG, or PSS) of the particle, demonstrated by some *in vitro* studies.[96,97] Generally, their surface chemistry must remain neutral, as the presence of charged surface agents, such as CTAB, induces binding of the particle to DNA and can cause degradation.[98] The removal of these toxic surfactants after the synthesis can reduce their toxicity.[99] Disappointingly, anisotropic shapes tend to increase their aggregation and thus their toxicity, and small AuNPs (10 – 15 nm) tend to be more toxic than their bigger counterparts (200 – 250 nm) by their accumulation in tissues, blood, liver, kidney, heart, spleen, and lung.[100,101] It is important to note that the global toxicity of gold nanoparticles remains unknown. Their complete clearance from the body and their long-term effects are still under discussion.[98] Even if gold nanoparticles can be safely used for therapeutic applications, they are not biodegradable. They are eliminated from the body via either renal clearance or biliary excretion, which unfortunately impacts their suitability for medical applications.[102]

The main drawback of classic chemical syntheses of AuNPs is the use of inherently toxic compounds, such as cationic surfactants like CTAB or CTAC (hexadecyltrimethylammonium chloride), which serve as templating agents, making them unsuitable for biological applications. This weakness calls for a switch to green chemistry synthesis and the use of more eco-friendly chemical reactants to produce less toxic nanoparticles, thereby bypassing the inherent problems of traditional chemical syntheses (more expensive, complex syntheses).[88]

In comparison to chemical syntheses, a physical technique can be employed by ablating bulk gold with laser irradiation. This more straightforward method has the advantages of being cheap, involving only bulk gold, and not forming any impurities. However, even if this alternative can be « greener », laser ablation requires a higher amount of energy, induces agglomeration of AuNPs, and the sizes can be very inhomogeneous.[103,104]

2.3. Green syntheses of anisotropic gold nanoparticles

The use of toxic surfactants and toxic reducing agents calls for a switch to green chemistry syntheses. Given that chemical routes for synthesizing AuNPs involve toxic compounds, eco-friendly agents offer a green alternative to classical chemical synthesis for fabricating gold nanoparticles, thereby bypassing the problem of precursor adsorption.[88]

From a point of view of green chemistry, three aspects should be respected for the preparation of AuNPs: 1) the use of an adequate solvent, 2) the use of a green reducing agent, and 3) stabilizing agents which must be from non-toxic materials.

By following a bottom-up strategy, the green *in situ* synthesis of gold nanoparticles can be described in two fundamental steps:[105] 1) the reducing step: the electrons in the surroundings of the green reducing agent will reduce the gold cation to Au(0), and 2) the stabilizing step: once formed, the AuNPs are stabilized and protected from aggregation by a capping or stabilizing agent, which control the size and the shape of the gold nanoparticles.

Possibly the greenest option for reducing metallic cations and stabilizing nanoparticles is using a plant extract. These organic green extracts, in addition to being non-toxic and suitable for bio-friendly applications,[106] can facilitate the large-scale and low-cost production of NPs.[107] Furthermore, by comparison to other green reducing agents like bacteria and fungi,[108,109] reducing agents from plant extracts have two main advantages: 1) the reduction of the metallic salt is instantaneous, and 2) there is no need to take care of the cultures.[110] In plant extracts, the chemical agents responsible for the gold reduction are the phytochemicals from the secondary metabolites (mainly flavonoids, terpenoids, phenolic compounds, proteins, polysaccharides). Also, flavonoids, terpenoids, polyphenols, alkaloids, or sugars can contribute to the stabilization of the AuNPs formed.[111]

For instance, flavonoids, among the most common polyphenols used for the green synthesis of NPs, were extracted from *Hibiscus rosa-sinensis* for the reduction of Au(III) and the stabilization of the gold nanoparticles.[112] The case of flavonoids is interesting because it demonstrates the importance of their phenol part and their hydroxyl groups, which are needed for the reduction of the metallic cation and the stabilization of the nanoparticles.

However, even if the use of direct plant extracts can be desirable because of their simplicity, the presence of a high diversity of molecules in the extract conveys an uncertainty about the exact molecule involved in the formation mechanism, and consequently, brings an unknown parameter for future interaction with the target in view of biological applications. Furthermore,

plant extracts are never the same over different seasons, harvesting location, or extraction procedures, making the gold nanoparticles synthesis more complex, energy and time consuming, and less reproducible, and ultimately, any biological outcome less replicable.[81]

Here, we propose a compromise: instead of using a crude plant extract, we choose to use two easily isolable, cheap, and available molecules: one from a rhizome medicinal plant, curcumin, and the second is an FDA-approved molecule, an analogue to the well-known indigo obtained from leaves of the *Tinctorial* plants, indigo carmine. These molecules are broadly described further in the manuscript in their respective chapters.

2.4. Photodynamic therapy

First reported by Raab and von Tappeiner in 1900,[113,114] photodynamic therapy is a non-invasive and non-selective technique based on the generation of reactive oxygen species as therapeutic agents induced by light irradiation. PDT can be used clinically in both cancer therapy and to overcome bacterial multidrug resistance.[115,116] Furthermore, PDT can improve the immune response to cancer.[117]

PDT is performed using a photosensitizer that is triggered by light at a specific wavelength. After irradiation of the PS, an intersystem crossing (ISC) takes place from the short-lived excited state (S_1, singlet state) of the PS toward the long-lived excited triplet state (T_1). Then, the excited PS can take three different pathways: 1) the excited T_1 can return to the ground state S_0 with phosphorescence emission or with non-radiative decay, 2) with an electron transfer reaction type, the transfer of an electron from the PS to the surrounding molecular oxygen (O_2 ($^3\Sigma_g^-$), or $^3O_2$) (oxygen ground state) will occur, leading to the formation of a first ROS, $O_2^{-\bullet}$. This radical agent can then lead to other reactive oxygen species: H_2O_2, or $HO^\bullet$ (Type I reaction). However, the transfer of an electron from the organic substrate (i.e., proteins, amino acids, lipids, or nucleic acids) to the excited PS does not lead to the formation of ROS. Moreover, 3) an energy transfer reaction type, from the PS to surrounding dissolved triplet molecular oxygen, which will then turn into highly reactive singlet oxygen (O_2 ($^1\Delta_g$), or $^1O_2$), another ROS (Type II reaction) (Figure 12). By comparison to the excitation of the PS, only a small quantity of energy is needed to form singlet oxygen (22 kcal or about 1 eV or about 1270 nm).[118] The three different pathways operate simultaneously, but the ratio of each reaction type depends mainly on 1) the chemical structure of the photosensitizer, and 2) the concentration of the surrounding oxygen.

Both electron and energy transfer reactions were first described by Foot in 1968 and 1991,[118,119] and then newly updated by Baptista in 2017 and 2021.[120,121]

Responsible for the cellular toxicity, reactive oxygen species are highly reactive chemicals formed from dioxygen. In the Type I mechanism, the outcome of the electron transfer reaction can be the formation of a crosslink between proteins and DNA or the oxidation of nucleobases, amino acids, or lipids. On the other side, in the Type II mechanism, singlet oxygen reacts with nucleic acids, amino acids, and lipids.[121] By oxidation of the biological material, they are responsible for their oxidative stress, leading to the death of the cell. The Type I reaction leads to necrosis, while the Type II reaction leads to apoptosis or autophagy of the cell; the latter is highly dependent on oxygen supply, [122] and is the principal reaction type in photodynamic therapy.[123]

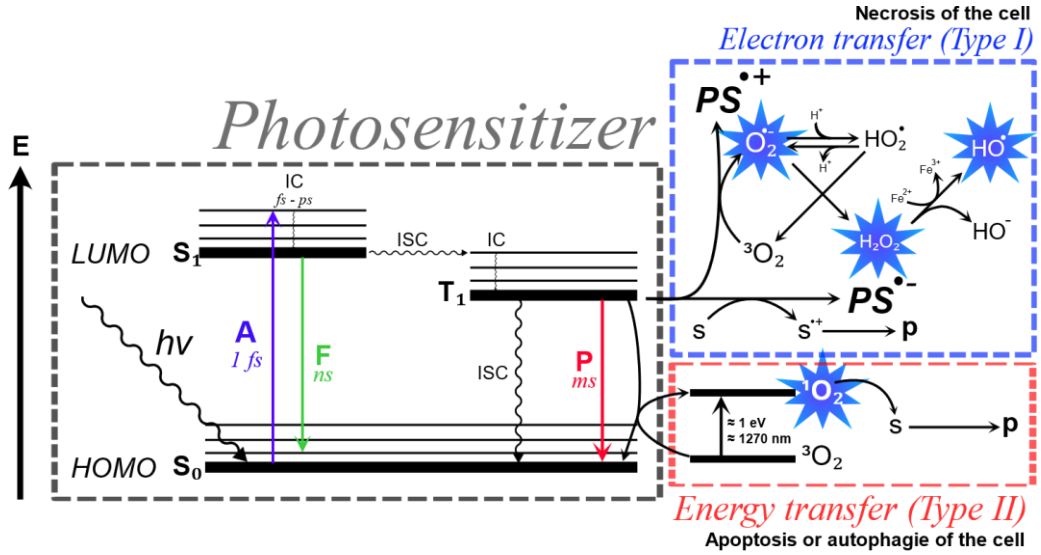

Figure 12: Simplified Jablonski Diagram of a single photon absorption by a PS and its energy transfer to dioxygen in photodynamic therapy; HOMO: highest occupied molecular orbital; LUMO: lowest unoccupied molecular orbital; S_n: singlet spin multiplicity; hν: photon energy; T_n: triplet spin multiplicity; A: absorbance; F: fluorescence; P: phosphorescence; IC: internal conversion; ISC: intersystem crossing; s: substrate (amino acids, nucleic acids, lipids, proteins); p: product.

The efficacy of PDT depends on the photosensitizer's effectiveness. To activate the PS, the wavelength used in PDT depends on its absorption, which is generally in the red and near-infrared regions, between 630 and 730 nm, due to the absorption of hemoglobin (Hb) and oxyhemoglobin (HbO_2).[18] To be efficient, a photosensitizer needs to have firstly a good singlet oxygen quantum yield (Φ_Δ) ($\Phi_\Delta \geq 0.5$) and a good conversion by ISC to triplet state yield ($\Phi_T \geq 0.5$), a long triplet state lifetime (microsecond order), a high light absorption, an excellent

photostability and solubility in water media, a good selectivity to the target (non-toxicity in dark conditions), and not to form aggregates.[124,125,126] Some of the most common photosensitizers are organic compounds, such as porphyrins, phthalocyanines, or BODIPY (boron-dipyrromethene). Metal-free inorganic, metal complexes, MOFs, or fullerenes, and pure metallic inorganic nanoparticles can also be used as PS.[127]

One of the limitations of the PS is the photobleaching of the dye, possible by two different ways: 1) the reaction between the PS at S_0 with singlet oxygen, resulting in an oxidized photoproduct, or 2) in the Type I electron transfer mechanism, the excited PS at T_1 can react with the biological material and become $PS^{\bullet-}$ or $PS^{\bullet+}$.[128] The main challenge of PDT is the extremely short lifetime of singlet oxygen in living systems. Its lifetime, in the range of 0.03 to 3 μs, is due to the unstable electronic configuration of $^1O_2$, which leads to high reactivity with the biological milieu,[129,130] and its range of action is approximately 0.01 – 0.02 μm in diameter.[131]

Since the lifetime of singlet oxygen depends on the milieu, due to the non-homogeneity of the cell and its changing viscosity, the nature and localization of the PS are crucial for efficient biological applications. After the administration of the drug topically or by intravenous,[132] due to their structure, each photosensitive molecule can have a different cellular uptake mechanism and be accumulated in a different part of the cell. Thus, the initial site of damage is very structure-dependent on the PS. Lipophilic photosensitizers are more commonly used in clinical applications due to their ability to bind to membranes.[37] Aside from its structure, the accumulation area of the photosensitizer in the cell can be dependent on other factors, like the solvent or its concentration. Its target itself can also influence the localization of the PS, such as cell density or the structure of the targeted cytoplasmic membrane (Gram-positive or Gram-negative bacteria).[133] Nevertheless, the intracellular location of the PS is not unalterable. After a long incubation time (about seven hours), the relocalization of porphyrin from the plasma to the nuclear membrane has been reported.[134] Similarly, after light irradiation, a photosensitizer can be repositioned through another process called photorelocalization. The mobility of the PS can be achieved after low irradiations, where the first ones induce the new mobility of the photosensitive molecule. Successive irradiations lead to photobleaching and are not involved in the relocalization process.[135]

One of the key advantages of PDT is its multi-targeting mechanism, which enables the degradation of primary biological intracellular structures, including nucleic acids, proteins, and lipids.[136] DNA and the plasma membrane are the two vital components of bacteria that, once

damaged by ROS, lead to bacterial death. This multi-targeting strategy prevents the bacteria from developing new resistance.[133,137]

To summarize, the PS can be found at three different localizations: 1) outside the cell where the photosensitizer will damage the plasma membrane; 2) linked or integrated to the cell wall and so, by diffusion, the PS can easily go into the intracellular area, or 3) the PS is connected and absorbed into the cell and will damage the intracellular components.[133] A photosensitizer without a vector, which is not able to penetrate inside the cells, will be highly ineffective in causing cell death.[138]

Additionally, unlike PTT, which can remain active for a short time after irradiation due to slower heat diffusion, the photosensitizer's action stops immediately when the light source is turned off.[18] Furthermore, the time needed to observe cell death is slower, and the initiation of the apoptosis mechanism can take up to three days.[138]

Even if PDT is not a selective technique in itself, selectivity can still be achieved for tumor destruction through the use of vectors or the accumulation of the PS at the target site. With the different properties tumorous and healthy cells have, the photosensitizer can aggregate because of: 1) the EPR effect; 2) the slight acidic milieu at the exterior of the target (between pH = 5 and 7) inducing a protonation of the PS and increasing their hydrophobicity;[139] 3) the cancer cells poor lymphatic system, allowing the PS to have a better retention time.[37]

In cancer therapy, PDT operates by three main mechanisms of action: 1) the ROS kill the cancerous cells directly; 2) the PDT damages the tumor vascular system; and 3) PDT can activate an inflammatory and immune response. These three mechanisms are necessary for a long-term effect. However, many drawbacks make photodynamic therapy alone not the most efficient technique for cancer therapy, such as the non-homogeneous dispersion of the photosensitizer within the cancerous cells. However, the most important one remains the lack of oxygen within tumors. This depletion can prevent the formation of $^1O_2$ and occurs due to the high oxygen consumption rate of the photosensitizer and the damaged microvasculature, a consequence of post-PDT treatment, leading to reduced oxygen supply.

Several solutions exist to overcome the lack of oxygen. For example, light delivered in short pulses (between 20 and 50 seconds) has been reported to facilitate reoxygenation during brief non-irradiated periods.[138] A fractionated injection of the photosensitizer before light irradiation can also be an effective way to prevent hypoxic conditions in cancerous cells and blood vessels by limiting the amount of oxygen consumed. This fractionated method also yields better results

and a more significant long-term effect on tumor growth than a single injection of photosensitizers.[140]

A combined PTT/PDT system is a promising strategy for combating multidrug resistance in cancer cells and bacteria. Since light is required in both treatments, if irradiated at the same correct wavelength, the photosensitive system can deploy PTT and PDT simultaneously for a multimodal strategy. Furthermore, additive or synergistic effects can manifest themselves. For instance, the irradiation of a photothermal agent can enhance the generation of singlet oxygen from a photosensitizer.[141,142] Alternatively, the ROS produced can decrease the target's heat resistance.[143] Other outcome: the heat generated by photothermal therapy may allow the disruption of the plasma membrane of the surrounding cells, increasing the permeability, and ultimately allowing other PS, ROS, or drugs to enter the intracellular area of the cell.[144] Finally, in the event of hypoxic conditions, photothermal therapy (which is independent of molecular oxygen concentration) can complement the photodynamic therapy to maintain treatment continuity and efficacy/efficiency of treatment.

It is worth noting that in cancer therapy, both PDT and PTT are typically used as complements to classical therapeutic modalities against solid tumors (chemotherapy and/or radiotherapy) to enhance their therapeutic effects. To date, these techniques are not sufficient to be used independently of chemotherapy or radiotherapy.[145] Cooperation of PTT and/or PDT with chemotherapy can induce a lower concentration of photothermal agent and/or photosensitizer for a higher selectivity towards tumoral cells by increasing their sensibility to heat and ROS.[146]

2.5. The quadruple function of the βCD polymer

The synthetic procedure proposed for the synthesis of AuNPs in the present work requires a green reducing agent, namely, curcumin, indigo carmine, or nitric oxide radical. To overcome the problem of curcumin solubility in aqueous solvents, which will be discussed in its chapter, cyclodextrins can be used as adjuvants and as green stabilizing and templating agents for the AuNPs synthesis. Progressively described by Villiers in 1891,[147] and by Schardinger in 1911,[148] natural cyclodextrins (CDs) are cyclic supramolecular oligomers, cone-shaped entities composed of units of six, seven, or eight (αCDs, βCDs, or γCDs) D-(+)-glycopyranose units

linked together by α-1,4-glycosidic bonds. Their distinctive conic shape is due to the chair configuration of these glycopyranose units (Figure 13).[149]

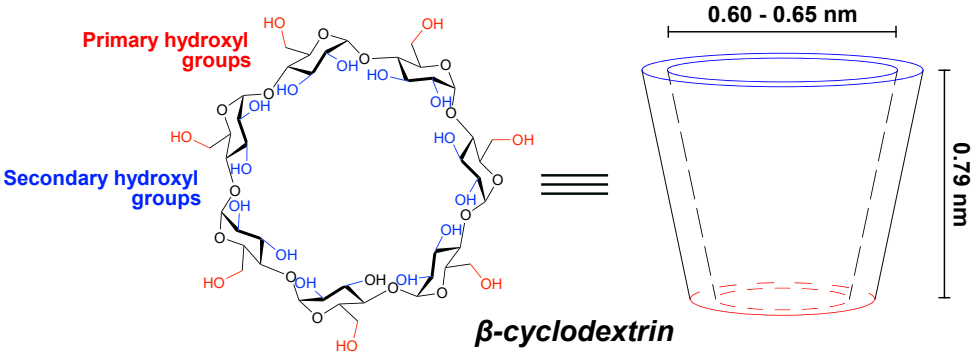

Figure 13: Molecular structure of βCD on the left and its schematic representation on the right. Primary hydroxyl groups are highlighted in red, while secondary ones are represented in blue.

CDs are water-soluble compounds that can form inclusion complexes (partially or entirely) with a wide variety of guest molecules (organic or inorganic, neutral or ionic, or even with noble gases) with compatible polarity and dimensions.[150] The cavity size is dependent on the number of glucose units. The capacity to form inclusion complexes with guest molecules arises from the presence of hydrogen atoms and nonbonding electron pairs on the internal hydrophobic side of the glycosidic oxygen atoms. The latter produces a high electron density at the cyclodextrin core and confers nucleophilic character to the cavity. *In fine*, the supramolecular structure of the host-guest complex is formed by non-covalent interactions, including hydrogen bonds and van der Waals forces, between the host and guest molecules.[150]

βCDs have a cavity size between 0.60 and 0.65 nm, and their height is about 0.79 nm.[151] Their use is preferred over αCDs because their cavity size is smaller (between 0.47 and 0.53 nm), and the guest drug, photosensitizer, or reductive agent cannot be well complexed with αCDs. While for γCDs, their larger opening (between 0.75 and 0.83 nm) allows the guest reductive agent to be more protected by a better fit of the phenol size with γCD's cavity;[152] however, since the photochemical properties of a guest photo-sensible molecule are highly dependent on its environment,[153] the higher protection may directly lead to less irradiation sensitivity.

The cyclodextrin's solubility is due to the presence on its external side of a ring of hydrogen bonds, increasing the rigidity and solubility of the cyclic molecule. However, the external ring is not present in the case of βCDs; indeed, since the belt of hydrogens formed by hydrogen bonds is complete and much more rigid, this increases the rigidity of the structure and decreases the capacity of βCDs to form hydrogen bonds with water molecules.[154] The βCD solubility can be enhanced by its integration into a polymer chain, reducing its self-complexation and aggregation by breaking the hydrogen bonding between βCDs monomers and water.[155,156] The cross-linking of βCDs is performed by a glyceryl bridge formed by epichlorohydrin precursor in an alkaline milieu (Figure 14).[157]

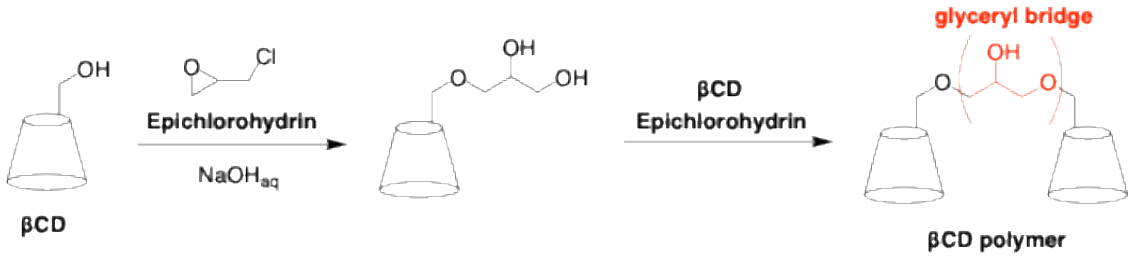

Figure 14: Schematic representation of a polymerization synthesis of βCD in alkaline medium, cross-linked with epichlorohydrin. Glyceryl bridges, represented in red, are formed between βCD monomers.

Their complexing and, consequently, their solubilization capacity can be modified and improved depending on whether the polymer exhibits ionic interactions.[158] If the charge between the host and the guest molecules is the same, due to Coulomb forces, the complex will be less stable. On the other hand, if the charges of the two constituents are opposed, it results in a higher complexation stability.[159] Is it important to note that the number and the position of cyclodextrin substitutions can influence the guest molecule complexation. Consequently, the βCDs polymer can exhibit different complexation towards targets, in our case green reducing agents, and thus alter their absorbance spectra.

The union of a photosensitizer with CDs for PDT application is essential. Due to the hydrophobic nature of most organic photosensitizers that absorb in biological windows, their tendency to aggregate in aqueous environments reduces light absorption, slowing singlet oxygen production and shortening fluorescence lifetimes.[127] The versatile structures of cyclodextrins allow the consideration of covalent or supramolecular approaches for incorporating the photosensitizer into the nanoscale system for further PDT applications. For the covalent approach, the βCDs polymer will be *ad hoc* modified and linked to a PS unit.

Conversely, the supramolecular procedure will utilize the cavities of the CDs and the binding properties of side chains to load the PS.

The choice to use βCD polymer instead of individual βCDs is also driven by the ability to participate in the formation of stable and activatable gold nanoparticles in the near-infrared region. As reported,[160,161] the βCD polymer will play the role of a stabilizer and templating agent for the synthesis of AuNPs. The polymer's stabilizing property is due to its proximity to gold, which quenches the redox process.

Regarding the choice of the polymer cross-linking agent, it is worth noting that epichlorohydrin, used as a precursor for the glyceryl bridge, can pose some toxicity concerns. Only citric acid has been proposed as a good green cross-linking agent for the synthesis of γCD polymers.[162] Despite the inherent toxicity of the glyceryl bridge precursor, no other green cross-linking agents have been proposed for βCD polymers.

* * *

To summarize, the βCD polymer will be used due to its ability to template and stabilize gold nanoparticles, enhance the solubility of the green reducing agent, and carry any other molecule of interest for the preparation of multimodal NPs (PS or a drug). Moreover, in the specific field of photothermal therapy, being able to monitor temperature variations is crucial to not induce any damage to healthy cells, and βCD polymers provide an opportunity to develop an innovative system that presents both photothermal properties and a fluorescent report of the thermal increase. This thermometer will be described in detail below in a dedicated chapter.

2.6. Light-induced green synthesis of anisotropic gold nanoparticles with PDT and PTT applications in the state of the art

Some papers have reported the light-induced fabrication of green AuNPs.[163,164] Sen *et al.* reported the synthesis of spherical AuNPs performed under sunlight irradiation using PEG as a green reducing agent. The light was generally used to initiate the radical formation directly from the solvent or to excite photoinitiator compounds.

Plasmon-mediated synthesis of anisotropic AuNPs was also reported. Unlike the one based on the reduction of the metallic salts, these are centered on the irradiation of already formed M-

NPs at their LSPR band, facilitating the easier reduction of metallic cations.[165] For instance, in 2016, Zhai *et al.* achieved plasmon-driven synthesis of gold nanoprisms using a PVP (polyvinylpyrrolidone) surfactant on spherical AuNPs seeds to direct particle growth during visible green irradiation.[166]

Kumar *et al.* reported the synthesis of AuNPs from the photoreduction of $HAuCl_4$ with the irradiation of curcumin. Although they report that changing the irradiation wavelength influences the reduction kinetics and the shape of the formed NPs, the red light used by the authors does not match the absorption spectrum of curcumin, leaving the mechanism involved unclear. Despite some anisotropic structures observed in TEM images, the majority of the particles are spherical, and no absorbance bands are observed in the reported UV spectra. The reported percentage of anisotropy achieved in the sample is approximately 40 %. The dark control also reports the synthesis of isotropic and anisotropic AuNPs. These particles were used only for catalytic applications.[167]

Our group has already had a great experience with the green synthesis of metallic nanoparticles using green reducing agents. Seggio, Laneri *et al.* reported the synthesis of AuNPs where the gold salts were reduced by pomegranate extract, with the latter beforehand solubilized in β-cyclodextrins polymer, without preformed seeds, external reducing agents, or classical chemical surfactants.[160]
Nocito *et al.* also succeeded in forming gold nanotriangles from light irradiation of nitroaniline, a nitric oxide photodonor, as a reducing agent linked to a branched βCD polymer, and achieved a rise of the temperature up to 18 °C in the near infrared region.[161]

A Chinese group, led by Lv and coworkers,[168] reported the green synthesis of gold nanotriangles for direct use in PDT and PTT applications. However, light was not involved in the fabrication of the particles, and their photothermal properties were not described.

There is a lack of reported light-induced green synthesis of seedless anisotropic gold nanostructures incorporating a ratiometric fluorescent thermometer, for both photothermal and photodynamic therapies applications, with *in vitro* and *in vivo* applications.

.

3. Methodology and characterization techniques

To achieve the green synthesis of AuNPs for PTT and PDT biological applications, we divided the project work into the development of three independent synthetic methodologies. In the first two chapters, we investigated respectively the green synthesis of anisotropic particles using curcumin (Cur) and then indigo carmine (IndC), followed, for each, by the study of their physical characteristics and photothermal properties. Then, research work was done on the *in vitro* photoinduced cytotoxicity of these AuNPs on both bacteria and cancer cells. Ultimately, we investigated the addition of a photosensitizer for potential use in photodynamic therapy applications. In the sixth chapter, we present the synthesis of an innovative platform featuring a ratiometric fluorescent thermometer, from the investigation of the optimal dye ratio to the final platform synthesis. A first attempt is made to assess the growth of AuNPs in this mixture of fluorescent polymer. In this final part, the tetrachloroauric acid trihydrate is reduced with a nitric oxide radical from different nitric oxide photodonors (NOPD) compounds: S-nitrosoglutathione (GSNO) and nitroaniline-adamantane (NA-Ad). We present the characterization of synthesized AuNPs, their biological properties, and the respective syntheses of the two NOPD all along the three chapters of this manuscript.

For each AuNPs synthesis described in the next section, we used light as a green reactant. The irradiated systems with different reducing agents, i.e., curcumin, indigo carmine, S-nitrosoglutathione, or nitroaniline-adamantane, were compared with their respective control samples kept in the dark to highlight any differences resulting from irradiation. Our strategy is to utilize light as a green reactant to control the synthesis of gold nanoparticles. The controlled irradiation (in terms of time and intensity) of the green reducing agent is intended to result in a controlled reduction of $HAuCl_4 \cdot 3H_2O$, thereby controlling the size and shape of the synthesized nanoparticles. We observed the absorbance evolution of both samples using a UV-Vis spectrophotometer with a measurement window extending into the NIR to monitor any LSPR band rise within the biological window.

To easily understand, discuss, and compare all the different AuNPs syntheses, a code name is attributed to each sample. The first letter (R) corresponds to the reducing agent or its photoinduced precursor employed for the formation of the gold nanoparticles: curcumin (C), indigo carmine (I), S-nitrosoglutathione (S), and nitroaniline-adamantane (N). Then, the letter of the reducing agent is followed by the experiment number (n = 1, 2, 3, etc.), and subsequently by the batch name (x = a, b, or c). A letter (p) is used to specify a combination of different

batches synthesized. Ultimately, the particles formed under light irradiation are marked with (L) and their dark control with (D) (Figure 15).

$$Rnx - L$$

Figure 15: Code name for samples of synthesized AuNPs. R: reducing agent, n: experiment number, x: batch number, L: irradiated conditions, D: dark conditions.

Along with their characterization by absorbance spectrum, the characterization of the gold nanoparticles synthesized is one of the most critical steps in this work. Indeed, a complete understanding of their structure is necessary for subsequent synthesis optimization and for accurately assessing their photophysical and biological properties. Unlike organic or organometallic molecules, we cannot achieve their characterization with a simple routine analysis technique. Multiple techniques and instruments are required to characterize all aspects (light absorption and emission, size, size distribution, shape, photothermal properties, surface characterization, crystalline structure) of the synthesized nanoparticles. Relying on only one or two techniques can yield an incomplete picture of nanoparticles and, consequently, lead to incorrect conclusions about their properties. For each experiment, nanoparticle's characteristics were investigated, whenever possible, for both irradiated and dark control samples.

Nevertheless, due to the ease and rapidity of absorbance measurements provided by a UV-Vis spectrophotometer, this characterization technique is the method of choice for a rapidly changing colored system, such as the formation of gold nanoparticles. Composed of a lamp (tungsten and deuterium lamps for visible and ultraviolet light), the monochromator selects the irradiation wavelength that passes through the sample. Then the detector subtracts the intensity difference from a blank sample.[85] The UV-Vis spectrum of the gold nanoparticles allows for an estimation of the colloidal concentration, size, and aggregation level.[169]

To have a better understanding of the absorbance evolution during the synthesis of the gold nanoparticles presented in the following sections, the time written in the legend is not a sum; instead, it represents the irradiation time and/or the stirring time. We stopped the gold nanoparticle syntheses (irradiation and/or stirring) when the absorbance system stopped evolving. Furthermore, we performed absorbance measurements after the end of the synthesis to monitor the evolution of absorbance over long time periods (typically represented by dotted lines). Additionally, we did not perform any further stirring except as explicitly mentioned. We choose not to consider the time needed for the spectrophotometer to perform the measurement,

since no physical or chemical change was introduced to the system. The measurement time varies depending on the UV-Vis spectrophotometer used; it is approximately 1 minute and 30 seconds, with a measurement window ranging from 190 to 1100 nm for the PerkinElmer UV-Vis spectrophotometer. Furthermore, in the legend of some absorption spectra, it is mentioned "t_n (scan X)" measures; we performed these absorbance spectra without any stirring or irradiation, under identical conditions from the previous spectra (t_n or t_n (scan (X-1)). We performed them to observe the system's immediate response to gold addition or to determine whether it evolved between measurements. The time between each "t_n (scan X)" is generally two minutes and forty-five seconds because of the time needed for: 1) the measure itself, 2) the renaming of the spectra on the spectrophotometer software, and 3) the launch of the measure.

All syntheses were performed directly in a 1 cm absorbance or fluorescence cuvette to monitor absorbance evolution during synthesis and to minimize physical changes to the system by avoiding the need to pipette the solution in and out of the cuvette for absorbance measurements. When the absorbance intensity was too high to monitor any evolution, we performed the synthesis in a 1 cm cuvette and measured the absorbance evolution in a 1 mm cuvette despite the unpredictable physical changes that occurred during pipetting.

We used Dynamic Light Scattering (DLS) to characterize the hydrodynamic diameter and polydispersity index (PDI) of spherical gold nanoparticles by the light scattering through the nanoparticles. DLS is generally used as a routine technique to define the particle size. The method is based on the Brownian motion of nanoparticles to determine their size; the larger the particles, the slower they move, and thus more light is scattered by large particles than by small AuNPs. Aggregated or anisotropic nanoparticles are not suited for DLS size measurements.[85]

We utilize Nanoparticle Tracking Analysis (NTA) to complement DLS measurements. The technique is also based on the Brownian motion of the particles and allows for determining the size of the NPs and their concentration per milliliter. Compared with DLS, NTA offers better peak resolution and can measure the Zeta potential of the particle surface. It is important to note that this characterization technique does not allow one to "see" the particle. The main drawbacks of NTA are the lengthy sample preparation, the highly user-dependent instrument configuration, and the camera parameter configuration.[170]

To obtain information about the surface topography of the AuNPs, Atomic Force Microscopy (AFM) can be used to visualize the 3D surface of the particles by a tip, which wanders the height variation to map the particles' surface with sub-nanometer precision. In the present work,

this technique can leverage the mechanical differences between polymeric organic structures (βCD polymers) and metallic objects (AuNPs) to discern the distinct spatial composition of the nanostructures.[171]

Transmission Electron Microscopy (TEM) is another characterization technique that provides information on the organization of particles at the atomic level, primarily used to observe the shape and the size of the NPs synthesized. The TEM imaging technique uses an electron beam rather than light to observe gold nanoparticles with, in the present work, a high contrast. With a contrast difference observed within the same or different nanoparticles, it is possible to identify thicker or thinner particles visually. To prepare the sample, a thin layer of colloidal solution is deposited onto a carbon film supported by a 200-square-mesh copper grid. From TEM images and with a high number of nanoparticles, it is also possible to estimate the size distribution of the NPs and their aspect ratio.[85]

All biological assays on cancerous cells and bacteria of the different formulations of the synthesized AuNPs were conducted, respectively, in collaboration with Prof. Tristan Montier and Dr. Tony Le Gall, in the GTCA Team, UMR INSERM 1078 (Brest, France).

.

4. *"Green" synthesis of a gold nanosystem from curcumin, a plant extract*

4.1. Curcumin, plant extract from *Curcuma longa L.*

Curcumin ((1*E*,6*E*)-1,7-bis(4-hydroxy-3-methoxyphenyl)-1,6-heptadiene-3,5-dione) is a low molecular (M = 368.38 g.mol^{-1}) plant extract compound from *Curcuma longa L.* rhizomes (Figure 16). This polyphenol is an orange powder used as a textile dye and as a spice. It is safe to be eaten up to 12 g per day,[172] and has numerous therapeutic properties, including antioxidant,[173] antitumoral,[174] antimutagenic,[175] anticarcinogenic,[176] anti-inflammatory,[177] antimicrobial, antihepatotoxic,[178] and antiviral effects.[179,180] However, its use for medicinal purposes remains limited because of its low solubility in water, resulting in a lower bioavailability.

Figure 16: Illustration of *Curcuma longa L.* by Franz Eugen Köhler, in Köhler's Medizinal-Pflanzen, 1887.[181]

The chemical structure of curcumin is characterized by two aromatic ring systems with two *ortho*-methyl phenolic groups and a bis-α,β-unsaturated β-diketone. Inherent to this structure, a keto-enol tautomerism is present. The equilibrium between diketo and keto-enol configurations is influenced by the pH value of the milieu and the solvent. Its predominant form in acidic and neutral media is the bis-keto form; otherwise, in alkaline solutions, the keto-enol configuration prevails (Figure 17).[182] About the nature of the solvent, protic solvents will induce intermolecular hydrogen bonding with the diketone group, and consequently will favor the bis-keto form.[183] The keto-enol form is also favored because of the presence of the conjugation between both phenol groups.

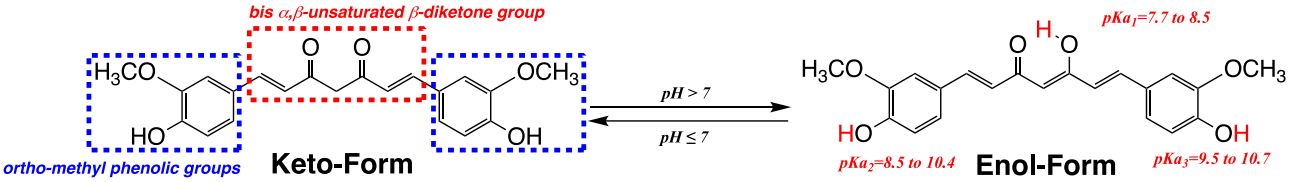

Figure 17: Keto-enol tautomerism of curcumin. Its chemical structure is different depending on the medium. The keto-enol form is predominant in alkaline media, and the bis-keto form is predominant in neutral and acidic media.

Curcumin is not soluble in water at neutral or acidic pH. Its solubility in alkaline water is due mainly to its acidic phenol group by the formation of a phenolate ion, increasing then the solubility of the dye.[184]

The curcumin deprotonation is characterized by three prototropic equilibria between each form of deprotonated curcumin. DFT calculations determined the position of the first deprotonation.[185] The latter occurs between pH 7.7 and 8.5 (pKa1) at the β-diketone proton position on the keto-enol form of the curcumin, which is predominant in alkaline media. The second and third deprotonations, responsible for curcumin's solubility in basic conditions, occur at pH values of 8.5–10.4 (pKa2) and 9.5–10.7 (pKa3), respectively. These broad pKa ranges arise from the solvent used and the methods employed to determine them. At physiological pH (pH = 7.4), from 10 to 25 % of curcumin has lost its enolic proton, while the rest is composed of the non-deprotonated form of curcumin.[186]

On account of this non-solubility in aqueous solvent at physiological pH, the bioavailability of curcumin is difficult, and consequently, its therapeutic effect seems misleading. The health benefits of curcumin appear to be caused not by the molecule itself but by the products of its degradation. In water, at pH = 7.4, the main products of curcumin degradation are

bicyclopentadione (by autooxidation), vanillin or ferulic acid (by carbon chain cleavage), or hexahydrocurcumin (by reduction of the double bonds).[184,187]

The main factors of curcumin degradation are various: alkaline conditions, oxygen, metallic ions, enzymes, ascorbic acid, and heat.[188] Also, curcumin is very unstable under light irradiation. Even though its photodegradation mechanism is still not fully understood, it appears that breaking the β-diketone bond leads to degradation products, notably vanillin and ferulic acid.[186]

If we use curcumin as a green reducing agent for the formation of metallic nanoparticles, two possible mechanisms can lead to the reduction of the gold salts: 1) redox and 2) photoinduced redox. In the first mechanism, the anionic curcumin reduces the cationic metallic center to M(0) and stabilizes the formed M-NPs. For the formation of gold nanoparticles, since curcumin redox potential, at pH = 7.4, is about E° = +0.66 V (SHE (Standard Hydrogen Electrode)),[189] and so is inferior to the one of the primary precursor for seedless AuNPs, tetrachloroauric (III) acid, with E° = +0.99 V (SHE),[190] the reduction of gold salts is possible. However, the oxidation of curcumin will spontaneously occur even in the absence of light. The second mechanism is initiated by irradiation of curcumin, which leads to its triplet state. This transient species will form a ketyl radical after the transfer of a hydrogen radical via a hydrogen-atom transfer (HAT) reaction, generally from the irradiated solvent.[183] Interactions between the transient species produced during curcumin irradiation and cationic gold may contribute to the formation of AuNPs (Figure 18).

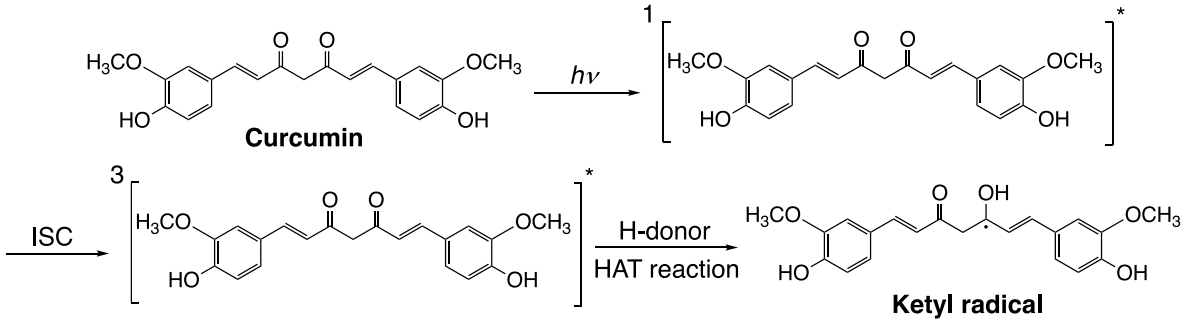

Figure 18: Possible photoinduced mechanism to induce the reduction of gold salts. The ketyl radical curcumin is formed from the irradiation of curcumin, followed by a HAT reaction. ISC: inter-system crossing; HAT: hydrogen-atom transfer.

Even if the photo-induced degradation of curcumin occurs already at the solid state, its bleaching occurs essentially in dissolved form. The byproducts of its degradation depend on

the wavelength (curcumin absorbs strongly in the visible part of the electromagnetic spectrum and undergoes greater damage than with UV irradiation) and the nature of the organic solvent.[191]

Curcumin can be used as a PS for photodynamic therapy, as its irradiation leads to the formation of a triplet excited state and the release of singlet oxygen upon irradiation in the visible range (420 – 480 nm).[192] Curcumin can induce both Type I and Type II reactions. At first, this feature may appear very appealing in the context of employing a bimodal system that presents PTT properties via AuNPs and PDT via curcumin. However, the obtention of this double feature is unlikely as it would require that a part of the curcumin remains pristine after the AuNPs formation. Moreover, curcumin's ability to produce $^1O_2$ is highly influenced by the microenvironment. It may fail in the presence of commonly used carriers (polymeric micelles, microemulsion, or Zein NPs (hydrophobic protein-based nanoparticles from maize extract)).[193] Moreover, curcumin is difficult to employ as a photosensitizer because of: 1) its low water solubility; 2) its absorption in the blue region; 3) its low singlet oxygen quantum yield, and 4) its ability to quench singlet oxygen.[193]

To improve the solubility of curcumin in aqueous solvents and, ultimately, its bioavailability, several methods have been reported, including the encapsulation of the plant extract in cells, in liposomes, or in micelles.[194,195,196,197] Unfortunately, liposome methods will need to overcome challenges such as low encapsulation efficiency, poor storage stability, or rapid leakage of water-soluble drugs in the presence of blood components. For the micelles, the drug-loading process remains a challenging task that requires improvement.[198]

In this context, we can utilize the encapsulation capacity of cyclodextrins to overcome the solubility and/or degradation problems associated with some compounds of interest. Greeted in the cavities of cyclodextrins, curcumin can benefit from a significant enhancement of its solubility, hydrolytic activity, and stability. In neutral/acidic media (pH = 5), the curcumin solubility is improved by a 10^4-fold factor. However, the increase in the hydrolytic activity allows a stronger degradation of curcumin upon light irradiation.[153] Thus, the use of a βCD polymer will likely increase curcumin solubility because of the possibility to encapsulate curcumin in the cavities of the CDs as well as to load it in the side chains of the polymer. The properties of the loaded curcumin need to be asserted as the complexation of curcumin inside βCDs cavities influences the structure of the dye,[152] and the inclusion of the dye is different in function of its keto-enol tautomerism. The bis-keto form is bent around the central carbon, while for the keto-

enol form, the presence of the hydrogen bonding between the hydroxyl and carbonyl group induces a planar geometry.[199]

4.2. AuNPs synthesis from curcumin

4.2.1. Synthesis of the gold nanoparticles with neutral βCD polymer

The initial procedure for synthesizing AuNPs was inspired by our group's previous work on synthesizing gold nanostructures, which used pomegranate fruit extract as a reducing agent.[160] The concentrations of the soluble βCD polymer crosslinked with epichlorohydrin (2 $mg.mL^{-1}$), and the gold salts (0.4 mM) were kept equal to those used in this previously described work, and commercial curcumin was used as a reducing agent. The first attempt, named C1-L, was unsatisfactory due to difficulty in solubilizing curcumin, resulting in a slight LSPR band near 520 nm for the synthesized AuNPs (Appendix I).

To improve the formation of AuNPs and ensure curcumin's action in reducing $AuCl_4^-$, the nanoparticle preparation procedure required adjustments. Additionally, in the initial experiment, the solubility of curcumin in the polymer matrix caused uncertainty about its concentration under these conditions. To well define the concentration of the reducing agent, enhance its solubility with the polymer, and employ a facile and repeatable procedure, we prepared the system Curcumin+βCDpolymer from a curcumin film as described in the experimental section (part 4.6.). The absorbance spectra of the curcumin complexed in the cyclodextrin polymer are presented in Figure 19A. When complexed inside cyclodextrin's cavities, we observe mainly two absorbance bands characteristic of two forms of the curcumin with a π-π transition. The first one with a λ_{max} at about 450 nm can be attributed to the protonated curcumin, $CurH_3$, while the other band at λ_{max} at about 520 nm can be credited to the deprotonated form of the curcumin, Cur^{3-}.[200] A deconvolution of the spectrum allows us to highlight the absorbance bands of the two forms of curcumin (Figure 19B). The third band at 270 nm is characteristic of the n-π* transition of curcumin.[201]

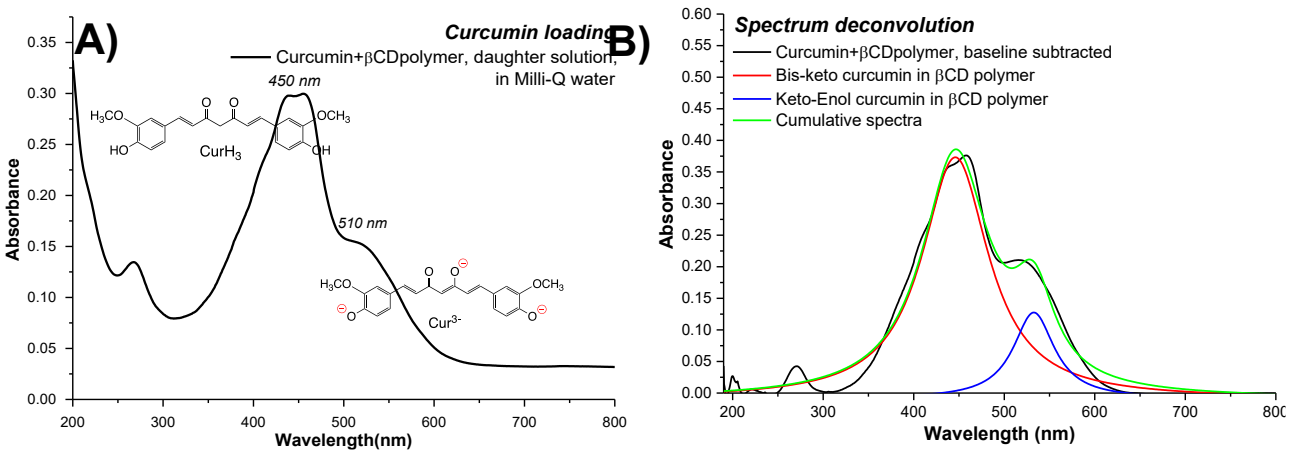

Figure 19: A) Absorbance spectrum of the system Curcumin+βCDpolymer in Milli-Q water. Measurements were performed in a 1 mm path-length absorbance cuvette using a PerkinElmer UV-Vis spectrophotometer with air as the blank. B) Deconvolution of the absorbance spectrum of Curcumin+βCDpolymer. Conditions: [Curcumin] = 0.2 mM; [βCDpolymer] = 4.04 mg.mL^{-1}.

We began investigating the irradiation of the system Curcumin+βCDpolymer before adding tetrachloroauric (III) trihydrate acid to determine whether a preliminary photodegradation of curcumin was occurring (Figure 20). Even if the signal at 447 nm is saturated due to the strong absorption of the plant extract, even with a 1 mm path-length cuvette, the one hour and fifteen minutes long irradiation with a 420 nm lamp (*ca.* 1 mW.cm^{-2}) of curcumin solubilized in the βCD polymer did not significantly decrease the absorbance of the protonated band indicating the relative stability of the extract under irradiation with a 420 nm lamp.

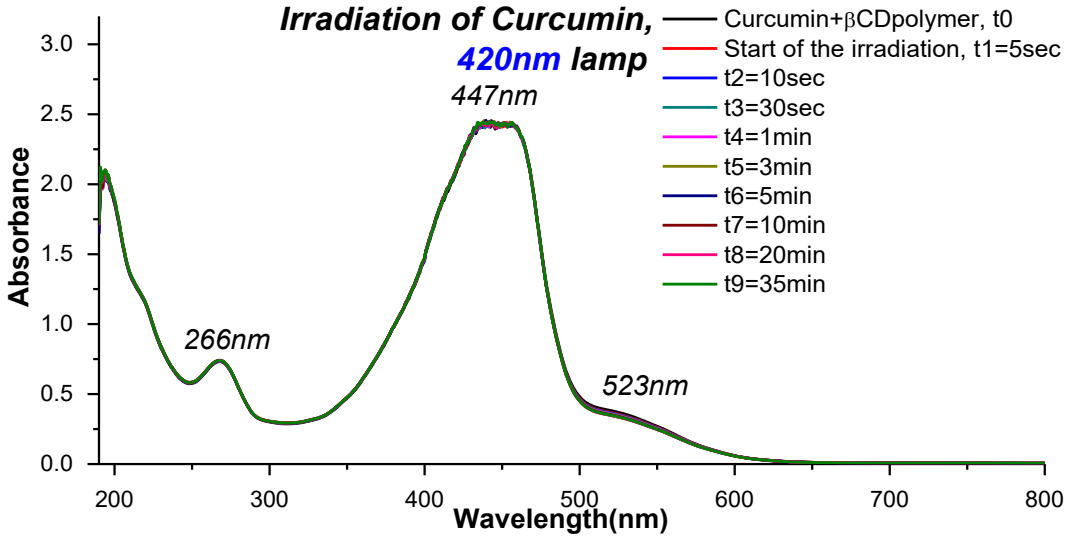

Figure 20: Comparison of the absorption evolution of Curcumin+βCDpolymer. Irradiation was performed in a 1 cm path-length fluorescence cuvette at 10 cm from the sample using a 420 nm lamp (*ca.* 1 mW.cm^{-2}). The sample was stirred during the irradiation. Measurements were performed in a 1 mm path-length absorbance cuvette using a PerkinElmer UV-Vis spectrophotometer with air as the blank. Conditions: [Curcumin] = 0.048 mM ; [βCDpolymer] = 2.0 mg.mL^{-1}.

Thus, when the complete solubility of curcumin was achieved, we added an aqueous solution of tetrachloroauric acid, $HAuCl_4 \bullet 3H_2O$ (C = 0.5 M), into the system (C2-L sample). Right after the addition of gold salts, the band of the deprotonated Cur^{3-} dropped immediately, while the absorbance band at λ_{max} = 450 nm decreased slowly over time. The sample was irradiated for 18 minutes under the same experimental conditions, 10 cm from the light source, and its absorbance evolution was monitored using a UV-Vis spectrophotometer (Figure 21). First, we observed degradation of the curcumin band at 450 nm with increasing curcumin irradiation time under the 420 nm lamp. We note the absence of a second near-infrared absorption band, characteristic of anisotropic gold nanoparticles, in contrast to the results reported by Seggio *et al.* using pomegranate extract as a reducing agent. Here, the shape of the AuNPs formed seems to be spherical because of the presence of the AuNPs' characteristic absorption band at 580 nm. Here, the AuNPs formation started some dozens of minutes after the beginning of the three-hour-and-thirty-minute-long irradiation, while Seggio reported a six-hour-long synthesis. Furthermore, it is noteworthy that no absorbance band of $AuCl_4^-$ is spotted near 310 nm, characteristic of the gold precursor in solution within the βCD polymer matrix;[202] the absence of this absorbance band (i.e., gold precursor at 310 nm) can be due to the thinner absorbance cuvette used (i.e., 1 cm path-length absorbance cuvette for C1-L and 1 mm path-length absorbance cuvette for C2-L), and to a more significant concentration of curcumin in solution, leading to an overlap of $AuCl_4^-$ absorbance band and to a faster reaction kinetic (i.e., seven days for C1-L and dozens of minutes for C2-L), leading to a fast consumption of $AuCl_4^-$.

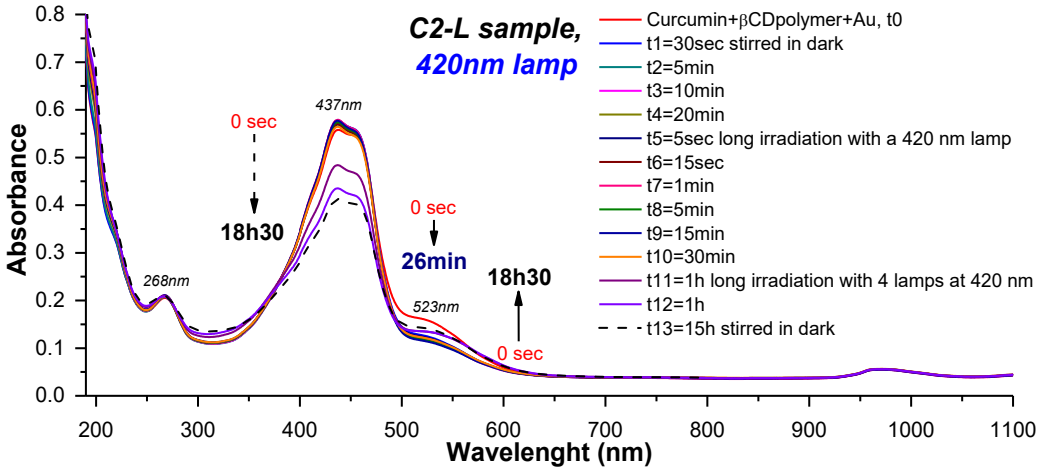

Figure 21: Comparison of the absorption evolution of Curcumin+βCDpolymer+Au (C2-L) during the irradiation for twenty-six minutes (full lines), and after fifteen hours stirred in dark conditions (black dotted line). The irradiation was performed in a 1 cm path-length fluorescence cuvette at 10 cm from the sample using a 420 nm lamp (*ca.* 1 $mW.cm^{-2}$). Measurements were performed in a 1 mm path-length absorbance cuvette using a PerkinElmer UV-Vis spectrophotometer with air as the blank. The sample was stirred during the irradiation. Conditions: [Curcumin] = 0.2 mM; [βCDpolymer] = 4.04 $mg.mL^{-1}$; $[HAuCl_4 \bullet 3H_2O]$ = 0.4 mM.

Furthermore, the mean nanoparticle size is quite considerable and differs from that previously reported for pomegranate. Seggio *et al.* reported a hydrodynamic diameter of 55 nm by DLS, whereas we obtained a mean diameter of 3378 nm using DLS (Appendix II). However, despite the nanoparticle's size, the polydispersity index is excellent with a mean PDI of 0.04. According to the reported literature, the synthesis of AuNPs with a comparable curcumin/gold ratio (1:5) yielded nanoparticles with an average diameter of 20 nm.[203] Since AuNPs with an LSPR band in the green region generally have sizes at this nanoscale order (i.e., near 10 – 100 nm), the high diameter mean observed in DLS can be due to the polymeric structure around the gold nanoparticles or to their substantial aggregation.

4.2.2. Investigations on the Curcumin/Au ratio

Since the preparation method using a curcumin film enabled easier, more efficient loading of the dye into the polymeric structure, its use with an exact, known concentration was possible, and spherical gold nanoparticles were formed under green conditions. Then, we focused our attention on the formation of anisotropic structures, with the investigation narrowing on the modification of the curcumin concentration. As mentioned, Seggio *et al.* observed that the shape of the particles formed was dependent on the ratio between the reducing agent and the gold salts.[160] Additionally, the formation of an absorbance band in the NIR region appears to be possible if the reducing agent concentration is lower than that of the gold precursor.

As a first attempt with a significant excess of gold salts, the Curcumin/Au (1:20) ratio was investigated (C3-L sample) (Figure 22). A similar Curcumin/Au ratio (1:25) has also been reported by Singh *et al.*[203,] who achieved a very characteristic pink color and excellent stability, up to one month, of the gold nanoparticles. Additionally, the reaction kinetics appear to be improved, as the absorption band characteristic of spherical gold nanoparticles appears only after some minutes and has a higher intensity than in C1-L and C2-L. With the Curcumin/Au (1:25) ratio reported by Singh, the intensity of the absorbance band at 580 nm seems to be the same aspect, and no absorbance band can be found in the near-infrared region, despite the far lower curcumin concentration compared to gold salts. Another observation is the dark control done in the same experimental conditions (C3-D sample): after nine days without any light source, no LSPR band can be observed, and no particles are formed; the band observed at approximately 510 nm can be attributed to the keto-enol form of the curcumin (Appendix III).

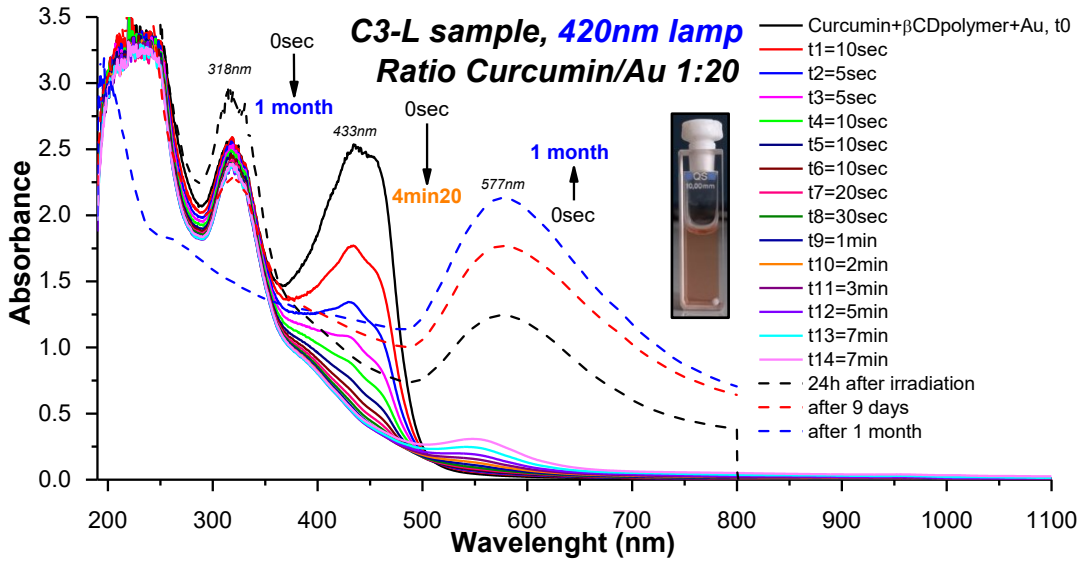

Figure 22: Comparison of the absorption evolution of Curcumin+βCDpolymer+Au (C3-L) during the twenty-seven-minute-long irradiation and after twenty-four hours (black dashed line), after nine days (red dashed line), and after one month (blue dashed line). Irradiation was performed using a 420 nm lamp (*ca.* 1 $mW.cm^{-2}$). The sample was stirred during the irradiation. The inset shows a picture of the irradiated sample C3-L after the end of the irradiation. Measurements and irradiation were performed in a 1 cm path-length absorbance cuvette using a PerkinElmer UV-Vis spectrophotometer with air as the blank. Conditions: [Curcumin] = $4.99x10^{-5}$ M ; [βCDpolymer] = 2.04 $mg.mL^{-1}$; [$HAuCl_4 \bullet 3H_2O$] = 0.4 mM.

Compared to the C2-L attempt, we observed an improvement in nanoparticle size, with a mean diameter of 755.8 nm and an excellent polydispersity index of 0.03, as determined by DLS, and a mean diameter of 133 nm, as measured by NTA (Appendix IV). For comparison, the dark control C3-D sample has a hydrodynamic diameter of about 1508.9 nm with a PDI of 1.92, as measured by DLS, which can be attributed to the βCD polymer.

Since the Curcumin/Au (1:20) ratio did not yield anisotropic gold nanoparticles as initially hoped, we attempted an equimolar ratio of curcumin to gold (C4-L sample). This ratio between gold and the reducing agent has also been investigated in the literature.[204,205] A red-aspect solution was obtained at the end of the irradiation (Figure 23). This color is likely due to the non-degraded curcumin remaining in the sample. It is noteworthy that after the experiment ended, the absorbance of curcumin at 420 nm continued to increase over time. This absorbance increase is likely due to the higher concentration of the reducing agent in the solution, and possibly also to the presence of insoluble residues or curcumin aggregates in the reaction medium. When curcumin is degraded, cavities of cyclodextrins seem to become once again available, and new units of curcumin may be solubilized inside these latter. The by-products of

curcumin degradation can be seen on the absorbance spectra with their characteristic absorbance band near 360 nm.[193]

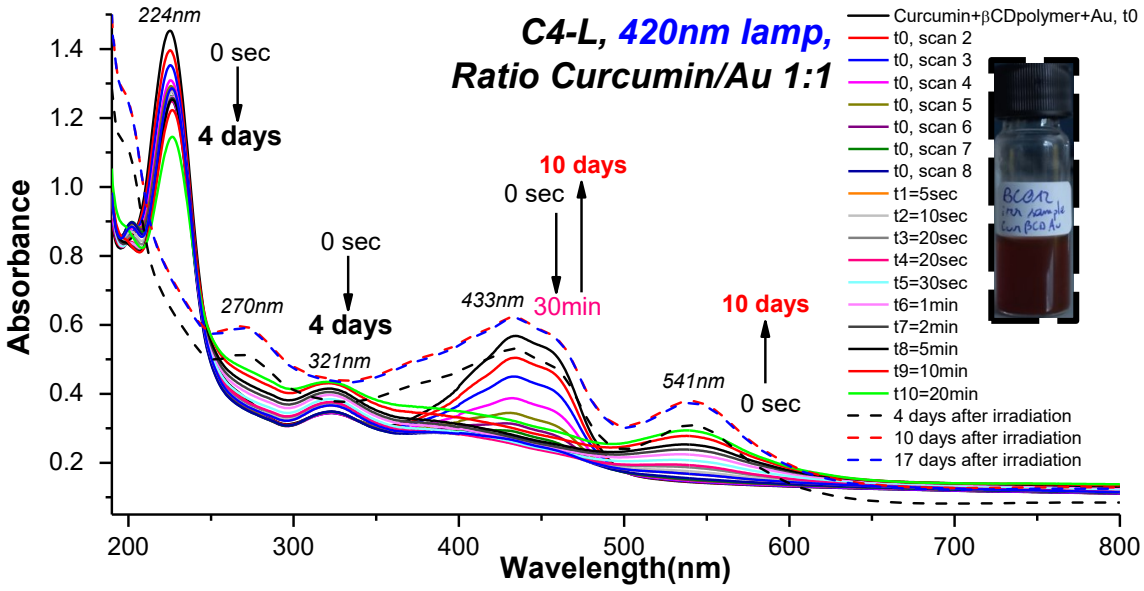

Figure 23: Comparison of the absorption evolution of Curcumin+βCDpolymer+Au (C4-L) during the thirty-nine-minute-long irradiation and after four days (black dashed line), after ten days (red dashed line), and after seventeen days (blue dashed line). Irradiation was performed in a 1 cm path-length fluorescence cuvette using a 420 nm lamp (*ca.* 1 mW.cm^{-2}). The sample was stirred during the irradiation. The inset shows a picture of the irradiated sample C4-L three days after the end of the irradiation. Measurements were performed in a 1 mm path-length absorbance cuvette using a PerkinElmer UV-Vis spectrophotometer with air as the blank. Conditions: [Curcumin] = 0.316 mM; [βCDpolymer] = 2.5 mg.mL^{-1}; [$HAuCl_4 \bullet 3H_2O$] = 0.316 mM.

We investigated the size and zeta potential of the nanoparticles obtained in C4-L. The nanoparticles formed by light irradiation had a diameter of 77 nm, as measured by NTA, and an excellent zeta potential value of -49.2 mV, which can be explained by the presence of co-products or deprotonated curcumin with negative charges on the particle's surface. The concentration of AuNPs obtained is about 8.9x10^{10} particles per mL.

* * *

Because of the better-sized gold nanoparticles obtained in an equimolar ratio of gold precursor to curcumin, we investigated the influence of light on curcumin degradation to control gold nanoparticle formation.

4.2.3. Influence of curcumin irradiation in a 1:1 ratio (Curcumin/Au)

During previous investigations of the absorbance evolution of Curcumin+βCDpolymer+Au, the dark control sample C3-D showed a green absorbance band, characteristic of AuNP formation. To elucidate the light influence on the AuNPs formation, a synthesis in the dark using a ratio of 1:1 between curcumin and gold salt is performed (C5-D sample). We observed that the oxidation of curcumin and the formation of AuNPs also occur independently of the system's light irradiation (Figure 24). Consequently, the formation of AuNPs, whether in irradiated or non-irradiated conditions, must be due to the dissociation of the enolic proton of the curcumin, with the latter responsible to the reduction of the added gold salts;[206] and because of the tautomeric equilibrium between the protonated and the deprotonated forms of the curcumin complexed inside the polymer in solution, the reduction of gold Au(III) to Au(0) occurs spontaneously under our experimental conditions without the need for light irradiation. However, we noticed that the velocity of the reducing agent degradation is faster when light is applied. Consequently, more nucleation sites must be formed, and less gold is required to grow the already existing ones. As a result, in theory, the nanoparticles should be smaller than those in the non-irradiated sample; as a result, the observed size of these dark-control nanoparticles is much more significant, with an average diameter of approximately 161 nm, as measured by NTA.

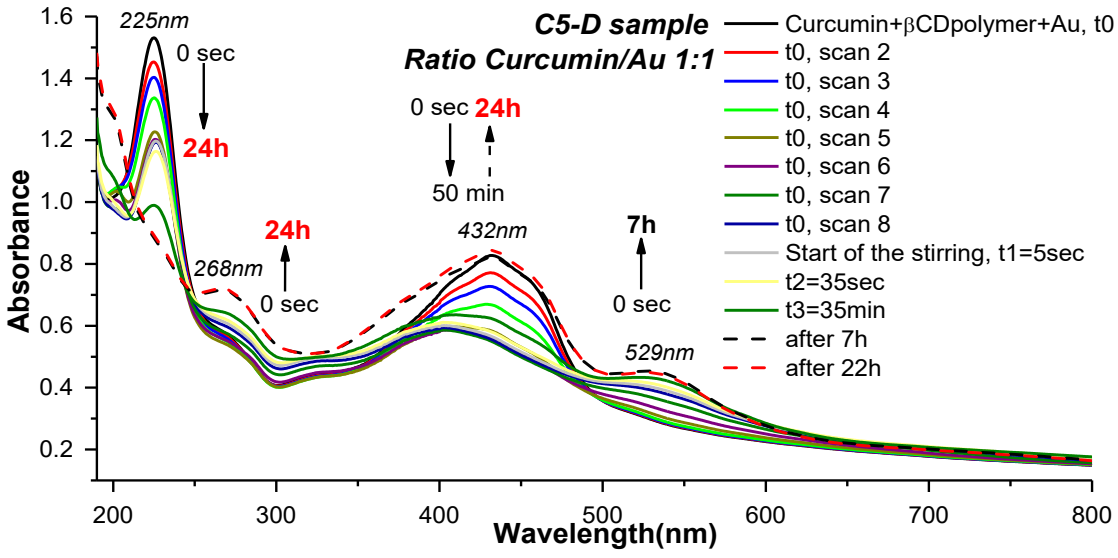

Figure 24: Comparison of the absorption evolution of the dark control of Curcumin+βCDpolymer+Au (C5-D), with a 1:1 ratio of curcumin and gold precursor, during the thirty-five-minute-long stirring, and after seven hours (black dashed line), and after twenty-two hours (red dashed line). Measurements were performed in a 1 mm path-length absorbance cuvette using a PerkinElmer UV-Vis spectrophotometer with air as the blank. Conditions: [Curcumin] = 0.365 mM ; [βCDpolymer] = 2.5 mg.mL^{-1} ; [$HAuCl_4 \bullet 3H_2O$] = 0.365 mM.

However, the irradiation of the curcumin in βCD polymer crosslinked with epichlorohydrin does not induce the decrease of its absorbance nor its degradation, and therefore is not necessary for the formation of gold nanoparticles. It seems that the gold salts themselves induce the curcumin band drop due to the spontaneous reduction of Au(III). The lack of selectivity in the formation of AuNPs in irradiated samples is a significant challenge, as it leads to a lack of control over AuNPs' properties (size and shape) during synthesis. This lack of light influence indicates that the metallic salt is reduced mainly by curcumin via a classic redox reaction, regardless of light presence or absence. Nevertheless, the comparison between the irradiated sample and its dark control shows a faster reaction rate in the presence of light, suggesting that curcumin photoproducts are involved in the formation of AuNPs. Further investigations must be performed (e.g., optimization of the reducing agent or $HAuCl_4$ concentration, irradiation intensity, and irradiation wavelength) to optimize this photoinduced process.

We pursued investigations into the formation of anisotropic gold particles to improve curcumin solubility. Moreover, the introduction of cationic surfactant can help to introduce the anisotropy.

4.2.4. Cationic βCD polymer cross-linked with epichlorohydrin

The solubility of the curcumin remains an issue; indeed, a non-complete dissolution of the curcumin is suspected, as unveiled by the evolution of the absorbance spectra in the area of the curcumin absorption. As mentioned in the second chapter (part 2.5), in order to enhance the curcumin solubility, the procedure was improved by using a positively charged modified βCD polymer, the (2-hydroxy-3-N,N,N-trimethylamino)propyl-β-cyclodextrin polymer (QAβCDPS). Additionally, the quaternary ammonium in this cationic polymer provides better stabilization of AuNPs through electrostatic interactions between the cationic quaternary ammonium and the gold nanoparticle surface, which makes it favorable for further investigations with cells. Since the quaternary ammonium stabilizes the particle, we can use some cyclodextrin cavities for complexation with a possible photosensitizer.[207] Furthermore, we can exploit the use of the quaternary ammonium to introduce anisotropy to the nanoparticles.[208] This anisotropy can occur when the quaternary ammonium covers one side of the particle, inducing a differential growth of the bare side of the AuNPs.

In the presence of QAβCDPS, the equilibrium between protonated and deprotonated forms of the curcumin evolved (Figure 25A). A color change of the system characterizes the evolution. After 64 hours, the system Curcumin+QAβCDPS changed from red/orange to purple. This color change must be due to the predominant deprotonated form of curcumin, which can be stabilized by electrostatic interactions with the polymer's positive charges.[209] After 6 days of stirring the Curcumin+QAβCDPS system, we observe a new equilibrium between both forms of curcumin. After 6 days of stirring, $HAuCl_4 \bullet 3H_2O$ was added in equimolar concentration and irradiated with a 420 nm lamp (C6-L sample). After about ten minutes of irradiation, we observed the formation of two absorbance bands at 550 nm and 780 nm, both characteristic of anisotropic gold nanoparticles (Figure 25B). Nevertheless, the dark control sample (C6-D sample) shows a similar evolution in its absorbance spectra, with the same two characteristic LSPR bands of anisotropic gold nanoparticles at 542 nm and 730 nm, which rise simultaneously (Appendix V). Consequently, in the presence of a cationic βCD polymer, the irradiation of the system does not seem to influence the curcumin absorbance evolution and gold nanoparticle formation.

It is important to note that this cationic polymer induced a markedly different evolution in the absorption of curcumin upon the addition of $HAuCl_4$. With the neutral polymer, we did not observe any absorbance shift. The curcumin's absorbance decreased slowly over the reaction time, whereas upon complexation of curcumin within the cationic polymer, a shift and an intensity drop were observed at the addition of $HAuCl_4 \bullet 3H_2O$ from λ_{max} = 425 – 525 nm to λ_{max} = 400 nm. During the synthesis, its absorbance did not decrease slowly over time.

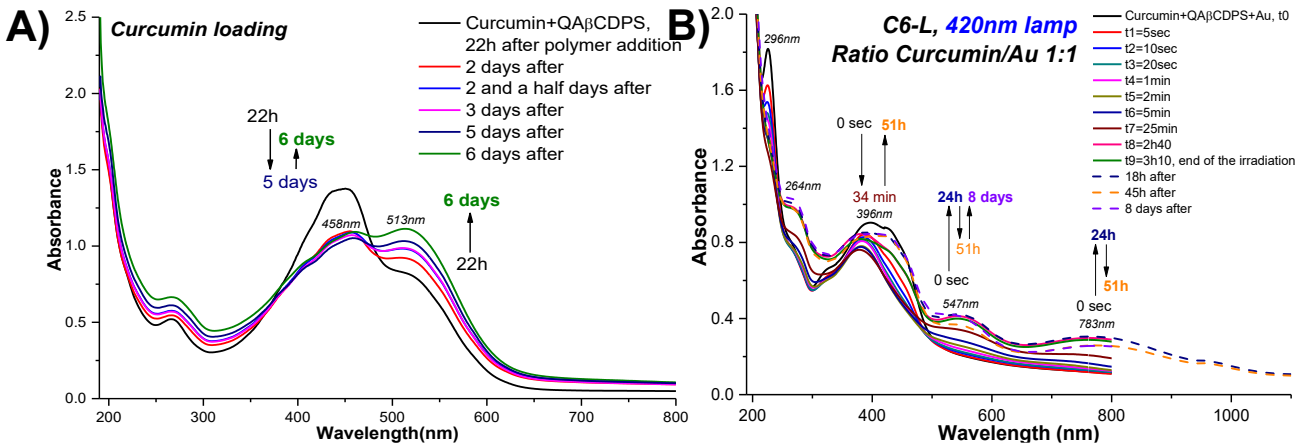

Figure 25: A) Comparison of the absorption evolution of Curcumin+QAβCDPS over time. Measurements were performed in a 1 mm path-length absorbance cuvette. B) Comparison of absorption evolution of Curcumin+QAβCDPS+Au (C6-L) during the six hours and thirty minutes long irradiation and after eighteen hours (dark blue dashed line), forty-five hours (orange dashed line), and eight days (light blue dashed line). Irradiation was performed in a 1 cm path-length fluorescence cuvette at 10 cm from the 420 nm lamp (*ca.* 1 $mW.cm^{-2}$). The sample was stirred during the irradiation. Measurements were performed in a 1 mm path-length absorbance cuvette using a PerkinElmer UV-Vis spectrophotometer with air as the blank. Conditions: [Curcumin] = 0.433 mM; [QAβCDPS] = 10.0 $mg.mL^{-1}$; [$HAuCl_4 \bullet 3H_2O$] = 0.433 mM.

The DLS size remains significant, with a mean diameter of 1767 nm. This high value is influenced by the presence of two populations in our samples: the first corresponds to the particles, while the second corresponds to their aggregated form (Figure 26). It should be noted that DLS cannot provide information on the NP shape.

The zeta potentials obtained for the irradiated and non-irradiated samples were -12 mV and -20 mV, respectively. By comparison with the previous measurement of the zeta potential, the reported value above, with the neutral polymer (in 4.2.2., for the C4-L sample, we reported a zeta potential of -49 mV), these increased values of surface charges are very characteristic of the presence of the positive charge of the quaternary ammonium (+1) in the polymer.[207] In the literature, classic chemical synthesis of AuNPs with quaternary ammonium surfactant CTAB and silver salts has been reported. The presence of these latter is due to favoring anisotropic characteristics with the presence of the quaternary surfactant.

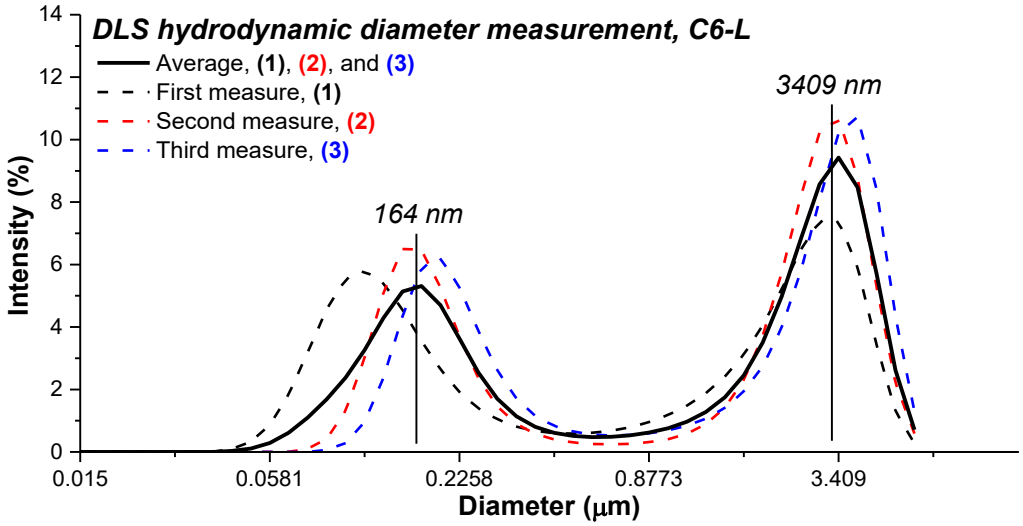

Figure 26: Average scattering light intensity distribution (%) of the measures of the irradiated Curcumin+QAβCDPS+Au (C6-L) over the hydrodynamic diameter (μm). The measurement was performed using a Dynamic Light Scattering HORIBA LB-550, at room temperature (T = 25 °C).

We investigated the photothermal properties of synthesized anisotropic gold nanoparticles (C6-L) with both 532 and 750 nm lasers (*ca.* 6 W.cm^{-2}), i.e., based on their LSPR bands. We have performed three consecutive cycles of measurements to observe any evolution in temperature over multiple cycles of irradiation. We observed the photothermal effect of the gold nanoparticles shown in Figure 27, where we can notice that the temperature difference is about ΔT = 13 – 14 °C for an irradiation at 532 nm, and about ΔT = 7 – 8 °C at 750 nm. This temperature difference remains consistent across multiple irradiation cycles, demonstrating that the photothermal performance of the synthesized AuNPs is stable over time. It is important to note that the photothermal study of the sample in the infrared region was conducted 4 months after the end of the synthesis, demonstrating the particles' performance and stability, as well as their photothermal properties over time.

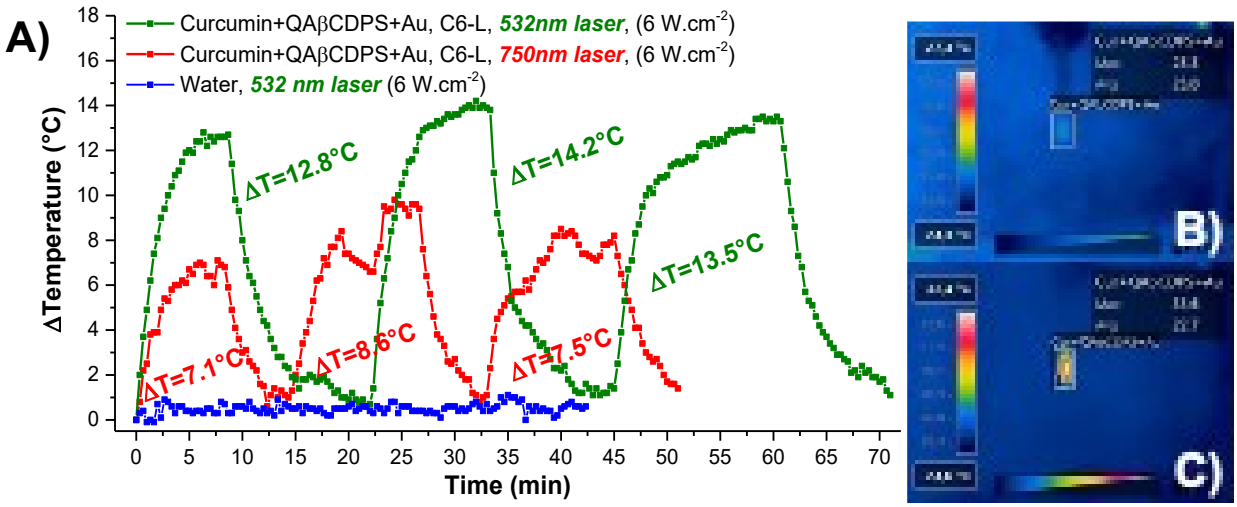

Figure 27: A) Evolution of the temperature over time by laser irradiation at 532 nm (in green), and at 750 nm (in red) (*ca.* 6 W.cm^{-2}), over three cycles of measurements of the irradiated sample of Curcumin+QAβCDPS+Au (C6-L). Comparison with the evolution of the temperature of a water sample irradiated in the same conditions (in blue). B) Thermal picture taken at the starting point of the second cycle. C) Thermal picture taken at the end of the second cycle of the 750 nm laser irradiation. The temperature measurements were performed with a FLIR C3 thermal camera.

We also investigated the formation of a curcumin-anionic βCD polymer complex, namely with the soluble sulfobutylated βCD polymer (SBβCDPS). However, even after raising the polymer concentration to 15.165 mg.mL^{-1} and stirring for up to one month, the reducing agent remained insoluble due to the Coulomb forces between deprotonated curcumin Cur^{3-} and the anionic polymer.

4.2.5. pH influence on Curcumin+QAβCDPS absorption

All previous studies have been conducted in water to simplify experimental conditions. Still, the successful procedure reported above with the cationic βCD polymer lacked reproducibility and did not consistently yield anisotropic AuNPs (i.e., about 43 % of successful formation of anisotropic gold nanoparticles, with the catanionic βCD polymer in extra pure water). We hypothesized that the rise of the second LSPR band was due to a specific equilibrium among the tautomeric forms of curcumin in the polymer matrix, based on the same level of absorbance bands from both forms of curcumin from the C6 experiment. Because of the influence of the pH on the deprotonated keto-enol tautomerism of curcumin, the bis-keto form is favored in acidic or neutral pH. In contrast, the keto-enol form is preponderant in alkaline media. This equilibrium between the protonated and deprotonated forms of curcumin is influenced not only by the presence of the cationic moieties in the polymer, as shown above, but also by the pH of the

medium. Investigations were conducted on the pH of the medium in which nanoparticles are formed. Accordingly, a set of three experiments has been performed at diverse pH values.

We performed the first experiment under acidic conditions (pH = 5.13). In that case, Curcumin+QAβCDPS shows a single absorbance band near 420 nm, characteristic of the keto-form of curcumin. Following the addition of $HAuCl_4 \bullet 3H_2O$ (sample C7-L), even if no clear LSPR band can be spotted, a few gold nanoparticles are formed as demonstrated by the baseline scattering days after the end of the irradiation (Figure 28). The pH of the milieu after gold addition was pH = 2.78. Furthermore, we observed no color change in the sample.

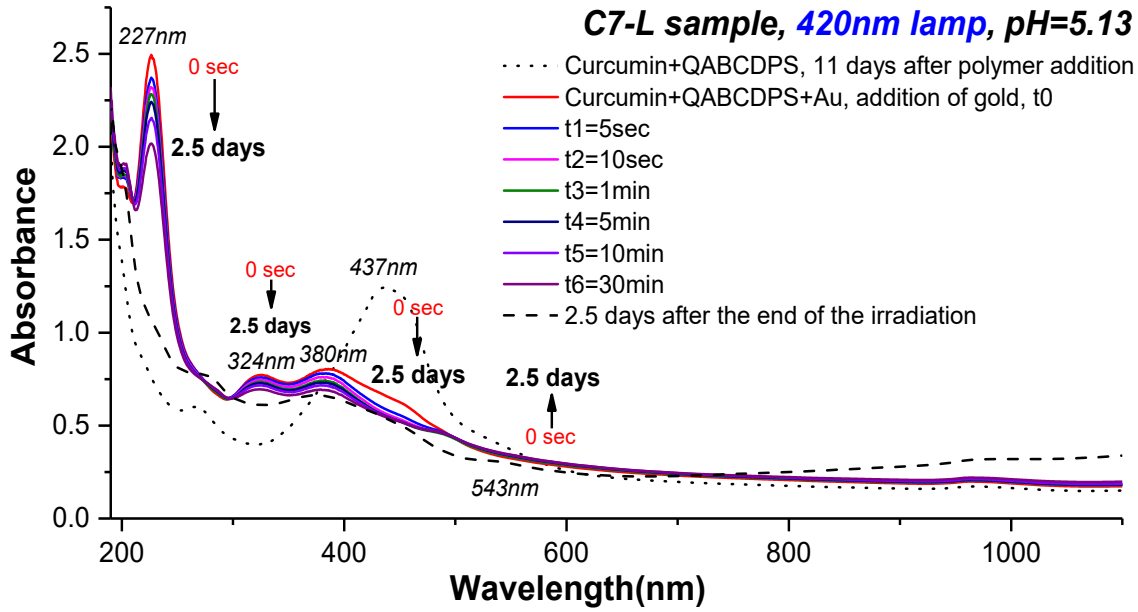

Figure 28: Comparison of the absorption evolution of Curcumin+QAβCDPS+Au (C7-L) during the forty-six-minute-long irradiation. Irradiation was performed in a 1 cm path-length fluorescence cuvette at 10 cm from the sample using a 420 nm lamp (*ca.* 1 $mW.cm^{-2}$). Measurements were performed in a 1 mm path-length absorbance cuvette using a PerkinElmer UV-Vis spectrophotometer with air as the blank. The sample was stirred during the irradiation. Conditions: [Curcumin] = 0.48 mM; [QAβCDPS] = 10.00 $mg.mL^{-1}$; $[HAuCl_4 \bullet 3H_2O]$ = 0.48 mM.

It should be noted that we designed the NPs for a biological environment; therefore, a synthesis performed in a biocompatible medium will be advantageous. Thus, in a second experiment, we solubilized curcumin in a QAβCDPS aqueous solution prepared in PBS buffer (pH = 7.52, 10 mM).

We attempted to reiterate the synthesis under the best conditions described above for C6 samples, while maintaining a controlled pH. The ratio between the deprotonated Cur^{3-} and protonated $CurH_3$ form is very similar to the one observed in water (Figure 29A). The use of a PBS buffer maintained a stable pH upon addition of the gold salts and, consequently, controlled

the stability of the keto-enol tautomerism before and during the synthesis. Besides the pH value, the only noticeable difference between the experiments performed with the QAβCDPS polymer at pH = 7.52 and in water was the lower intensity of the Cur^{3-} band in the absorbance spectra at physiological pH. Under irradiation with a 426 nm lamp (*ca.* 1 $mW.cm^{-2}$), the rise of the two LSPR bands at 532 nm and the second at 848 nm (not well defined) is observed, similar to the spectra obtained in water conditions (C8-L sample). Besides the fact that the second band in the red region is less intense in PBS than in water solution, both characteristic LSPR bands appeared more rapidly and did not evolve (Figure 29B). It should be noted that the same results were observed for the dark control (Appendix VI).

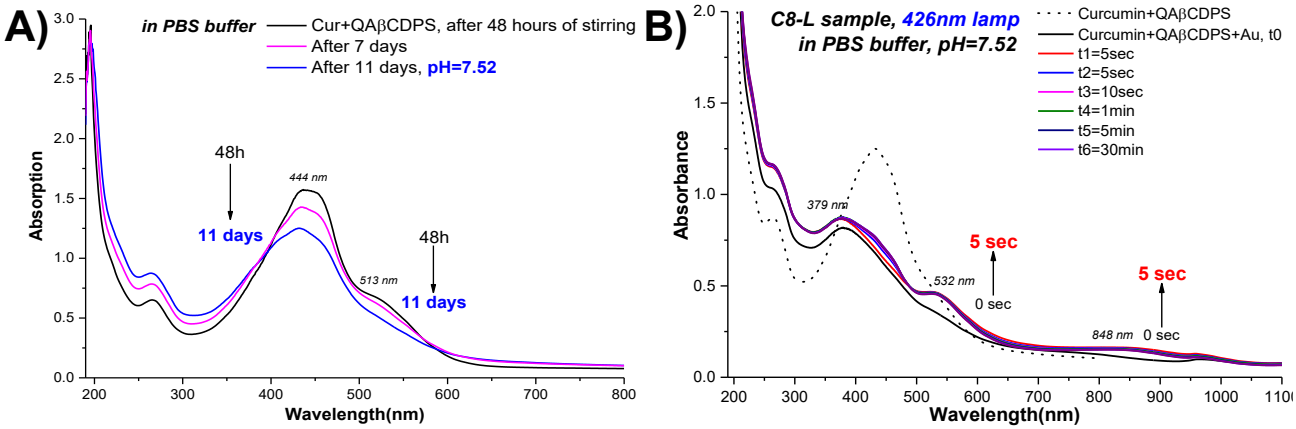

Figure 29: A) Absorbance spectra of the system Curcumin+QAβCDPS in PBS buffer. Measurements were performed in a 1 mm path-length absorbance cuvette using a PerkinElmer UV-Vis spectrophotometer with air as the blank. B) Absorption evolution of Curcumin+QAβCDPS+Au (C8-L) irradiated for 37 minutes using a 426 nm lamp (*ca.* 1 $mW.cm^{-2}$) in a 1 cm path-length absorbance cuvette. Measurements were performed in a 1 mm path-length absorbance cuvette using a PerkinElmer UV-Vis spectrophotometer with air as the blank. Conditions A) & B): [PBS] = 10 mM; [Curcumin] = 0.47 mM; [QAβCDPS] = 10.00 $mg.mL^{-1}$; [$HAuCl_4 \bullet 3H_2O$] = 0.47 mM.

The photothermal properties of C8-L were measured with a temperature rise of only ΔT = 6 – 8°C under irradiation in the green region at 532 nm with a laser at 6 $W.cm^{-2}$ (Figure 30). This temperature increase is less pronounced than the variation observed in water. Still, this feature does not outweigh the benefit of a controlled pH, as weak absorbance intensity can be mitigated by concentrating the sample after preparation.

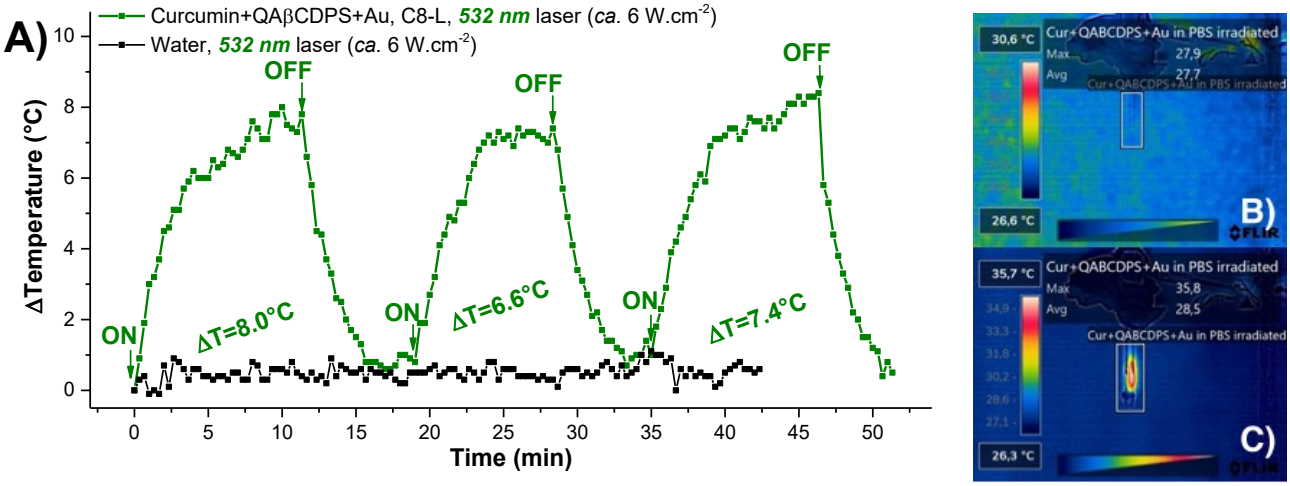

Figure 30: A) Evolution of the temperature over time by laser irradiation at 532 nm (*ca.* 6 W.cm^{-2}) over three cycles of measures of irradiated Curcumin+QAβCDPS+Au (C8-L) (in green). Comparison with the evolution of temperature of a water sample irradiated in the same conditions (in black) (control sample). B) Thermal picture taken at the starting point of the first cycle. C) Thermal picture taken at the end of the first cycle of the 532 nm laser irradiation. The temperatures were measured with a FLIR C3 thermal camera.

Moreover, TEM images performed and captured in collaboration with the University of Padova revealed exciting shapes. We observed gold nanospheres, and surprisingly, both irradiated (C8-L) and non-irradiated (C8-D) samples formed nanotriangles, as well as nanopentagons and nanohexagons. Their proportions were similar in both conditions (Figure 31).

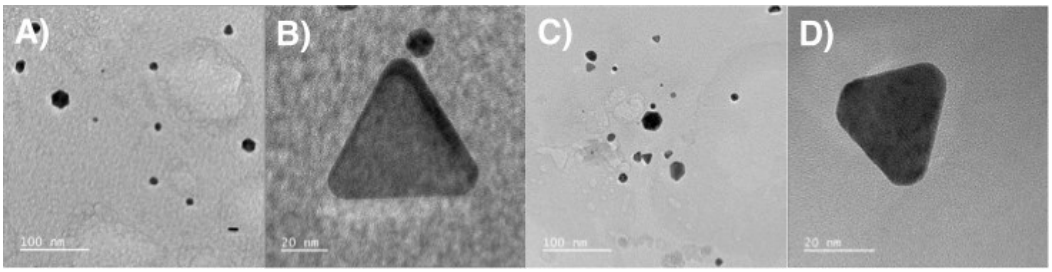

Figure 31: Transmission electron microscopic images of the first batch of Curcumin+QAβCDPS+Au. A) & B) irradiated sample (C8-L); C) & D) non-irradiated sample (C8-D).

Regarding the reported particle sizes, no size measurements of the gold nanoparticles were performed based on a specific particle shape, and the number of AuNPs in the TEM images was insufficient to provide a representative size distribution of the entire sample; therefore, the reported sizes should be interpreted with caution and are not reliable. Small spherical particles of 5 – 20 nm constitute the majority of the sample, while the larger structures are anisotropic. Nanoprisms have an average size of 30 – 50 nm. Even if, in the C8-L sample (Figure 32A), a

second population can be spotted (i.e., between 50 and 60 nm), whereas in the C8-D sample (Figure 32B), only one population seems to stand out. We measured particle sizes from TEM images using ImageJ, an open-source image-processing software, and calibrated them using the 20 and 100 nm scales of the images. We measured the diameter of a spherical particle and the base and height of one nanoprism once.

We also measured the particle sizes of C8-L using DLS (Figure 33). Once again, because the DLS technique is suited to isotropic particles, the presence of non-spherical particles leads to an imprecise measurement and is hardly reliable. The first population can be attributed to AuNPs particles with a mean diameter of about 80 nm, while the second population can be attributed to aggregated particles or to aggregated QAβCDPS. El Kurdi *et al.* reported the synthesis of gold nanowires with a diameter of *ca.* 20 nm at an alkaline pH (pH = 13). However, at acidic and neutral pH, El Kurdi reports only nanospheres with a diameter of about 50 – 70 nm.[208]

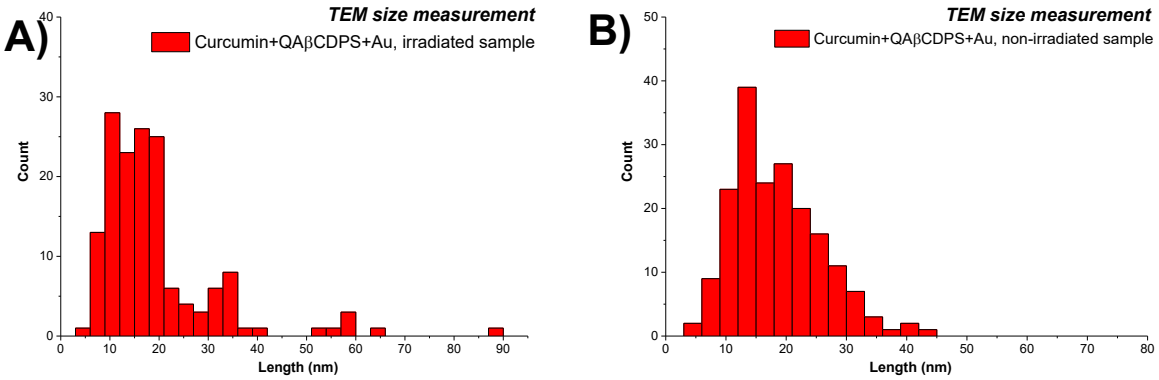

Figure 32: Population distribution in function of the number of measures done of the length of gold nanoparticles measured from TEM images with ImageJ software in A) the irradiated sample (C8-L) and B) the non-irradiated sample (C8-D).

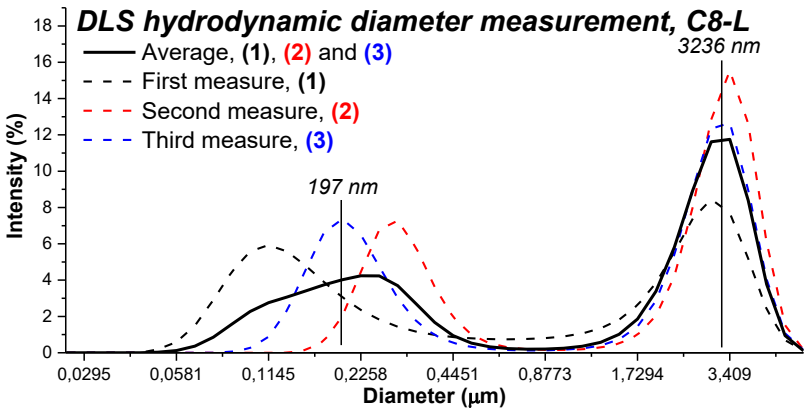

Figure 33: Average scattering light intensity distribution (%) of the measures of the irradiated Curcumin+QAβCDPS+Au (C8-L) over the hydrodynamic diameter (μm). The measurement was performed using a Dynamic Light Scattering HORIBA LB-550, at room temperature (T = 25 °C).

Consequently, by correlation of previous results collected in different reaction conditions, the more curcumin is deprotonated before the addition of gold precursor, the more AuNPs and more especially anisotropic AuNPs will be formed. However, as mentioned above, upon addition of $HAuCl_4 \bullet 3H_2O$ to the mixture, the absorbance band of the deprotonated curcumin decreases immediately due to the solution's pH drop. In PBS, the presence of the buffer ([PBS] = 10 mM) prevented a significant pH drop; the pH dropped from 7.52 to 7.07 upon the addition of the gold salt, leading to the deprotonated curcumin during gold nucleation.

In classical chemical synthesis with curcumin under alkaline conditions, it has been reported that AuNPs were formed at pH = 9.3 upon addition of gold salts, with the pH reached within minutes to prevent rapid curcumin degradation in basic media.[198,204,205] The high pH value, which was achieved by the addition of NaOH and K_2CO_3, is necessary for the deprotonation of the enolic proton of the curcumin (pKa1 between 7.7 and 8.5) for the formation of the AuNPs, and for the deprotonation of a first phenol proton (pKa2 between 8.5 and 10.4) to increase curcumin's solubility in water.[186] However, from these reported investigations, no anisotropic nanoparticle is noticed on the absorbance spectra, and contrary to the decrease of the 520 nm absorbance band or the pH drop at the addition of the $AuCl_4^-$, only the yellow-color solution upon the addition of gold salt at the start of the reaction is mentioned.

To complete this set of experiments and to reproduce these conditions and promote the formation of the deprotonated curcumin form, an alkaline NH_4Cl buffer was investigated as the medium of the reaction in the presence of neutral βCD polymer to induce the deprotonated form, with the latter believed to be at the origin of the reduction of the gold salts. However, despite the strong absorbance band of the deprotonated form at pH = 10.40 (Figure 34), we observed a very fast degradation of the curcumin in alkaline media, and no gold particles were formed after the addition of the gold precursor (C9-L sample). This substantial absorbance drop of the curcumin band can be due to its degradation in alkaline medium and not to its oxidation by the gold precursor. This hypothesis is reinforced by the rise of the absorbance band of $AuCl_4^-$ at 334 nm, some days after the synthesis.

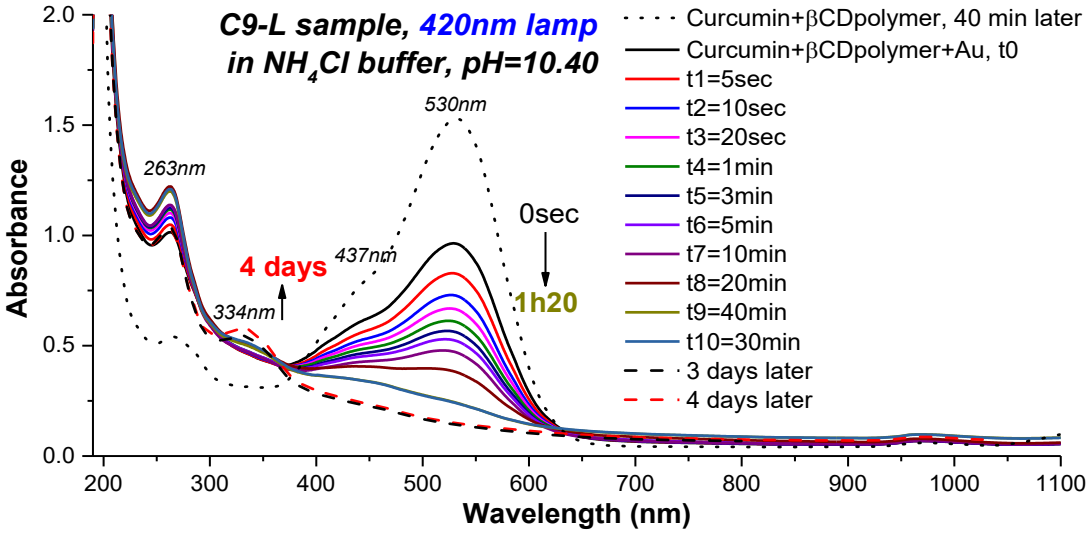

Figure 34: Comparison of the absorption evolution of Curcumin+βCDpolymer+Au (C9-L) during the one-hour and fifty-minute-long irradiation. The irradiation was performed in a 1 cm path-length fluorescence cuvette at 10 cm from the sample using a 420 nm lamp (*ca.* 1 $mW.cm^{-2}$). The sample was stirred during the irradiation. Measurements were performed in a 1 mm path-length absorbance cuvette using a PerkinElmer UV-Vis spectrophotometer with air as the blank. Conditions: [NH_4Cl] = 100 mM; [Curcumin] = 0.49 mM; [βCD-polymer] = 4.00 $mg.mL^{-1}$.

In light of these results, as the exclusive presence of the deprotonated form of the curcumin does not seem to be a fundamental requisite to observe the particle formation, the pH of the milieu does not seem to be the main factor for the formation of anisotropic particles. When we take a look at the ratio of the concentration of curcumin over the concentration of cationic polymer, it seems that this ratio has a role in the curcumin form in solution, and so in the formation of the AuNPs. Indeed, anisotropic particles were formed only when the ratio of [Curcumin]/[QAβCDPS] is equimolar. Empirically, we found that if the ratio [Curcumin]/[QAβCDPS] is too high, the protonated band of the curcumin is present, there is an acidic pH value, and consequently, the bis-keto form of curcumin is predominant. Otherwise, if the ratio is too low, the keto-enol form is prevalent. However, if not enough polymer is added relative to curcumin, the solubility of the latter is reduced.

After extensive work on the optimization of the synthesis methodology, the selected conditions to perform the gold nanoparticles with an absorbance band in the NIR, using curcumin as green reducing agent, are: 1) an equimolar ratio of Au/Cur; 2) the use of QAβCDPS (10 $mg.mL^{-1}$), and 3) the use of a PBS buffer. To better characterize the system and verify the reproducibility of Curcumin+QAβCDPS preparation in PBS, we investigated a second batch using the selected conditions.

4.2.6. Confirmation of the procedure, and photothermal properties investigations in NIR

After careful preparation of the Curcumin+QAβCDPS system, we attempted to repeat the synthesis a second time in PBS (C10). This second batch, irradiated with a 405 nm laser (C10-L sample) (*ca.* 6 W.cm^{-2}), does not yield a reproducible result with only a single LSPR band at 524 nm, characteristic of spherical AuNPs (Figure 35A). Nevertheless, the band extends to 800 nm, which may be due to the presence of larger structures. However, the dark control demonstrated a different absorbance evolution (C10-D sample). Indeed, a steady increase of the two characteristic LSPR bands of anisotropic gold nanoparticles, one near 518 nm and another clear one at 837 nm is observed (Figure 35B). Even if C10-L does not exhibit a second LSPR band at higher wavelengths, the nanoparticles form more rapidly under irradiation than in the dark control, reaffirming the hypothesis of enhanced kinetic formation under irradiation (i.e., the absorption maximum is reached after 1h for the irradiated C10-L sample, while the C10-D sample needed 1h30min).

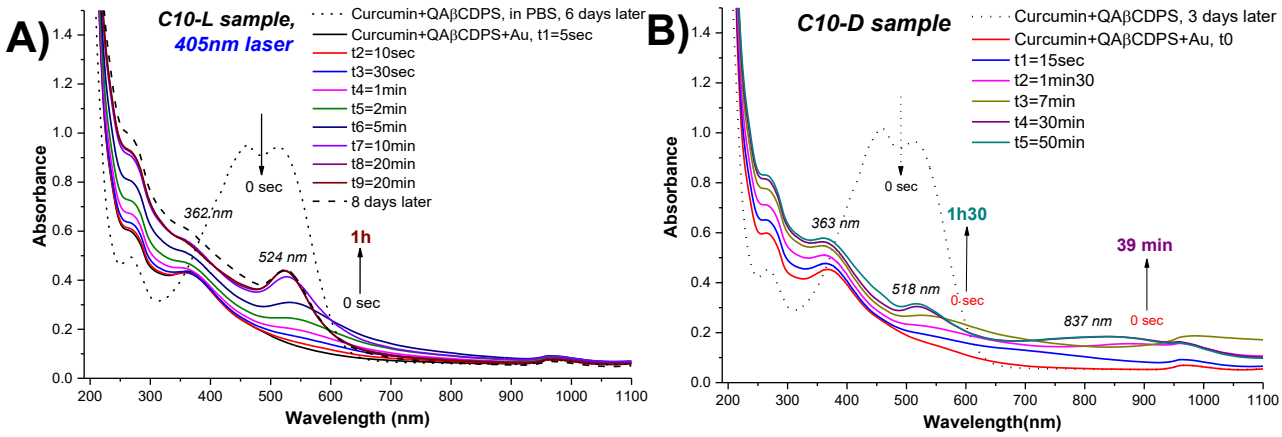

Figure 35: A) Comparison of the absorption evolution of Curcumin+QAβCDPS+Au (C10-L) irradiated for one hour and twenty-five minutes using a 405 nm laser (*ca.* 6 W.cm^{-2}). The sample was stirred in a 1 cm absorbance cuvette. Measurements were performed in a 1 mm path-length absorbance cuvette using a PerkinElmer UV-Vis spectrophotometer with air as the blank. B) Comparison of the absorption evolution of dark control Curcumin+QAβCDPS+Au (C10-D) stirred for one hour and thirty minutes. The sample was stirred in a 1 cm absorbance cuvette. Measurements were performed in a 1 mm path-length absorbance cuvette using a PerkinElmer UV-Vis spectrophotometer with air as the blank. Conditions for A) and B): [PBS] = 10 mM; [Curcumin] = 0.56 mM; [QAβCDPS] = 10.00 mg.mL^{-1}; [$HAuCl_4 \bullet 3H_2O$] = 0.56 mM.

To characterize the anisotropic AuNPs, we also investigated their shapes and sizes by TEM (Figure 36). Regarding the shapes, the C10-L showed only spherical particles in its UV-Vis spectrum; however, TEM images revealed some anisotropic particles resembling “nanoworms.”

The C10-D sample revealed spherical particles and nanoworms. We calibrated the software for measurements with the 20, 100, and 200 nm scales on the images. We measured the diameter of each spherical particle and the short and long sides of each nanoworm once. The reason for the formation of nanotriangles in the previous batch (C8-L and C8-D), rather than nanoworms or *vice versa*, may be due to the slight pH difference, since we did not make any other significant changes between these two batches. Regarding this hypothesis, further investigations are needed to assess the impact of the pH of the medium on the shape of the gold nanoparticles produced.

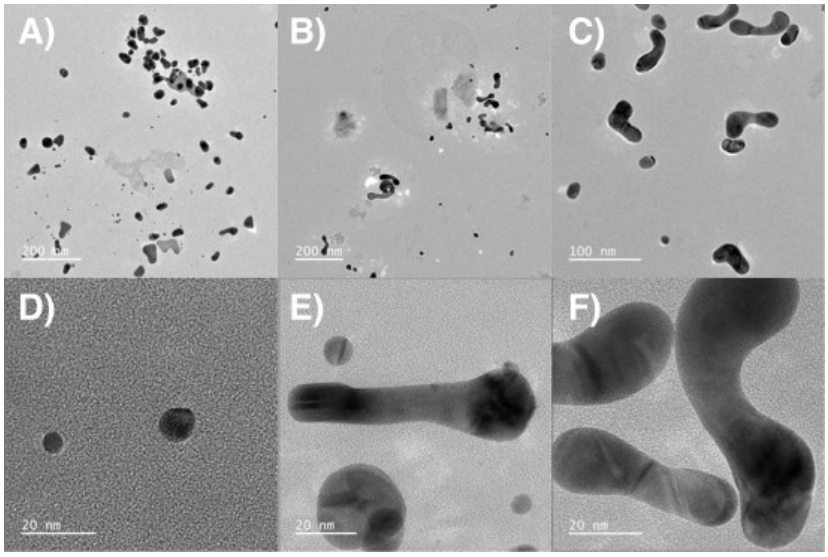

Figure 36: Transmission electron microscopic images of Curcumin+QAβCDPS+Au. A) & D) irradiated sample (C10-L); B) C) E) & F) non-irradiated sample (C10-D).

The number of AuNPs in these images was also too small to provide a satisfactory representation of the entire samples; consequently, once again, the sizes reported below must be considered carefully. About the size distribution defined by TEM, small spherical particles near 5 – 20 nm are the majority in the sample, while larger anisotropic AuNPs are also observed. The nanoworms, in their short axis, have an average width of 20 – 30 nanometers, while their long axis ranges between 30 and 140 nm; this latter broad range can be due to a heterogeneous sample. The short-axis measures are mixed up with the nanosphere sizes in the first population (Figure 37B). By comparison, only one population distribution arises for the C10-L sample (Figure 37A). At the same time, a second one seems to stand out for the C10-D sample, corresponding to the presence of anisotropic gold nanoparticles only in the dark control sample C10-D and only isotropic structures in C10-L, in accordance with their absorbance spectra.

Despite DLS not being a reliable technique for diameter measurement of anisotropic gold nanoparticles, the same diameter distribution differences were observed across two different populations. The first population near 35 nm can be attributed to isotropic AuNPs or the short side of anisotropic particles synthesized. In contrast, the second, near 170 - 250 nm, can be attributed to the long axis of the 'nanoworms' particles. However, by comparison to the size measurements performed from TEM images, two different diameter size populations are noticeable for C10-L despite the absence of an LSPR band in the near-infrared region of its absorbance spectrum (Figure 38A). The population close to 2257 nm can be attributed to the βCD polymer.

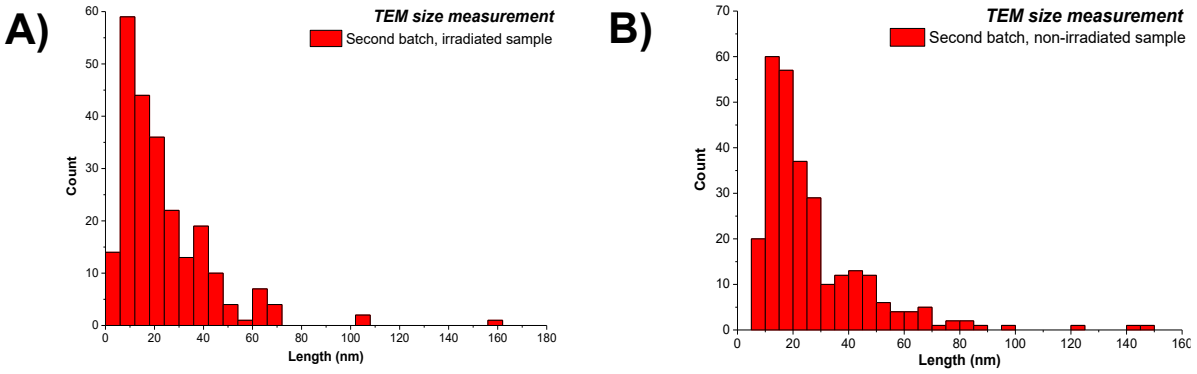

Figure 37: Population distribution in function of the number of measures done on the length of the synthesized gold nanoparticles, measured from TEM images with ImageJ software in A) the irradiated sample (C10-L), and B) the non-irradiated sample (C10-D).

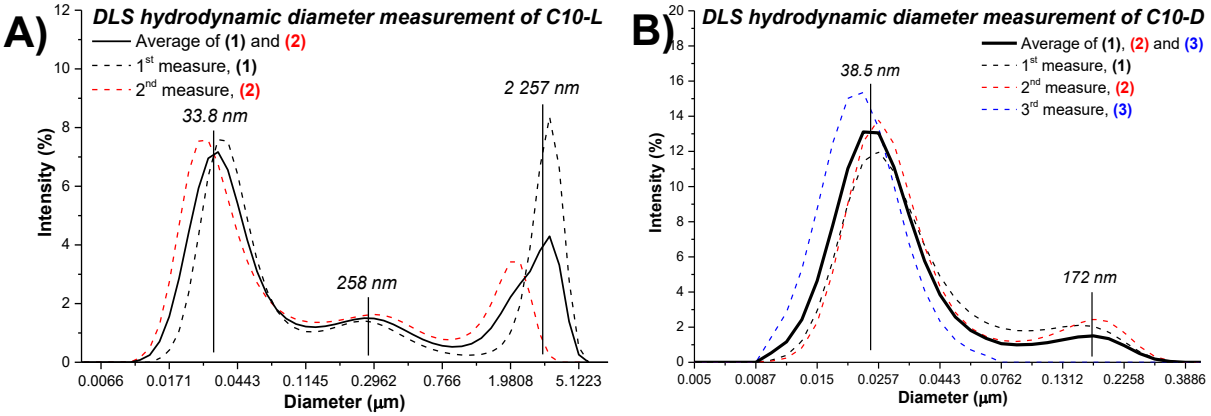

Figure 38: Average scattering light intensity distribution (%) of the measures of A) irradiated (C10-L) and B) non-irradiated (C10-D) Curcumin+QAβCDPS+Au over the hydrodynamic diameter (μm). The measurement was performed using a Dynamic Light Scattering HORIBA LB-550, at room temperature (T = 25 °C).

We investigated the photothermal properties of synthesized anisotropic gold nanoparticles with 532, 750, and 808 nm lasers (*ca.* 6 W.cm^{-2}), and compared them with an irradiated water sample under the same conditions (control sample). To enhance the absorbance in the red region and the photothermal response, we concentrated both C10 samples by centrifugation.

Among the different assays summarized in Table 1, the concentrated C10-D sample showed satisfactory heat generation in the infrared region upon irradiation, with 750 and 808 nm lasers, and related temperature differences of about ΔT = 15 – 17 °C and ΔT = 14 – 15 °C, respectively (Figure 39). By comparison with the anisotropic particles and like with the water control sample, the supernatant with curcumin complexed within QAβCDPS showed no heat generation, demonstrating that it is indeed the synthesized gold particles that are responsible for the heat generation. All temperature differences remained stable across multiple irradiation cycles, and no change in the absorbance spectrum was observed after the photothermal studies, demonstrating the stability of the photothermal performance for the anisotropic AuNPs over time. It is also important to note that even if the irradiated C10-L sample did not show a clear second band in the near-infrared region, AuNPs generated weak heat upon laser irradiation at 750 and 808 nm, possibly due to the presence of light-absorbing structures in the NIR, like anisotropic gold nanoparticles (Appendix VII).

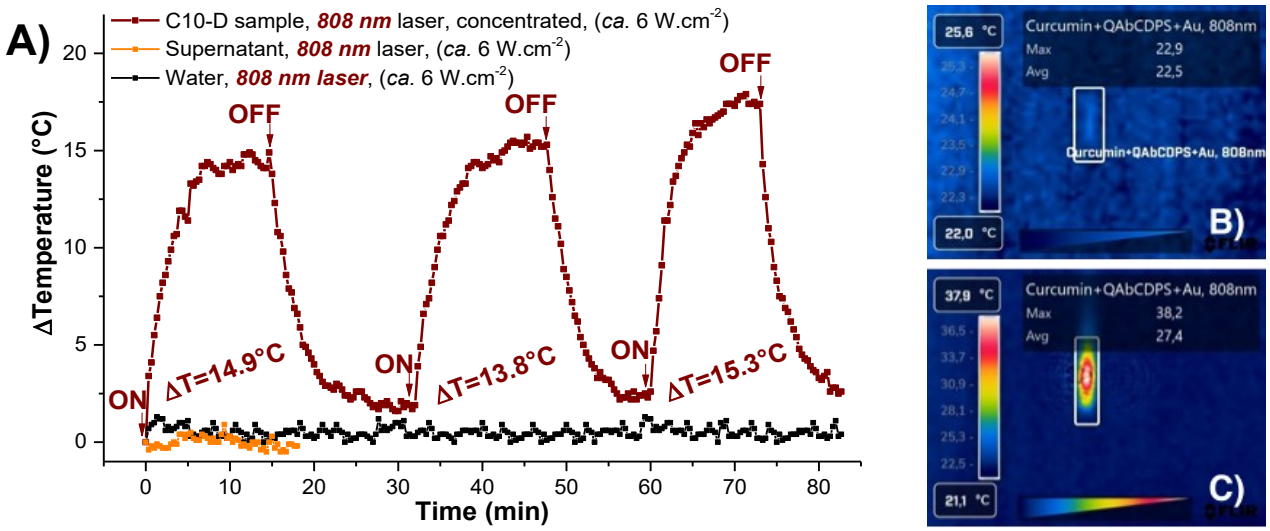

Figure 39: A) Evolution of temperature over time by laser irradiation at 808 nm (*ca.* 6 W.cm^{-2}) over three cycles of measures of the concentrated sample of the non-irradiated Curcumin+QAβCDPS+Au (C10-D) (in dark red). Comparison with the evolution of temperature of a water sample irradiated in the same conditions (in black), and with the supernatant (in orange) (control samples). B) Thermal picture taken at the starting point of the third cycle. C) Thermal picture taken at the end of the third cycle of the 808 nm laser irradiation. The temperatures were measured with a FLIR C3 thermal camera.

Table 1: Summary table of the results of photothermal studies of Curcumin+QAβCDPS+Au (C10) in near-infrared irradiations, with 750 or 808 nm lasers (*ca.* 6 W.cm^{-2}).

Sample	Concentrated	Irr. wavelength (PT) (nm)	ΔT (°C)
C10-L	No	750	3.7
		808	2.6
C10-D	No	808	~ 11
	Yes	**532**	**~ 17.1**
		750	**~ 16.5**
		808	**~ 14.9**
Supernatant of C10-D	/	808	1

4.3. Biological studies

4.3.1. Antibacterial assays

For the *in vitro* essays on bacteria, we investigated the heat produced by the gold nanoparticles on two different bacterial strains: *E. coli* Xen5 and *P. aeruginosa* pGEN-Lux. These two strains are Gram-negative bacteria, and *P. aeruginosa* is known to exhibit strong resistance to antibacterial drugs and easily develop biofilms.[210] By comparison with common *E. coli* and *P. aeruginosa*, they present bioluminescence properties used to observe and quantify the viability of the bacterial population after the irradiation of the gold formulations.

To observe a satisfying photothermal response (i.e., approximately ΔT = 5 – 10 °C), we perform multiple syntheses of AuNPs (C11a and C11b samples), before combining their pellets (C11p samples) after centrifugation to improve heat generation. The absorbance spectra of the AuNPs used for photothermal studies on the *E. coli* and *P. aeruginosa* are reported in Figure 40. Both C11a-L and C11b-L samples exhibit the same absorbance spectrum after 45 minutes of irradiation with a 420 nm lamp (*ca.* 1 mW.cm^{-2}): a first band near 540 nm, and another in the NIR at 650 nm (Figure 36A). The obtention of the same data for both C11a-L and C11b-L is an excellent example of the reproducibility of the AuNPs synthesis. We report both dark control C11a-D and C11b-D samples in Appendix VIII.

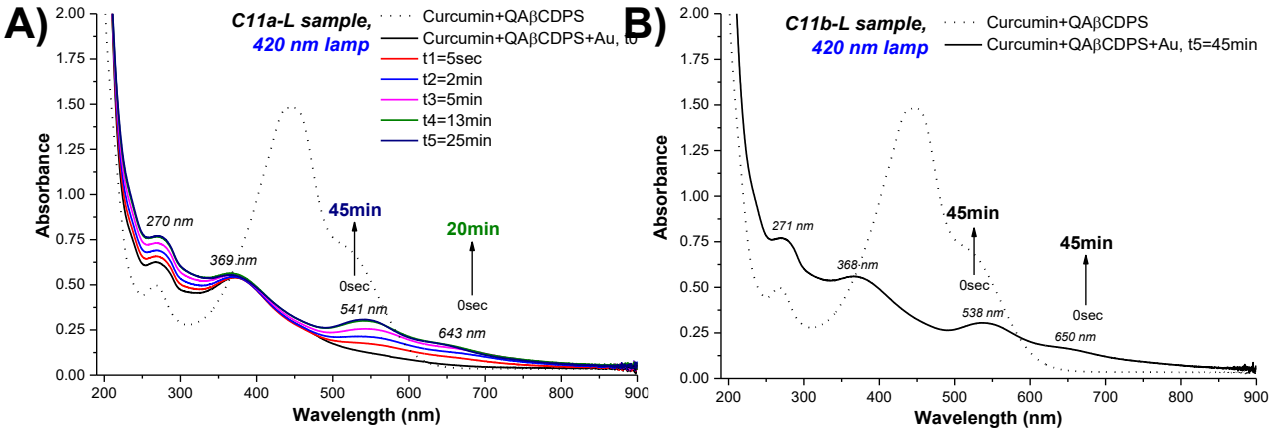

Figure 40: Comparison of the absorbance evolution of Curcumin+QAβCDPS+Au irradiated for forty-five minutes using a 420 nm lamp (*ca.* 1 $mW.cm^{-2}$) for A) the first batch (C11a-L) and B) the second batch (C11b-L). Each sample were stirred in a 1 cm absorbance cuvette. All measurements were performed in a 1 mm path-length absorbance cuvette using a Jasco V-760 UV-Vis spectrophotometer with air as the blank. Conditions: [PBS] = 10 mM; [Curcumin] = 0.31 mM; [QAβCDPS] = 10.00 $mg.mL^{-1}$; [$HAuCl_4 \bullet 3H_2O$] = 0.5 mM.

We photographed both combined samples (C11p-L and C11p-D samples) using TEM after biological studies (Figure 41). The sample was diluted anew in PBS before preparing the membrane for TEM images. In the images, gold nanotriangles and gold nanorods are visible. At the same time, isotropic structures remain the main shape in the sample, with the latter mostly responsible for the temperature rise observed during the photothermal studies. However, because we diluted both C11p-L and C11p-D samples beforehand, the particle population on the TEM images was neither significant nor representative of the combined samples before purification, nor of the pellet used for biological assays.

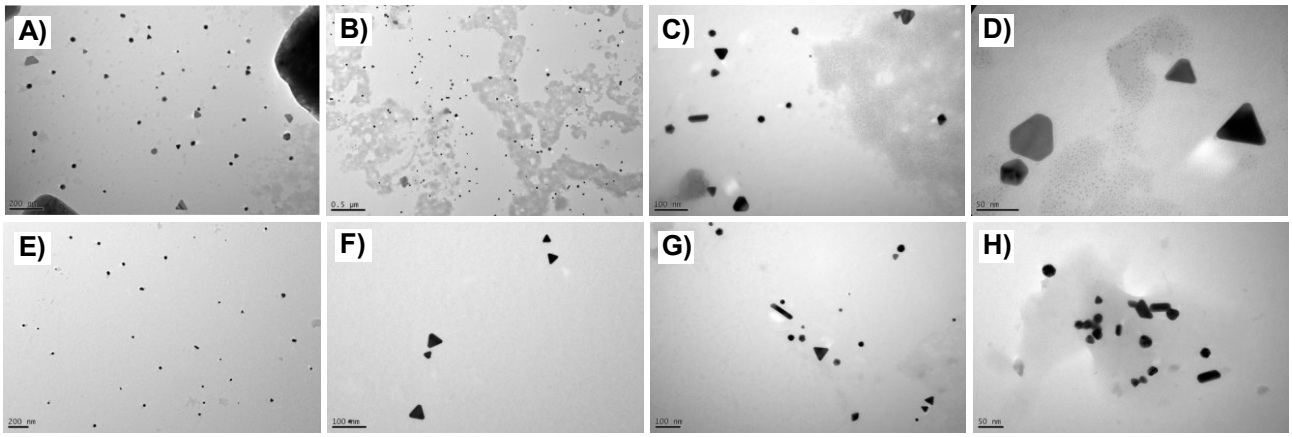

Figure 41: Transmission electron microscopic images of Curcumin+QAβCDPS+Au. A) B) C) & D) irradiated sample combined (C11p-L); E) F) G) & H) non-irradiated sample combined (C11p-D).

We investigated the photothermal effect of gold nanoparticles by combining two pellets from different centrifuged batches to increase nanoparticle concentration and enhance the photothermal response under irradiation. We placed the microplate on a heating plate, before and throughout the irradiation experiment, to keep the wells at *ca.* 37 °C to reproduce physiological temperature. After preparing a 20 % concentrated solution of gold nanoparticles in the biological medium, the wells were each irradiated with a 532 nm laser (*ca.* 15 $W.cm^{-2}$) equipped with a beam expander to cover the entire surface (Figure 42). The wells were irradiated for only a relatively short time (i.e., 3 minutes) due to the number of wells and the time required to complete the experiment. The cytotoxicity of the photothermal agent was inferred from the evolution of the bioluminescence in both bacterial strains.

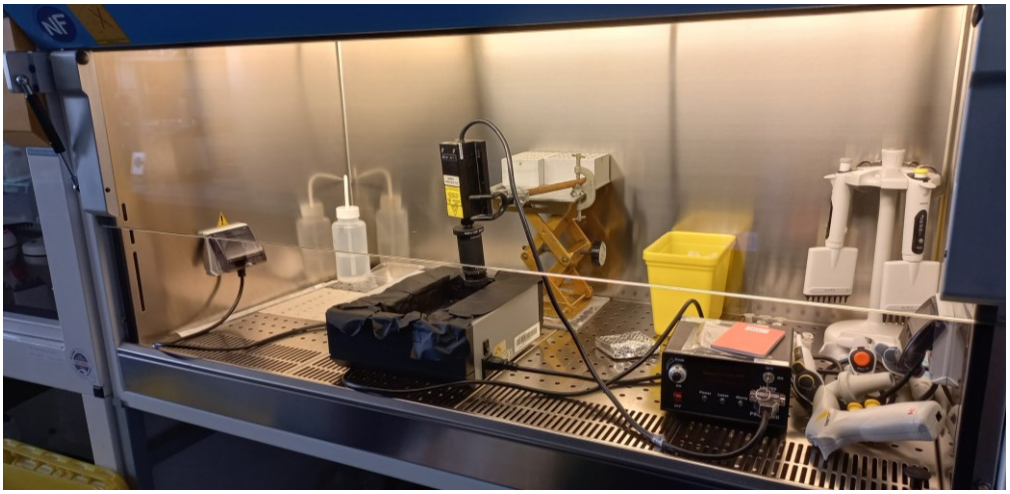

Figure 42: Picture of the experimental set-up used for all biological assays on bacteria and cancerous cells. The 532 nm laser, equipped with the beam expander, is suspended above the 98-multiwell for the irradiation of the formulations.

After the 3-minute irradiation, the temperature increase from C11p-L and C11p-D gold nanoparticles was about ΔT = 5 – 7 °C (Figure 43C & 43D), reaching then a maximum temperature of 45.4 °C. By comparison with the previous results reported above for classical photothermal studies (C6-L, C8-L and C10-D samples, part 4.2.4., 4.2.5. and 4.2.6., respectively), the low-temperature elevation observed in the present study may be due to the shorter irradiation time used here (i.e., 3 minutes).

In this chapter, only results with curcumin-based nanoparticles have to be considered. The next chapter (part 5.3.1.) will focus on the results with indigo carmine-based nanoparticles.

In assays with the two bacterial strains, samples from irradiated C11p-L and non-irradiated C11p-D syntheses exhibited a decrease of the bacteria's bioluminescence after three minutes

of irradiation. Furthermore, the survival rate decreased by a factor of 10 compared to the control, demonstrating the formulations' satisfactory cytotoxicity under light. Thus, no significant difference is observed between the irradiated and non-irradiated wells for both bacterial strains without gold nanoparticles and containing the βCD polymer, demonstrating then the non-toxicity induced by the polymer. It is also important to highlight that this toxicity is due to the photothermal effect of the AuNPs; the absence of bioluminescence decrease in the formulations without irradiation is observed for both bacterial strains, demonstrating the cytotoxicity of the gold nanoparticles exclusively under irradiation (Figure 43A and 43B). We noticed that *E. coli* appears more sensitive to the treatment compared to *P. aeruginosa*.

However, we observed a bacteriostatic effect. Days after irradiation, the growth of both bacterial strains continued at a slower rate than in non-irradiated wells (Appendix IX).

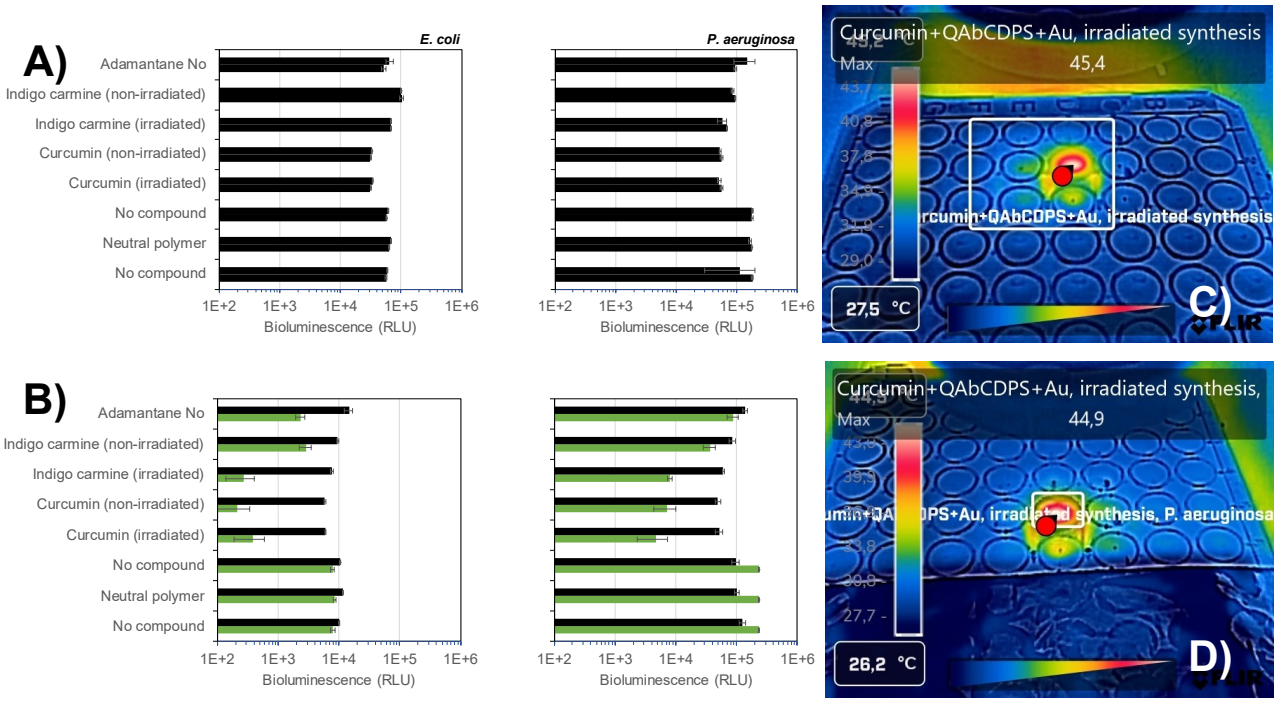

Figure 43: Bioluminescence evolution of different formulations of Curcumin+QAβCDPS+Au (C11p-L and C11p-D) A) before and B) after irradiation with 532 nm laser (*ca.* 15 W.cm^{-2}) for both bacterial strains *E. coli* and *P. aeruginosa*. Thermal pictures taken at the end of the irradiation of the formulation with C) *E. coli* and D) *P. aeruginosa.*

4.3.2. Antitumoral assays on ovarian cancer cells

OVCAR3 and its cisplatin-resistant counterpart, CR-OVCAR3, were used as model cell lines to study the photothermal effect of the synthesized gold nanoparticles on ovarian cancer cells. Cisplatin is a well-known drug used to treat ovarian cancer, but this molecule suffers from the MDR effect, with the fast development of resistance that dramatically reduces its efficacy.

The absorbance spectra of the three syntheses of the AuNPs used for the photothermal studies (C12a, C12b, and C13 samples) are reported in Appendices X and XI. The first two batches (C12a and C12b) present the same absorbance spectrum at the end of the 1h25 extended irradiation with a 420 nm lamp (*ca.* 1 $mW.cm^{-2}$): a single absorbance band near 540 nm. However, the absorbance spectrum of the third batch (C13) shows two LSPR bands, the first one at 540 nm and the second at 650 nm. Since the Zeta potential is consequential for biological applications, the average ZP of the samples has been measured, after biological studies and after resolubilization with PBS, with values of *ca.* +7.51 mV and +0.82 mV for the pooled irradiated and non-irradiated samples, respectively.

For the biological assays on cancerous cells, we centrifuged three batches of gold nanoparticles and combined their pellets to increase particle concentration (C12p-L and C12p-D samples). Once again, we studied only the photothermal effect of AuNPs irradiated using a 532 nm laser, as this wavelength is closest to the AuNPs' maximum absorption. We irradiated the wells for 3 minutes; we added a beam expander to increase the irradiation radius and cover the entire well surface and set the light source intensity to 15 $W.cm^{-2}$. After the 3-minute irradiation, the temperature increase of the gold nanoparticles was about ΔT = 15 – 16 °C, reaching a maximum temperature of 52.8 °C (Figure 45).

The laser irradiation of the cells alone, without particles, did not demonstrate cytotoxicity (CS+I) (Figure 44). We can make the same assessment for the control of the quaternary ammonium βCDs polymer (F2+I), which also did not show any characteristic reduction in cell viability. Furthermore, it is noteworthy that the formulations alone (F3 & F4) in the dark did not demonstrate cytotoxicity. Under light irradiation, the two cell lines exhibit different behavior. We observe no cytotoxicity for OVCAR3 under light exposure. In contrast, in the CR-OVCAR3, the resistant cell line, both formulations of gold nanoparticles induce a decrease in cell viability upon light exposure, by nearly 30 % for formulation F4 (F4+I). In comparison, the F3 formulation

(F3+I) only demonstrated a 20 % reduction in viability. Encouragingly, resistant cells to cisplatin seem more sensitive to AuNPs photothermal treatment.

In Figure 44, the F5 and F6 data concern indigo carmine-based formulations; we discussed these results in the next chapter.

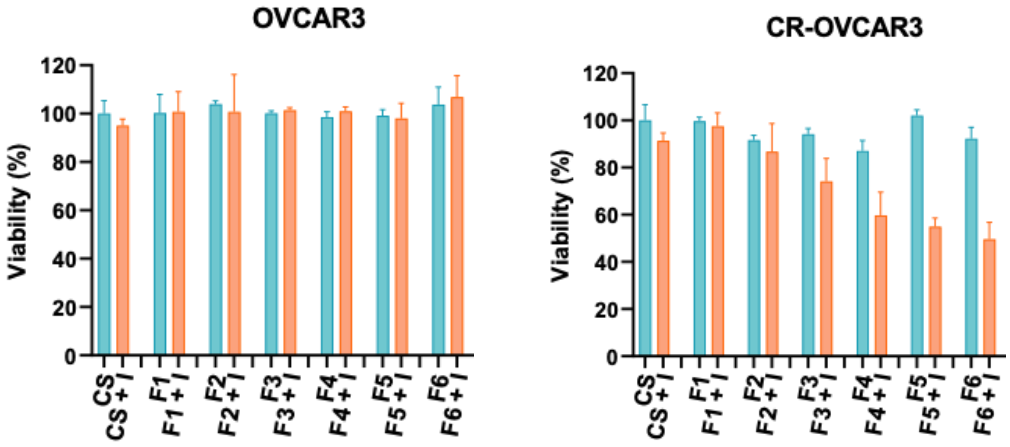

Figure 44: Viability assays on OVCAR3 and CR-OVCAR3. Data in orange: irradiated samples; data in blue: dark control. CS: cells alone; F3: Dark control of the formulation with Curcumin+QAβCDPS+Au (from irradiated AuNPs synthesis, (C12p-L)); F3+I: Irradiated formulation with Curcumin+QAβCDPS+Au with 532 nm laser with beam-expander (from irradiated AuNPs synthesis (C12p-L)) (*ca.* 15 W.cm^{-2}); F4: Dark control of the formulation with Curcumin+QAβCDPS+Au (from non-irradiated AuNPs synthesis (C12p-D)); F4+I: Irradiated formulation with Curcumin+QAβCDPS+Au with 532 nm laser with beam-expander (from non-irradiated AuNPs synthesis (C12p-D)) (*ca.* 15 W.cm^{-2}).

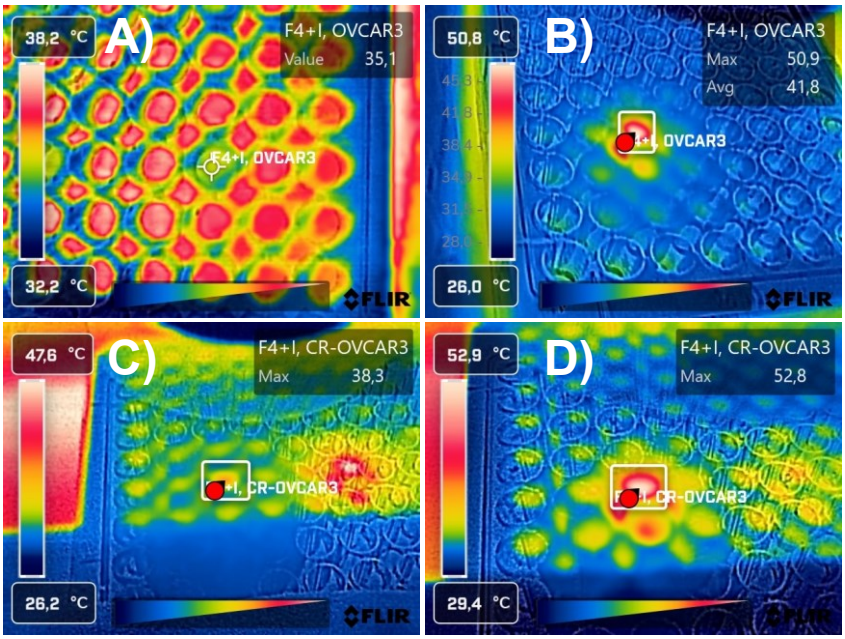

Figure 45: Photothermal pictures at the beginning and at the end of the irradiation of the F4+I formulation with A) & B) OVCAR3 cells and C) & D) CR-OVCAR3 cells.

* * *

With the satisfying results obtained above for both bacterial strains and encouraging results for cisplatin-resistant OVCAR3 cells, we believe better results are achievable. To increase the temperature and to enhance the photothermal effect, investigations have been conducted to explore 1) a longer irradiation time of the wells since we observed no cytotoxicity for the non-irradiated formulations, and 2) the increase of the concentration of the gold nanoparticles in the formulations. In both cases, the photothermal effect alone does not allow a complete cellular death; consequently, we investigated a multimodal approach.

4.4. Investigation for photodynamic therapy

4.4.1. Addition of a photosensitizer absorbing in the NIR

Because of the promising results of the photothermal properties of the AuNPs synthesized in the lab and tested *in vitro*, we pursued investigations for a bi-modal therapy with the incorporation of a photosensitizer in the gold nano system for the investigation of singlet oxygen production under light irradiation as an additive/synergistic effect to enhance the efficacy of the treatment.

We investigated the addition of different PS, namely zinc phthalocyanine (ZnPc) (C14 sample), verteporfin (VP) (C15 sample), and THPP (C17 sample). Loading ZnPc, a second-generation NIR-absorbing photosensitizer, was the first choice. Indeed, phthalocyanines generally exhibit a strong absorbance band in the infrared region, and the presence of the diamagnetic cationic center Zn^{2+} results in a longer triplet-state lifetime and, consequently, a higher singlet oxygen quantum yield, a lower toxicity, and a better stability.[211] ZnPc is an efficient photosensitizer already used in PDT applications and is a perfect fit for our systems, as it excites at 650 nm for singlet oxygen production.[212]

Despite its water solubility, ZnPc forms inactive dimer aggregates in solution. To address the issue, it has already been demonstrated that, in the presence of βCD polymer, a substantial amount of PS is monomerized upon complexation within the βCD cavity, as evidenced by the evolution of the absorption spectrum, with the rise of the characteristic monomer band at 680 nm.[213] After two days of stirring, despite the rise of the non-aggregated absorption band at 680 nm, the photosensitizer was still mainly present in its aggregated form (Figure 46A). Once the photosensitizer solubilized and its absorbance controlled, we performed fluorescence and

singlet-oxygen measurements of the system. The detection of singlet oxygen is based on observing its phosphorescence band in the near-IR; it exhibits a characteristic, weak signal near 1275 nm, far from other characteristic fluorophores, PS, or other substrates, which generally occur at wavelengths below 1000 nm. Furthermore, the solvent does not significantly influence that band's position.[131] The experiment must be done in deuterium oxide since the lifetime of $^1O_2$ in D_2O is improved by a factor of 20, from 3.1 μs in pure water to 68 μs.[214,215] However, the phosphorescence band of $^1O_2$ was not spotted in the sample (Appendix XII). In the present situation, the absence of the singlet oxygen signal can be due to predominant aggregated forms of the PS. Consequently, the aggregated complex is less sensitive to light excitation, and the production of singlet oxygen is less important.[216,217] This aggregation of the photosensitizer can be caused by the lack of ZnPc complexation by the cyclodextrin polymer, due to cavities already occupied by curcumin or its degradation product. Furthermore, as reported in the introduction (part 4.1.1), curcumin's ability to scavenge singlet oxygen can prevent the formation of singlet oxygen.[218]

For the addition of the verteporfin, another red-absorbing photosensitizer, the loading was more challenging. Upon complexation of the PS in the cyclodextrin polymer, its absorbance band at 680 nm began to decrease 20 hours after the polymer was added to the VP film. (Figure 46B). We detected no $^1O_2$ generation, and the PS degraded during the experiment.

The absence of singlet oxygen phosphorescence from ZnPc and VP can be mainly due to the lack of water solubility of VP and ZnPc aggregation, and so by their lack of complexation in βCDs cavity, which can be overcome by their incorporation by a covalent way to the βCD polymer chain, like the one reported by Baigorria *et al.*, using a chitosan polyethylenimine to solubilize ZnPc.[219] Furthermore, the irradiation in the red/near-infrared region of the system led to a photon absorption by anisotropic AuNPs, absorbing a greater photon ratio by their second LSPR band than the PS because of an overlap of the absorbance band of the complexed photosensitizer.

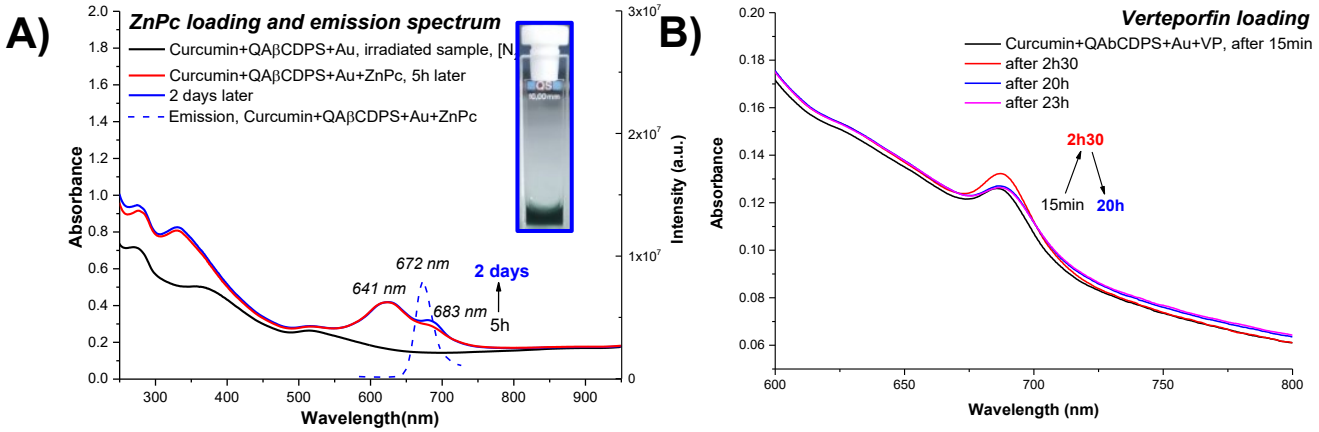

Figure 46: A) Comparison of the absorbance evolution over time and emission spectrum of Curcumin+QAβCDPS+Au+ZnPc (C14) with λ_{exc} = 400 nm. Measurements were performed using a PerkinElmer UV-Vis spectrophotometer and a fluorolog-2 spectrofluorometer. The inset shows a picture of Curcumin+QAβCDPS+Au+ZnPc after stirring. B) Comparison of the absorbance evolution over time of Curcumin+QAβCDPS+Au+VP (C15). Measurements were performed using a PerkinElmer UV-Vis spectrophotometer in a 1 cm path-length fluorescence cuvette. Conditions: [Curcumin] = 0.56 mM; [QAβCDPS] = 10.00 mg.mL^{-1}; [$HAuCl_4 \bullet 3H_2O$] = 0.56 mM.

4.4.2. Singlet oxygen production investigation

Since the investigation on the generation of singlet oxygen from ZnPc and VP failed, another porphyrin-type photosensitizer absorbing in the blue region, 5,10,15,20-Tetrakis(4-hydroxyphenyl)-21*H*23*H*-porphine (THPP), an analogue of the approved PDT drug Foscan, was investigated (C17).

THPP was also chosen for its strong absorbance near 420 nm, which will facilitate irradiation of this PS. We prepared the photosensitizer under the same conditions as for film preparation and studied both its emission and the $^1O_2$ phosphorescence (Figure 47A). Upon irradiation of the system with a blue 405 nm laser (*ca.* 12 W.cm^{-2}), the THPP photosensitizer demonstrated a slight emission of singlet oxygen phosphorescence, indicating that this active species is generated even in the presence of the AuNPs (Figure 47B). To enhance this slight singlet oxygen generation, we must investigate the incorporation of the THPP covalently linked to the polymer matrix, increasing its presence in solution. Otherwise, the incorporation of a drug (i.e., cisplatin or doxorubicin) can also be investigated to observe additional or synergistic effects, performed either with the drug loaded into the cyclodextrin cavity or covalently linked to modified βCD polymers.[220]

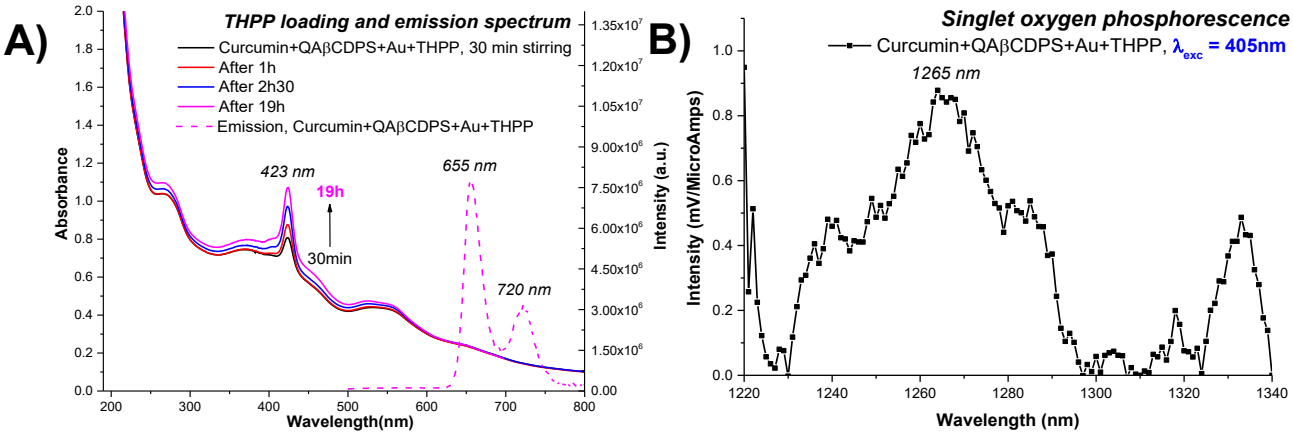

Figure 47: A) Comparison of the absorbance evolution over time and emission spectrum of Curcumin+QAβCDPS+Au+THPP (C17) with λ_{exc} = 405 nm (*ca.* 12 W.cm^{-2}). Measurements were performed using a Perkin UV-Vis spectrophotometer and a fluorolog-2 spectrofluorometer; B) Evolution of intensity (mV) of singlet oxygen phosphorescence of Curcumin+QAβCDPS+Au+THPP over wavelength (nm), excited at 405 nm (*ca.* 12 W.cm^{-2}). Measurement was performed using a fluorolog-2 spectrofluorometer. Conditions: [Curcumin] = 0.54 mM; [QAβCDPS] = 10.00 mg.mL^{-1} ; [$HAuCl_4 \bullet 3H_2O$] = 0.54 mM.

Then, we performed flash spectroscopy technique to investigate the presence of the THPP triplet state (Figure 48). This transient species is the key intermediate in generating $^1O_2$, and its presence is fundamental to achieving PDT action. We irradiated the sample with a pulsed laser at 335 nm. Absorbance measurements were performed at different delay times to compare and highlight any absorbance differences due to the presence of transient species and their decay lifetimes. Figure 48 shows the typical transient spectrum of porphyrin derivatives with a maximum at *ca.* 450 nm.[221] This signal is undoubtedly attributed to the triplet excited state of THPP, and not to residual curcumin. Since photo-excited curcumin has been reported to act as a photosensitizer, the presence of any transient species during its irradiation was also monitored.

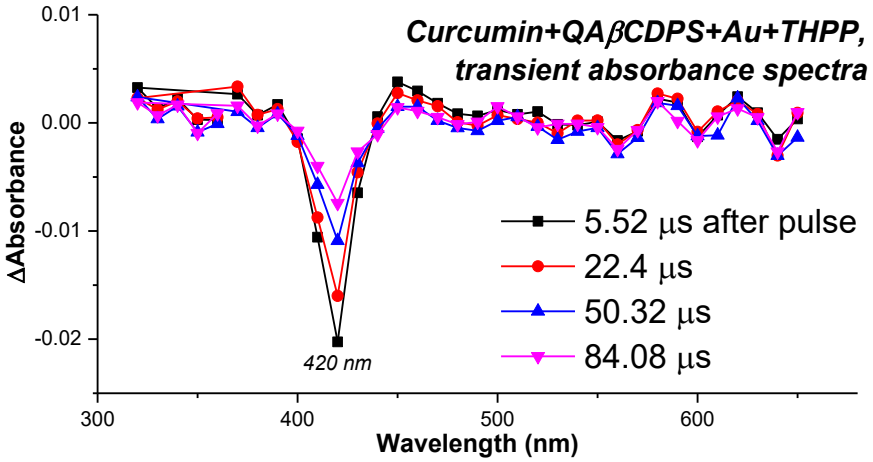

Figure 48: Transient absorption spectra of Curcumin+QAβCDPS+Au+THPP (C17) under [N_2], with pulsed 355 nm laser irradiation (E_{355} = 10 mJ $pulse^{-1}$) and recorded at different delay times of the laser pulse to observe the THPP transient species. Measurements were performed in a 1 cm path-length fluorescence cuvette. Conditions: [PBS] = 10 mM; [Curcumin] = 0.54 mM; [QAβCDPS] = 10.00 $mg.mL^{-1}$; [$HAuCl_4 \bullet 3H_2O$] = 0.54 mM.

Solutions of Curcumin+QAβCDPS were irradiated in the presence and in the absence of dioxygen with a pulsed 355 nm laser. In Figure 49, we present the typical spectrum of the ketyl radical discussed in part 4.1. (a broad band centered at approximately 520 nm) formed upon irradiation of curcumin, confirming the generation of the radical species rather than the curcumin triplet state.[193] Consequently, the production of singlet oxygen is not due to the irradiation of curcumin residues, but to the irradiation of the THPP.

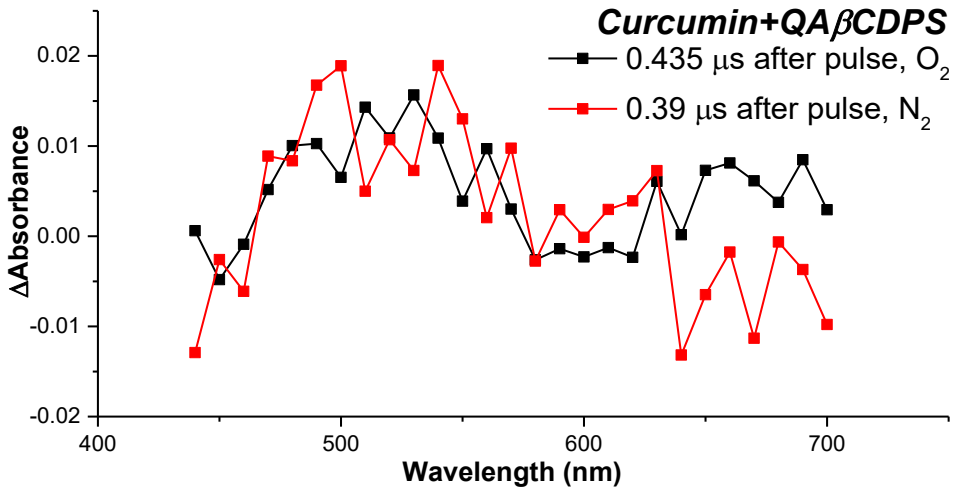

Figure 49: Comparison of transient absorption spectra of Curcumin+QAβCDPS under O_2 and [N_2] at different times after laser pulsation. The irradiation was performed using a pulsed 355 nm laser (E_{355} = 10 mJ $pulse^{-1}$), and the absorbance was recorded at different delay times of the laser pulse to observe the curcumin's transient species. Measurements were performed in a 1 cm path-length fluorescence cuvette. Conditions: [PBS] = 10 mM; [Curcumin] = 0.54 mM; [QAβCDPS] = 10.00 $mg.mL^{-1}$.

Due to the presence of a second band in the red region of the visible spectrum, we studied the photothermal properties of the system with a 671 nm laser (*ca.* 12 W.cm^{-2}) before and after addition of the PS. By comparison with precedent photothermal studies (C10), before the addition of THPP, the irradiated C16-L sample displayed better heat generation, with a temperature difference ΔT = 13.4 °C, while the dark control C16-D shows only a rise of ΔT = 10.8 °C. We then studied the photothermal properties of the system in the presence of the THPP (C17). The sample containing the PS demonstrated a similar temperature increase to that observed with the system before the addition of THPP. As proof of that, the addition of the PS did not have any impact on the heating properties of the gold particles (Figure 50).

Further investigations must be performed on this Curcumin+QAβCDPS+Au+THPP system, with the investigation of the singlet oxygen generation after photothermal studies of the gold nanosystem in the presence of THPP, performed with multiple cycles of irradiation, to observe the resistance and the performance of the PS after heating, and consequently, on the stability of the photothermal and photodynamic properties of this gold nanosystem.

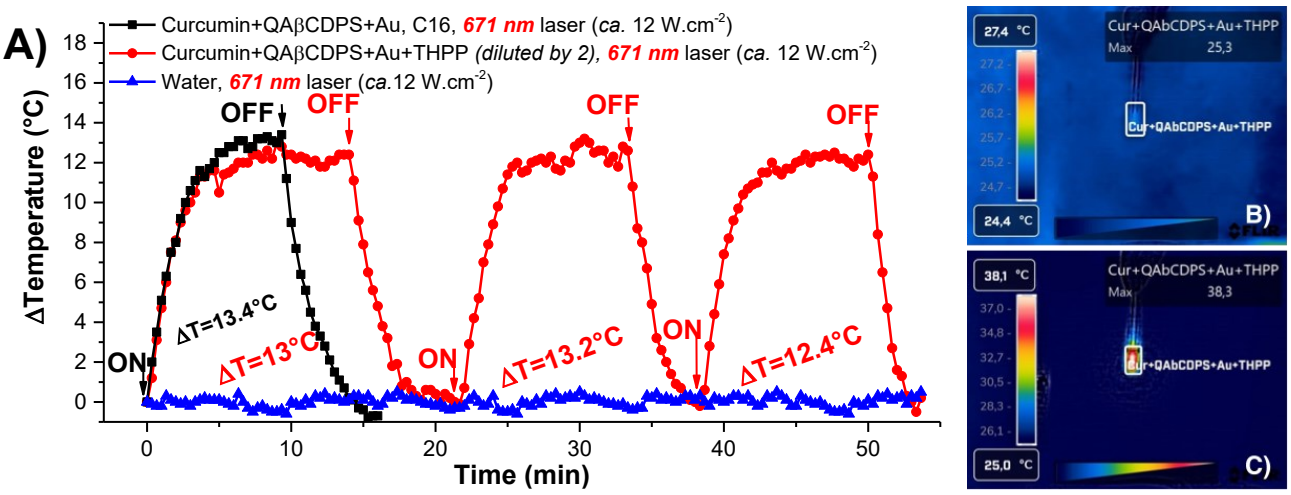

Figure 50: A) Evolution of the temperature (°C) over time (min) by laser irradiation at 671 nm (*ca.* 12 W.cm^{-2}), three cycles of measures of the diluted sample of Curcumin+QAβCDPS+Au+THPP (C17) (in red). Comparison with the evolution of the temperature of Curcumin+QAβCDPS+Au (C16-L) (in black), and a water sample (control sample) irradiated in the same conditions (in blue); B) Thermal picture taken at the starting point of the third cycle. C) Thermal picture taken at the end of the third cycle of the 671 nm laser irradiation. The temperatures were measured with a FLIR C3 thermal camera.

We also shot TEM images of this batch, taken 9 months after synthesis, to observe the shape of the AuNPs and evaluate their stability over time (Figure 51). The shapes are similar to those already observed (C8 and C11 samples). Indeed, we observed anisotropic structures like gold nanotriangles, gold nanoprisms, and some gold nanorods. However, no worm-like gold

nanoparticles (‘gold nanoworms’) were formed. Nonetheless, the main objects in the sample are still isotropic structures responsible for the band in the green region. These images, taken 9 months after the end of irradiation, clearly demonstrate the stability of these gold nanoparticles (synthesized from curcumin) and the robustness of their anisotropy over a relatively long period.

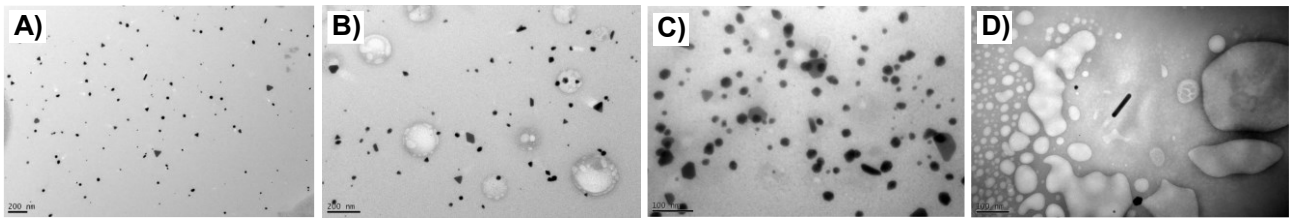

Figure 51: Transmission electron microscopic images of irradiated Curcumin+QAβCDPS+Au (C16-L).

4.5. Conclusion

Due to its therapeutic properties, curcumin is of strong interest for use as a reducing agent in a bimodal therapeutic strategy. However, its use as a green reducing agent for the one-step synthesis of anisotropic AuNPs is very challenging, as several equilibria (e.g., tautomeric and pH-dependent) and reactions (e.g., redox and photobleaching) can occur with such an unstable molecule, making it difficult to reproduce the synthesis.

Nonetheless, after significant work on the synthesis methodology, anisotropic particles were synthesized. We first investigated a procedure to enhance the solubility of curcumin in aqueous media. We demonstrated the formation of these anisotropic particles at an equimolar ratio of gold/curcumin, with a cationic βCD polymer serving as a templating and stabilizing agent for AuNPs, and in the presence of a PBS buffer to stabilize the pH of the medium during addition of the gold precursor. Even though some reproducibility problems remain (i.e., inconsistent shape of the LSPR band in the NIR, and inconsistent nanoparticles size, polydispersity index, and shape), gold nanotriangles seem systematically to be the preponderant anisotropic shape. Their photothermal properties are very satisfactory, with a highly repeatable and stable heat generation of about ΔT = 16 – 17 °C in the near-infrared region. Next, we plan to optimize the AuNPs formation procedure (with adjustments to the curcumin/Au ratio, the pH of the medium, and irradiation parameters) to better control the intrinsic gold nanoparticle properties. Furthermore, we want to achieve reproducibility in size and shape characteristics to assess photothermal performance in biological media correctly.

The biological assays of these nanotriangles as a photothermal agent demonstrated encouraging antibacterial activity, reducing *E. coli* bioluminescence by up to 10-fold. Encouraging results were also obtained against ovarian cancerous cells resistant to cisplatin, with a reduction of their viability up to 30 %.

Finally, the addition of a photosensitizer, the THPP, was investigated for a bi-modal PTT/PDT therapeutic application. The irradiation of the photosensitizer THPP resulted in a slight production of singlet oxygen, indicating potential for further photodynamic therapy applications. Furthermore, the presence of the PS did not affect the photothermal properties of the gold nanotriangles. However, the impact of heat generation on the photosensitizer stability during and after photothermal studies has not been assessed. Consequently, we need to measure singlet oxygen before and after multiple cycles of photothermia to assess the stability of singlet oxygen generation. Also, we will perform further investigation to associate the AuNPs with a conventional drug such as cisplatin or doxorubicin, covalently linked to the cyclodextrin polymer or hosted in the βCDs cavity, to observe additive or synergistic effects between PDT and chemotherapy for the improvement of singlet oxygen generation or tumor death.

4.6. Experimental part

Methods :

Spectroscopic-purity solvents (i.e., methanol and ethanol) were used. The solutions were prepared in ultrapure (Milli-Q) water or in PBS buffer. D_2O (≥99.8%) was purchased from Carlo Erba. The PBS buffer was prepared by adding one phosphate-buffered saline tablet to 100 mL of extra pure water (10 mM). After solubilization of the tablet, the pH is measured with a pH meter (inoLab): (T = 27 °C) pH = 7.52. Fluorescence cuvettes (1 cm path-length, 3 mL capacity) and absorbance cuvettes (1 mm path-length and 1 cm path-length, 3 mL capacity) were cleaned with *aqua regia* before each experiment.

The Phosphate Buffered Saline tablet was purchased from VWR Life Science. The βCD polymer, the quaternary ammonium βCD polymer (QAβCDPS), and the soluble sulfobutylated βCD polymer (SBβCDPS) were prepared by Cyclolab and used without any purification. Curcumin (≥94% curcuminoid content; ≥80% curcumin), Tetrachloroauric (III) acid trihydrate ($HAuCl_4•3H_2O$) (≥99.9% trace metals basis) (C = $5.08×10^{-1}$ M), Verteporfin (≥94.0%), and 5,10,15,20-Tetrakis(4-hydroxyphenyl)-21*H*,23*H*-porphine were purchased from Sigma Aldrich and used without any purification. Zinc phthalocyanine was purchased from Frontier Scientific.

Instrumentation:

Irradiations of the samples were carried out in a 1 cm path-length fluorescence quartz cuvette (3 mL capacity) using either 405 or 532 nm continuum-wave lasers (*ca.* 6, 12, or 15 $W.cm^{-2}$) with a beam diameter of *ca.* 1.5 mm, or a 420 or 426 nm lamp (*ca.* 1 $mW.cm^{-2}$). Absorbance spectra were measured using a 1 mm length quartz cuvettes or a 1 cm path-length absorbance quartz cuvettes (3 mL capacity), either using a PerkinElmer Lambda 365 UV-Vis spectrophotometer (Measurement window: from 180 to 1100 nm; SBW: 1.0; Data interval: 0.5 nm; Scan rate: 300 $nm.min^{-1}$), Jasco V-560 UV-Vis spectrophotometer (Measurement window: from 180 to 800 nm), or using a Jasco V-760 UV-Vis spectrophotometer (Measurement window: from 190 to 900 nm).

The centrifugation was performed using an Eppendorf Centrifuge 5430 with FA-45-30-11 rotor at room temperature (T = 25 °C).

The fluorescence was recorded using a Spex Fluorolog-2 (mod. F-111) spectrofluorometer, using quartz cuvettes with a 1 cm path-length.

$^1O_2$ emission was registered with the same above-mentioned spectrofluorometer equipped with a NIR-sensitive liquid nitrogen cooled photomultiplier. The hydrodynamic size of the nanoparticles was measured at room temperature (T = 25 °C) using a Dynamic Light Scattering HORIBA LB-550 apparatus equipped with a diode laser at 650 nm. Samples were shaken by hand before each measurement. After formation of the AuNPs, the samples were diluted 20-fold by adding 100 μL of the AuNPs preparation and 1.9 mL of Milli-Q water. For each sample, three measures were performed. The measurements were performed in a fluorescence quartz cuvette (1 cm path-length, 3 mL capacity), and were performed at room temperature (T = 25 °C). Size and Zeta potential were measured by NTA and performed at room temperature (T = 25 °C) with NanoSight. Samples were shaken by hand and vortexed before any measurement. The samples were diluted 100-fold with 10 μL of the AuNPs preparation and with 1.99 mL of Mili-Q water.

The pH values were measured with an inoLab pH meter at room temperature (T = 25 °C). The instrument was calibrated before each measurement using two buffer solutions at pH = 7.00 and pH = 4.01.

Particle sizes were measured from TEM images using ImageJ, an open-source image-processing software, and calibrated using image scales. Except for some zoom-in images that were discarded, every capture obtained was analyzed.

βCD-polymer solution preparation: The mass of βCD polymers used was measured with a Sartorius analytical balance, and then solubilized in Milli-Q water. The solution was magnetically stirred for 20 minutes using an IKA Topolino at medium velocity at room temperature (T = 25 °C).

Curcumin film preparation: The curcumin film was prepared by adding about 5 mg of commercial curcumin diluted in ethanol in a 4 mL amber flask, which was then covered with aluminum foil. The mother solution was diluted, and its absorbance was monitored with a PerkinElmer Lambda 365 UV-Vis spectrophotometer in a 1 mm path-length cuvette, with air as the blank. After baseline correction, the concentration of curcumin was calculated using the Beer-Lambert law ($A = l \times \varepsilon \times C$); it was measured in ethanol solvent at λ_{max} = 427 nm with ε = 61864 $M^{-1}.cm^{-1}$ for ethanol.[222] Then, the solvent was evaporated with nitrogen flux until the formation of a film of curcumin.

Preparation of the solution of Curcumin+QAβCDPS: Addition of the solution of QAβCDPS in PBS buffer to the film of curcumin in an amber flask of 4 mL, covered with aluminum foil. Then, the solution was stirred using an IKA Topolino at maximum velocity until all the curcumin was solubilized.

Preparation and irradiation of the system Curcumin+QAβCDPS+Au: Addition of $HAuCl_4 \cdot 3H_2O$ (C = 0.5M) in two samples of Curcumin+QAβCDPS: a first one was irradiated, and the second one was kept in dark conditions for further comparison with the former sample. The irradiation was performed in a fluorescence 1 cm path-length cuvette with a 426 nm lamp (*ca.* 1 $mW.cm^{-2}$), or a 405 nm laser (*ca.* 6 $W.cm^{-2}$). Both irradiated and dark control samples were magnetically stirred using an IKA Topolino at low velocity. A UV-Vis spectrophotometer was used to follow the absorbance evolution of both samples.

Purification of Curcumin+QAβCDPS+Au: 2 mL of the Curcumin+QAβCDPS+Au sample was centrifuged at 14 000 rpm for 10 minutes. The supernatant was discarded. The precipitate is resolubilized in 2 mL of PBS buffer. The absorbance spectra of both the precipitate and the supernatant are measured.

Preparation of a film of PS: About 5 mg of PS is solubilized in methanol in a 4 mL amber flask covered with an aluminum foil. The PS was added to the solution until the absorbance was close to A = 1 at λ = 680 nm for ZnPc and VP, and to A = 2 at λ = 400 nm for THPP, using a PerkinElmer UV-Vis spectrophotometer in a 1 mm path-length cuvette with air as the blank. Then, methanol was evaporated under a nitrogen flux to form a PS film.

Preparation of a solution of Curcumin+QAβCDPS+Au+PS: Curcumin+QAβCDPS+Au was added to the PS film in a 4 mL amber flask covered with aluminum foil, and the mixture was stirred in the dark. The sample was stirred until no absorbance evolution was observed.

Measurement of singlet oxygen production: The sample was diluted 10-fold with D_2O. The absorbance spectra were recorded before and after each measurement using the fluorolog spectrofluorometer. The photosensitizer was excited using a continuous-wave laser at 405 or 671 nm (*ca.* 15 $W.cm^{-2}$) with a beam diameter of *ca.* 1.5 mm.

Flash spectroscopy measurements: Samples were degassed for 20 minutes before the flash photolysis experiments. All of the samples were excited with the third harmonic of Nd–YAG Continuum Surelite II–10 laser (355 nm, 6 ns FWHM), using quartz cells with a path length of 1.0 cm. The excited solutions were analyzed with a Luzchem Research mLFP–111 apparatus with an orthogonal pump/probe configuration. The probe source was a ceramic xenon lamp coupled to quartz fiber-optic cables. The laser pulse and the mLFP–111 system were synchronized by a Tektronix TDS 3032 digitizer, operating in pre-trigger mode.

Photothermal studies: Irradiations during photothermal studies were performed with four different continuum-waves lasers: at λ_{exc} = 532, 671, 750, or 808 nm (*ca.* 6 or 12 $W.cm^{-2}$), with a beam diameter of *ca.* 1.5 mm. Samples (150 or 200 µL) were irradiated in an NMR tube. The thermal evolution was captured with a FLIR C3 thermal imaging camera, with temperatures reported every twenty seconds. Three cycles of measures were performed consecutively for each sample. Thermal pictures of the sample were taken at the beginning and the end of each irradiation cycle. The measurements were performed at room temperature (T = 18 or 25 °C), depending on the time of the year. Thermal images of the measurements were processed with FLIR software and presented with a linear temperature color scale.

TEM samples and images were prepared and captured by Dr Marta Maria Natile from the University of Padova and Philippe Elies from the University of West Brittany.

Biological assays on bacteria were performed in collaboration with Dr Tony Le Gall, and assays on cancer cells were performed in collaboration with Prof. Tristan Montier and Dr Manh Nguyen Quoc from the GTCA Team, UMR INSERM 1078.

5. "Green" synthesis of a gold nanosystem with a plant extract analogue: Indigo carmine

5.1. Indigo carmine, blue dye

Since we observed no selectivity in the irradiation of curcumin for the reduction of gold salts compared to conditions in the absence of light, a second green reducing agent, indigo carmine (IndC), was investigated.

Indigo carmine (disodium [2(2′)E]-3,3′-dioxo-1,1′,3,3′-tetrahydro[2,2′-biindolylidene]-5,5′-disulfonate) is also a low molecular compound (M = 466.367 g.mol^{-1}). This synthetic dark blue powder is water-soluble and is obtained by sulfonation of indigo, a plant extract primarily derived from the leaves of *Indigofera Tinctoria* (Figure 52).[223] Indigo carmine is mainly used as a food colorant, and has been approved by both the Food and Drug Administration in the United States and by the European Union.[224,225] Indigo carmine is also used as a pH indicator; IndC turns from blue to yellow between pH = 11.4 and 13, as the deprotonation of the two amino groups of indigo carmine occurs at pH = 12.2.[226] In medicine, even if IndC is used to stain cells and demonstrates excellent biocompatibility, some toxicities have been reported, like skin coloration,[227] or hypertension.[228]

Figure 52: Illustration of *Indigofera Tinctoria* by Francisco Manuel Blanco, in Flora de Filipinas [...] Gran edición [...] [Atlas I], 1880-1883?.[229]

The chemical structure of indigo carmine is characterized by: 1) the $NaSO_3$ moiety, enhancing the solubility of the indigo analogue in aqueous media, 2) a H-chromophore group, consisting of a cross-conjugated system involving two carbonyls acceptors and two amines donors groups positioned on the two sides of the double carbon-carbon bond at the center of the molecule, and responsible for the characteristic blue color of the dye, and 3) a C_{2h} symmetry and two intra-molecular hydrogen bonds between the carbonyl and amine groups.[230,231]

Indigo carmine can be present in solution under two forms: keto- or leuco-indigo carmine. An intermediate from the first reduction of keto-indigo carmine is also present. The structure of the leuco form differs from the keto one by the absence of the central double bond and by the two intra-molecular hydrogen bonds (Figure 53).

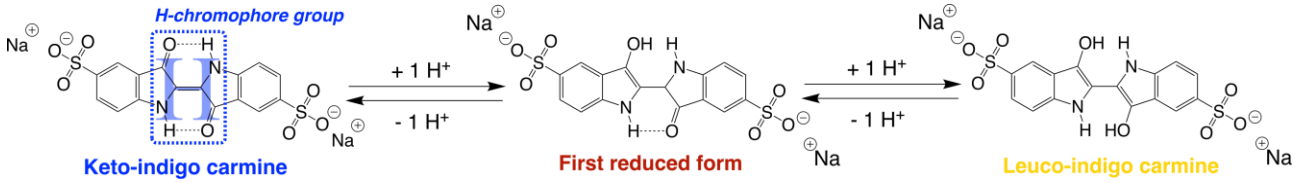

Figure 53: Keto form of indigo carmine. The H-chromophore group is responsible of its characteristic blue color.

Because of the two hydrogen bonds between the carbonyl acceptors and the amine donor groups on each side of the central double bond, excited-state proton transfer (ESPT) can occur under light irradiation, accounting for the dye's stability under irradiation. In polar solvents, the ESPT is influenced by a change in dipole moment, resulting in a faster excited-state decay (<10 ps) than in a non-polar solvent (130 ps).[232] However, because of the same intramolecular hydrogen bonds, no photochromism resulting from the photoisomerization around the central carbon-carbon bond is witnessed.[233] ESPT has a strong influence on the relaxation of the keto-IndC form, leading to internal conversion from S_1 to S_0.

However, for the leuco form, since no proton transfer can occur, the rotational isomerization at the excited state is possible, and its triplet state, absorbing near 540 nm (T_1 to T_n transition), can lead to the formation of emissive species.[234,235]

Consequently, if indigo carmine is used as a reducing agent for the AuNPs formation, the keto form must be reduced beforehand into the leuco one, and once excited, the transient species may reduce the gold Au(III) to Au(0). The leuco form can be achieved at high pH in the presence of a reducing agent such as $Na_2S_2O_4$ or monosaccharides,[236] but the particular inclusion properties and charges of βCD polymers may displace the equilibrium between the different forms of IndC to allow the preparation of AuNPs in less drastic conditions.

CDs can also encapsulate indigo carmine, with its two anionic sulfonate groups at the exterior of the cavity; the blue dye shows slightly better stability after encapsulation.[237]

Indigo carmine is also an antioxidant species and can consequently scavenge singlet oxygen.[238] This property must be considered when developing bimodal PDT-PTT strategies, further discussed.

5.2. AuNPs synthesis and their characterization

5.2.1. Synthesis of anisotropic gold nanoparticles with neutral βCD polymer

The procedure for the synthesis with indigo carmine as a reducing agent was inspired by that of curcumin. Since indigo carmine is already soluble in PBS buffer, the investigation of its solubility in an aqueous solution was not problematic. As mentioned above, the cyclodextrin cavity can host IndC, and we first wanted to study how interactions between the βCD-based polymer and the dye can influence the formation of indigo carmine forms suitable for initiating AuNPs formation. As previously described for curcumin, distinct neutral, cationic, and anionic polymers were investigated using a similar protocol: a concentrated stock solution of IndC in PBS buffer is prepared, and its concentration is adjusted by UV-Vis spectroscopy to reach about [IndC] = 0.4 mM, using Beer-Lambert law with ε_{max} = 15000 cm^{-1} at λ_{max} = 608 nm.[239] This concentration of indigo carmine was similar to that used in the previous chapter with curcumin. Then, the gold precursor is added before polymer addition in an equimolar ratio with the reducing agent. Gold nanoparticle formation was observed only with the neutral βCD polymer (I1 sample). The following paragraph will be focused only on the results obtained with the latter.

Besides a rise of its absorbance due to the improvement of its solubility, the addition of βCD polymer in a solution of IndC in PBS induces no changes in its 610 nm band, i.e., the band characteristic of the oxidized keto-indigo carmine (Figure 54A). After the addition of the gold precursor, the band at 610 nm bleaches rapidly, while another one centred near 400 nm clearly appears in the absorption spectrum of IndC encapsulated in the polymer. We can ascribe this newly formed band to leuco-indigo carmine, the form of the dye that we hypothesized to be active for the preparation of AuNPs. The sample was irradiated using a 405 nm laser (I1-L sample) and compared to a control kept in the dark (I1-D sample). The irradiated sample I1-L showed an absorbance band at 520 nm and a broad shoulder extending into the near-IR region

(Figure 54B). The I1-D sample exhibited the formation of gold nanoparticles with two absorption bands, with the second in the infrared region (Figure 54C). However, the particles synthesized under both conditions were not very stable, and most adhered to the cuvette walls after syntheses (Appendix XIII).

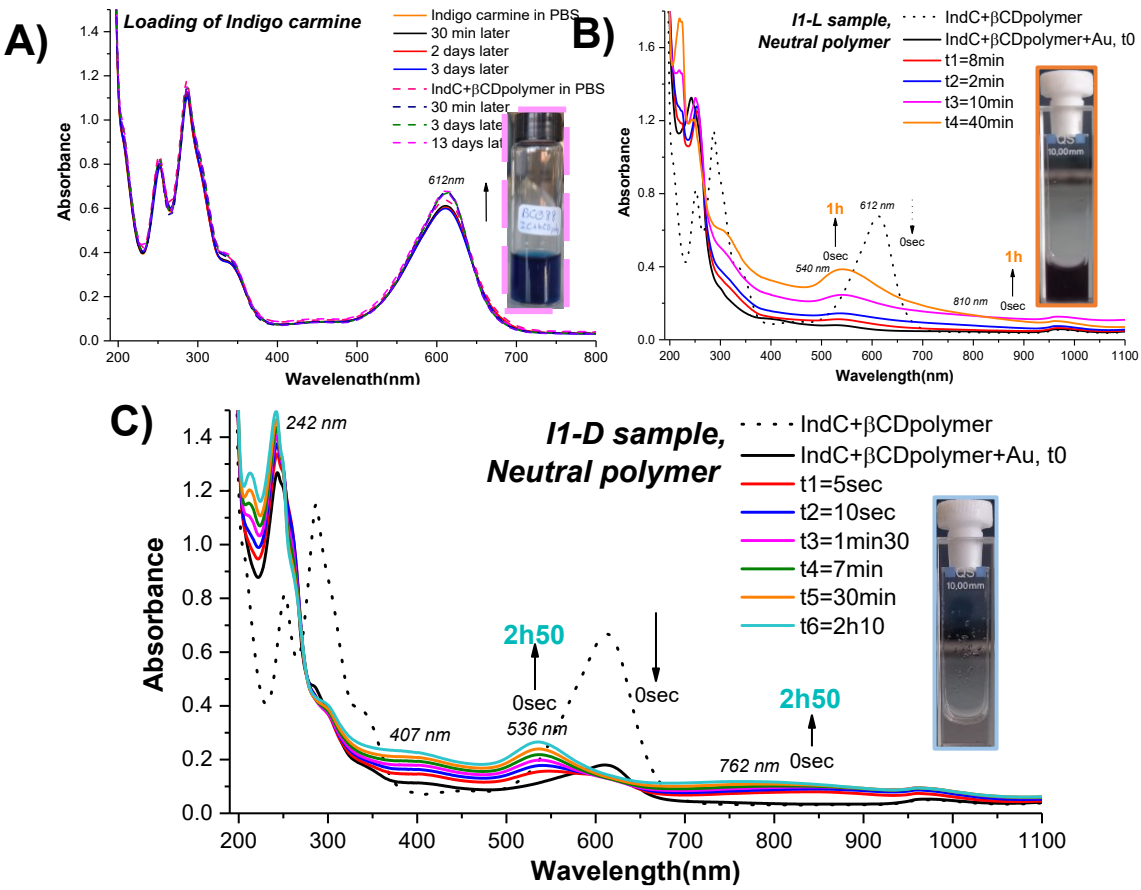

Figure 54: A) Comparison of the absorbance evolution of indigo carmine and IndC+βCDpolymer in PBS stirred over time. The inset shows a picture of the sample, thirteen days after polymer addition. B) Comparison of the absorbance evolution of IndC+βCDpolymer+Au (I1-L) stirred and irradiated using a 405 nm laser (*ca.* 6 W.cm^{-2}) for one hour. The inset shows a picture of the irradiated sample I1-L at the end of the irradiation; C) Comparison of the absorbance evolution of the dark control IndC+βCDpolymer+Au (I1-D), stirred for two hours and fifty minutes. The inset shows a picture of the dark control I1-D sample at the end of the synthesis. Measurements were performed in a 1 mm path-length absorbance cuvette with air as the blank using a PerkinElmer UV-Vis spectrophotometer. Conditions: A), B) & C) [PBS] = 10 mM; [IndC] = 0.349 mM; [βCDpolymer] = 2.58 mg.mL^{-1}; [$HAuCl_4 \bullet 3H_2O$] = 0.349 mM.

5.2.2. Investigations on the influence of the atmosphere on gold nanoparticles formation

As dioxygen is known to interfere with redox and photo-induced redox reactions, we performed the synthesis under inert conditions, with the sample degassed beforehand under a nitrogen flux to observe the influence of the absence of dioxygen on gold salt reduction (I2 sample).[240] It is noteworthy that, contrary to precedent synthesis I1, we carried out the measurements of the absorbance spectra in a 1 cm fluorescence cuvette because of the requirement of inert atmosphere, it was not possible to open the 1 cm cuvette and to do transfer the solution in a 1 mm cuvette to perform the measure because of refilling if the solution in dioxygen; consequently, the absorbance bands are more intense than the ones presented above, and the comparison of the band intensities is less accurate. Despite the previous results (I1), we observed a difference in the spectral evolution during NPs formation between the synthesis performed in the dark (I2-D) and that performed under irradiation (I2-L).

Unlike in I1, upon addition of the gold precursor to the degassed IndC+βCDpolymer, the LSPR band formation of AuNPs is not straightforward: we observe a two-phase evolution of the absorption spectrum. During the first irradiation time (up to 1 min 35 s), a band appears in the green region, which we attribute to the formation of isotropic AuNPs. After 1 min 35 of irradiation, the absorbance band decreases, and a shoulder at about 600 nm begins to appear. Forty minutes after the start of the synthesis, the maximum absorption at 700 nm is reached (Figure 55). In contrast to the curcumin system and the precedent synthesis with indigo carmine I1, we can make two hypotheses about the gold nanoparticles formed: either the first-formed gold nanoparticles tend to aggregate during the synthesis process,[241] or the already-formed AuNPs evolve into anisotropy. More characterization of the sample must be performed to determine the particles' shape and, thus, to confirm either of these two hypotheses.

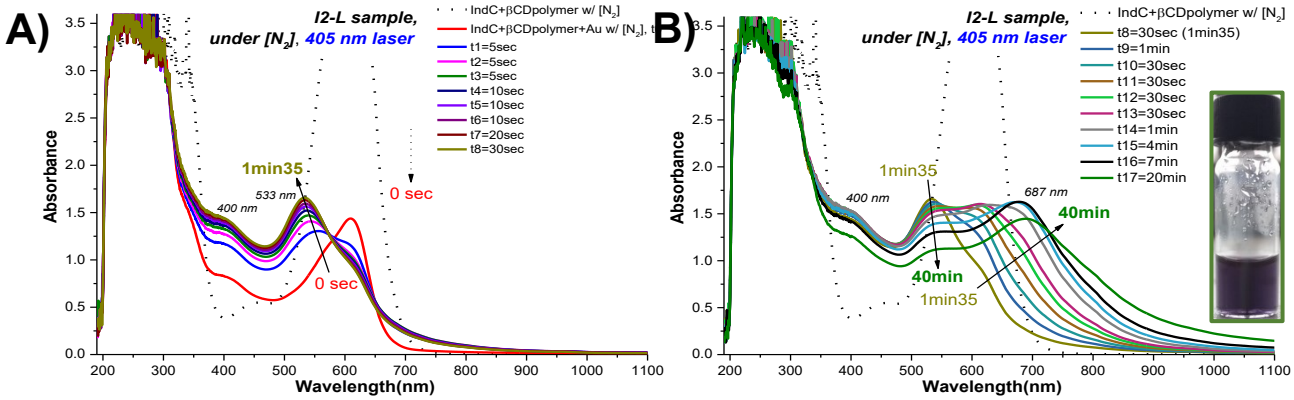

Figure 55: Comparison of the absorbance evolution of IndC+βCDpolymer+Au (I2-L), previously degasses under [N_2], irradiated with 405 nm laser (*ca.* 6 W.cm^{-2}), in a PBS solution. A) Irradiation of the system up to one minute and thirty-five seconds; B) Irradiation of the system from one minute and thirty-five seconds to forty minutes. The inset shows a picture of the I2-L sample at the end of the irradiation. Measurements were performed in a 1 cm path-length absorbance cuvette using a PBS as the blank using a Perkin-Elmer UV-Vis spectrophotometer. Conditions: [PBS] = 10 mM; [IndC] = 0.391 mM; [βCDpolymer] = 1.59 mg.mL^{-1}; [$HAuCl_4 \bullet 3H_2O$] = 0.391 mM.

A non-irradiated sample under [N_2], I2-D, demonstrated the same absorbance evolution discussed above, with first a band at 520 nm progressively and slightly decreasing, then the appearance of a second band in the red region near 610 nm and a third band near 750 nm in the near-infrared region (Figure 56). The second band formed in the red region can be due either to a second population of AuNPs, or to the plasmon coupling of close spherical particles, or, more probably, when considering the band wavelength, because of the residual presence of keto-indigo. On the other hand, the band in the infrared region can be attributed to the aggregation of isotropic AuNPs or to the presence of anisotropic particles.[242]

We still observe the drop in absorbance after the end of the synthesis under an inert atmosphere. Because the band in the near-infrared region is the only one showing a decrease in absorbance, it seems that a loss of the anisotropy characterizes the degradation of the AuNPs. Thus, because the synthesized anisotropic nanoparticles were still degraded, most of the characterization was challenging to perform.

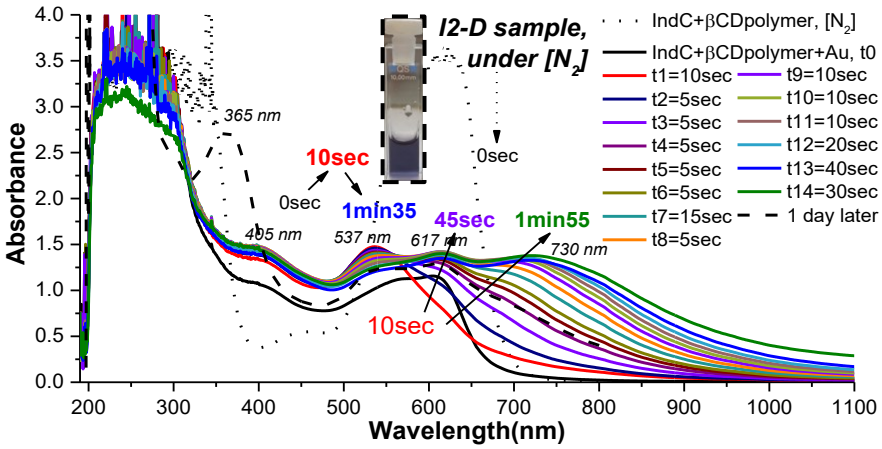

Figure 56: Comparison of the absorbance evolution of the dark control IndC+βCDpolymer+Au (I2-D) stirred for two minutes in a PBS solution. The inset shows a picture of the I2-D sample under [N_2], one day after the end of the stirring. Measurements were performed in a 1 cm path-length absorbance cuvette with PBS as the blank using a PerkinElmer UV-Vis spectrophotometer. Conditions: [PBS] = 10 mM; [IndC] = 0.381 mM; [βCDpolymer] = 2.00 mg.mL^{-1}; [$HAuCl_4$•$3H_2O$] = 0.381 mM.

However, the absorbance shifts or the better formation of the second band in degassed conditions were not always the same (i.e., hypochromic shift for I3-L or a broad band in the NIR for I3-D samples, for Appendices XIV and XV, respectively). In other attempts, both irradiated and dark-control samples under [N_2] (I4-L and I4-D) showed no clear LSPR band in the near-infrared region (Figure 57). However, compared to I2 or I3 samples, the particles show a notable improvement in stability over time. For all four samples (i.e., I3-L, I3-D, I4-L, and I4-D), the synthesized particles remained stable over multiple days, with their absorbance bands increasing over time.

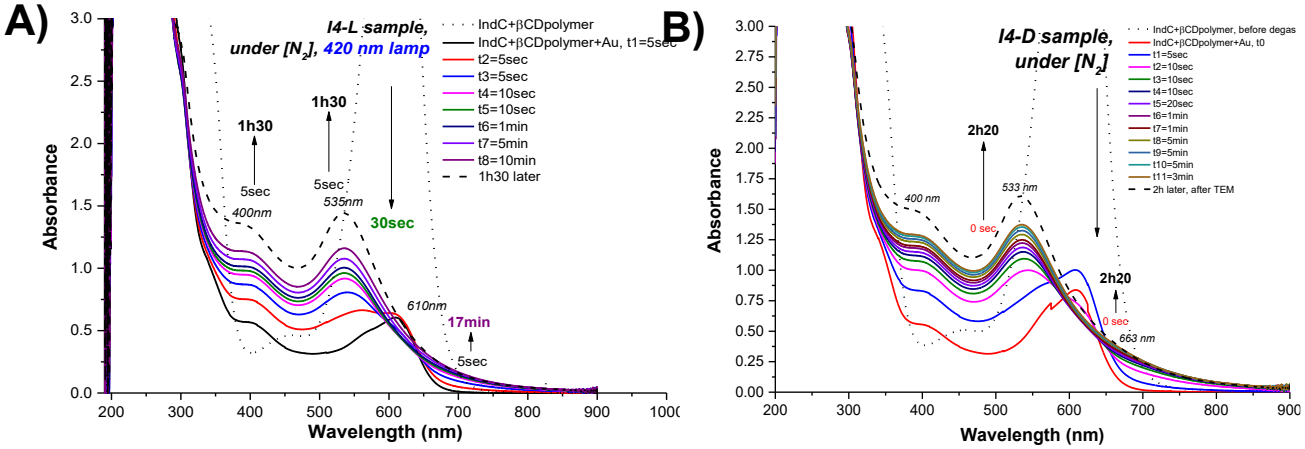

Figure 57: A) Comparison of absorbance evolution of IndC+βCDpolymer+Au (I4-L), under [N_2], irradiated using a 420 nm lamp (*ca.* 1 mW.cm^{-2}) for seventeen minutes under stirring; B) Comparison of absorbance evolution of the dark control of IndC+βCDpolymer+Au (I4-D), under [N_2], with a stirring of seventeen minutes. Measurements were performed in a 1 cm path-length absorbance cuvette with PBS as the blank using a Jasco V-760 spectrophotometer. Conditions: [PBS] = 10 mM; [IndC] = 0.387 mM; [βCDpolymer] = 2.00 mg.mL^{-1}; [$HAuCl_4$•$3H_2O$] = 0.387 mM.

The synthesis under an inert atmosphere for I2 samples yielded different populations of gold nanoparticles with very broad LSPR bands in the visible and near-infrared regions. Even if this absence of shape selectivity can be an important drawback for reproducible biological applications, the formation of different populations and their diverse shapes can be useful, as we can then perform irradiation for photothermal studies over a broader wavelength range. Because of the better particle stability over time of particles synthesized in inert conditions, their sizes, shapes, and photothermal properties were investigated.

We observed very similar spectral evolution of the irradiated samples compared to their dark controls, leading us to revise the previously postulated hypothesis that attributed the band at *ca.* 400 nm to leuco-indigo carmine. Indeed, the evolution of the absorbance spectra of indigo carmine during synthesis is very similar to that observed by Kandelbauer *et al.* when investigating the oxidation of keto-indigo carmine into isatin, a side-product resulting from IndC cleavage.[243] The hypothesis is that the addition of tetra chloroauric(III) acid induces the oxidation of the IndC and consequently the cleavage of the keto-indigo carmine molecule. The 400 nm band would then be attributed to the isatin derivative as a product of this cleavage. Thus, neither the light nor the presence of an inert atmosphere had any impact on the synthesis since the cleavage of the IndC happens spontaneously upon the addition of the gold precursor. However, by acting as a template and stabilizing agent, the polymeric network of cyclodextrins is essential for the formation of gold nanoparticles; in their absence (I5-L sample), no particles are formed, and only the absorbance spectrum of isatin is observed at the end of the reaction (Figure 58).

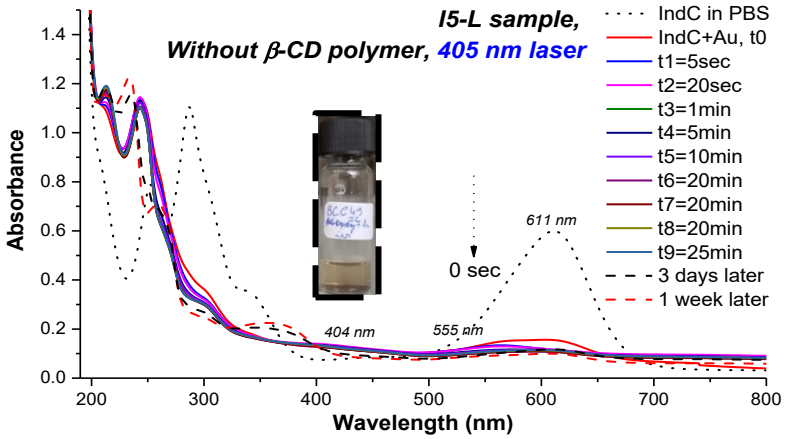

Figure 58: Comparison of absorbance evolution of IndC+Au (I5-L), irradiated with 405 nm laser (*ca.* 6 W.cm^{-2}) for one hour and forty minutes. The inset shows a picture of IndC+Au (I5-L) three days after the addition of the gold precursor. Measurements were performed in a 1 mm path-length absorbance cuvette with air as the blank using a PerkinElmer UV-Vis spectrophotometer. Conditions: [PBS] = 10 mM; [IndC] = 0.39 mM; [$HAuCl_4 \bullet 3H_2O$] = 0.39 mM.

5.2.3. Size and shape studies

After another synthesis under an inert atmosphere (I6-L sample, Appendix XVI), which showed the same absorbance evolution as observed previously for the I2-L sample, we occasionally had the opportunity to capture AFM images in collaboration with Prof. Giovanni di Destri from the University of Catania (Figure 59). Figure 59A shows particle sizes ranging from 10 nm to 100 nm, while Figure 59B can be used to identify the composition differences (metallic or polymeric) of the structure; however, the population is still insufficient to generalize this value to the sample. Particles around 100 nm in diameter exhibit a core-shell structure (with a core around 20 – 30 nm). The core of the object (light contrast on the color scale) can be attributed to AuNPs, while the shell structure (stronger contrast on the color scale) can be the polymer matrix rolled around the core. The dimensions of the AuNPs, around 20 – 30 nm, are compatible with the band observed at *ca.* 530 nm in the absorption spectra. Moreover, the "hundred nm" size is coherent with DLS measurements described below (Figure 60).

Regarding shape, it is difficult to accurately assess the nanoparticles' shapes from these AFM images because the polymer wraps around the AuNPs. The 'rods' observed are not gold nanoparticles but, in fact, artefacts.

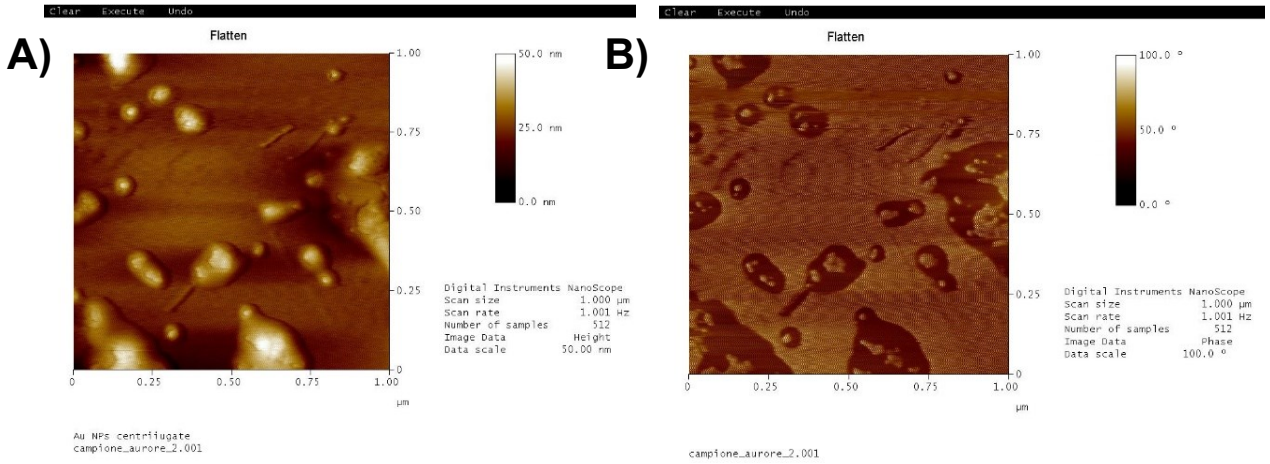

Figure 59: AFM images of IndC+βCDpolymer+Au (I6-L); A) image in height, the color scale indicates the particles size; B) phase image, the color scale indicates the different nature of the observed structure.

By DLS, the synthesized object size of I6-L is near 100 nm, and, as measured above with AFM, these sizes correspond to the gold nanoparticles wrapped in the βCD polymer. Furthermore, the size does not change after purification with centrifugation: both the pellet and the supernatant have a mean size of 100 nm.

Based on the results obtained above with AFM, we deduced that the nanostructure is composed of AuNPs of about 20 – 30 nm, and when wrapped in the polymeric matrix, the object is about 100 nm. Consequently, if the mean size of the structures in the pellet is about 100 nm, this indicates that the polymer is still close to the particles and so still in the sample, even after centrifugation of the particles (Figure 60).

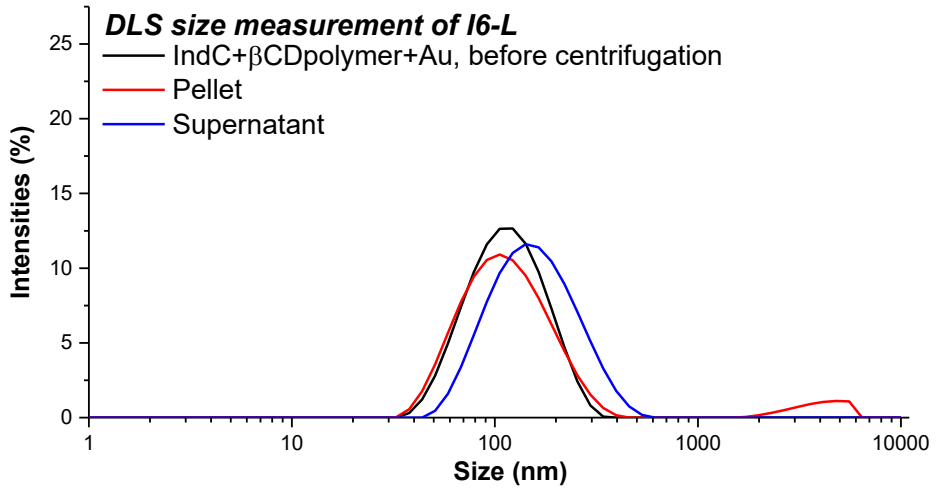

Figure 60: Scattering light intensity (%) distribution over hydrodynamic diameter (nm) of the irradiated IndC+βCDpolymer+Au (I6-L) sample under [N_2] (in black), of its pellet after purification (in red), and its supernatant (in blue). The measurement was performed using a Dynamic Light Scattering HORIBA LB-550, at room temperature (T = 25 °C).

We pursued the shape studies using TEM images. However, this time we performed nanoparticle synthesis before TEM analysis to observe the sample, ensuring it was analyzed just before any degradation or loss of anisotropy.

We prepared a new batch of gold nanoparticles (I7-L and I7-D samples, Appendices XVII and XVIII), and the sample for microscopy was prepared immediately upon completion of the synthesis. As soon as the gold nanoparticles are deposited on the TEM membrane, no degradation or any physical or chemical change is possible.

Both irradiated and dark control samples exhibited anisotropic structures, including gold nanorods, gold nanoprisms, and gold nanotriangles. For the irradiated sample (Figures 61A – 61D), particle concentration is less important than in the dark control sample (Figures 61E – 61H). Most of the nanorods and nanotriangles are concentrated in small heaps; however, isolated anisotropic structures can be spotted elsewhere on the membrane. In these samples, we observed no spherical particles.

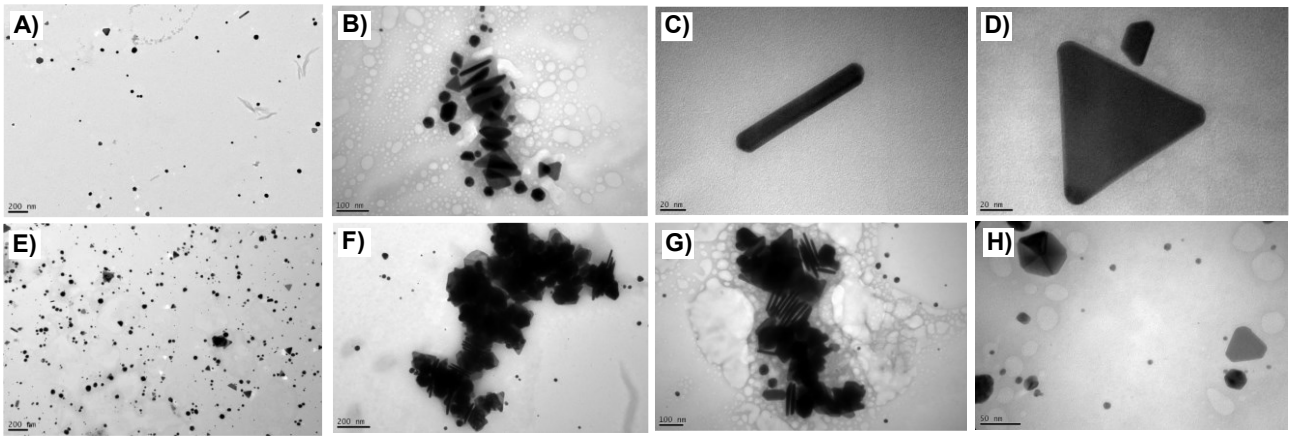

Figure 61: TEM images of the irradiated sample I7-L (A to D) and dark control I7-D (E to H).

5.2.4. Photothermal properties

For the photothermal properties of the IndC+βCDpolymer+Au system, we investigated the heating properties in the visible and infrared regions using 532 nm (*ca.* 12 W.cm^{-2}) and 671 nm (*ca.* 15 W.cm^{-2}) lasers of the I6-L sample, according to the LSPR bands. When irradiated at 532 nm, AuNPs increased the solution's temperature to ΔT = 23 °C. Once we concentrated the sample by centrifugation, the resulting pellet showed a rise up to ΔT = 28 °C. In comparison, the supernatant showed a temperature increase of only 11 °C. We also investigated the heat generation of two control samples, a βCD polymer solution and a water sample, and as expected, did not demonstrate any temperature rise (Figure 62A). The observed rise in the supernatant sample's temperature is likely due to insufficient centrifugation cycles, leading to the presence of AuNPs, which are responsible for the weak temperature rise. Then, for the photothermal study at 671 nm, the full sample showed a temperature rise of ΔT = 12 °C; the corresponding pellet and supernatant (prepared by centrifugation) showed weaker temperature rises of ΔT = 8 °C and 4 °C, respectively (Figure 62B). As with gold nanoparticles from curcumin's system, the repeatability of the rise in temperature across multiple irradiation cycles is an excellent indicator of the photothermal agent's stability. We report the thermal camera images in Appendix XIX.

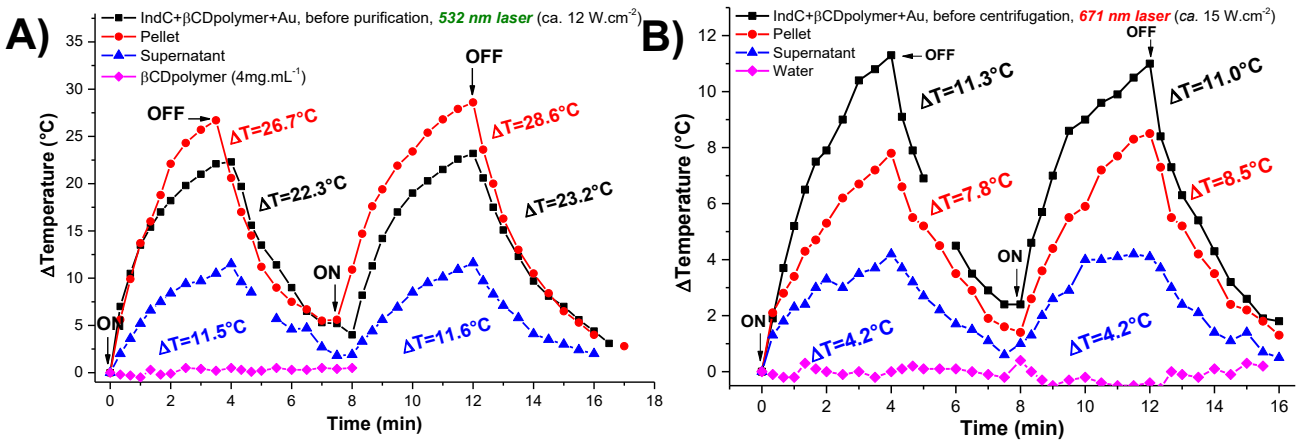

Figure 62: A) Evolution of temperature over time by laser irradiation at 532 nm (*ca.* 12 W.cm^{-2}) over two cycles of measurements of the irradiated IndC+βCDpolymer+Au (I6-L) in a PBS solution (in black square). Comparison with the evolutions of temperature with the corresponding pellet (in red circle), and with control samples: the supernatant (in blue triangle), a βCD polymer solution (in pink diamond); B) Evolution of temperature over time by laser irradiation at 671 nm (*ca.* 15 W.cm^{-2}) over two cycles of measurements of the irradiated IndC+βCDpolymer+Au (I6-L) in a PBS solution (in black square). Comparison with the evolutions of temperature with the corresponding pellet (in red circle), and with control samples: the supernatant (in blue triangle), and a water solution (in pink diamond).

5.3. Biological studies

5.3.1. Antibacterial assays

As in the previous chapter with curcumin (i.e., part 4.3.1.), similar antibacterial assays were conducted with the AuNPs synthesized from IndC. We studied the photothermal effect of the gold nanoparticles by combining three pellets from three different centrifuged batches to improve the photothermal response of the AuNPs (I8a, I8b, and I8c samples; Appendix XX), resulting in the I8p sample. As previously described in the experiment above for biological assays using curcumin's system, we did not elevate the temperature from room temperature, as performed in the preliminary experiment described in paragraph 5.2.4.; instead, we started at *ca.* 37 °C to reproduce physiological temperature. Furthermore, optimizations were necessary to adapt the irradiation setup to *in vitro* experimental conditions; the samples containing 20 % of concentrated particles in the biological media, and the wells were irradiated for three minutes with a 532 nm laser (*ca.* 15 W.cm^{-2}) using the beam expander.

After a 3-minute irradiation, the temperature increase of the gold nanoparticles was about ΔT = 5 – 10 °C, reaching a maximum of 47.6 °C (Figure 63C & 63D). By comparison with the previous results reported above for classical photothermal studies, the lower temperature

elevation may be due to the relatively shorter irradiation time and the diverse experimental setup used in the photothermal studies performed in NMR tubes reported above (i.e., part 5.2.4, with the I6-L sample).

In both assays with *E. coli* and *P. aeruginosa* strains, both attempts from the same I7p sample (I8p-a and I8p-b attempts) with indigo carmine AuNPs formulations present a decrease in bacterial bioluminescence after the 3-minute irradiation. However, we observed a significant difference between the two bacterial strains: the bioluminescence of the I8-a formulation decreased in both *E. coli* and *P. aeruginosa,* falling by a factor of 10 or more compared to the control, demonstrating the satisfactory cytotoxicity of the formulations under irradiation. For the second batch, I8p-b, compared to the control, the survival rate was only about 5 times lower (Figure 63A and 63B). This difference in survival rate between the two formulations, I8p-a and I8p-b, demonstrates that heterogeneity (nanoparticle size and shape) across synthesis batches has an important impact on the heat generation and must be considered to improve the system. Nevertheless, the decrease in bioluminescence between the two bacterial strains remains relatively the same in both cases.

Moreover, similar to the assays involving formulations of AuNPs with curcumin, a bacteriostatic effect is observed. Days after irradiation, both bacterial strains continue to grow at a slower rate than the control strains in non-irradiated wells (Appendix IX).

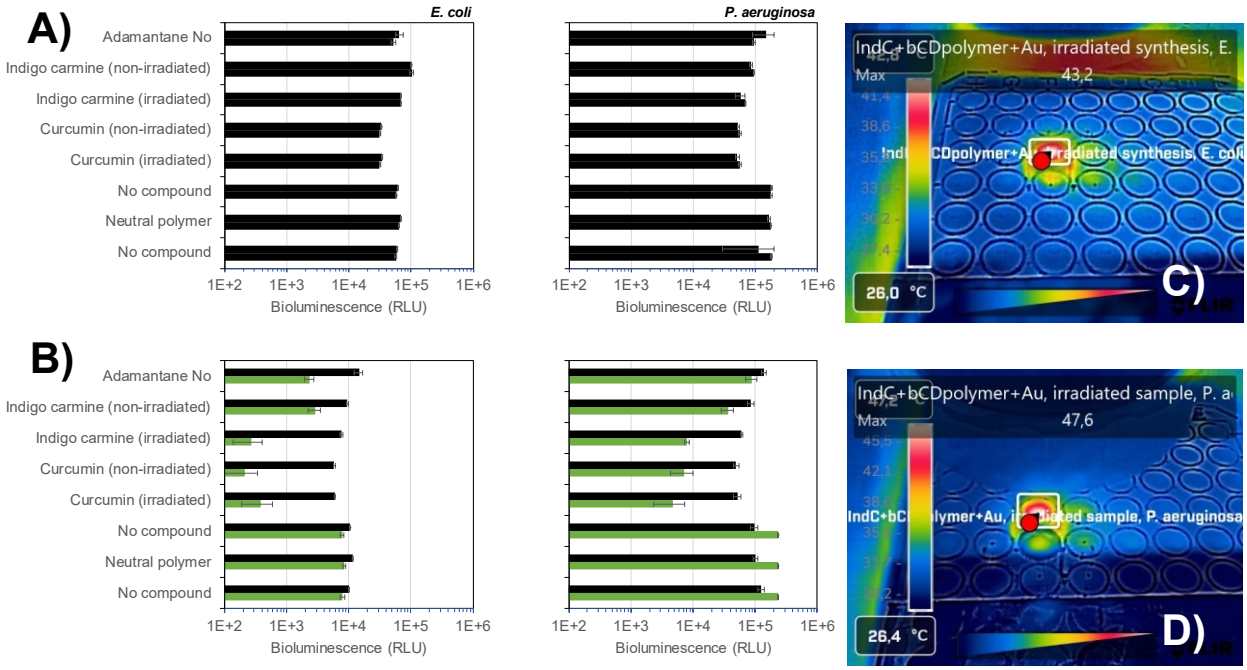

Figure 63: Bioluminescence evolution of different formulations of IndC+βCDpolymer+Au (I8) A) before and B) after irradiation with 532 nm laser (*ca.* 15 W.cm^{-2}) for the two bacterial strains *E. coli* and *P. aeruginosa*. C) Thermal pictures taken at the end of the irradiation of the formulation with *E. coli* and D) *P. aeruginosa.*

5.3.2. Antitumoral assays on ovarian cancer cells

For the biological assays on cancerous cells, three batches of gold nanoparticles, along with their dark controls, were centrifuged, and their pellets combined to increase particle concentration (I9a, I9b, and I10 samples, Appendix XXI).

Once again, we observed only the photothermal effect of the AuNPs irradiated with a 532 nm laser. We irradiated the wells for three minutes with the light source at *ca.* 15 W.cm^{-2}. We added a beam expander to increase the irradiation radius to irradiate the surface of each well. As with QAβCDPS in part 4.5.3., the neutral polymer did not report toxicity (F1+I). For the formulation of particles synthesized with curcumin (i.e., F3 and F4), we observed no cytotoxicity in OVCAR3 cells; in contrast, in cisplatin-resistant cells, both gold nanoparticle samples (i.e., from I9p-a and I9p-b) showed a decrease in cell viability of about 50 % (F5+I and F6+I) (Figure 64). After 3 minutes of irradiation, we checked the temperature of each irradiated well using the thermal camera, and each formulation showed a temperature increase of about 17 – 18°C (Figure 65).

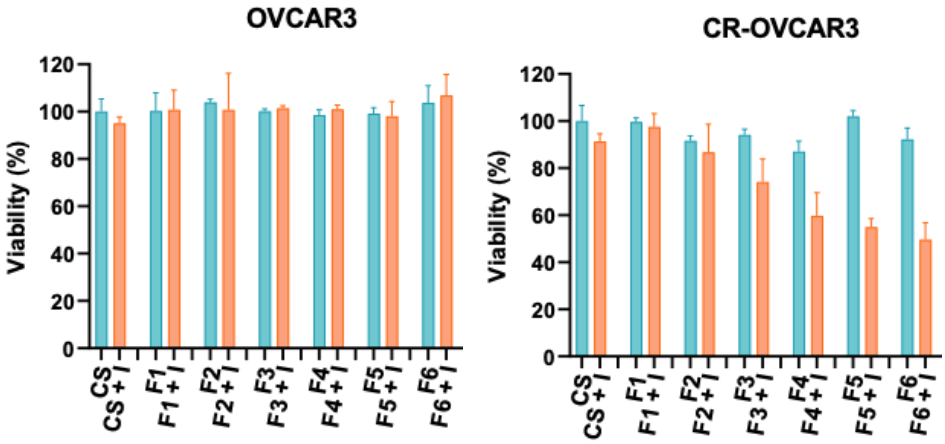

Figure 64: Viability assays on OVCAR3 and CR-OVCAR3. Data in orange: irradiated wells; data in blue: dark control. CS: cells alone; F5: Dark control of the formulation with IndC+βCDpolymer+Au (I9p-a); F5+I: Irradiated formulation with IndC+βCDpolymer+Au with 532 nm laser with a beam-expander (I9p-a) (*ca.* 15 W.cm^{-2}); F6: Dark control of the formulation with IndC+βCDpolymer+Au (I9p-b); F6+I: Irradiated formulation with IndC+βCDpolymer+Au with 532 nm laser with a beam-expander (I9p-b) (*ca.* 15 W.cm^{-2}). Samples F1 to F4 refer to the experiment with curcumin as comparison (see dedicated section, part 4.3.2.)

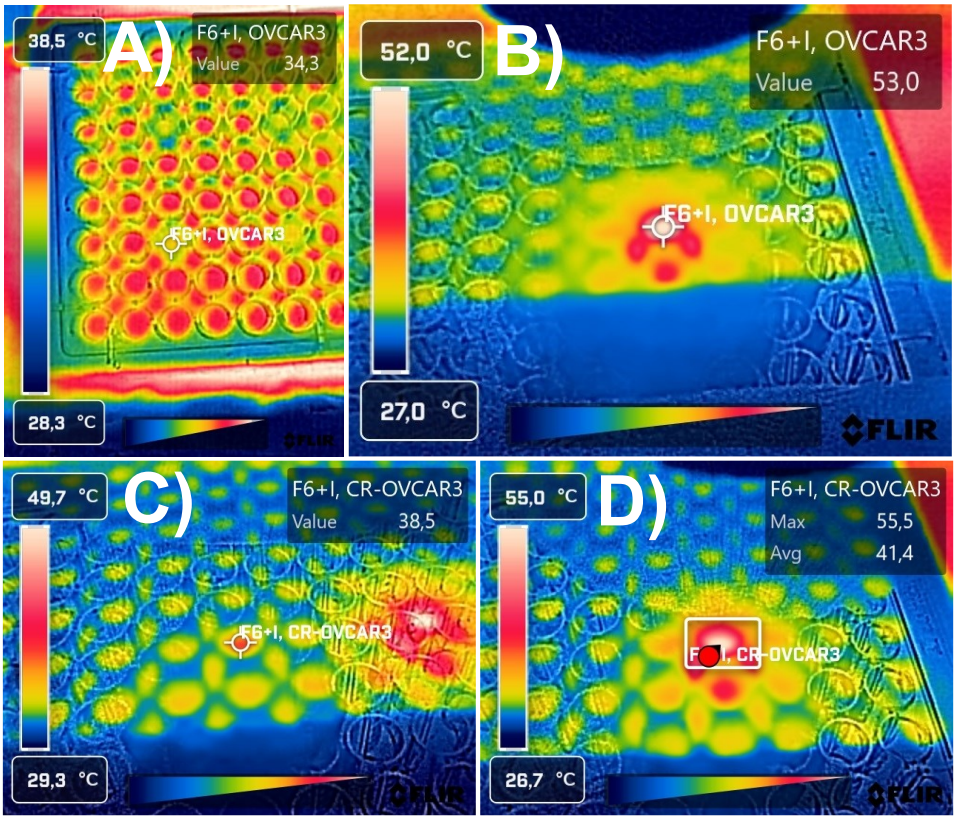

Figure 65: Thermal pictures taken at the beginning and at the end of the irradiation of the F6+I formulation with A) & B) OVCAR3 cells and C) & D) CR-OVCAR3 cells.

* * *

Following the formation of anisotropic AuNPs with different shapes, and the auspicious results of original photothermal agent against different bacterial strains and ovarian cancer cells, we then pursued the investigations with the addition of a PS for photodynamic therapy applications.

5.4. Singlet oxygen investigation

For $^1O_2$ investigations, we directly synthesized gold nanoparticles in a PBS buffer in D_2O to enhance the singlet oxygen lifetime and enable better detection of this transient species via its characteristic phosphorescence (I11 sample, Appendix XXII). The study was initiated by loading the ZnPc or THPP photosensitizers described in the previous chapter (i.e., part 4.4.2). However, as with analogous samples involving curcumin, only THPP demonstrated a satisfying loading within the polymer matrix (Figure 66A); indeed, when the latter is irradiated at 405 nm, a satisfying generation of singlet oxygen over two measures is observed, with a maximum of phosphorescence intensity in the range of emission consistent with the production of $^1O_2$

(Figure 66B). By comparison with the results obtained in the previous chapter, these better results may be due to a more efficient loading of the PS by the neutral polymer or to an exclusive use of deuterated water in the solution, which improves the singlet oxygen lifetime.

The weak loading of the monomeric form of zinc phthalocyanine was not enough to observe the phosphorescence of $^1O_2$ (Appendix XXIII).

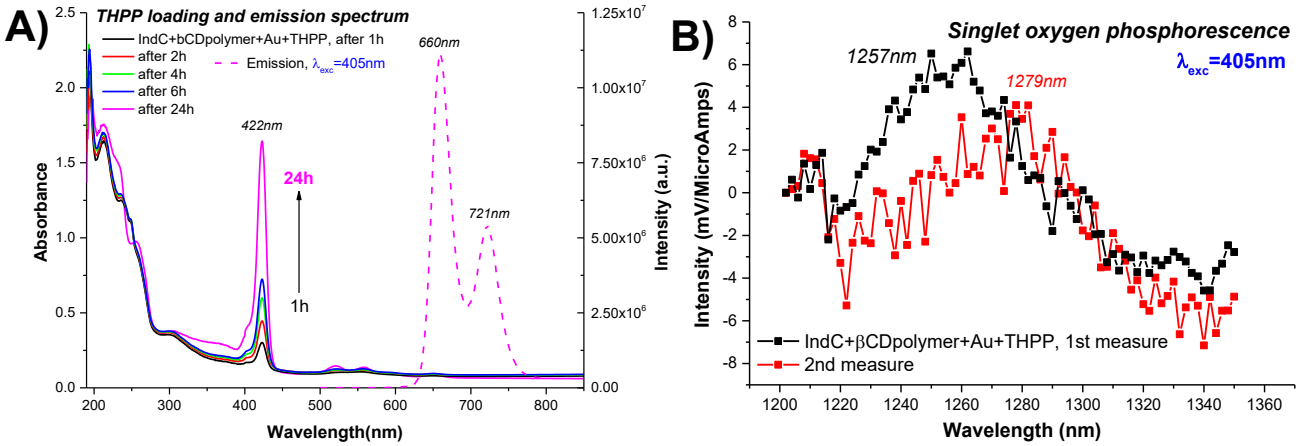

Figure 66: A) Absorbance and emission spectra of IndC+βCDpolymer+Au+THPP. The emission spectrum was performed using at 405 nm laser (*ca.* 12 W.cm^{-2}). Measurements were performed using a PerkinElmer UV-Vis spectrophotometer and fluorolog-2 spectrofluorometer; B) Evolution of intensity (mV) of phosphorescence of singlet oxygen measured in function of the wavelength (nm) of IndC+βCDpolymer+Au+THPP excited using a 405 nm laser (*ca.* 12 W.cm^{-2}). Measurements were performed using a fluorolog-2 spectrofluorometer. Conditions: [IndC] = 0.54 mM; [βCDpolymer] = 2.00 mg.mL^{-1} ; [$HAuCl_4 \bullet 3H_2O$] = 0.54 mM.

5.5. Conclusion

The methodology for forming anisotropic gold nanoparticles using indigo carmine as a green reducing agent resulted in a more straightforward process than for the system with curcumin discussed in the previous chapter (i.e., part 4). The direct formation of anisotropic gold nanoparticles was achieved with a neutral βCD polymer and with an equimolar ratio of indigo carmine and tetrachloroauric acid. Based on the literature, the behavior of indigo carmine under light irradiation was promising, with the goal of taking advantage of the excited leuco-indigo carmine for the selective reduction of the gold precursor to synthesize controlled anisotropic gold nanoparticles. However, after multiple attempts, the addition of $HAuCl_4 \bullet 3H_2O$ only led to the spontaneous oxidation of the blue dye, its degradation in solution, and the formation of AuNPs. Furthermore, we demonstrated the influence of an inert atmosphere on the formation of distinct particle populations, providing a panel of NPs spanning a broad wavelength range in the near-infrared, suitable for irradiating AuNPs at different wavelengths. The reproducibility

problems of the syntheses (i.e., inconsistent shape, presence or evolution of the LSPR band in the NIR, and inconsistent nanoparticles size, polydispersity index, and shape) must be corrected; we plan to optimize the procedure with adjustments on the concentration of indigo carmine and on the stirring velocity during the nucleation phase. Along with the lack of reproducibility, the main challenge of these AuNPs syntheses was the loss of the anisotropy of the objects over time, resulting in a difficult intrinsic characterization and study of the photothermal properties of these non-isotropic gold nanostructures.

Nonetheless, AFM studies demonstrated that the βCD matrix was wrapped around the gold nanoparticle. The total size of the system (i.e., the βCD polymer wrapped around gold nanoparticles) is about 100 nm, while the AuNPs are about 20 – 30 nm. Moreover, UV-Vis spectra and TEM images showed the formation of distinct populations of anisotropic structures, including gold nanorods and gold nanotriangles. Furthermore, the photothermal properties of the AuNPs synthesized were very satisfying, with a repeatable and stable rise of the temperature of about $\Delta T = 27 – 28$ °C when irradiated in the green region, and up to $\Delta T = 11 – 12$ °C when irradiated in the near infrared region. The further improvement of AuNPs' stability will enable more precise characterization and identification of different shape populations of these anisotropic structures.

The *in vitro* assays demonstrated a satisfactory photo-induced decrease in the bioluminescence of both *E. coli* and *P. aeruginosa* strains for the formulation I8p-a, up to a factor of 10. Furthermore, we achieved a 50% reduction in viability against cisplatin-resistant ovarian cancer cells, driven by the PTT effect generated by the particles.

Finally, we began investigating the production of singlet oxygen for a multimodal PTT/PDT therapy objective. The excellent loading of THPP enabled the repeatable and notable observation of $^1O_2$ phosphorescence near 1260 nm. As with the system with curcumin, we must investigate the impact of singlet oxygen on the photothermal properties of the gold nanoparticles and the impact of heat generation on the PS stability during and after photothermal investigations. The addition of red-absorbing photosensitizers via covalent or supramolecular link must also be investigated for deep multimodal PTT/PDT biological applications.

5.6. Experimental part

Methods:

Spectroscopic-purity solvent (i.e., methanol) was used. The solutions were prepared in ultrapure (Milli-Q) water or in PBS buffer. D_2O (≥99.8%) was purchased from Carlo Erba. The PBS buffer was prepared by adding one phosphate-buffered saline tablet to 100 mL of extra pure water (10 mM). After solubilization of the tablet, the pH is measured with a pH meter (inoLab): (T = 27 °C) pH = 7.45. Fluorescence cuvettes (1 cm path-length, 3 mL capacity) and absorbance cuvettes (1 mm path-length and 1 cm path-length, 3 mL capacity) were cleaned with *aqua regia* before each experiment.

The Phosphate Buffered Saline tablet was purchased from VWR Life Science. The βCD polymer, the quaternary ammonium βCD polymer (QAβCDPS), and the soluble sulfobutylated βCD polymer (SBβCDPS) were prepared by Cyclolab and used without any purification. Tetrachloroauric (III) acid trihydrate ($HAuCl_4 \bullet 3H_2O$) (≥99.9% trace metals basis) ($C = 5.08 \times 10^{-1}$ M), indigo carmine and 5,10,15,20-Tetrakis(4-hydroxyphenyl)-21*H*,23*H*-porphine were purchased from Sigma Aldrich and used without purification. Zinc phthalocyanine was purchased from Frontier Scientific.

Instrumentation:

Irradiations of the samples were carried out in a 1 cm path-length fluorescence quartz cuvette (3 mL capacity) using either 405, 532, or 671 nm continuum-wave lasers (*ca.* 6, 12, or 15 $W.cm^{-2}$) with a beam diameter of *ca.* 1.5 mm, or by a 420 nm lamp (*ca.* 1 $mW.cm^{-2}$). Absorbance spectra were measured using 1 mm length quartz cuvettes or a 1 cm path-length absorbance quartz cuvette (3 mL capacity), either using a PerkinElmer Lambda 365 UV-Vis spectrophotometer (Measurement window: from 180 to 1100 nm; SBW: 1.0; Data interval: 0.5 nm; Scan rate: 300 $nm.min^{-1}$), Jasco V-560 UV-Vis spectrophotometer (Measurement window: from 180 to 800 nm), or using a Jasco V-760 UV-Vis spectrophotometer (Measurement window: from 190 to 900 nm).

The centrifugation was performed using an Eppendorf Centrifuge 5430 with FA-45-30-11 rotor at room temperature (T = 25 °C).

The fluorescence was recorded with a Spex Fluorolog-2 (mod. F-111) spectrofluorometer using quartz cuvettes with a 1 cm path-length.

$^1O_2$ emission was measured with the same above-mentioned spectrofluorometer equipped with a NIR-sensitive liquid-nitrogen-cooled photomultiplier. Hydrodynamic sizes of nanoparticles

were measured at room temperature (T = 25 °C) with a Dynamic Light Scattering HORIBA LB-550 apparatus equipped with a diode laser with a wavelength of 650 nm. Samples were shaken by hand before each measurement. After formation of the AuNPs, the samples were diluted 20-fold from 100 μL of the AuNPs preparation and 1.9 mL of Milli-Q water. For each sample, three measures were performed. The measurements were performed in a fluorescence quartz cuvette (1 cm path-length, 3 mL capacity), and were performed at room temperature (T = 25 °C).

The pH values were measured with an inoLab pH meter at room temperature (T = 25 °C). The instrument was calibrated before each measurement using two buffer solutions at pH = 7.00 and pH = 4.01.

βCD-polymer solution preparation: The mass of βCD polymers used was measured with a Sartorius analytical balance, and then solubilized in Milli-Q water. The solution was magnetically stirred for 20 minutes using an IKA Topolino at medium velocity at room temperature (T = 25 °C).

Preparation of an aqueous solution of indigo carmine: Indigo carmine is added to PBS buffer inside a transparent flask of 4 mL, and stirred for 30 minutes with IKA Topolino, and then homogenized with an ultrasound bath. The absorbance was monitored with a PerkinElmer Lambda 365 UV-Vis spectrophotometer. After diluting the mother solution with PBS buffer, the IndC concentration of the daughter solution was determined from the baseline-corrected absorbance ($A = l \times \varepsilon \times C$) using the Beer-Lambert law. The measurement was performed in water solvent at λ_{max} = 608 nm with $\varepsilon_{monomer}$ = 15000 $M^{-1}.cm^{-1}$ for water.[239]

Preparation of the solution of IndC+βCDpolymer: The βCD polymer was added to the diluted solution of IndC. The sample was stirred for 30 minutes using an IKA Topolino at medium velocity until all the polymer was solubilized.

Preparation and irradiation of the system IndC+βCDpolymer+Au with O_2: $HAuCl_4 \bullet 3H_2O$ (C = 0.5 M) is added in the IndC+βCDpolymer solution. A first absorbance measurement was performed immediately after the addition of the gold precursor. Then, the IndC+βCDpolymer+Au solution was separated into two equal volumes: the first was irradiated, and the second was kept in the dark as a control, both stirred magnetically using an IKA Topolino at low speed. A UV-Vis spectrophotometer was used to monitor the absorbance changes in both irradiated and dark control samples. For the irradiated sample, the irradiation

was performed in a 1 cm path-length fluorescence cuvette with a continuum-wave 405 nm laser (*ca.* 6 $W.cm^{-2}$).

Preparation and irradiation of the system IndC+βCDpolymer+Au with [N_2]: The solution of IndC+βCDpolymer is degassed for 20 minutes by a nitrogen flux. Then, $HAuCl_4 \bullet 3H_2O$ (C = 0.5 M) is added to the IndC+βCDpolymer solution. The first absorbance measurement was taken immediately after the addition of the gold precursor. For the irradiated sample, irradiation was performed in a 1 cm fluorescence cuvette using a continuum-wave 405 nm laser (*ca.* 6 $W.cm^{-2}$), with stirring using an IKA Topolino. For the dark control sample, the sample is stirred in the dark using an IKA Topolino.

Preparation of a film of PS: About 5 mg of PS is solubilized in methanol in a 4 mL amber flask covered with an aluminum foil. The PS was added to the solution until the absorbance was close to A = 1 at λ = 680 nm for ZnPc, and to A = 2 at λ = 400 nm for THPP, using a PerkinElmer UV-Vis spectrophotometer in a 1 mm path-length cuvette with air as the blank. Then, methanol was evaporated under a nitrogen flux to form a PS film.

Preparation of a solution of IndC+βCDpolymer+Au+PS: IndC+βCDpolymer+Au was added to the PS film in a 4 mL amber flask covered with aluminum foil, and the mixture was stirred in the dark. The sample was stirred until no absorbance evolution was observed.

Purification of IndC+βCDpolymer+Au: 2 mL of the IndC+βCDpolymer+Au sample was centrifuged at 14 000 rpm for 10 minutes. The supernatant was discarded. The precipitate is resolubilized in 2 mL of PBS buffer. The absorbance spectra of both the precipitate and the supernatant are measured.

Measurement of singlet oxygen production: Absorbance spectra were recorded before and after each measurement using a fluorolog spectrofluorometer. The photosensitizer was excited using a continuous-wave laser at 405 or 671 nm (*ca.* 15 $W.cm^{-2}$) with a beam diameter of *ca.* 1.5 mm.

Flash spectroscopy measurements: Samples were degassed for 20 minutes before the flash photolysis experiments. All of the samples were excited with the third harmonic of the Nd–YAG Continuum Surelite II–10 laser (355 nm, 6 ns FWHM), using quartz cells with a path-length of 1.0 cm. The excited solutions were analyzed with a Luzchem Research mLFP–111 apparatus with an orthogonal pump/probe configuration. The probe source was a ceramic xenon lamp coupled to quartz fiber-optic cables. The laser pulse and the mLFP–111 system were synchronized by a Tektronix TDS 3032 digitizer, operating in pre-trigger mode.

Photothermal studies: Irradiations during photothermal studies were performed with four different continuum-waves lasers: at λ_{exc} = 532 or 671 nm (*ca.* 6, 12, or 15 W.cm^{-2}), with a beam diameter of *ca.* 1.5 mm. Samples (150 or 200 µL) were irradiated in an NMR tube. The thermal evolution was captured with a FLIR C3 thermal imaging camera, with temperatures reported every twenty seconds. Three cycles of measures were performed consecutively for each sample. Thermal pictures of the sample were taken at the beginning and end of each irradiation cycle. The measurements were performed at room temperature (T = 18 or 25 °C), depending on the time of the year. Thermal images of the measurements were processed with FLIR software and presented with a linear temperature color scale.

TEM samples and images were prepared and captured by Philippe Elies from the University of West Brittany.

Biological assays on bacteria were performed in collaboration with Dr Tony Le Gall, and assays on cancer cells were performed in collaboration with Prof. Tristan Montier and Dr Manh Nguyen Quoc from the GTCA Team, UMR INSERM 1078.

6. "Green" Synthesis of a gold nanosystem from a nitric oxide photodonor with a ratiometric fluorescent thermometer for in vivo applications

The synthesis of anisotropic AuNPs demonstrated interesting results (i.e., formation of gold nanotriangles, gold nanorods, or gold 'nanoworms') and satisfying heat generation (i.e., from curcumin's system, $\Delta T = 16 – 17$ °C; and from indigo carmine's system, $\Delta T = 11 – 12$ °C) during photothermal studies in the near-infrared region. Nonetheless, it is a challenge to monitor the temperature variation within the cellular environment; consequently, the development of a system capable of generating heat and exhibiting measurable thermosensitive properties would be a significant advantage for the development of PTT therapeutic strategies. We can functionalize the βCD polymer used in previous experiments with different dyes for ratiometric measurements, in particular rhodamine-B and fluorescein, both of which are temperature-sensitive fluorophores.

6.1. Ratiometric fluorescence thermometer for *in vivo* applications: definition

Traditional thermometers for PTT applications have several apparent drawbacks, including an unsuitable size that can cause cell damage and difficulty in use in a therapeutic setting. Correct temperature monitoring during photothermal therapy will help prevent overheating of the photothermal agent and thus avoid burn damage to surrounding healthy biological material. Many fluorescent thermometers have been developed over the last few years, including lanthanide complexes, [244] carbon and quantum dots, [245,246] fluorescent proteins, [247] molecular beacons, [248] nanodiamonds, [249] and small organic dyes. Temperature evolution can induce different mechanisms in the emission spectrum or emission properties of the fluorophore, such as intensity variation, band position (i.e., blue-shift or red-shift), bandwidth variation, or lifetime variation (Figure 67).[250] A known variation of the emission spectrum or emission properties of the fluorescent probe will allow a precise monitoring of the photothermal agent's activity using a non-invasive method. Most fluorescence thermometers are based on intensity variation; from a physical point of view, a temperature rise changes the number of photons emitted per second, thereby altering the intensity of the emission spectrum.

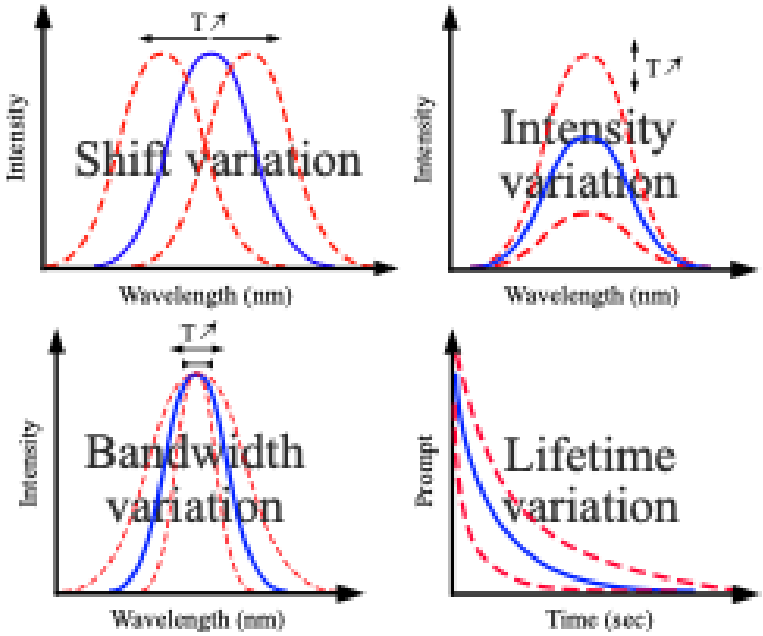

Figure 67: Representation of the different emission spectrum and emission properties evolution of the fluorescent probe in function of temperature evolution. In blue is represented the system properties in cold temperature, and in red at hot temperature.

Furthermore, the use of a ratiometric thermometer with two different fluorophores (a first one with a stable emission intensity and another with a temperature-dependent intensity) will allow us to monitor and compare the temperature evolution, independently of experimental conditions (concentration of the fluorophores, irradiation intensity, etc.).

For *in vivo* applications, both fluorophores must also absorb and emit light in the biological window, not only to allow the light to reach the thermometer but also to read their emitted fluorescence response through tissues.[251]

βCD polymer can be modified with a ratiometric fluorescent thermosensitive probe to track temperature changes, as the probe exhibits an inherent fluorescence intensity evolution during the heat generation of the AuNPs upon near-infrared irradiation.

Rhodamine B (RhB), a xanthene analogue, is an organic dye with a high fluorescence emission, a high quantum yield, a high extinction coefficient, and good stability.[252] We can use RhB as a single-wavelength thermometer with a decreasing fluorescence response. Its emission intensity is decreasing, and its fluorescence lifetime is increasing when a non-radiative process (heat) reaches the fluorophore.[253] The evolution of the fluorescence intensity of the rhodamine can be explained by the free rotation of its two diethylamino groups.[253] At low

temperatures, the rotation is slower or non-existent; however, as the temperature rises, the amine group begins to rotate freely, breaking the conjugation system and decreasing fluorescence intensity. Even though this fluorescent thermometer provides simple signal readings, a decrease in the emission response can be caused by several external factors (e.g., ambient autofluorescence, quenching), which may lead to imprecision during measurement.[253] Another drawback of these single-wavelength thermometers is that their fluorescence response depends on concentration, excitation intensity, and the spatial distribution of the target, which creates many obstacles to effective fluorescence measurement.[253]

In the literature, other fluorescent thermometers have been investigated, with relative sensitivities generally in the range of 1 to 5 % of intensity per °C.[244,253] The RhB thermometer has already been applied in the 20 – 48 °C temperature range with a sensitivity of 6.50 % per °C and remains an evergreen candidate for this application.[254]

The introduction of a second fluorescent thermometer into the system will allow overcoming the drawbacks of using a single fluorescent probe.

Fluorescein, another xanthene analogue first synthesized by von Bayer in 1871,[255,] is also a dye that exhibits a decrease in fluorescence emission as the temperature of the milieu increases, but it is less heat-sensitive than rhodamine B and can therefore be used as a reference in a ratiometric thermometer.[256] Like for rhodamine B, the fluorescence properties of the molecule are based on its spirolactam part. This dye is an excellent chromophore, with good solubility and photostability under irradiation. Furthermore, it is essential to note that when fluorescein is close to AuNPs, FRET can occur, leading to fluorescence quenching. Furthermore, because of the structure of fluorescein, its fluorescence properties are sensitive to the pH of the milieu.[257]

Due to these observations, an intensive photo-characterization of the new platforms developed in this work will be needed even if a rhodamine B/fluorescein ratiometric thermometer has already been used with cyclodextrin metal-organic framework.[256]

Suppose the presence of FRET between AuNPs and fluorescein conduces to a quenching of the fluorescence. In that case, an alternative is to replace fluorescein with the dansyl dye (DNSA) in combination with RhB. Compared with the two previous fluorophores, dansyl shows a fluorescence intensity that rises with increasing temperature.

The use of a DNSA as a single-wavelength fluorescent thermometer has already been done with carbon dots. Davi *et al.* reported a relative sensitivity between +0.45 and +0.55 % of intensity per °C in the 20 – 60 °C temperature range.[258]

The three dyes' structures used for the investigations of the ratiometric fluorescent thermometer are represented in Figure 68.

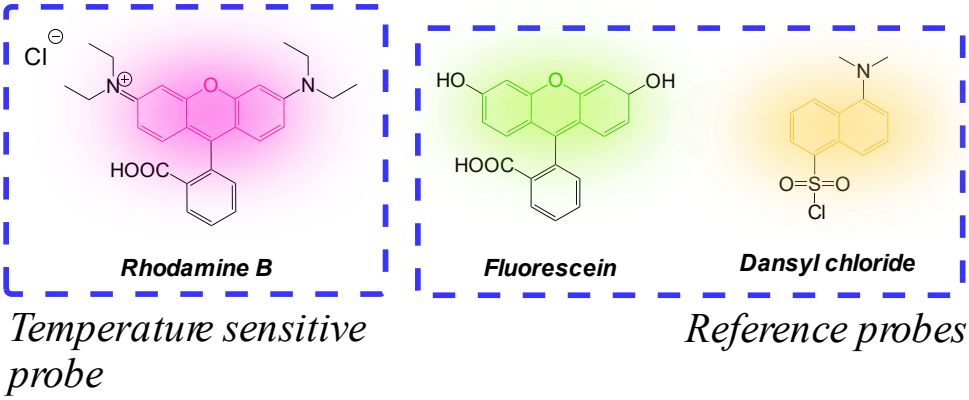

Figure 68: Representation of the temperature sensitive probe, rhodamine B, and the reference probes, fluorescein and/or dansyl, investigated in a ratiometric fluorescent thermometer.

* * *

The research described in this chapter aims to develop a bichromophoric ratiometric system that provides information on the evolution of the surrounding environment's temperature through fluorescence measurement. Furthermore, modified bi-labeled βCD polymers will be used not only for their fluorescent and thermosensitive properties, but also to overcome the problems of a single fluorophore thermometer, for their capacity to stabilize AuNPs, to act as a template agent during AuNPs synthesis, and host organic molecules (i.e., a photosensitizer, a reducing agent, or a drug) (Figure 69). To achieve this goal, it will first imply studying separately the polymers bearing each single chromophore, and then describing their properties when the chromophores are together. Two different approaches will then be explored: 1) a supramolecular approach using two distinct polymers, each one modified with a single chromophore; and 2) a covalent approach using a unique polymer modified with the selected chromophores. Both methods present advantages and drawbacks. Regarding the first one, we will use available polymers, and the supramolecular approach will allow us to tune the ratio of the photosensitive units easily. Nevertheless, in a complex biological environment, the stability of the particles formed of two separate polymers is uncertain. The second approach will offer

the conviction that both chromophores remain co-localized in known proportions but will require the synthesis of new polymers modified with two or three distinct chromophore units.

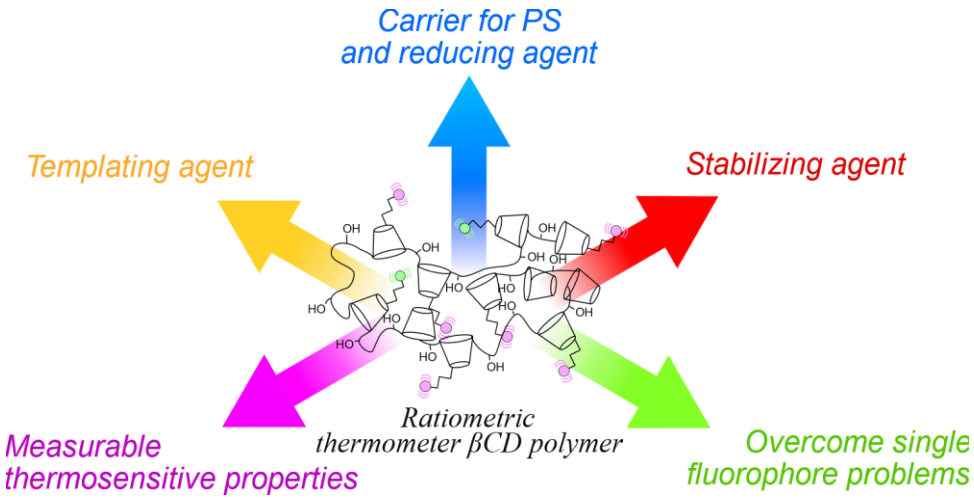

Figure 69: Schematic representation of the five different properties of the modified water-soluble βCD polymer.

6.2. Ratio investigations between rhodamine B and fluorescein

Before the synthesis of the original βCD polymer, the first objective was to define the optimal ratio of rhodamine B and fluorescein to incorporate into the βCD polymer to obtain a satisfying fluorescence response. An optimal ratio of fluorescent dyes must have both emission intensities easily visible and comparable (i.e., free of noise, sensitive to temperature changes, and with no emission spectrum overlap). We performed initial investigations into the relative sensitivity of RhB fluorescence emission as a function of temperature and the influence of gold nanoparticles on the evolution of RhB fluorescence intensity.

6.2.1. Evolution of the fluorescence of RhB in function of the temperature

For a proper understanding and comparison of the effect of gold nanoparticles on the fluorescence evolution of the rhodamine probe, we first investigated the fluorescence evolution of the rhodamine B probe linked to the βCD polymer (RhB-βCD polymer) (Figure 70) and compared it to the free rhodamine dye. The emission spectra were measured first at room temperature, then we set the sample temperature to 20°C using a specific cuvette holder with an integrated temperature control, and we double-checked the temperature manually with a thermometer. We progressively raised the temperature to 70 °C, collecting the fluorescence spectrum every 5 °C, and, upon reaching the application range of the photothermal agent for

PTT biological applications (i.e., between 37 °C and 50 °C), the emission spectrum was collected every 1 °C. Because fluorescence intensity depends on its environment and concentration and is expressed in arbitrary units, another proper parameter, namely the relative sensitivity, is used to compare nanothermometers with different indicators. The relative sensitivity is utilized to observe the relative change of fluorescence intensity with the degree of temperature change.[256] We can calculate this parameter according to Equation 2:[259]

$$S_r = 100 \times \frac{1}{I} \times \frac{\partial I}{\partial T}$$

Equation 2: Relative sensitivity formula: S_r: relative sensitivity (%. K^{-1}); I: intensity of fluorescence; T: temperature (°K).

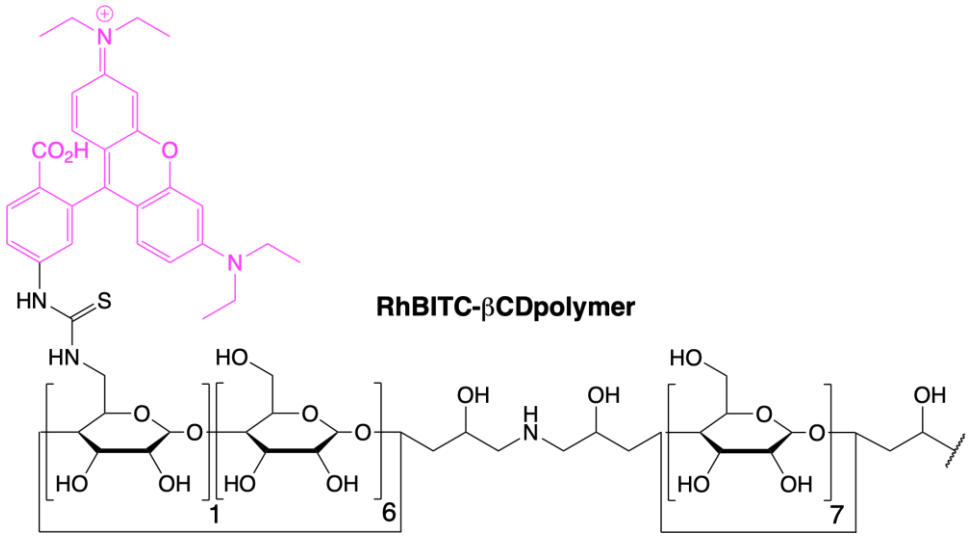

Figure 70: Structure of the βCD polymer modified with rhodamine B (pink), cross-linked with epichlorohydrin.

Two solutions of rhodamine B and rhodamine B-modified polymer optically matched at the excitation wavelength, showed the evolution of intensity during heating (Figure 71). The evolution of the absorbance is very similar for both samples.

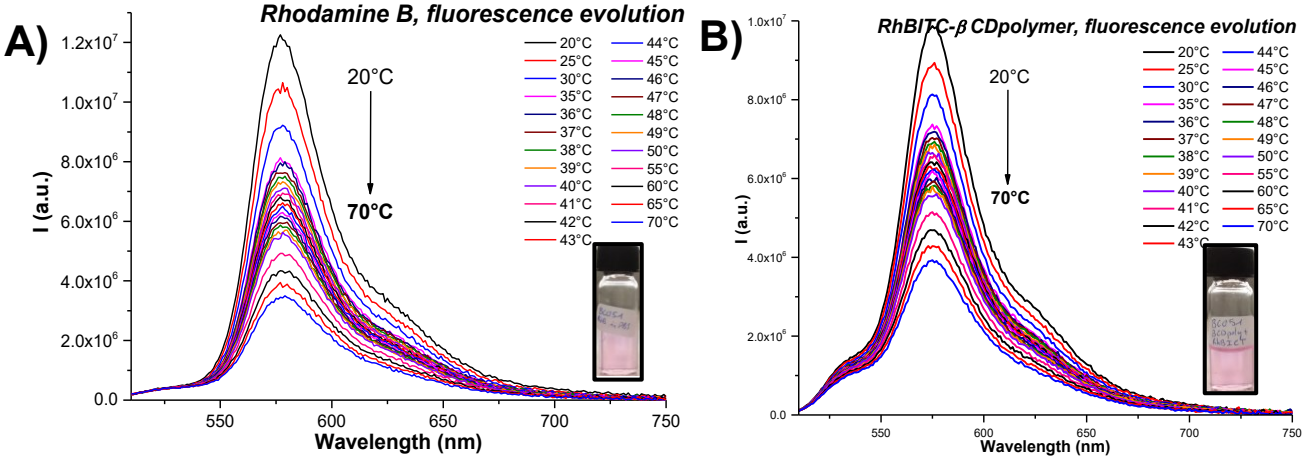

Figure 71: A) Comparison of the fluorescence intensity (arbitrary units) evolution over temperature (°C) of rhodamine B dye in a PBS solution. The inset shows a picture of the sample at the end of the heating at room temperature. B) Comparison of the fluorescence intensity (arbitrary units) evolution over temperature (°C) of RhBITC-βCD polymer in a PBS solution. The inset shows a picture of the sample at the end of the heating process at room temperature. Measurements were performed in a 1 cm path-length fluorescence cuvette using a fluorolog-2 spectrofluorometer. Both samples were excited at λ_{exc} = 500 nm; Slit = 1.5. Conditions: [PBS] = 10 mM; [RhB] = 1.00 mg.mL^{-1}; [RhBITC-βCDpolymer] = 1.00 mg.mL^{-1}.

Moreover, from these spectra, it is possible to calculate the relative sensitivity S_r, which is about -1.52 %. K^{-1} for rhodamine B alone, and about -1.30 %. K^{-1} when RhB isothiocyanate is linked to the polymer matrix. Since both relative sensitivities are close, we can assume that the polymer graft does not affect the emission properties of the rhodamine fluorophore upon heating, since the rigidity and planarity of the emissive xanthene core is not modified. Furthermore, the decrease in the intensity of their absorbance spectra is negligible over two cycles of heating to 70 °C (Figure 72), indicating good stability of the chromophore toward temperature changes.

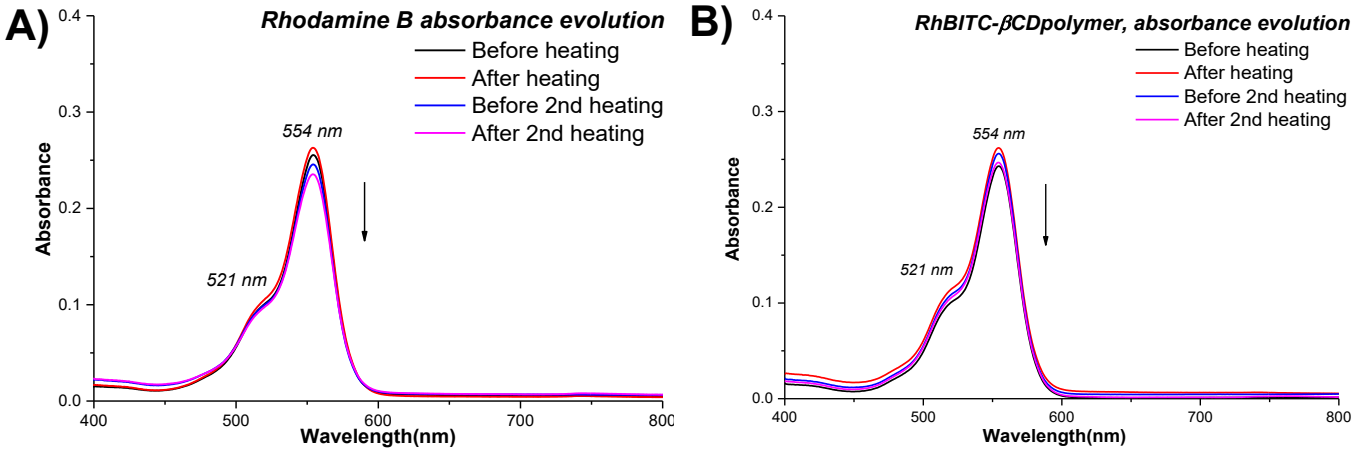

Figure 72: Comparison of the absorbance spectra evolution over multiple cycles of heating of A) rhodamine B and B) RhBITC-βCDpolymer in PBS solutions. Measurements were performed in a 1 cm path-length absorbance cuvette, using a PerkinElmer UV-Vis spectrophotometer, with PBS as the blank. Conditions: [PBS] = 10 mM; [RhB] = 1.00 mg.mL^{-1}; [RhBITC-βCDpolymer] = 1.00 mg.mL^{-1}.

6.2.2. Evolution of the fluorescence of fluorescein in function of the temperature

With reference to 6.2.1., we performed the same experiment using fluorescein isothiocyanate covalently linked to the βCD polymer (FITC-βCD polymer) to assess the emission stability at different temperatures (Figure 73). The relative fluorescence sensitivity is about -0.28 %. K^{-1}; a far less significant value than the S_r reported above for the rhodamine B βCD polymer equivalent (i.e., -1.30 %. K^{-1}, part 6.2.1.). Furthermore, as reported by Peng et al.,[256] we can observe in Figure 73A, a slight shift of the maximum emission intensity over the rise of temperature, from 20 °C, I_{max} is at λ_{max} = 517 nm; to 70 °C, at λ_{max} = 520 nm. Besides this minor shift in intensity, the same I_{max} value (i.e., I_{max} = 517 nm) was considered for the study across the temperature elevation.

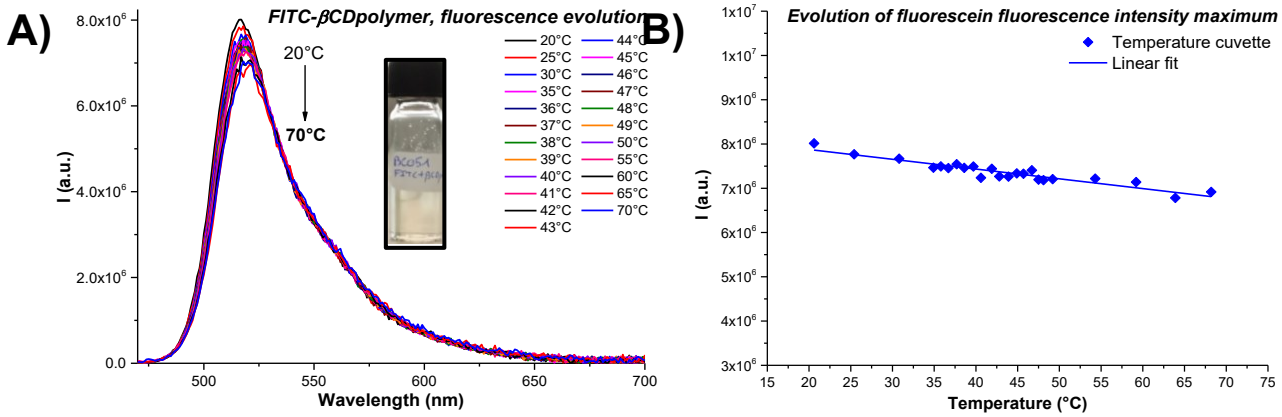

Figure 73: A) Comparison of the fluorescence intensity (arbitrary units) evolution over temperature (°C) of FITC-βCDpolymer in a PBS solution. The inset shows a picture of the sample at the end of the heating process at room temperature. Measurements were performed in a 1 cm path-length fluorescence cuvette using a fluorolog-2 spectrofluorometer. The sample was excited at λ_{exc} = 460 nm; Slit = 1.5. B) Evolution of the intensity maximum of fluorescence (arbitrary units) of FITC-βCDpolymer over the temperature set (°C) (blue diamond) at I_{max} = 517 nm. Conditions: [PBS] = 10 mM; [FITC-βCDpolymer] = 1.00 $mg.mL^{-1}$.

Figure 74 compares the fluorescence intensity of the dyes investigated so far as a function of temperature. As expected, the fluorescence intensity of fluorescein is far less sensitive to the temperature increase than rhodamine B, more specifically in the area of interest (i.e., between 36 and 50 °C). Consequently, the choice to use both fluorophores in a ratiometric thermometer and to use fluorescein as a reference is relevant to its very stable fluorescence intensity. Furthermore, to ensure the reproducibility of the variation observed with the rhodamine-modified polymer, we performed two successive heating cycles from 20 to 70 °C. Good reproducibility of the measurements is obtained, indicating that the fluorophore is not degraded by elevated temperature.

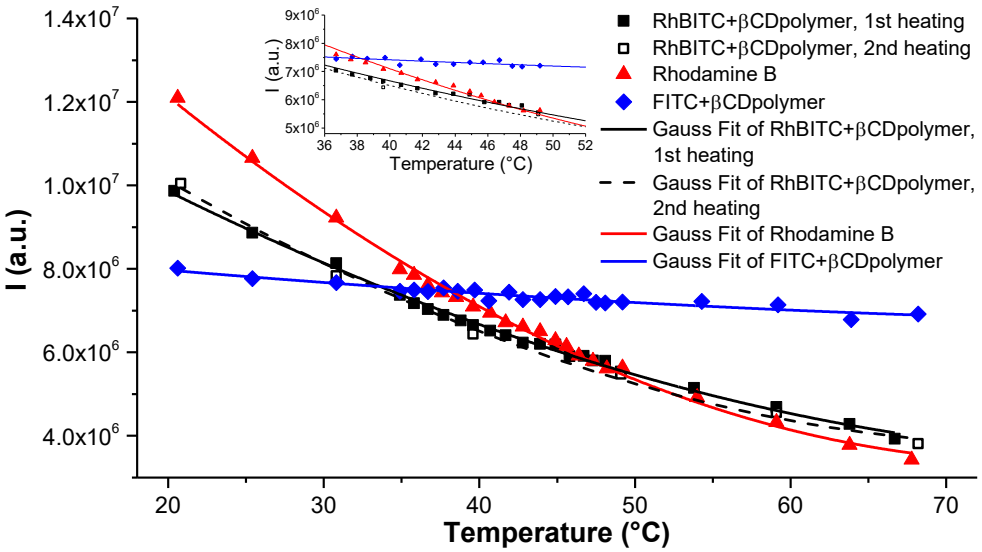

Figure 74: Comparison of the fluorescence maximum intensity (I_{max}) evolution over temperature (°C) measured in the fluorescence cuvette between RhBITC-βCDpolymer first (black squares) and second heating (white squares), rhodamine B (red triangles) and FITC-βCDpolymer (blue diamonds). The inset shows a zoom between 36 and 50 °C. Conditions: [PBS] = 10 mM; [RhB] = 1.00 mg.mL^{-1}; [RhBITC-βCDpolymer] = 1.00 mg.mL^{-1}; [FITC-βCDpolymer] = 1.00 mg.mL^{-1}.

6.2.3. Fluorophores ratio investigation

Since we demonstrated that the βCD polymers modified with the fluorophores of interest preserved the peculiarity of the single dye molecule, we pursued investigations on a mixture of both polymers to obtain a supramolecular system decorated with RhB as a temperature sensor and fluorescein as a reference emitter. As a critical factor, the investigation of the optimal RhB/Fluorescein ratio for the synthesis of the ratiometric βCD polymer is emphasized. Furthermore, if the concentration of the reference dye is high, both chromophore emission intensities must decrease at the same rate.[256]

We performed a first attempt with an equivalent ratio (1:1) of the two polymers. Figure 75 compares the absorption spectra of the individual solutions and their mixture, highlighting any possible interactions between rhodamine B and fluorescein. The last spectrum perfectly matches the sum of the singular polymers' spectra, demonstrating that no electronic interactions occur between the chromophores at the ground state.

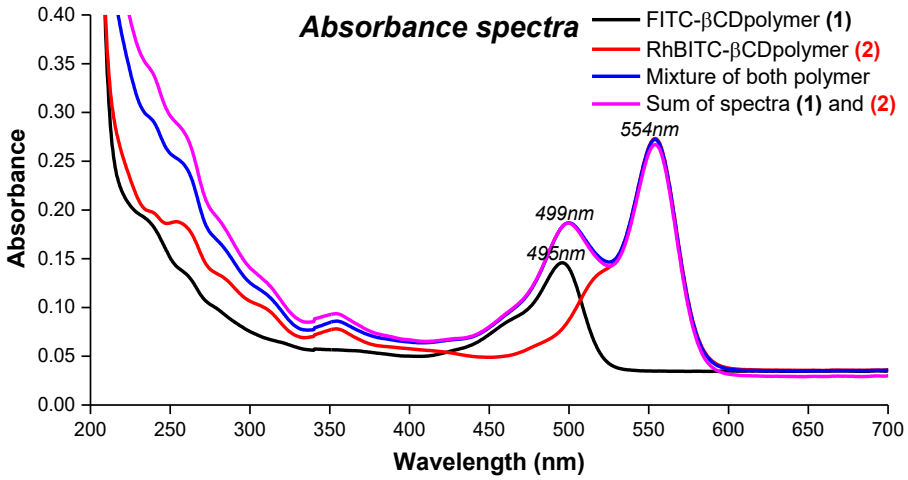

Figure 75: Comparison of the absorbance spectra of both fluorescein- (1) and RhB-isothiocyanate (2) polymers, of a FITC/RhBITC (1:3) polymers mixture, and of the mathematical sum of (1) and (2) absorbance spectra. Measurements were performed in a 1 mm path-length cuvette using a PerkinElmer UV-Vis spectrophotometer with air as the blank. Conditions: [PBS] = 10 mM; [RhBITC-βCDpolymer] = 1.00 mg.mL^{-1}; [FITC-βCDpolymer] = 1.00 mg.mL^{-1}.

Due to the respective wavelengths of absorption and emission of each fluorophore, and the possible proximity of the rhodamine B and fluorescein dyes in the mixture, we cannot exclude a FRET phenomenon where the fluorescein will transfer its energy to the rhodamine moiety. The advent of this energy transfer will not interfere with the ratiometric effect desired in this system. However, in any case, Figure 76A demonstrates that such a phenomenon is negligible as the emission of the mixture of polymers is very similar to the sum of each single fluorescence (fluorescein and rhodamine B); furthermore, the fluorescence lifetimes measured for the fluorescein chromophore in the single polymer solution or in the mixture of polymer are identical (4.25 ns and 4.27 ns respectively) (Figure 76B & 76C).

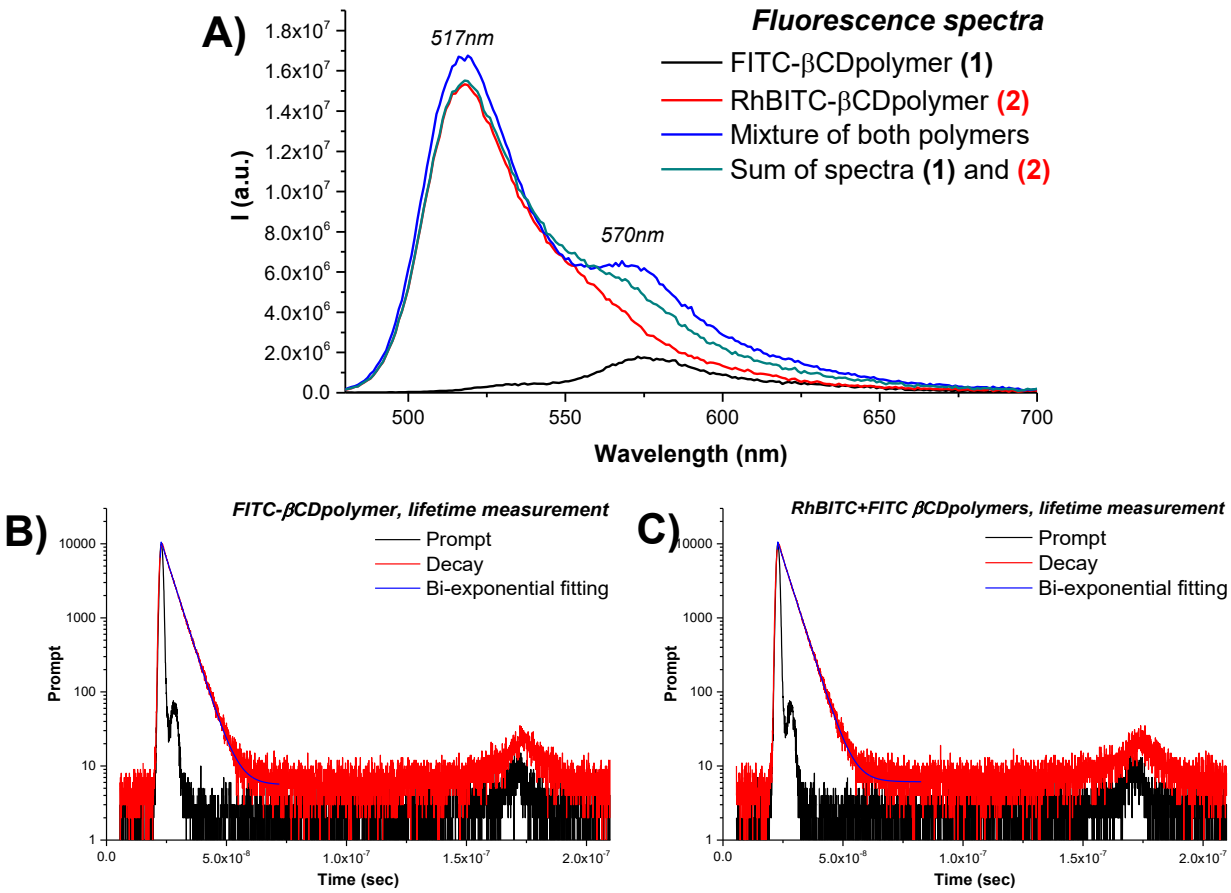

Figure 76: A) Comparison of the emission spectra (arbitrary units) over wavelength (nm) of both fluorescein- (1) and RhB-isothiocyanate (2) polymers, of a FITC/RhBITC (1:1) polymers mixture, and of the mathematical sum of (1) and (2) fluorescence spectra. B) Lifetime measurement of FITC-βCDpolymer in a PBS solution; and C) lifetime measurement of a mix of RhBITC-βCDpolymer and FITC-βCDpolymer in a 1:1 ratio in a PBS solution. Measurements were performed in a 1 cm path-length fluorescence cuvette using a fluorolog-2 spectrofluorometer. Conditions: [PBS] = 10 mM; [RhBITC-βCDpolymer] = 1.00 mg.mL^{-1}; [FITC-βCDpolymer] = 1.00 mg.mL^{-1}.

Even if no FRET mechanism is observed in a fluorescein/RhB 1:1 ratio, results obtained during the study during the temperature rise were inconclusive, as the system's sensitivity was unsatisfactory due to the fluorescein's excessive contribution to the sample's global emission (i.e., between 35 °C and 50 °C, S_r is equal to -0.46 %. K^{-1}) (Appendix XXIV). Thus, we used a 1:3 ratio of fluorescein to rhodamine B to minimize fluorescein emission relative to rhodamine fluorescence. Consequently, we monitored the emission intensity as a function of temperature (Appendix XXV). Figure 77A shows the evolution of the maximum fluorescence intensity of the fluorescein moiety (520 nm) and the rhodamine B moiety (570 nm) in the mixture of the two polymers of FITC-βCD and RhBITC-βCD in a 1:3 ratio, and compared to the intensity of the same polymer mixture in a 1:1 ratio. Furthermore, to determine whether a fluorescent thermometer can be used, multiple heating cycles must be performed to observe potential

fatigue in the fluorescence response.[256] Thus, we performed a second heating with the same Fluorescein/RhB 1:3 system. By comparison with the 1:1 ratio, the 1:3 polymer ratio shows a more pronounced fluorescence intensity from the rhodamine B moiety.

This stability of the 1:3 system in the biological range of temperature (i.e., between 35 °C and 50 °C) can be correctly compared with the ratio of the fluorescence intensities at 570 nm and 520 nm, which can be used to assess the system temperature and to determine its relative sensitivity (Figure 77B).

For a dual thermometer, the thermometric parameter (R) can be defined as the ratio of the second fluorescence intensity (I_2) over the first fluorescence intensity (I_1) (Equation 3):

$$R = \frac{I_2}{I_1}$$

Equation 3: Thermometric parameter formula for a dual ratiometric thermometer. R: thermometric parameter; I_2: second fluorescence intensity; I_1: first fluorescence intensity.

Then, to obtain the relative sensitivity of a ratiometric thermometer, the fluorescence intensity (I) of the dye in Equation 2 is replaced by the thermometric parameter value obtained from Equation 3 (Equation 4):

$$S_r = 100 \times \frac{1}{R} \times \frac{\partial R}{\partial T}$$

Equation 4: Relative sensitivity formula for a ratiometric thermometer. S_r: relative sensitivity (%. K^{-1}); R: thermometric parameter; T: Temperature (°K).

Consequently, for comparison between the two ratios (i.e., 1:1 and 1:3), the relative sensitivity between 35 °C and 50 °C is about -0.46 %. K^{-1} for the 1:1 ratio, while for the 1:3 ratio, S_r is equal to -1.03 %. K^{-1} for the first heating cycle and equal to -0.87 %. K^{-1} for the second cycle. Consequently, using a 1:3 ratio of fluorescein/RhB βCD polymer results in better temperature sensitivity than using both dyes at equal ratios. By comparison with the work of *Peng et al.*, their system demonstrated a close relative sensitivity with both ratios (i.e., for a 1:1 ratio, near 43 °C, S_r is close to -0.46 %. K^{-1}; while for a 1:3 ratio, near 43 °C, S_r is close to -1.3 %. K^{-1}).[256]

However, even if the S_r values of the 1:3 ratio polymer in the first and second heating cycle are close, the weaker relative sensitivity in the second cycle than for the first one can be observed; furthermore, at 70 °C, the emission intensity of both dyes drop significatively (i.e.,

λ_{exc} = 500 nm, first cycle: I_{max} = 1.02x10^7; second cycle: I_{max} = 1.92x10^5). This intensity difference may be due to system fatigue induced by dye degradation during high-temperature exposure. Consequently, the mix of FITC-βCD and RhBITC-βCD polymer system is not sustainable beyond multiple heating cycles. By comparison, Peng *et al*. reported in their MOF system with the same ratio of fluorescein/RhB (1:3) an excellent stability of the performances over three heating cycles (repeatability near 95 %).[256]

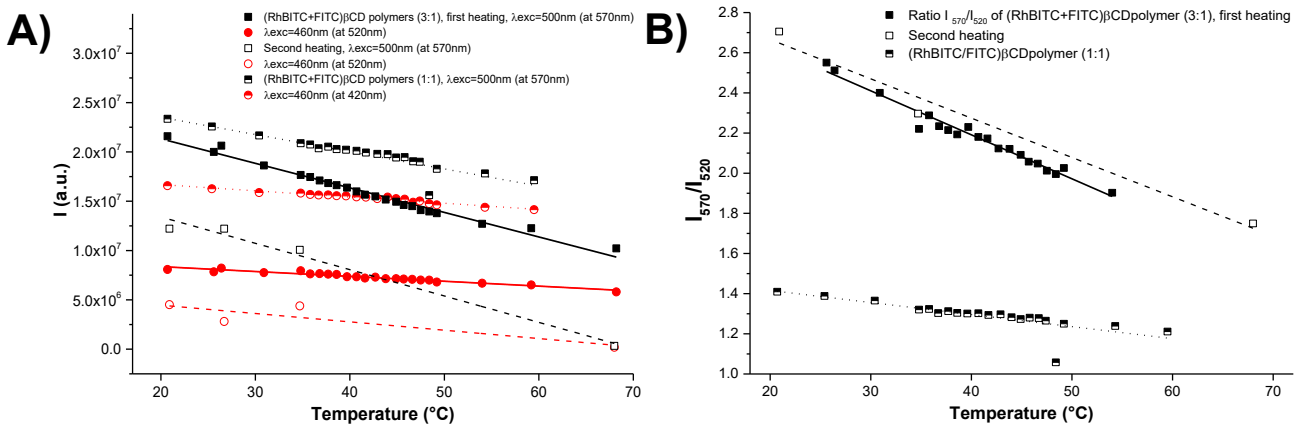

Figure 77: A) Comparison of the fluorescence maximum intensity (I_{max}) evolution over temperature (°C) of a mixture of FITC-βCDpolymer and RhBITC-βCDpolymer in a 1:3 ratio (first and second heating cycle), and in a 1:1 ratio, at I_{max} = 520 nm when excited at λ_{exc} = 460 nm, and at I_{max} = 570 nm when excited at λ_{exc} = 500 nm. B) Evolution of the ratio of I_{max} = 570 nm over I_{max} = 520 nm, over temperature (°C) of a mixture of FITC-βCDpolymer and RhBITC-βCDpolymer in a 1:3 ratio (first and second heating cycle), and in a 1:1 ratio. Conditions: [PBS] = 10 mM; [FITC-βCDpolymer] = 0.50 mg.mL^{-1}; [RhBITC-βCDpolymer] = 1.50 mg.mL^{-1}.

6.2.4. First attempt with gold nanoparticles with the RhBITC-βCD polymer

We attempted a preliminary synthesis of gold nanoparticles in the presence of the RhB-modified polymer (I12 sample). The synthesis of AuNPs was done with indigo carmine over curcumin as a reducing agent because of the strong absorption of the light by curcumin. By comparison, as stated before, the indigo carmine residue shows only a small band at 410 nm and is almost colorless. The latter does not interfere with that of rhodamine B. The I12-L sample is prepared using the same methodology as reported in the previous chapter dedicated to the synthesis of AuNPs with indigo carmine (part 5.1.). After solubilization of the reducing agent in the RhBITC-βCD polymer, the gold precursor $HAuCl_4 \cdot 3H_2O$ is added, and the sample is irradiated for thirty-two minutes with a 405 nm laser (*ca.* 6 W.cm^{-2}). Like in a previously reported synthesis (i.e., I1-D, part 5.1.), a similar absorbance evolution is observed. We observe first a rise of both LSPR bands near 537 nm and 837 nm characteristic of anisotropic AuNPs. The

broadening of the LSPR band in the near-infrared region can be due to multiple AuNPs populations. (Figure 78).

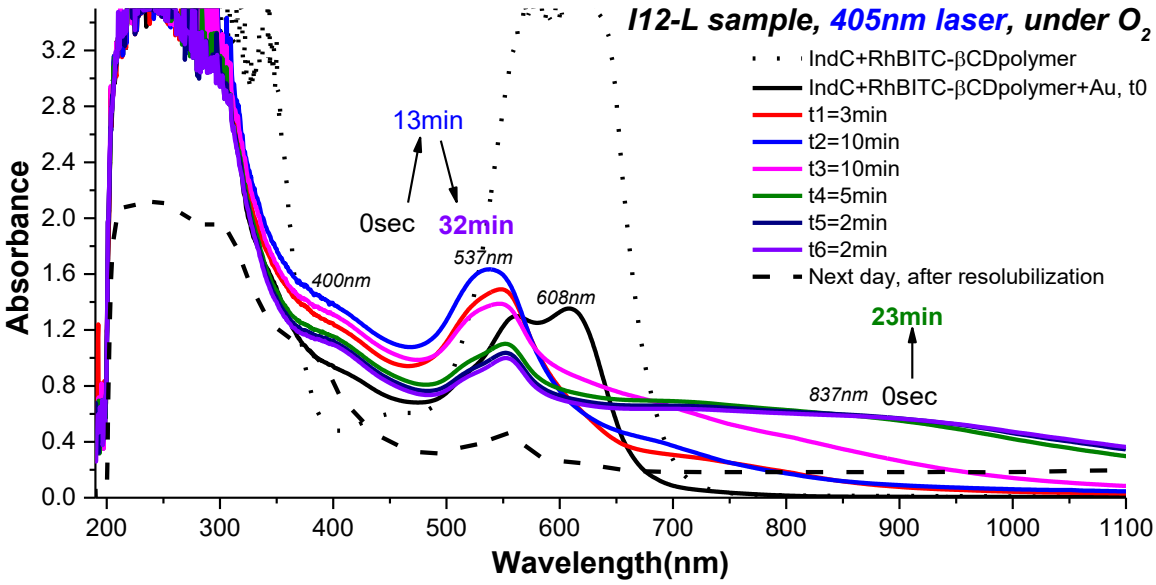

Figure 78: Comparison of the absorbance evolution of IndC+RhBITC-βCDpolymer+Au (I12-L), under O_2, irradiated using a 405 nm laser (*ca.* 6 $W.cm^{-2}$) for thirty-two minutes, in a PBS solution, while magnetically stirred. Measurements were performed in a 1 cm path-length absorbance cuvette using a PerkinElmer UV-Vis spectrophotometer. Conditions: [PBS] = 10mM; [IndC] = 0.41 mM ; [RhBITC-βCDpolymer] = 1.00 $mg.mL^{-1}$; [$HAuCl_4$] = 0.41 mM.

After the successful synthesis of anisotropic gold nanoparticles with the marked polymer, the fluorescence response of the dye over temperature evolution in the presence of the AuNPs I12-L was studied (Figure 79A). Then, we compared the resulting fluorescence intensity evolution with the emission intensity of rhodamine B alone and with the marked polymer without gold nanoparticles (Figure 79B). We observed a similar evolution across the three systems, with a decrease in fluorescence intensity as temperature increased. While the temperature was increasing, the fluorescence of the system with AuNPs was decreasing correspondingly with a relative sensitivity of S_r = -1.23 % K^{-1} (from Equation 2),[259] which is similar to the relative sensitivity observed for Rhodamine B linked with the cyclodextrin polymer (about -1.30 % K^{-1}) and the one of Rhodamine B alone (about -1.52 % K^{-1}) (Figure 79B).

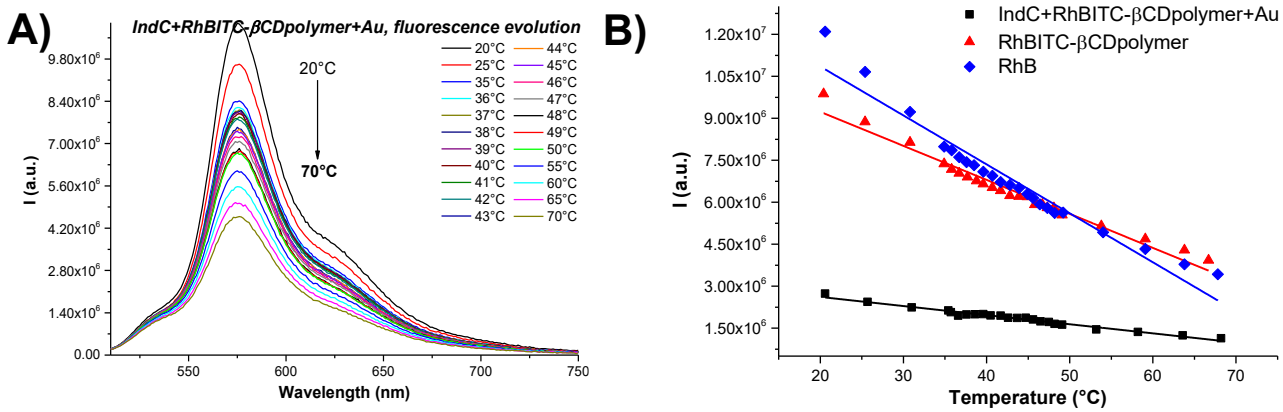

Figure 79: A) Comparison of the fluorescence intensity over temperature evolution of IndC+RhBITC-βCDpolymer+Au (I11-L) in a PBS solution. Measurements were performed in a 1 cm path-length fluorescence cuvette using a fluorolog-2 spectrofluorometer. Excitation wavelength = 500 nm; Slit = 1.5; B) Comparison of the fluorescence intensity maximum over the temperature measured manually in the fluorescence cuvette of RhB (data in black), RhBITC-βCDpolymer (data in red), and IndC+RhBITC-βCDpolymer+Au (I12-L) (data in blue), when excited at λ_{max} = 575 nm. The inset shows a zoom between 35 and 50 °C. Conditions: [PBS] = 10 mM; [IndC] = 0.41 mM; [RhB] = 1.00 mg.mL^{-1}; [RhBITC-βCDpolymer] = 1.00 mg.mL^{-1}; [$HAuCl_4$] = 0.41 mM.

Unfortunately, the AuNPs formed were unstable (i.e., loss of anisotropy; the LSPR band at 837 nm decreased one day after synthesis), and photothermal measurements and investigations into the possibility of measuring temperature variation through fluorescence modification were not possible. Then, it is mandatory to establish a procedure for *in situ* synthesis of gold nanoparticles. Indeed, the precursor used to reduce Au(III) to Au(0) has to be compatible with the presence of both rhodamine B and fluorescein; more precisely, the precursor and the products of the redox reaction have to absorb at different wavelengths with respect to the fluorophores.

6.3. "Green" synthesis of gold nanoparticles with a nitric oxide photodonor: S-nitrosoglutathione

As previously described in chapter 4 and 5, for curcumin and indigo carmine respectively, we achieved the green synthesis of anisotropic gold nanoparticles. However, depending on the batches synthesized, we generally obtained a higher proportion of anisotropic nanoparticles than spherical nanoparticles and, consequently, we achieved satisfactory NIR heat generation for both curcumin and indigo carmine systems. However, until now, spectral behaviors during syntheses and TEM images realized suggest the formation of a mixed population of spherical and anisotropic particles (C6, C8, C10, C11p, I1, I2-D, I3, I8p, I9p-L, I11 samples). Furthermore, it was not possible to use light as an exclusive trigger for the formation of AuNPs. Therefore, a

new reducing agent, nitric oxide radical, generated in a controlled manner using a •NO-photodonor precursor, was studied for the formation of anisotropic AuNPs. The use of a nitric oxide donor for the synthesis of anisotropic particles was inspired by a previously reported work from our group;[161] in that work, a βCD polymer covalently modified with a nitric oxide photodonor was used both as a generator of reducing agent and template/stabilizing agent.

To try to mimic this synthesis reported by Nocito *et al.*, we investigated using an unlabeled βCDs polymer.[161] Since Nocito *et al.* reported the synthesis of gold nanotriangles and gold nanoflowers with the irradiation of βCD polymer labeled with an NOPD, we assumed that using our non-functionalized neutral βCD polymer in the presence of a photodonor able to release •NO with a kinetic similar to the one already described would lead to the selective formation of AuNPs under light exposure. We choose S-nitrosoglutathione as a photogenerator of •NO, activable under green light, since, after radical release, glutathione, a molecule widely distributed in the bioenvironment, will be produced as a co-product. Furthermore, the presence of the thiol groups from the co-product will allow a possible stabilization of the AuNPs with the formation of Au/thiolate bonds.[260] The absorbance spectrum of S-nitrosoglutathione (GSNO) (i.e., about 240 and 330 nm), nor its residual glutathione (GSH) (i.e., about 210 nm),[261] will interfere with the absorbance spectrum of the labelled polymer (i.e., between 480 and 560 nm).

6.3.1. S-nitrosoglutathione and nitric oxide radical: definition

S-Nitrosoglutathione is a nitric oxide photodonor. This pink solid can be synthesized by nitrosating glutathione in acidic media. *In vivo*, GSNO is metabolized by the GSNO reductase.[262] Therapeutic properties attributed to GSNO, like antibacterial, antithrombosis, or antiinflammation, are due to its capacity to release •NO (nitric oxide radical).

GSNO is a very sensible molecule, and its degradation to GSH can easily be done. Exposure to UV or visible light for several hours at room temperature is sufficient to degrade the pink solid.[263] Besides, sulphated derivatives can induce the degradation of GSNO by transnitrosation. While metallic cations such as Cu^{2+} can catalyze the degradation of GSNO.[264] However, compared to alkaline conditions, in acidic medium, GSNO shows a higher stability because of the protonation of the oxygen, favoring its stable form (Figure 80).[265]

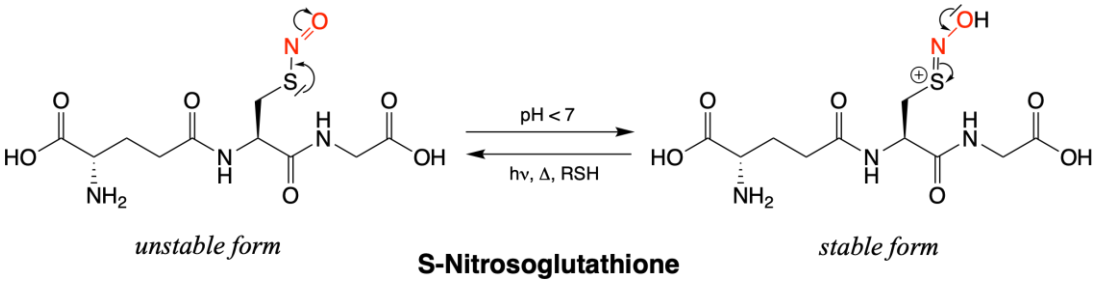

Figure 80: Equilibrium of S-nitrosoglutathione between its stable and unstable forms. The equilibrium is dependent of the pH, temperature, light or on the presence of sulphated derivates.

Nitric oxide is a diatomic water-soluble free radical gas with a relatively short half-life (up to 5 seconds), mainly acting as a signaling molecule.[266] It is a reactive nitrogen species (RNS), and •NO is used for its antioxidant,[267] antimicrobial,[268] or antitumoral activity.[269] The therapeutic effect of nitric oxide on cancer is dependent on its concentration. Low •NO influx can improve cancer progression, while high concentration may lead to biological material degradation and enhance chemotherapy efficacy.[270]

Once the unstable form of GSNO is photoinduced, •NO is released, which we can use to reduce gold salts and initiate nucleation. Thus, the redox potential of •NO to cationic nitric oxide is E^0 = +0.5 V (NHE) or E^0 = +0.494 V (SHE), which is inferior to the redox potential of $AuCl_4^-$ to Au(0).[271]

6.3.2. Synthesis of S-nitrosoglutathione

We synthesized S-nitrosoglutathione according to the procedure reported by Hart *et al.*;[272] we obtained GSNO from the S-nitrosation of reduced L-glutathione carried out with sodium nitrite in acidic conditions (Figure 81).

We initiated the synthesis in an acidic medium and carried it out in a cold and dark environment to favor the stable form of GSNO and, consequently, prevent its denitrosation. These conditions must be carefully followed; otherwise, the thiolate will easily react with other monomers to form disulfide bridges.[272] At the end of the synthesis, with a yield of up to 35% (Table 2, Entry G3), a pink precipitate is formed, the characteristic color of the stable form of nitrosothiols.[273]

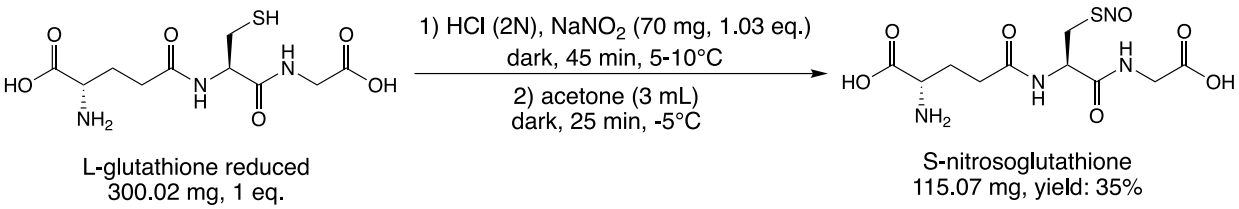

Figure 86: S-Nitrosation of L-glutathione reduced with $NaNO_2$. Formation of S-nitrosoglutathione.

Table 2: Summary of the three attempts for the nitrosation of L-glutathione reduced (GSH) with $NaNO_2$ in different conditions.

Entry	GSH	Light/Dark	GSNO	Yield
G1	200.00 mg	Light	0 mg	0 %
G2	200.00 mg	Dark	36.84 mg	17 %
G3	**300.02 mg**	**Dark**	**115.07 mg**	**35 %**

The UV-Vis absorbance spectrum of the light-pink solid showed the formation of the nitroso group, with a characteristic, very low-intensity band at 545 nm (Figure 82). Nonetheless, because of the low absorbance intensity (i.e., A = 0.01 at λ = 545 nm), a new measurement at a higher GNSO concentration must be performed to assess the reliability and significance of this measurement. No further purification of the synthesized GSNO was performed before the synthesis of the gold nanoparticles.

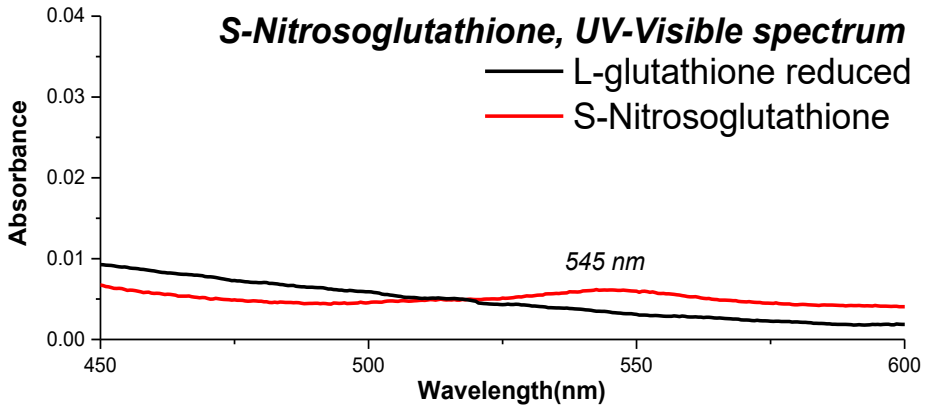

Figure 82: Absorbance spectra of L-glutathione reduced (GSH) and S-nitrosoglutathione (GSNO) in a pure water solution. Measurements were performed in a 1 cm path-length absorbance cuvette using a PerkinElmer UV-Vis spectrophotometer, with air as a blank.

6.3.3. Synthesis of AuNPs from GSNO irradiation

Firstly, we assessed the ability of GSNO to release nitric oxide radical under light irradiation and in the presence of βCD polymer.

We performed these measurements using an electrode sensitive exclusively to •NO in the nM range, with irradiation carried out using a 528 nm green light lamp. In Figure 83A, the concentration of nitric oxide measured by the electrode increased at the start of the irradiation, and then slowed down after the end of the first cycle of irradiation. The total irradiation time was 3 minutes and 30 seconds. The nitric oxide radical release profile is similar to that required to observe the formation of AuNPs (i.e., about 1000 nM of •NO released in 100 seconds), based on previously published results (Nocito *et al.* reported a 500 nM release of •NO in 100 seconds).[161] We measured the absorbance spectrum before and after the nitric oxide release experiment, and the band near 540 nm did not decrease (Figure 83B). This absence of intensity evolution during the experiment can be due to the short irradiation time (i.e., 3 minutes and 30 seconds) and the small laser diameter (*ca.* 1.5 mm), which does not cover a large surface of the sample during nitric oxide radical measurement.

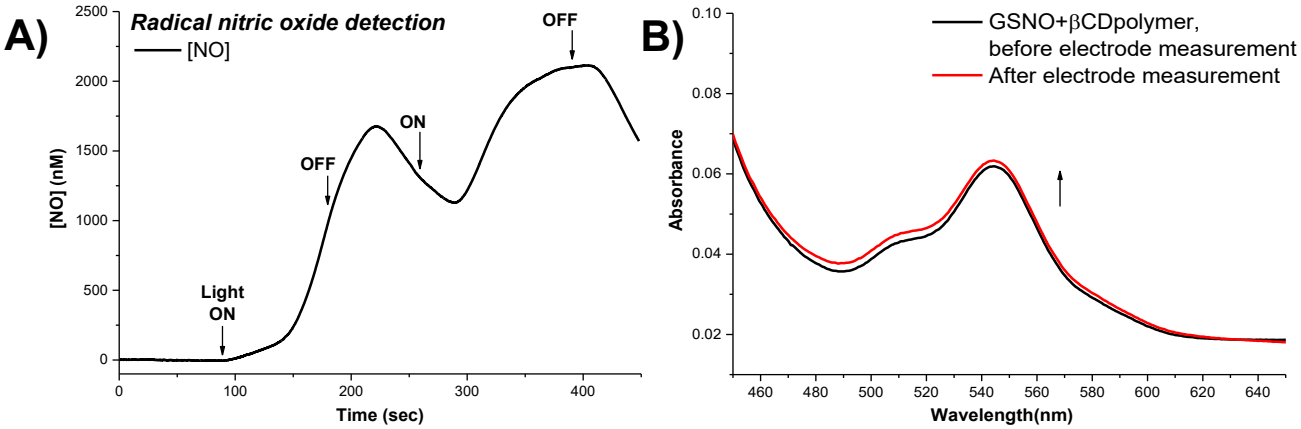

Figure 83: A) Radical NO release profile measured for the system GSNO+βCDpolymer under 528 nm lamp (*ca.* 1 mW.cm^{-2}) irradiation; B) Comparison of the absorbance evolution of the system before and after the irradiation during the measurement with the nitric oxide electrode. Measurements were performed in a 1 cm path-length fluorescence cuvette using a PerkinElmer UV-Vis spectrophotometer, with air as the blank. Conditions: [GSNO] = 1.00 mg.mL^{-1}; [βCDpolymer] = 1.00 mg.mL^{-1}

After these preliminary assessments, we performed an experiment with the presence of the tetrachloroauric(III) acid (S1-L and S1-D samples). During irradiation, even though we observe a decrease in the GSNO band, suggesting the release of nitric oxide, we observe no formation of other absorbance bands in the visible or in the near-infrared region. We witnessed the

formation of a white precipitate during irradiation, which induced a light scattering responsible for the baseline increase. We observed this precipitate during syntheses under irradiated S1-L and non-irradiated S1-D conditions (inset, Figure 84 and inset, Appendix XXVI). This white precipitate formation can be due to the aggregation of the βCD polymer, caused by disulfide bridge formation during the denitrosation of S-nitrosoglutathione. This precipitate can be produced even in the absence of light, as GSNO can also degrade thermally.

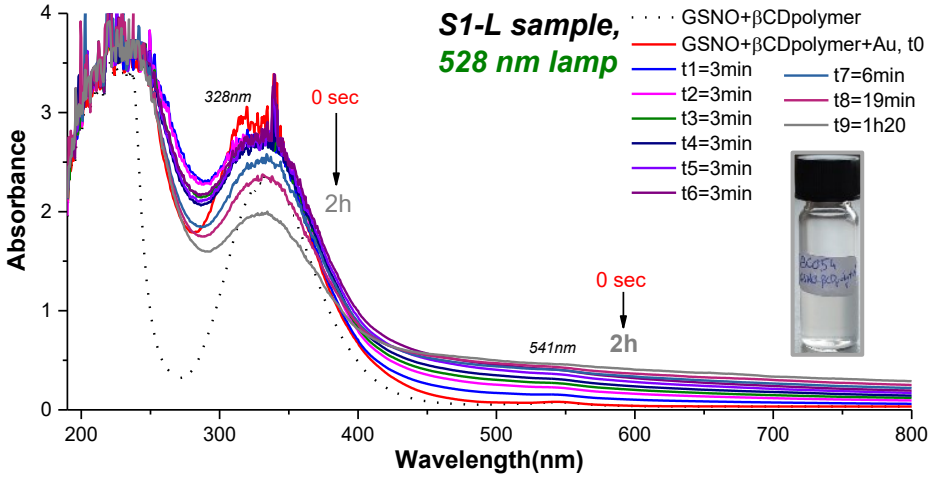

Figure 84: Comparison of the absorbance evolution of GSNO+βCDpolymer+Au (S1-L) during a two-hour-long irradiation; the irradiation was performed in a 1 cm path-length fluorescence cuvette at 10 cm of the sample with a 528 nm lamp (*ca.* 1 $mW.cm^{-2}$). The sample was stirred during the irradiation. The inset shows a picture of the sample at the end of the irradiation. Measurements were performed in a 1 cm path-length fluorescence cuvette using a PerkinElmer UV-Vis spectrophotometer with water as the blank. Conditions: [GSNO] = 1.0 $mg.mL^{-1}$; [βCDpolymer] = 1.0 $mg.mL^{-1}$; [$HAuCl_4 \bullet 3H_2O$] = 0.43 mM.

However, once we substituted the solvent from Milli-Q water to PBS, precipitate formation was absent, and the baseline remained stable throughout the synthesis. The absorbance band at 540 nm decreased slightly during irradiation because of the •NO release in solution (S2-L sample, Appendix XXVII). A cationic polymer was then investigated instead of the neutral one to reach a better complexation of GSNO with the cyclodextrin cavity, to reduce the distance between the cyclodextrin and the NOPD (S3-L sample), but results remained the same (Figure 85); i.e., AuNPs did not form under these conditions.

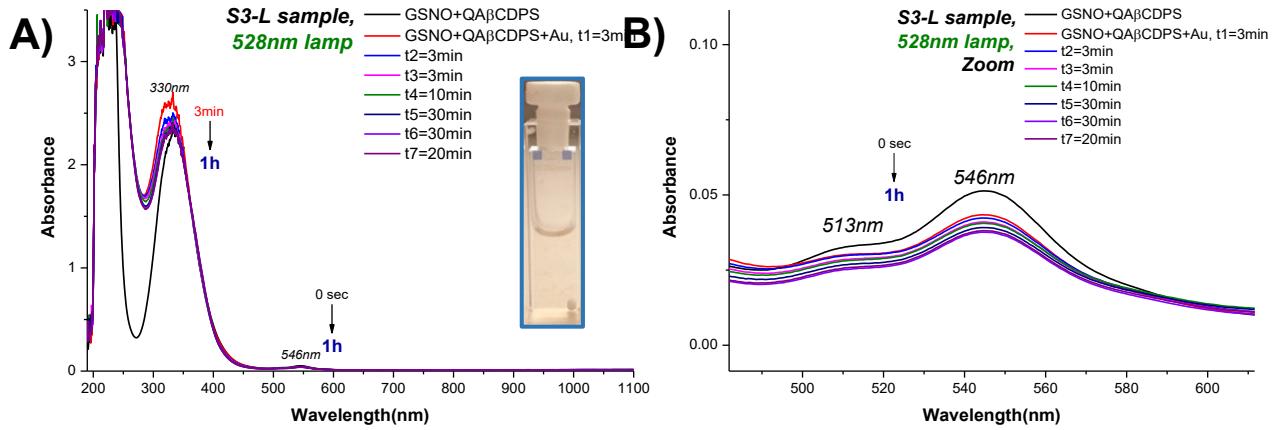

Figure 85: A) Comparison of the absorbance evolution of GSNO+QAβCDPS+Au (S3-L) during a one hour and thirty-nine minutes long irradiation. The irradiation was performed in a 1 cm path-length fluorescence cuvette at 10 cm of the sample using a 528 nm lamp (*ca.* 1 $mW.cm^{-2}$) while magnetically stirred. The inset shows a picture of the sample at the end of the irradiation. B) Zoom of Figure 85A between 450 and 650 nm. Measurements were performed in a 1 cm path-length fluorescence cuvette using a PerkinElmer UV-Vis spectrophotometer using PBS as the blank. Conditions: [PBS] = 10 mM; [GSNO] = 1.0 $mg.mL^{-1}$; [QAβCDPS] = 1.0 $mg.mL^{-1}$; [$HAuCl_4 \bullet 3H_2O$] = 0.5 mM.

Following this initial set of experiments, despite the higher •NO release ([•NO] = 1.5 μM compared to 0.5 μM, in about 100 seconds) and the optimization of both GSNO concentration and polymer template, AuNPs were not synthesized; this may suggest that, like presented by Nocito *et al.*,[161] the covalent binding, or at least a close proximity, of the NO-photodonor to the polymeric scaffold requisite to achieve the gold reduction.

6.4. "Green" synthesis of gold nanoparticles with another NOPD: nitroaniline-adamantane (NA-Ad)

6.4.1. Synthesis of NA-Ad

Despite the unsuccessful synthesis with GSNO, we investigated another NOPD: a molecular conjugate linking covalently a nitroaniline moiety as photoactive unit able to release NO, and an Adamantane (Ad) known for its high affinity for βCD cavity. We hypothesize that the host-guest interaction between Ad and βCD will bring the NOPD moiety into proximity with the polymer, mimicking then the polymer used by Nocito *et al.*, without the constraint of an additional covalent modification. Also, another benefit of using this NOPD instead of S-nitrosoglutathione is its greater stability; indeed, nitroaniline derivatives are stable in the dark and do not release NO thermally. Moreover, the absorbance of this nitroaniline derivative (near

400 nm) and its phenol co-product will not overlap with the absorbance of rhodamine B and fluorescein (i.e., near 500 – 600 nm).

In this context and as reported in the experimental part, we performed the synthesis of the nitroaniline-adamantane, from adamantylamine and the nitroaniline derivative (NA) (Figure 86). We obtained a yellow solid (NA-Ad) after purification by column chromatography prior to the AuNP synthesis.

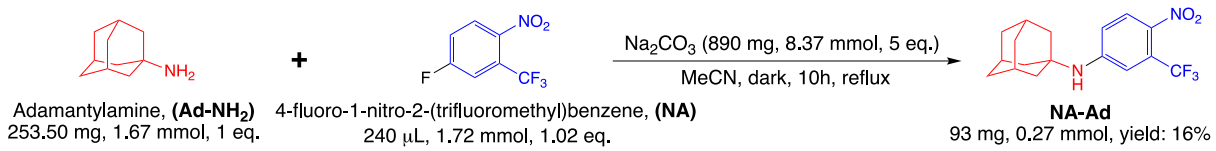

Figure 86: Synthesis of nitroaniline-adamantane (NA-Ad) from adamantylamine (Ad-NH_2) and a nitroaniline (NA) derivative.

^{1}H NMR spectroscopy confirmed the structure of the obtained yellow solid (Figure 87). The appearance of a broad singlet at approximately 4.5 ppm, integrating for one proton, is consistent with the successful nucleophilic substitution of the fluorine atom in NA by the adamantane moiety. Furthermore, on the ^{19}F NMR spectrum, the presence of the singlet attributed to the trifluoromethyl group near -60 ppm demonstrates the achievement of the reaction (Appendix XXVIII).

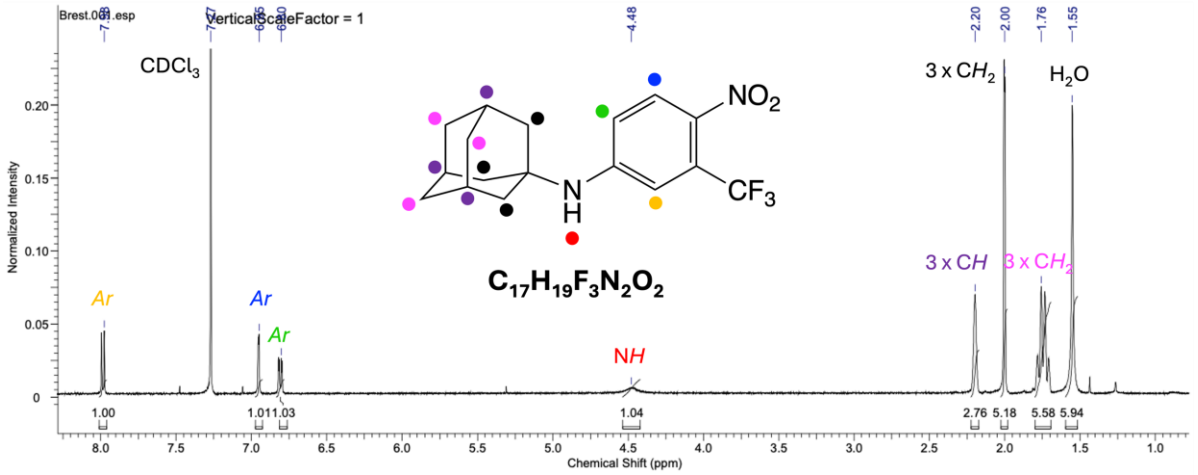

Figure 87: ^{1}H NMR spectrum of NA-Ad. Data collected using a 500MHz NMR spectrometer in $CDCl_3$, at T = 298 °K.

6.4.2. Synthesis of AuNPs from NA-Ad irradiation

After NA-Ad synthesis, we loaded the NOPD into a mixture of fluorescein and rhodamine B labeled polymers at a 1:3 ratio, respectively. We monitored the loading of NA-Ad using a UV-Vis spectrophotometer and observed increases in the absorbance of its two bands at 240 nm and 395 nm (Figure 88A), the latter is characteristic of a $\pi\pi^*$ transition by a charge transfer between the amine, the benzene ring, and the nitro group of the nitroaniline part.[274] Then, we investigated NA-Ad bleaching under blue-light irradiation for 37 minutes using a 405 nm laser (Figure 88B). The decrease in the absorbance band at 395 nm characteristic of the nitroaniline moiety, the rise in the one near 281 nm characteristic of the phenol product obtained after the release of the radical, and the presence of an isosbestic point at 319 nm, provide evidence for the photo-induced release of •NO into solution and its conversion into the phenol co-product.

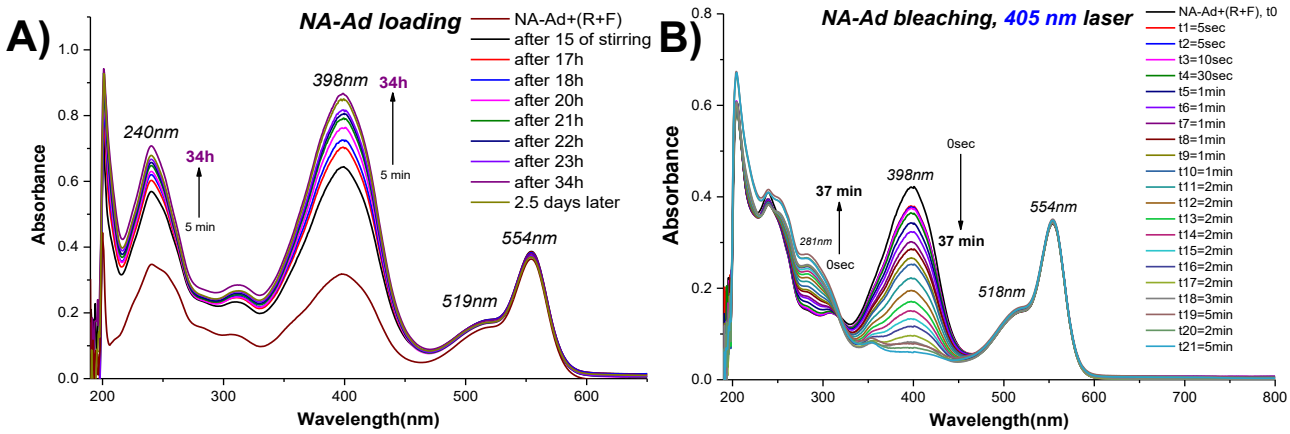

Figure 88: A) Comparison of the absorbance evolution of the loading of NA-Ad inside a mixture both FITC-βCDpolymer and RhBITC-βCDpolymer in a 1:3 ratio in a PBS solution. The sample is magnetically stirred. B) Comparison of the absorbance evolution of NA-Ad+(RhBITC-βCDpolymer+FITC-βCDpolymer) magnetically stirred and irradiated with a 405 nm laser (*ca.* 6 $W.cm^{-2}$) for thirty-seven minutes, in a PBS solution. Measurements were performed in a 1 cm path-length fluorescence cuvette using a PerkinElmer UV-Vis spectrophotometer, with PBS as the blank. Conditions: A) and B) [PBS] = 10 mM; [RhBITC-βCDpolymer] = 1.50 $mg.mL^{-1}$; [FITC-βCDpolymer] = 0.50 $mg.mL^{-1}$.

In a new batch (N1 sample), we then added the gold precursor to the new system composed of the NOPD and the polymer mixture. After the addition of $HAuCl_4 \cdot 3H_2O$, and based on the absorbance of the nitroaniline, we irradiated the sample at 405 nm (N1-L sample) (Figure 89A). We compared it with another sample kept in the dark (N1-D sample) (Figure 89B). During the irradiation, despite the decrease of the band of the gold salt at 320 nm and the band of the nitric oxide photodonor at 395 nm, no characteristic band of AuNPs is observed in the green nor the

near-infrared regions. However, 2 – 3 days after the end of the irradiation, we monitored the characteristic LSPR bands of gold nanoparticles near 520 nm, while a second band appeared in the near-infrared region at about 800 nm, which decreased over the following days. On the other hand, the non-irradiated sample doesn't share the same results. Indeed, upon addition of $HAuCl_4$, only its absorbance band at 320 nm decreases over time, and even after multiple days, we observed no increase in absorption in the green or near-infrared regions.

The color of both samples after the synthesis is also a good indicator of the light selectivity of this NOPD. Days after the synthesis, the irradiated N1-L sample has the characteristic purple color of gold particles, while the dark control N1-D remains light pink due to the polymer color (insets in Figure 89).

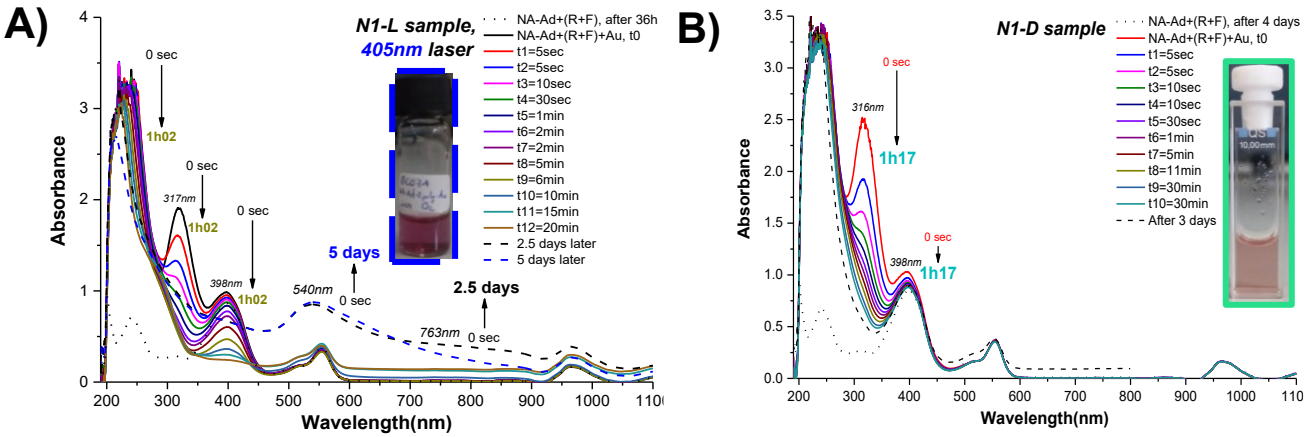

Figure 89: A) Comparison of the absorbance evolution of NA-Ad+(RhBITC-βCDpolymer+FITC-βCDpolymer)+Au (N1-L) magnetically stirred and irradiated with a 405 nm laser (*ca.* 6 $W.cm^{-2}$) for one hour in a PBS solution. The inset shows a picture of the sample five days after the end of the synthesis; B) Comparison of the absorbance evolution of the dark control NA-Ad+(RhBITC-βCDpolymer+FITC-βCDpolymer)+Au (N1-D) stirred for one hour in a PBS solution. The inset shows a picture of the sample at the end of the synthesis. Measurements were performed in a 1 cm path-length absorbance cuvette using a PerkinElmer UV-Vis spectrophotometer, using PBS as the blank. Conditions: A) & B) [PBS] = 10 mM; [RhBITC-βCDpolymer] = 1.50 $mg.mL^{-1}$; [FITC-βCDpolymer] = 0.50 $mg.mL^{-1}$; [$HAuCl_4 \bullet 3H_2O$] = 0.5 mM.

Another batch under the same conditions (N2 sample) ended with the same absorbance evolution and results (Appendix XXIX). Based on the absorbance spectra, the synthesis of AuNPs via irradiation of NA-Ad as NOPD demonstrated excellent selectivity. However, due to time constraints and limited access to instruments for size measurements, we were unable to investigate the sizes and polydispersity indices of the gold nanostructures synthesized (N1 and N2 samples). Consequently, it is not possible to report a complete reproducibility of the synthesis. Further investigations into the size of these gold nanoparticles must be pursued.

6.4.3. Shape studies

The shape of the nanoparticles obtained from the first procedure, N1-L, was observed 6 months after the end of irradiation by TEM microscopy, demonstrating their excellent stability in colloidal suspension over time. The shapes observed are structures like gold “nanoworms” similar to those observed with curcumin. However, the particle concentration observed was greater than that from the gold “nanoworms” sample from curcumin-based nanoparticles. We observed most of the anisotropic particles as substantial aggregates with a very high number of particles (Figure 90A and 90B) and other smaller clusters (Figure 90C and 90D). In the images, we did not observe spherical nanoparticles. We observed contrast differences for these roughened particles, characteristic of quasi-spherical and crystalline AuNPs (Figure 90C and 90D); these particles must be responsible for the band at 520 nm observed in the absorbance spectrum.[275]

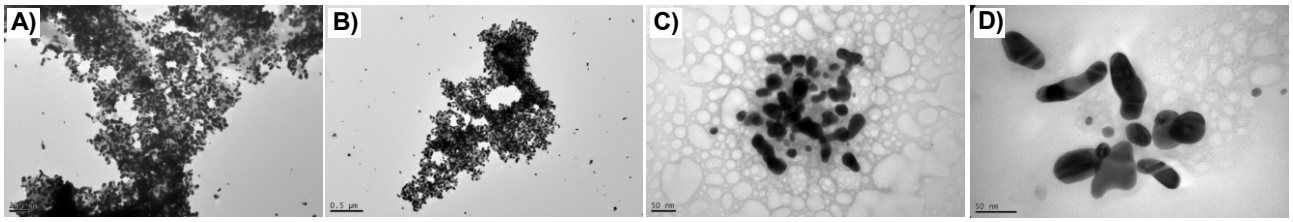

Figure 90: TEM images of the irradiated sample NA-Ad+(RhBITC-βCDpolymer+FITC-βCDpolymer)+Au (N1-L).

6.4.4. Photothermal study and investigation of the fluorescence sensitivity of the system during photothermia of the nitroaniline-adamantane system

Before the investigation of the fluorescence sensitivity of the system NA-Ad+(RhBITC-βCDpolymer+FITC-βCDpolymer)+Au, the photothermal properties of the synthesized AuNPs from the irradiated sample had to be determined. We performed the study using a 532 nm laser (*ca.* 6 $W.cm^{-2}$) on the N1-L sample because of its main LSPR band in the green region; as a result, a temperature rise of 12.6 °C was achieved (Figure 91). We did not perform irradiation in the near-infrared region. These first results are a proof-of-concept to determine whether a change in the fluorescence intensity of the polymer mixture is observable in the presence of gold nanoparticles during a photothermal study.

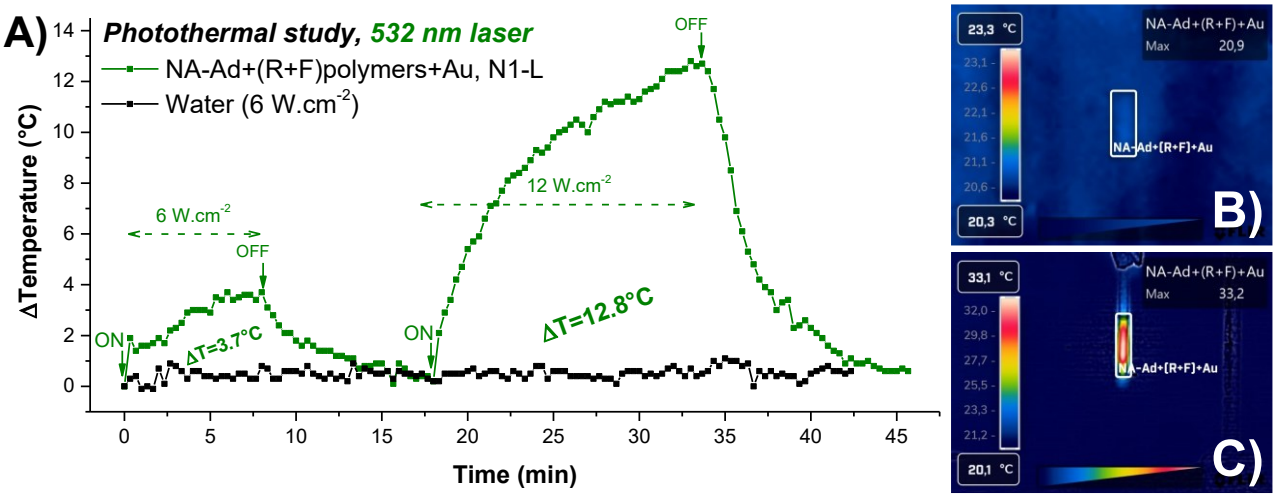

Figure 91: A) Evolution of the temperature over time of the irradiated NA-Ad+(RhBITC-βCDpolymer+FITC-βCDpolymer)+Au (N1-L) (in green) by laser irradiation at 532 nm at *ca.* 6 W.cm^{-2} over the first cycle of measurement and at *ca.* 12 W.cm^{-2} over the second cycle of measurement. Comparison with the evolution of temperature of a water sample irradiated in the same conditions (in black) (control sample). B) Thermal picture taken at the starting point of the second irradiation cycle. C) Thermal picture taken at the end of the 532 nm laser of the second irradiation cycle. The temperatures were measured with a FLIR C3 thermal camera.

It should be noted that it is not trivial to generate a photothermal effect and to complement the measurement of fluorescence evolution.[276,277] Preliminary investigations were performed to find a suitable experimental setup capable of irradiating and monitoring the solution temperature while simultaneously keeping the sample in the dark to obtain a correct measurement of the emission spectrum without loss of solution temperature. The sample was irradiated in a thin fluorescence cuvette with a 1 mm path-length to avoid thermal diffusion within the sample. The irradiation conditions were the same as those previously described (i.e., 532 nm laser (*ca.* 12 W.cm^{-2})). The temperature increase observed in the cuvette was about ΔT = 6.4 °C (Figure 92). The lower temperature achieved in the photothermal study in the NMR tube described above may be due to the higher solution volume, which leads to greater heat dispersion. Furthermore, during the fluorescence measurement, the laser source must be turned off to avoid interference from monochromatic light; consequently, the end of the irradiation marks the start of the sample cooling; however, this effect must be modest since the measurement time is short.

The optimal setup for direct temperature measurement via fluorescence to avoid the cooling effect during the measurement, and the use of an optimal cuvette to reduce thermal diffusion, are currently under investigation.

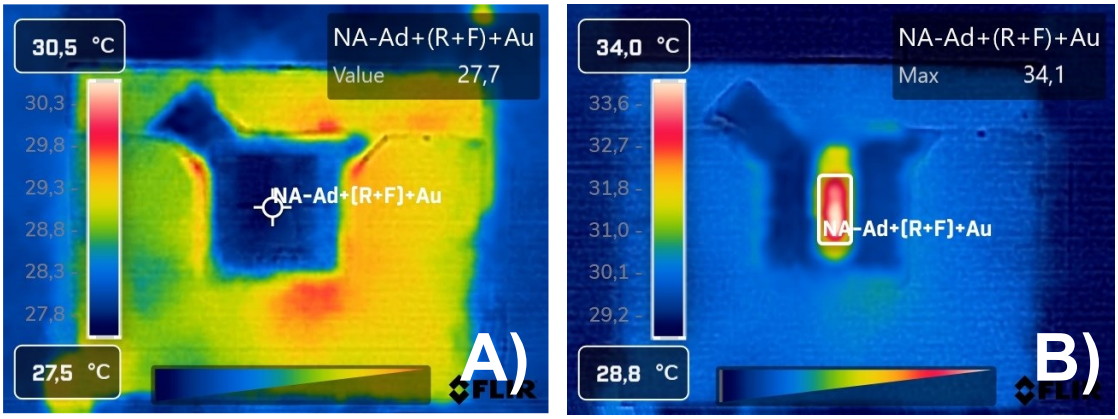

Figure 92: A) Thermal picture taken at the starting point of the irradiation inside the fluorophotometer. B) Thermal picture taken at the end of the 532 nm laser (*ca.* 15 W.cm^{-2}) irradiation. Temperatures were measured using a FLIR C3 thermal camera.

* * *

Nonetheless, because of the promising results of the photo-induced synthesis of AuNPs from NA-Ad using fluorescent cyclodextrin polymers, we pursued investigations into the synthesis of a unique bifunctionalized polymer with both fluorescent probes covalently linked to achieve a better control of the fluorescein/RhB 1:3 ratio. Furthermore, we also investigated new fluorescent βCD polymers to develop original alternatives to the couple fluorescein/RhB thermometer.

6.5. Synthesis of novel βCD polymers labeled with fluorophores

The project focuses on the design, implementation, and optimization of synthetic routes for novel βCD polymers labeled with two fluorophores, fluorescein and rhodamine B, in a controlled 1:3 ratio. Furthermore, derivative libraries will be developed by introducing alternative fluorophore configurations, including systems with pure dansyl, dual-labeled rhodamine-dansyl polymers, and trichromophoric constructs combining rhodamine B, fluorescein, and dansyl. These variations will enable systematic tuning of photophysical properties, expanding the spectral range of the polymers. This synthetic work was conducted under the supervision of Dr Milo Malanga at CarboHyde, a private preclinical pharmaceutical based in Budapest, Hungary, specializing in cyclodextrin synthesis (CarboHyde website link: https://www.carbohyde.com).

As reported by Malanga *et al.*,[278] two complementary strategies are possible for the synthesis of an epichlorohydrin branched CD-based polymer: a polymerization of βCDs before or after their functionalization with fluorophores. The first approach involves polymerization of unmodified βCD-(CH_2-OH)$_7$ monomers, followed by dye incorporation into the preformed polymers. The second strategy proceeds in the opposite direction: firstly, the monomers of βCDs are labeled, and then the polymerization step combines the different units (Figure 93). Each has advantages and drawbacks. The first one allows better branching among all monomers due to the utilization of all free hydroxyl groups and reduced hindrance from the CDs. However, the functionalization and control of the FITC/RhBITC ratio are more challenging, as several steps would be required to insert them into the polymer scaffold. On the other hand, the second strategy allows better control over the resulting polymer (i.e., branching complexity and monomer proportions). Still, the new properties (solubility, viscosity) of the modified monomer units can introduce complications (e.g., decreased reactivity of the CD monomers or complexation of the label within the CD cavity) at the branching site due to increased steric hindrance from the linked dyes. Another critical point is the medium pH during polymerization. Under acidic conditions, the uncontrolled opening of the epoxide moiety of epichlorohydrin leads to over-polymerization, and the isothiocyanate linkage between the cyclodextrin and the dye can be cleaved, yielding free dyes in solution. Consequently, the second strategy, performed in alkaline conditions, was chosen to prevent gel formation, to facilitate the free release of the dye in solution, and to enable easy "build" of a polymer with an adjustable ratio and different combinations of fluorescent βCD monomers.

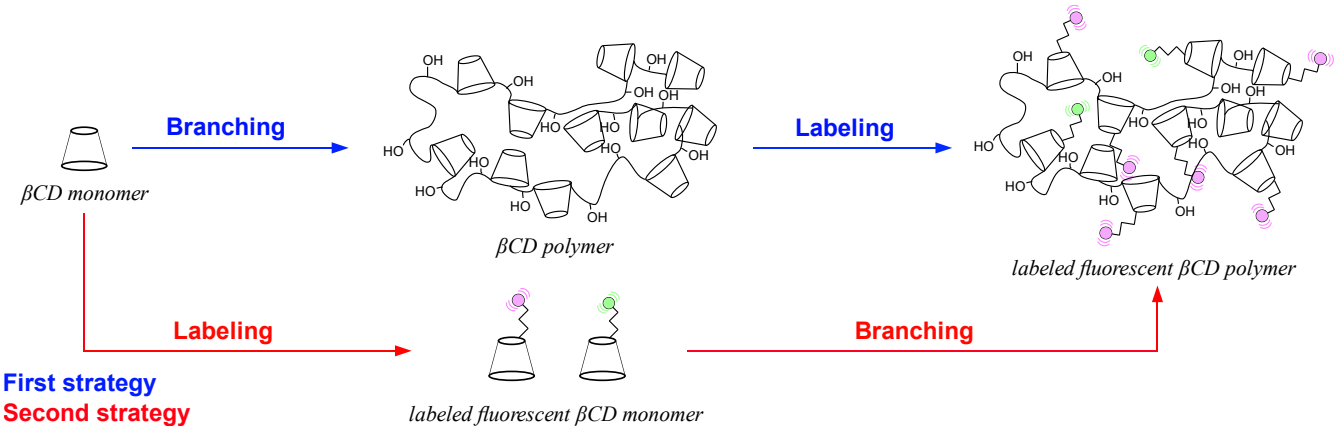

Figure 93: Schematic representation of the two synthetic strategies for generating fluorescent βCD water-soluble polymer. The first route (shown in blue) involves polymerizing unmodified βCD monomers prior to the fluorophore incorporation. In contrast, the second route (shown in red) proceeds by first labelling βCD monomers, followed by their polymerization.[278]

Due to technical limitations, we chose to perform the polymerization step on a large scale, using a minimum mass of βCD monomer of 21 grams in 50 mL of water. Furthermore, even if a small amount of labeled fluorescent cyclodextrins (i.e., βCD-(FITC)$_1$ and βCD-(DNSA)$_1$) is needed for the polymerization (about 10 – 30 mg), we wanted to prepare a larger scale to investigate multiple experimental conditions with time constraints without repeating the multi-step synthesis.

The purification of the labeled ratiometric fluorescent βCD polymer will be performed by dialysis against distilled water with a 12 kDa molecular weight cut-off (MWCO) membrane to easily separate the polymer from free dyes and other small impurities accumulated during the multi-step synthesis. Consequently, the purification of every intermediate was not necessarily needed.

6.5.1. Reduction of βCD-(N$_3$)$_1$

Since CarboHyde had already performed the syntheses of βCD-(N$_3$)$_1$ (monoazido-βCD derivative) and βCD-(RhBITC)$_1$ monomers, according to procedures already reported,[279] in sufficient amount for the investigations planned, the work at the company's laboratory in Budapest was focused first on synthesizing βCD-(NH$_2$)$_1$ (monoamino-βCD derivative) to add fluorescein and reach the βCD-(FITC)$_1$ monomer. The tosylation step and subsequent azidation from βCDs, which were required to reach βCD-(N$_3$)$_1$, did not need to be performed again (Figure 94).

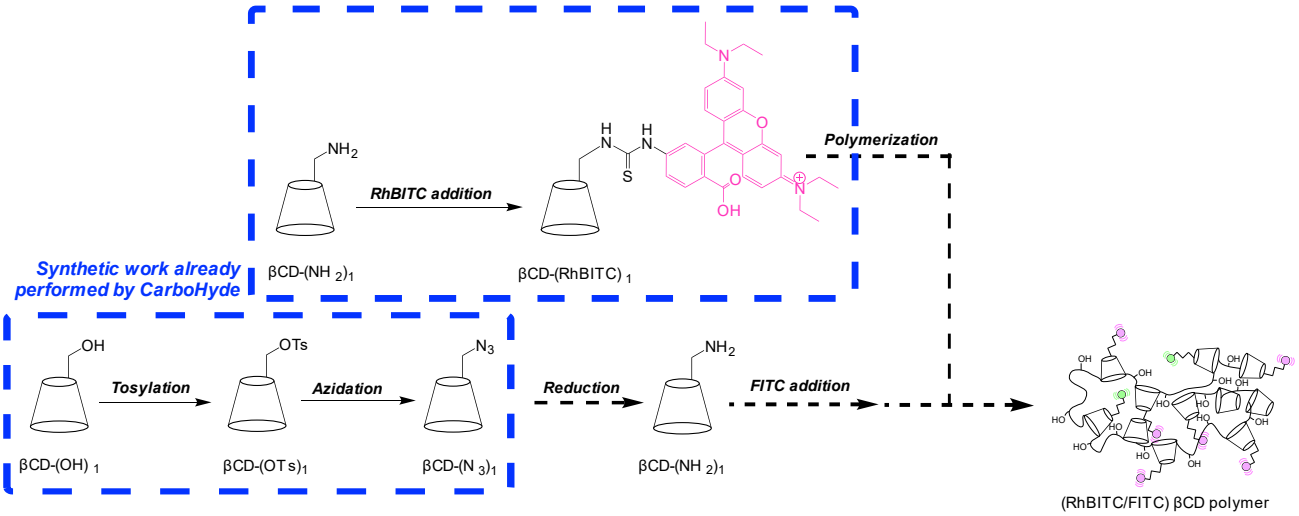

Figure 94: Schematic representation of the synthetic strategy pursued for the synthesis of the ratiometric fluorescent RhBITC/FITC βCD water soluble polymer. In blue are represented the synthetic steps already made by CarboHyde before the start of the synthesis work.

The synthetic work began with the βCD-$(N_3)_1$ derivative and its reduction to the βCD-$(NH_2)_1$ monomer. The procedure for preparing the mono-amine derivative is reported in the experimental section. We performed the reaction in a distilled water and n-propanol (4:1) mixture. n-Propanol exhibited a strong ability to solubilize the βCD-$(N_3)_1$ precursor, while the addition of water mitigated safety risks; indeed, water helped to prevent overheating of the reaction mixture, thereby reducing the risk of fire hazards associated with the simultaneous presence of hydrazine, palladium, and a reflux system (Figure 95). The reaction was monitored by TLC (Figure 96A), and we further assessed the purity of the resulting product (Figure 96B) using a semi-quantitative TLC evaluation. Since cyclodextrins and hydrazine are not visible under classic detection (UV detection), we used other methods, such as the sulfuric acid/ethanol detection solution, which allows the visualization of the components as a "black spot", characteristic of carbon-containing compounds, such as carbohydrates and, in particular, CDs. We visualized the reducing agent N_2H_4 with a ninhydrin/ethanol solution as purple/red/yellow spots, depending on the concentration of amine-containing molecules. The reaction was performed directly on a large scale using 10 grams of βCD-$(N_3)_1$, yielding about 75% of the βCD-$(NH_2)_1$ monomer. We achieved isolation and purification (i.e., Büchner filtrations and liquid/solid extractions with methanol) of the product without chromatography, in line with CarboHyde's general industrial setting.

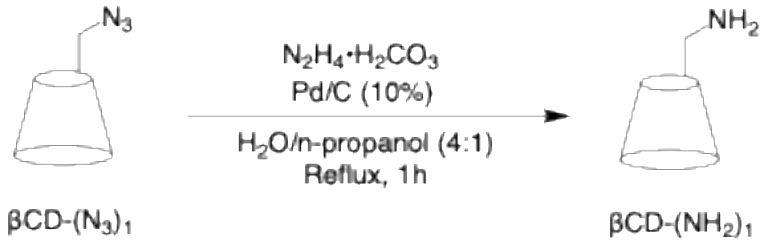

Figure 95: Reaction scheme for the reduction of βCD-$(N_3)_1$ into the monomer βCD-$(NH_2)_1$.

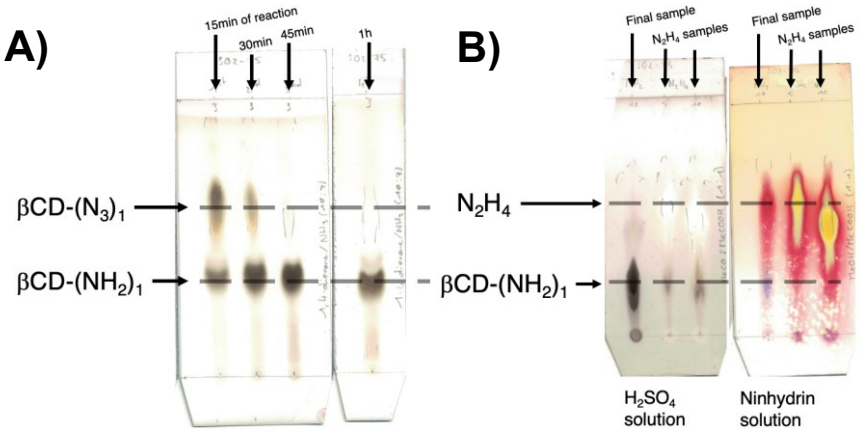

Figure 96: A) TLC plates for monitoring the reduction of βCD-$(N_3)_1$ into βCD-$(NH_2)_1$. The spotting was performed at 15, 30, 45 minutes, and 1 hour of reaction. Eluant: 1,4-dioxane/NH_3 (10:7). The detection method was achieved with a H_2SO_4/EtOH (1:1) solution. B) TLC plates for purity check of the final product, with respect to hydrazine samples spotted as 5 and 10 μL of a 1 % concentrated solution; on the left: the detection was performed using a H_2SO_4/EtOH (1:1) solution, and on the right: the detection was performed using a ninhydrin/EtOH (1:1) solution.

In addition to TLC analysis, which confirms the reduction of βCD-$(N_3)_1$, further evidence can be obtained from the ^{1}H NMR (Appendix XXX) and ^{1}H-^{13}C DEPT HSQC (Heteronuclear Single Quantum Coherence) (Figure 97) spectra. In βCD-$(N_3)_1$ (Appendix XXXI), the unsubstituted methylene protons at the C6 position of the cyclodextrin exhibit the same chemical shift as the methylene groups of the primary hydroxyl moieties in the native cyclodextrin (around 3.6 ppm). In contrast, in the βCD-$(NH_2)_1$ monomer, the C6 methylene group is directly adjacent to a primary amine. Replacing the azide with an amine modifies the local electronic environment: the azide group, being more electronegative, induces stronger deshielding of the adjacent protons, whereas the amine group is less electron-withdrawing and can donate electrons through its lone pair. In the ^{1}H NMR spectrum, this change results in an upfield shift of the CH_2 protons, which now appear as two non-equivalent signals, observed as doublets of doublets at 2.80 and 3.00 ppm, each integrating for one proton, while for the ^{1}H-^{13}C HSQC spectrum, the reduction of the azide part led to an upfield shift with the CH2 protons appearing near 2.80 and 3.00 ppm, respectively (F2 axis), and 40.0 ppm (F1 axis).

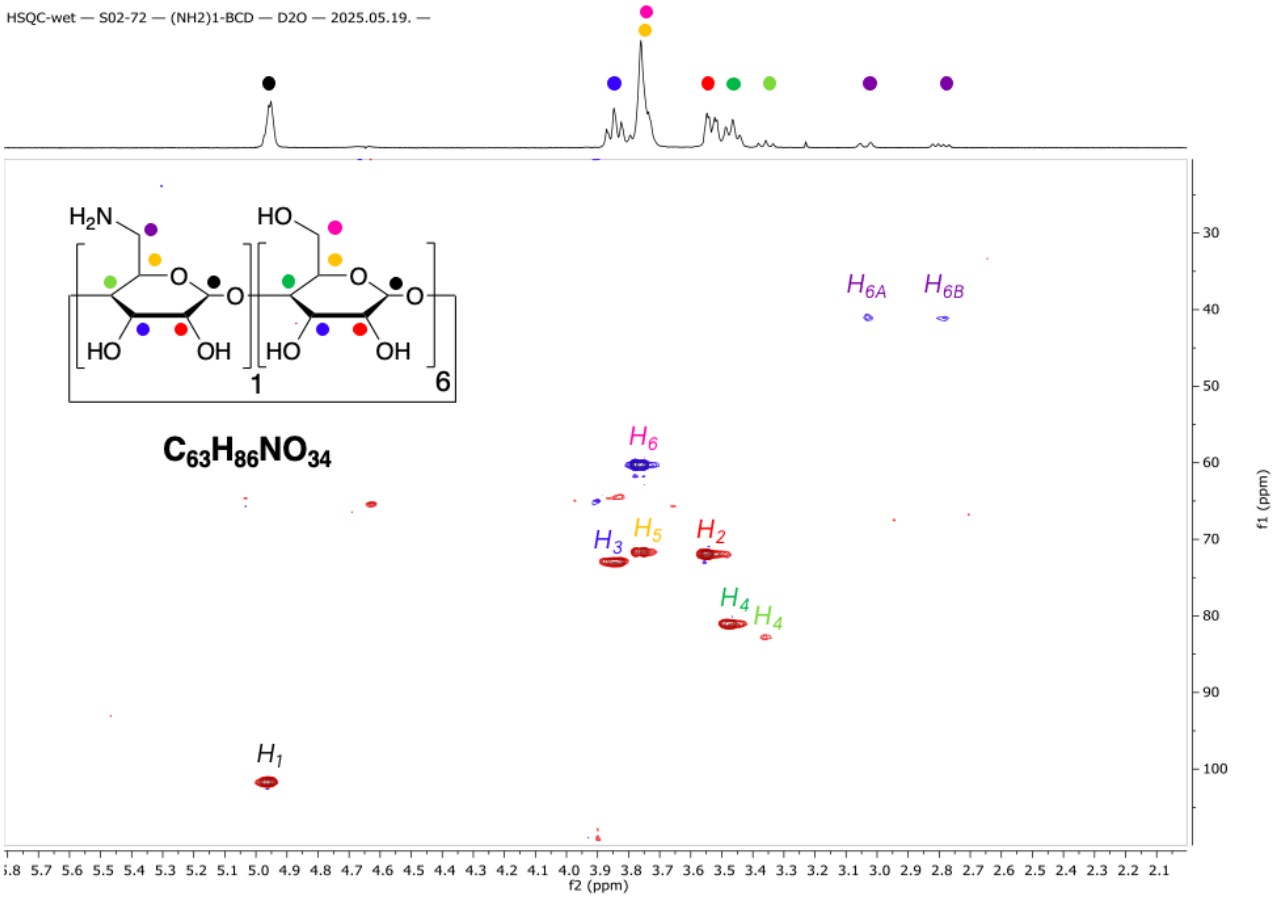

Figure 97: ^{1}H-^{13}C DEPT HSQC NMR spectrum of βCD-$(NH_2)_1$. Data collected using a 400MHz NMR spectrometer, in D_2O. F2 axis: ^{1}H NMR (ppm); F1 axis: ^{13}C DEPT NMR (ppm).

6.5.2. Coupling of fluorescein isothiocyanate to βCD-$(NH_2)_1$

Having obtained the βCD-$(NH_2)_1$ derivative (i.e., m = 7.25 g), we investigated and optimized its conjugation with fluorescein-isothiocyanate (βCD-$(FITC)_1$). The synthetic strategy employed pyridine as both solvent and base to deprotonate the primary amine, thereby enhancing its nucleophilicity toward the electrophilic isothiocyanate group of FITC (Figure 98). Heating the reaction mixture improved the reaction conversion by increasing the solubility of both the βCD derivative and FITC.

Purification was achieved through selective precipitation to remove unreacted FITC and other poorly soluble byproducts. A preliminary small-scale reaction (F1, Table 3) was conducted initially, followed by a larger-scale synthesis (F2, Table 3) to obtain sufficient material for subsequent polymerization studies. Despite optimization efforts, the isolated yield for the scaled-up reaction remained moderate at 39 %. This low yield can be attributed to two main factors: 1) the multiple washing and precipitating steps required to eliminate residual FITC, and 2) thermal degradation of the fluorophore under the elevated temperatures necessary to

dissolve FITC, consistent with previous observations by Malanga *et al.*[279] Any traces of unreacted dye remaining after purification could be efficiently removed following polymerization through dialysis, as FITC and its degradation products are low-molecular-weight compounds that readily pass through a 12 kDa MWCO membrane.

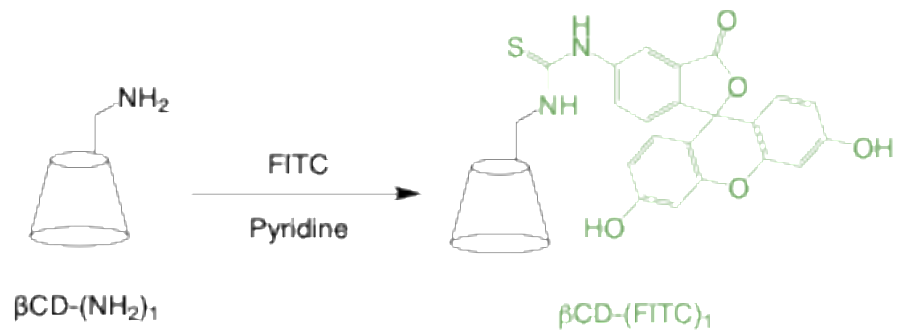

Figure 98: Addition of the fluorescein-isothiocyanate dye on the βCD-$(NH_2)_1$ with pyridine as solvent for the synthesis of the monomer βCD-$(FITC)_1$.

Table 3: Summary of the two F1 and F2 attempts for the addition of the fluorescein-isothiocyanate on βCD-$(NH_2)_1$ monomers in different conditions.

Entry	βCD-$(NH_2)_1$	Δ	Time	Product	Yield
F1	50.9 mg	RT → 60°C	6 h	49 mg	**72 %**
F2	501.2 mg	60°C	3.5 h	261 mg	39 %

The addition of the fluorescent dye is confirmed by ^{1}H NMR analysis (Appendix XXXII). The simultaneous presence of the protons of the cyclodextrin core and the ones on the aromatic rings of the dye (i.e., between 5.9 ppm and 8.25 ppm), and their integration evaluation (i.e., about one proton for each peak between 5.9 ppm and 8.25 ppm), corroborate the expected structure. Also, the presence of the link between fluorescein and cyclodextrin is indicated by a broad singlet near 10.1 ppm, assigned to the NH protons of the thiourea linkage. Furthermore, its low integration (i.e., 0.34) must be due to hydrogen bonding with nitrogen atoms and solvent molecules, such as DMSO and residual water.

6.5.3. Coupling of dansyl chloride to βCD-$(NH_2)_1$

As for the addition of the fluorescein isothiocyanate described above, we performed the synthesis under basic conditions to allow the deprotonation of the amine group of βCD-$(NH_2)_1$, which is required for the addition of dansyl chloride to the nitrogen via an S_N2 (Figure 99). We first investigated the procedure on a small scale with different combinations of bases and

solvents (D1, D2, and D3, Table 4). We increased the base quantity and the reaction temperature to determine the optimal experimental conditions for achieving the highest conversion ratio into βCD-$(DNSA)_1$. In the D1 attempt, the better addition of the dye with pyridine may be due to a competition by the base with the dansyl for the occupation of cyclodextrin cavities, as reported by Malanga *et al.* for the rhodamine B dye.[279] The higher the pyridine equivalent number, the better the competition for the CD cavity, leading to a better addition of the dye on the deprotonated amine. By using DMF as a solvent instead of pyridine (D2, Table 4), the complexation of the dye in the cavities may be worse since DMF cannot form such complexes and consequently leads to a lower addition of the dye. Ultimately, the use of triethylamine (D3, Table 4) was intended to yield greater complexation with CD and, consequently, greater competition with dansyl chloride; however, the dye exhibited limited solubility, and pyridine was necessary to solubilize dansyl. Because of the low conversion ratios observed for D2 and D3 attempts by TLC, we did not pursue further investigation.

Since the reaction with pyridine, as base and solvent, proved to generate the highest conversion ratio into the product (about 70 % of βCD-$(DNSA)_1$), the reaction was then scall up on one gram of the starting material and a similar conversion ratio was reached after five hours of reaction (about 70 % of βCD-$(DNSA)_1$) (D4 attempt, Table 4); however, the purification of the resulting material was challenging to achieved due to the succession of solid-liquid purification, and resulting in a lower yield than the first attempt D1. Furthermore, this lower yield may also be due to the constant high temperature employed all over the reaction time (80 °C for five hours), leading to a possible degradation of the isothiocyanate derivative.[279] We ultimately purified the final product by gel chromatography with a 1,4-dioxane/NH_3/n-propanol (10:7:3) eluant mixture.

Figure 99: Addition of the dansyl chloride dye on the βCD-$(NH_2)_1$ via a nucleophilic substitution for the synthesis of the monomer βCD-$(DNSA)_1$.

Table 4: Summary of the D1, D2, D3, and D4 attempts for the addition of the dansyl dye to βCD-$(NH_2)_1$ monomers in different conditions. No mass product and yield are reported for entries 2 and 3 because of the interruption of reaction investigations.

Entry	βCD-NH_2	Base	Δ	Solvent	Time	Product	Yield
D1	**50.7 mg**	**Py (1→2eq.)**	**RT→80°C**	**Py**	**22h**	**38 mg**	**63%**
D2	49.2 mg	Py (1→2eq.)	RT→60°C	DMF	22h	/	/
D3	50.8 mg	$N(Et)_3$ (1→2eq.)	RT→60°C	DMF	22h	/	/
D4	1.000 g	Py (2eq.)	80°C	Py	5h	146 mg	13 %

The ^{1}H NMR (Appendix XXXIII), and ^{1}H-^{13}C DEPT HSQC (Figure 100) spectra confirmed the successful addition of the dansyl part to the cyclodextrin amine group. Indeed, the methylene proton signal at 3.63 ppm (F2 axis) and 60.38 ppm (F1 axis) exhibits a downfield shift compared to the one in βCD-$(NH_2)_1$ (i.e., 2.80 and 3.00 ppm, respectively (F2 axis), and 40.0 ppm (F1 axis), Figure 97, part 6.5.1.). This deshielding effect indicates a modification of the local electronic environment, consistent with the covalent attachment between the fluorophore unit and the cyclodextrin monomer.[278] It is noteworthy that aromatic signals were not investigated because of the experiment time.

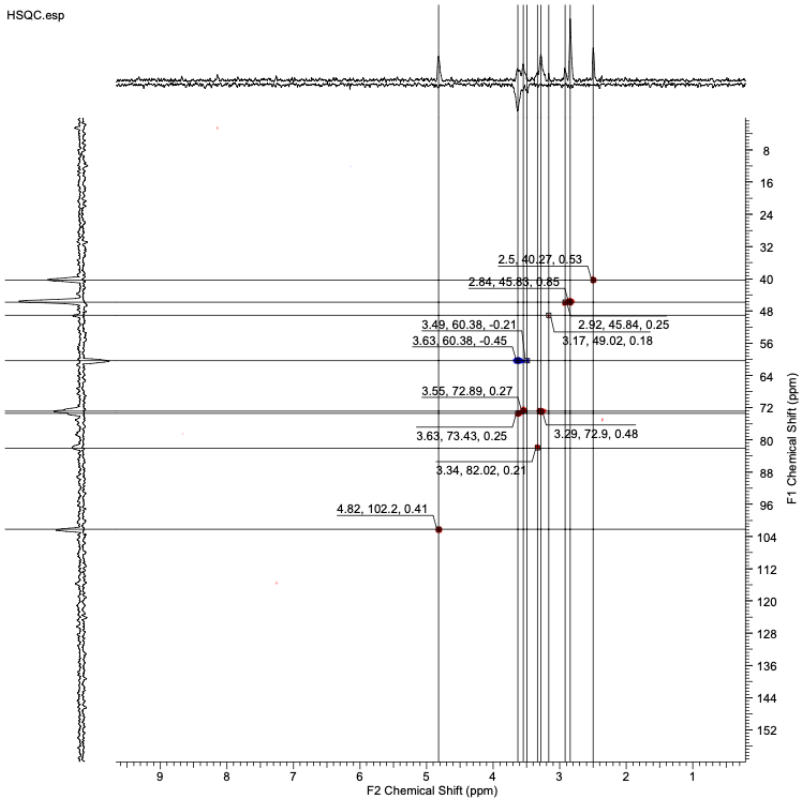

Figure 100: ^{1}H-^{13}C DEPT HSQC NMR spectrum of βCD-$(DNSA)_1$ before column chromatography. Data collected using a 400MHz NMR spectrometer, in DMSO-d6. Cross-peaks are defined by the F2 Chemical Shift (ppm) (^{1}H NMR axis), the F1 Chemical Shift (ppm) (^{13}C DEPT NMR axis), and the intensity, respectively.

6.5.4. Polymerization of the fluorescent labeled βCD monomers

After the synthesis of the βCD-(FITC)$_1$ monomer, we performed the polymerization step using both βCD-(FITC)$_1$ and βCD-(RhBITC)$_1$ monomers at a 1:3 ratio, respectively, combined with neutral βCD monomers. The polymerization is carried out under strongly alkaline conditions to initiate nucleophilic attack on epichlorohydrin, the cross-linking agent (Figure 101).

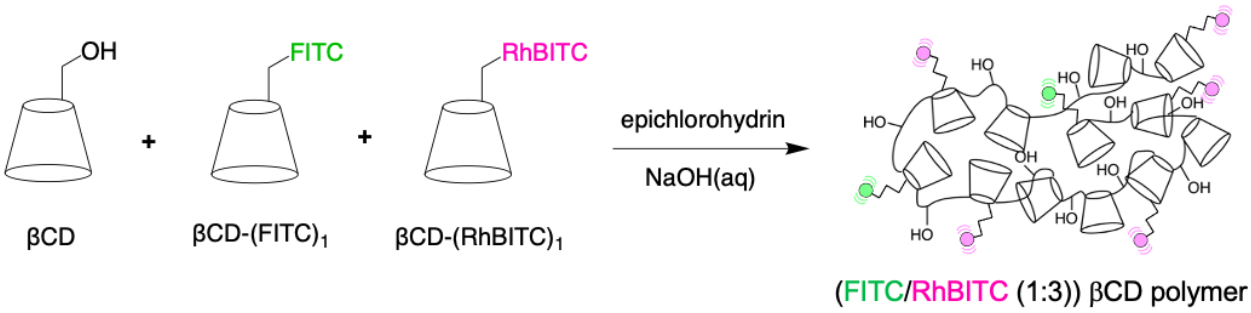

Figure 101: General scheme of the polymerization step from neutral βCDs, βCD-(FITC)$_1$ and βCD-(RhBITC)$_1$ monomers for the formation of a (FITC/RhBITC (1:3)) βCD water soluble polymer.

As reported by Malanga *et al.*, CD polymers cannot be easily monitored by TLC due to their strong interaction of high molecular weight CD polymers with the stationary phase of the TLC plate.[278] Consequently, their syntheses must follow a precise control of the temperature and stirring to obtain a correct branching of the cyclodextrin monomers. Indeed, the reaction must be conducted at 60 °C and under vigorous stirring to promote the controlled formation of the polymer network. Maintaining these two conditions is essential to avoid either over-polymerization, which could result in gelation and loss of material processability, or under-polymerization, which would yield polymeric systems with insufficient size, leading to reduced solubility of the guest molecule in the polymer matrix or to harder templating or stabilization of AuNPs. We synthesized distinct polymers with different combinations of dyes as alternatives to address potential challenges with the fluorescein/rhodamine B fluorophore combination (i.e., FRET between the two dyes); we summarized the results in Table 5. We performed all syntheses directly on a large scale (i.e., 21 grams of starting cyclodextrin monomers), since any scale-down of this polymerization was difficult to implement due to the need for efficient stirring during the reaction to avoid gel formation. We purified all synthesized polymers via dialysis against distilled water for 1 week. We detailed the general procedure for the polymerization in the experimental part.

The labeled βCD-(RhBITC)$_1$, βCD-(FITC)$_1$, and βCD-(DNSA)$_1$ monomers were only added in very small proportions by comparison to the simple βCD monomers (between 10 – 30 milligrams against up to 21 grams respectively) to obtain a suitable fluorescence intensity response (i.e., the intensity maximum must be included between 10^6 and 10^7). After taken in hand the polymerization procedure with the neutral βCD polymer (P1a), we optimized the experimental procedure (i.e., stirring and heating parameters) in a second attempt (P1b, Table 5); however, even if the solution mixture was less viscous due to a better stirring, and a stabler temperature during the synthesis, the polymer yield did not improve. For all polymer syntheses, we achieved yields of about 50 – 60 %. Higher yields seem difficult to achieve, as the auto-polymerization of epichlorohydrin, induced by the opening of the epoxy group in alkaline medium, is difficult to prevent at the high temperature (i.e., T = 60 °C) required for the polymerization of the CD monomers.

After optimization of the procedure, the focus was set on the synthesis of the ratiometric FITC/RhBITC polymer (P2, Table 5). Then, we used βCD-(DNSA)$_1$ monomer to synthesize original βCD polymers: only with DNSA (P3, Table 5), with RhBITC (P4, Table 5), or with the three dyes together (i.e., fluorescein, rhodamine B, and dansyl dyes) (P5, Table 5). For the βCD polymer RhBITC/DNSA (P4), the goal was to provide an alternative to the FITC/RhBITC polymer and to replace fluorescein with DNSA to avoid potential challenges arising from the close emission of fluorescein to the absorption band of rhodamine B. Since we did not perform ratio investigations for the different dye combinations beforehand, it was kept as 1:1. For the three-dye polymer (P5), the goal was to present an original polymer with three different dyes demonstrating a great flexibility in the absorbance window, from the dansyl absorption in the UV window up to the rhodamine B emission window near 600 nm.

Table 5: Summary of polymerizations performed with different combination and ratio of fluorescent CD monomers used.

Entry	Dyes	Ratio	Polymer mass	Yield
P1a	None	/	20.11 g	53 %
P1b			19.65 g	52 %
P2a	**FITC/RhBITC**	**1:3**	**22.16 g**	**59 %**
P2b			21.05 g	56 %
P3	DNSA	/	21.84 g	58 %
P4	RhBITC/DNSA	1:1	23.09 g	61 %
P5	FITC/RhBITC/DNSA	1:1:1	22.38 g	59 %

We characterized the FITC/RhBITC-βCD polymer using UV-Visible spectrometry (Figure 102A). By comparison with the mixture of the two RhBITC-βCD and FITC-βCD polymers at the same concentration, the absorbance spectrum of the FITC/RhBITC-βCD polymer is lower (i.e., for a concentration of 2.00 mg.mL^{-1}, at λ = 552 nm, A = 0.0859; while the absorbance mixture of both fluorescent polymers is at A = 0.4052). To achieve the same absorbance intensity (for a final polymer mixture concentration of 2.00 mg.mL^{-1}), the bifunctionalized fluorescein/rhodamine B (1:3) polymer concentration must be close to 11.78 mg.mL^{-1} (Figure 102B). We must perform further characterization of the synthesized polymers (with NMR, IR (Infrared), DLS, TG-MS (Thermal Gravimetric Mass Spectroscopy), viscosity, emission spectrum, and fluorescence lifetime).

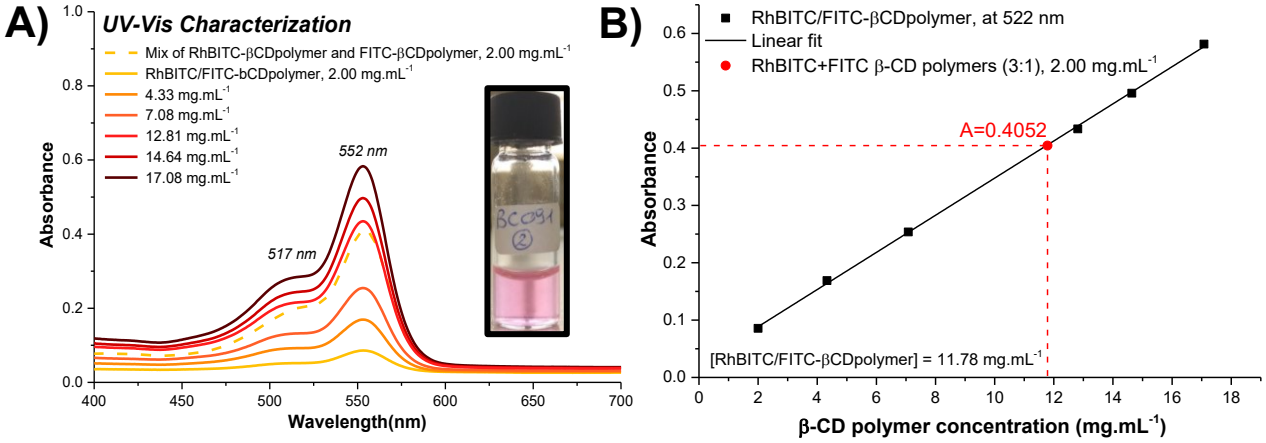

Figure 102: A) Comparison of the UV-Visible absorption spectra of FITC/RhBITC-βCD polymer at different concentrations (plain lines) compared to a mixture of RhBITC-βCD polymer and FITC-βCD polymer (dotted line) at 2.00 mg.mL^{-1}, at a 1:3 ratio, respectively, in a PBS solution. The inset shows a picture of the sample at a 12.81 mg.mL^{-1} concentration of the FITC/RhBITC-βCD polymer. Measurements were performed in a 1 cm path-length cuvette, using a PerkinElmer UV-Vis spectrophotometer, using air as the blank. B) Evolution of the absorbance in function of the concentration of the FITC/RhBITC-βCD polymer at 522 nm. At the same absorbance value, the concentration of the bi-labeled FITC/RhBITC βCD polymer is reported

6.6. Conclusion

After the successful results obtained during photothermal biological studies of AuNPs from curcumin and indigo carmine oxidation (parts 4.3. and 5.3.), we work on the elaboration of a fluorescent, bi-labeled thermometer to monitor the temperature of the target *in vivo*. However, because of the strong absorbance of curcumin and indigo carmine, a new green synthesis of AuNPs, this time from nitric oxide radical as a green reducing agent, was investigated. Even though the S-nitrosoglutathione, as a NOPD, did not allow for the formation of gold

nanoparticles. Instead, nitroaniline-adamantane, as a nitric oxide photodonor under blue light irradiation, did demonstrate the selective formation of gold nanoworms. Further investigations (i.e., DLS, photothermal studies under NIR irradiation, SEM, AFM, and Zeta potential) must be performed to accurately assess their properties for biological applications. However, by comparison to the precedent syntheses from curcumin and indigo carmine's systems, no clear LSPR band was observed in the NIR region. We must investigate improvements to the synthesis (i.e., replacing the neutral βCD polymer with the cationic QAβCDPS and varying the NA-Ad/Au ratio) to obtain gold nanoparticles with better NIR light absorption.

To develop a ratiometric fluorescent thermometer, the focus was on determining an optimal dye ratio to easily monitor fluorescence intensity evolution as temperature rises. A FITC/RhBITC (1:3) dye combination was chosen, with fluorescein as reference and rhodamine B as sensitive probe, with a relative sensitivity S_r equal to -1.03 %. K^{-1} between 35 and 50 °C.

Next, the design and achievement of multi-step syntheses of novel fluorescent epichlorohydrin branched βCD-based polymers was performed under the supervision of Dr Milo Malanga at CarboHyde. We prepared fluorescent monomers βCD-$(FITC)_1$ and βCD-$(DNSA)_1$ via a multi-step synthesis: βCD-$(N3)_1$ was reduced to βCD-$(NH_2)_1$, and then fluorescein isothiocyanate or dansyl chloride was added. The targeted polymer, (FITC/RhBITC)-βCD polymer (1:3), was obtained with a yield of 59 % and in large quantity (m = 22.16 g) to pursue further investigations. Besides, we synthesized four other novel βCD polymers with very satisfying yields of approximately 50 – 60%, yielding roughly the same polymer mass. Further investigations into the characterization (i.e., NMR, IR, DLS, TG-MS, viscosity, emission spectrum, and fluorescence lifetime) of the synthesized βCD polymers are needed before their use as templating and stabilizing agents in gold nanoparticle synthesis.

Then, studies will focus on the synthesis and complete characterization (i.e., UV-Vis, DLS, Zeta potential, TEM, SEM (Scanning Electron Microscopy), AFM, emission spectrum, fluorescence lifetime) of these gold nanosystems with these novel βCD polymers synthesized at CarboHyde. Investigations must also be pursued into the loading of a red-absorbing photosensitizer, such as zinc phthalocyanine, and into the generation of singlet oxygen for a multimodal PTT/PDT biological application. Finally, after taking care of the stability and the performances of the photothermal agent and the photosensitizer, investigations will be performed on the relative sensitivity of the fluorescence intensity of the system, first in a fluorescence cuvette, then *in vivo* during photothermal irradiation alone, and then in the company of the PS for the release of the transient species heat and $^1O_2$.

6.7. Experimental part

Methods:

High synthetic-purity grade solvents (i.e., methanol, ethanol, acetonitrile, and n-propanol) were used. The solutions were prepared in ultrapure (Milli-Q) water or in PBS buffer. The PBS buffer was prepared by adding one phosphate-buffered saline tablet to 100 mL of extra pure water (10 mM). After solubilization of the tablet, the pH is measured with a pH meter (inoLab): (T = 27 °C) pH = 7.45. The fluorescence cuvettes (1 cm path-length, 3 mL capacity) and absorbance cuvettes (1 mm path-length and 1 cm path-length, 3 mL capacity) were cleaned before each experimentation with *aqua regia*.

The Phosphate Buffered Saline tablet was purchased from VWR Life Science. The βCD polymer, the quaternary ammonium βCD polymer (QAβCDPS), the FITC-βCD polymer, and the RhBITC-βCD polymer were prepared by Cyclolab and used without purification. Tetrachloroauric (III) acid trihydrate ($HAuCl_4 \bullet 3H_2O$) (≥99.9% trace metals basis) ($C = 5.08 \times 10^{-1}$ M), indigo carmine, reduced L-glutathione (≥98.0%), $NaNO_2$, adamantylamine, 4-fluoro-1-nitro-2-(trifluoromethyl)benzene, and (±)-Epichlorohydrin (≥99.0%) were purchased from Sigma Aldrich. βCD-$(NH_2)_1$ and βCD-$(RhBITC)_1$ were prepared by CarboHyde.[279] $N_2H_4 \bullet H_2CO_3$, Na_2CO_3, pyridine, and triethylamine were purchased from Molar Chemicals KFT. Fluorescein 5(6)-isothiocyanate (≥90.0%) and dansyl chloride were purchased from Fluka.

Instrumentation:

Irradiations of the samples were carried out in a 1 cm path-length fluorescence quartz cuvette (3 mL capacity) using either 405 or 532 nm continuum-wave lasers (*ca.* 6, 12, or 15 $W.cm^{-2}$) with a beam diameter of *ca.* 1.5 mm, or a 528 nm lamp (*ca.* 1 $mW.cm^{-2}$). Absorbance spectra were measured using a 1 mm length quartz cuvettes or a 1 cm path-length absorbance quartz cuvette (3 mL capacity), either using a PerkinElmer Lambda 365 UV-Vis spectrophotometer (Measurement window: from 180 to 1100 nm; SBW: 1.0; Data interval: 0.5 nm; Scan rate: 300 $nm.min^{-1}$) or using a Jasco V-560 UV-Vis spectrophotometer (Measurement window: from 180 to 800 nm).

The fluorescence was recorded with a Spex Fluorolog-2 (mod. F-111) spectrofluorometer using quartz cuvettes with a path-length of 1 cm.

The pH values were measured with an inoLab pH meter at room temperature (T = 25 °C). The instrument was calibrated before each measure by two buffer solutions at pH = 7.00 and pH = 4.01.

•NO release was performed by amperometric detection with a World Precision Instrument, ISO-NO meter, equipped with a data acquisition system, and based on direct amperometric detection of NO with short response time (< 5 s) and sensitivity range (1 nM – 20 µM). The analogue signal was digitized with a four-channel recording system and transferred to a computer. NO measurements were carried out without stirring, with the electrode positioned outside the light path to avoid NO signal artefacts caused by photoelectric interference on the ISO-NO electrode.

Synthesis of βCD-$(NH_2)_1$: Inside a 4-neck 500mL flask, 6-monoazido-6-monodeoxy-βCD (10.03 g, 8.63 mmol) is solubilized in 200 mL of distilled water and n-propanol (50 mL). The solution is stirred (250 rpm), Pd/C (10 %) (280 mg), and then N_2H_4•H_2CO_3 (17 mL) is added dropwise into the solution. The solution is heated to reflux (from 30 to 120°C), and its evolution is checked by TLC (1,4-dioxane/NH_3 (10:7)) at the start and then every 15 minutes of reaction time. After 2 h 30, the reaction is cooled down with a cold-water bath. The pH medium of the reaction is then measured, pH = 8 – 9. Pd/C is then filtered and washed with a small volume of water. The solvent is evaporated under reduced pressure, and 25 mL of water is added and evaporated twice to eliminate the hydrazine. The resulting white solid is then solubilized in MeOH (80 mL) and filtered using a Büchner funnel; the mixture is washed six times with MeOH (10 mL). The resulting white solid is poured into a 100 mL flask and solubilized in water (40 mL); then HCl is added dropwise until pH = 5 is reached. The Pd/C remaining (i.e., from precedent filtration) is filtered with a membrane filter. The resulting mixture is concentrated under reduced pressure. An ammonia solution is added dropwise to reach pH = 10. 30 mL of MeOH is then added, and the precipitate is filtered and washed twice with MeOH (10 mL). The resulting white solid is then dried under reduced pressure. Its purity is checked by TLC (1,4-dioxane/NH_3 (10:7)). **m = 7.27 g; yield: 75 %. ^{1}H NMR** (400 MHz, D_2O): δ 4.96 (m, 7H, 7xCH), 3.87 (m, 7H, 7xCH), 3.76 (m, 18H), 3.49 (m, 14H, 14xCH), 3.34 (t, 1H, CH), 3.04 (dd, 1H, CH2), 2.80 (dd, 1H, CH2).

Synthesis of βCD-$(FITC)_1$: Inside a 12 mL flask, 6-monoamino-6-monodeoxy-βCD (50.9 mg, $4.5x10^{-5}$ mol) and FITC (19.5 mg, $5.00x10^{-5}$ mol) are solubilized in 3.6 mL of pyridine. The yellow solution is stirred at 500 rpm, and the evolution of the reaction is checked by TLC (1,4-dioxane/NH_3 (10:7)). After 3h of reaction at RT, the mixture is heated up to 60 °C for 3 hours. Then, the reaction is cooled down at RT, the pH is checked (pH = 6 – 7), and the solution is concentrated under reduced pressure. The resulting mixture is then solubilized in acetone (7

mL). The orange precipitate is then filtered by Büchner (porosity: 3) and washed 3 times with acetone (2.5 mL). The resulting orange solid is then dried under reduced pressure. Its purity is checked by TLC (1,4-dioxane/NH_3 (10:7)). **m = 49 mg; yield: 72 %. ^{1}H NMR** (400 MHz, DMSO-d6): δ 8.26 (s, 1H, *Ar*), 7.9 (d, 1H, *Ar*), 7.64 (m, 1H, *Ar*), 7.18 (m, 1H, *Ar*), 6.74 (d, 1H, *Ar*), 6.28 (m, 1H, *Ar*), 5.92 (m, 1H, *Ar*), 5.74 (m, 14H, 7xCH_2), 4.82 (m, 7H, 7xCH), 3.65 (m, 14H, 14xCH), 3.32 (m, 14H, 14xCH).

Synthesis of βCD-(DNSA)$_1$: Inside a 3-neck 250 mL flask, 6-monoamino-6-monodeoxy-βCD (1 g, 8.83x10^{-4} mol) and dansyl chloride (263.3 mg, 9.76x10^{-4} mol) are solubilized in 68 mL of pyridine. The pale-yellow solution is stirred at 500 rpm, heated at 80°C, and the evolution of the reaction is checked by TLC (1,4-dioxane/NH_3 (10:7)). After 5 hours, the reaction is cooled down at RT and stirred for 4 days. The mixture is poured into a 100 mL flask and concentrated under reduced pressure. Then, a white solid is precipitated by the addition of acetonitrile (10 mL), filtered by Büchner (porosity: 3), and washed eight times with MeCN (5 mL) and once with DCM (10 mL). The resulting pale-yellow solid is purified by column chromatography (eluant: 1,4-dioxane/NH_3/n-propanol (10:7:3)), and then dried under reduced pressure. Its purity is checked by TLC (1,4-dioxane/NH_3 (10:7)). **m = 146 mg; yield: 13 %. ^{1}H NMR** (400 MHz, DMSO-d6): δ 8.41 (d, 1H, *Ar*), 8.28 (d, 1H, *Ar*), 8.15 (d, 1H, *Ar*), 7.56 (m, 2H, *Ar*), 7.24 (d, 1H, *Ar*), 5.70 (m, 14H, 7xCH_2), 4.83 (m, 7H, 7xCH), 3.64 (m, 14H, 14xCH), 3.34 (m, 14H, 14xCH).

Synthesis of (RhBITC/FITC (3:1)) βCD polymer crosslinked with epichlorohydrin: In a 3-neck 250 mL flask, NaOH (8.1 g) and βCDs (20.957 g, 1.85x10^{-2} mol) are solubilized in 50 mL of distilled water under stirring at 720 rpm. After full solubilization, βCD-(FITC)$_1$ (10.3 mg, 6.73x10^{-6} mol) is added, turning the solution from uncolored to yellow; after the addition of βCD-(RhBITC)$_1$ (34.4 mg, 2.10x10^{-5} mol), the mixture color turns to pink/purple. The temperature is set to 64 °C, and the epichlorohydrin (14.5 mL, 1.85x10^{-1} mol) is added dropwise for 2 hours. The stirring is increased up to 900 rpm and the temperature is set to 67 °C. After 2 hours, the red mixture is cooled down to RT, and the stirring is stopped. The solution is neutralized with HCl (3N) addition to reach pH 6 – 7. The mixture is purified by dialysis against deionized water for one week. The solvent is then evaporated under reduced pressure, resulting in a solid. **m = 22.16g; yield: 59 %.**

Synthesis of NA-Ad: In a 100 mL flask, 240 µL of NA (1.72 mmol, 1.02 eq.), 253.50 mg of Ad-NH_2 (1.68 mmol, 1 eq.), and 890 mg of Na_2CO_3 (8.40 mmol, 5 eq.) are solubilized in 50 mL of acetonitrile in dark conditions under stirring. After 10 hours, the solution colour turned from light-

yellow to yellow. The reaction is followed by TLC (cyclohexane/ethyl acetate (80:20) (R_f = 0.71). The Na_2CO_3 is filtered with a Büchner funnel, and the mixture is concentrated under reduced pressure with a temperature bath set at 28°C. After solubilization in 50 mL of DCM, the solution is washed with water (1 x 20 mL). The organic layer is dried with $MgSO_4$ and filtered with glass wool. The mixture is purified with column chromatography (cyclohexane 100 %, and then cyclohexane/ethyl acetate: 95:05 at first, then 90:10 and 80:20, and ultimately MeOH 100 %). The solvent is evaporated under reduced pressure. The product obtained is a yellow solid. **m = 93 mg; yield:16%. ^{1}H NMR** (500 MHz, $CDCl_3$): δ 7.98 (d, 1H, *Ar*), 6.95 (d, 1H, *Ar*), 6.80 (dd, 1H, *Ar*), 4.48 (s, 1H, N*H*), 2.20 (m, 3H, 3xC*H*), 2.00 (d, 6H, 3xCH_2), 1.76 (q, 6H, 3xCH_2). **^{13}C NMR** (500 MHz, $CDCl_3$): δ 44.89 (CH), 38.85 (CH), 32.14 (6x*C*H_2); **^{19}F NMR** (500 MHz, $CDCl_3$): δ -60.58 (3F, C*F*$_3$). **MS:** calculated for $C_{17}H_{19}F_3N_2O_2$ [M+H]+: found 338.53.

Preparation of a solution of NA-Ad in MeOH: A mother solution in methanol of NA-Ad is prepared from 5 milligrams of the yellow solid. After absorbance measurement in a 1 cm cuvette using a Perkin UV-Vis spectrophotometer, a daughter solution from a factor-3 dilution is prepared with A = 1. The absorbance is checked once again.

βCD-polymer solution preparation: The mass of βCD polymers used was measured with a Sartorius analytical balance, and then solubilized in Milli-Q water. The solution was magnetically stirred for 20 minutes with IKA Topolino at medium velocity at room temperature (T = 25 °C).

Preparation of the solution NA-Ad+βCDpolymer: 4 mL of the daughter solution NA-Ad in MeOH is evaporated with a nitrogen flux. Then, 4 mL of the solution of βCD polymer in PBS is poured on the film of NA-Ad. The absorbance is measured over time to monitor the loading of the NA-Ad in the polymer.

Preparation and irradiation of the system NA-Ad+βCDpolymer+Au: $HAuCl_4$•$3H_2O$ (C = 0.5 M) is added in the NA-Ad+βCDpolymer+Au solution in 2 samples of 2 mL each: the first one was irradiated with a 405 nm laser (*ca.* 6 W.cm^{-2}) at 5 cm from the laser without any cover; the other sample was kept in dark conditions as a control. Then, each sample was stirred, and the absorbance evolution was followed. $HAuCl_4$•$3H_2O$ was added to the NA-Ad+(βCDpolymer) solution, 44 hours after polymer addition.

Photothermal studies: Irradiations during photothermal studies were performed with a continuum-waves laser, at λ_{exc} = 532 nm (*ca.* 6, 12, or 15 W.cm^{-2}) with a beam diameter of *ca.* 1.5 mm. Samples (150 or 200 µL) were irradiated in an NMR tube. The thermal evolution was

captured with a FLIR C3 thermal imaging camera, with temperatures reported every twenty seconds. Three cycles of measures were performed in a row for each sample. Thermal pictures of the sample were taken at the beginning and the end of each irradiation cycle. The measurements were performed at room temperature (T = 18 or 25 °C), depending on the time of the year. Thermal pictures of the measurements were modified with FLIR software and presented with a linear color scale of temperature.

Photothermal study in fluorimeter: The irradiation was performed with a continuum-wave laser (*ca.* 6 $W.cm^{-2}$) at λ_{exc} = 532 nm with a beam diameter of *ca.* 1.5 mm. The sample (1 mL) was irradiated inside the Fluorolog-2 spectrofluorometer. The capture of the thermal evolution was done with a thermal imaging camera FLIR C3. The measurements were performed at T = 30 °C. Thermal pictures of the measurements were modified with FLIR software and presented with a linear color scale of temperature.

Measurements of fluorescence with evolution of the temperature: The emission spectra were recorded at room temperature, and the fluorescence evolution was observed with a rise in temperature from 20 °C to 70 °C. Sample temperatures were also manually measured with a TRACEABLE thermometer and a FLIR thermal camera. Absorbance spectra of the systems were recorded before fluorescence spectra were measured with the spectrofluorometer Fluorolog.

TEM samples and images were prepared and captured by Philippe Elies from the University of West Brittany

7. General Conclusion

Throughout this work, we investigated various green synthesis methodologies for anisotropic gold nanoparticles for multimodal therapeutic applications in view of biological applications.

Anisotropic gold particles are highly relevant for achieving photo-induced thermal degradation of cancerous cells and bacteria in deep tissues. The LSPR band of these nanoparticles can be tuned, allowing AuNPs to absorb light in a biological window in the near-infrared region, a wavelength range where light can penetrate superficial tissues. In sight of the biological applications, the goal was to synthesize these particles in accordance with green chemistry principles using green reactants.

We investigated the use of different green reducing agents for the reduction of the gold precursor and the influence of their irradiation on the synthesis of gold nanoparticles. In the fourth and fifth chapters, we investigated two plant extracts, namely curcumin and indigo carmine, and in the sixth chapter, two nitric oxide photodonor compounds (i.e., S-nitrosoglutathione and nitroaniline-adamantane). Furthermore, we investigated the fabrication and synthesis of a fluorescent thermometer with a view to *in vivo* photothermal therapy applications.

7.1. With Curcumin, a plant extract, as reducing agent

This orange dye exhibits interesting properties and a promising response to light irradiation. When excited, the goal was to take advantage of the ketyl radical to induce the reduction of the gold precursor and control AuNPs synthesis.

However, the syntheses involving this dye were challenging. Indeed, because of its low solubility in aqueous medium, the presence of the keto-enol tautomerism, a pH-dependent equilibrium, made the syntheses difficult to master and led to many inaccuracies. After extensive work on adjusting the pH of the solution, the nature of the βCD polymer, and the gold/curcumin ratio, we achieved the formation of gold nanotriangles. Their irradiation in the NIR demonstrated a satisfying rise of the temperature up to $\Delta T = 16 – 17$ °C after about fifteen minutes of light exposure.

In vitro studies were performed in collaboration with Inserm in Brest, France. The gold nanosystem derived from curcumin reduction was investigated in two bacterial strains, *E. coli* and *P. aeruginosa*, and in non-cisplatin-resistant and cisplatin-resistant ovarian cancer cells. The formulations demonstrated satisfactory cytotoxicity against *E. coli* and cisplatin-resistant cells with only 3 minutes of irradiation.

To enhance the cytotoxicity of the nanosystem upon irradiation, we extended the research to include the addition of a photosensitizer for photodynamic therapy. We investigated different photosensitizers for a bimodal approach. However, only the THPP reported a correct loading in the polymer matrix of the nanosystem. Irradiation of the PS in the blue region showed a slight phosphorescence from singlet oxygen. Further studies with flash spectroscopy confirmed the successful formation of singlet oxygen with the presence of the transient species of THPP in solution. Furthermore, the presence of the PS did not affect the photothermal properties of the gold nanotriangles.

Next, we plan to investigate the synthesis of AuNPs via curcumin oxidation. We want to optimize the procedure (i.e., achieved by a better control of the tautomeric equilibria) to obtain reproducible anisotropic AuNPs (i.e., reproducible size and shape), needed to assess correctly the photothermal biological results. We hypothesize that a reproducible nanoparticle shape can be achieved by further optimization of the pH value of the medium.

Moreover, investigations must be pursued into the photothermal properties of the photothermal agent in the presence of the photosensitizer to assess the stability of the PS agent under irradiation and heat. Next, to release both therapeutic agents (i.e., heat and singlet oxygen) via a single-wavelength irradiation of the system, we plan to investigate the incorporation of an NIR-absorbing photosensitizer. A possible approach can be the modification of the βCD polymer to link the PS to the branches of the polymer covalently.

Finally, a new approach to multimodal therapy can be employed by incorporating a cisplatin drug into cyclodextrin's cavity to enhance the antitumoral properties of the system.

7.2. With Indigo Carmine, a plant extract analogue, as reducing agent

The approach with this blue, water-soluble dye was the same as for the curcumin approach. Despite a more straightforward synthesis, the formed anisotropic AuNPs exhibited a significant loss of anisotropy over time. Another inconvenience of using indigo carmine was the lack of shape selectivity in the resulting gold nanoparticles, leading to different populations of gold nanorods, gold nanotriangles, and, mainly, gold nanospheres. Despite these various shapes, since the goal is to irradiate in the biological window, large wavelength ranges with different shapes can be an advantage, offering a versatile approach to the irradiation wavelength. Using AFM characterization, we found that the βCD polymer matrix was wrapped around gold particles with a size of 20 – 30 nm.

The photothermal properties of these particles are satisfactory with a rise of the temperature up to ΔT = 27 – 28 °C when irradiated in the green region, and up to ΔT = 11 – 12 °C when irradiated in the near infrared region.

The *in vitro* assays demonstrated a significant decrease in the bioluminescence of the *E. coli* strain for the formulation under irradiated conditions. Against cisplatin-resistant ovarian cancer cells, we achieved a 50% reduction in viability. As described for the NPs including curcumin, these nanoparticles offer the possibility to incorporate a photosensitizer for a dual PTT/PDT treatment, but we also consider the possibility to load the particle with a conventional drug such as cisplatin to overcome the MDR resistance observed with some cancer cell lines.

With indigo carmine, future investigations will be focused on the improvement of the stability of the anisotropy characteristic of yielded gold nanoparticles. And as for curcumin's system, research work will be pursued on the incorporation of an NIR-absorbing photosensitizer in the polymer matrix, to achieve a bimodal therapeutic strategy with a single-wavelength irradiation of the nanosystem.

7.3. With a ratiometric fluorescent thermometer

In light of the biological applications of anisotropic gold nanoparticles for PTT, we developed a ratiometric fluorescent thermometer to monitor temperature evolution during photothermal activity. In that context, we chose to work with two different fluorophores: rhodamine B, a sensitive fluorophore, and fluorescein, a stable one. After a significant preliminary work to establish the influence of each part of the nanosystem on the relative fluorescence sensitivity of the dyes, we then defined a satisfactory ratio of chromophores, FITC/RhBITC (1:3), to achieve a satisfactory fluorescence intensity response over temperature elevation.

Because of the strong absorbance of both curcumin and indigo carmine, and their challenging syntheses of AuNPs, we investigated nitric oxide photodonors as new reducing agents (i.e., S-nitrosoglutathione and nitroaniline-adamantane). As a result, the irradiation of the solution with the nitric oxide photodonor nitroaniline-adamantane led to the selective formation of gold nanoworms under blue light irradiation.

We performed the synthesis of the new βCD polymer in collaboration with CarboHyde, under the supervision of Milo Malanga, in Budapest, Hungary. After the synthesis of the different monomeric dyes βCD-$(FITC)_1$ and βCD-$(DNSA)_1$, up to four different polymers were synthesized with a general satisfying yield of 50 – 60 %. The research work should focus on

the characterization of the synthesized polymer and on the synthesis of AuNPs via irradiation of NA-Ad, with the original βCD polymer incorporating both RhB and fluorescein. This work will be continued by performing measurements of the temperature elevation induced by the irradiation of the AuNPs in the cuvette cell and ideally *in vitro* using fluorescent imaging.

8. References

1 B. E. Wilson, S. Jacob, M. L. Yap, J. Ferlay, F. Bray and M. B. Barton, *Lancet Oncol.*, 2019, **20**, 769–780.

2 G. Ioele, M. Chieffallo, M. A. Occhiuzzi, M. De Luca, A. Garofalo, G. Ragno and F. Grande, *Molecules*, 2022, **27**, 5436.

3 H. Nikaido, *Annu. Rev. Biochem.*, 2009, **78**, 119–146.

4 M. R. W. Brown and P. Gilbert, *J. Appl. Bacteriol.*, 1993, **74**, 87S-97S.

5 P. Anastas and N. Eghbali, *Chem Soc Rev*, 2010, **39**, 301–312.

6 B. Hildebrandt, *Crit. Rev. Oncol. Hematol.*, 2002, **43**, 33–56.

7 S. C. Meredith, *Ann. N. Y. Acad. Sci.*, 2006, **1066**, 181–221.

8 H. H. Kampinga, J. F. Brunsting, G. J. J. Stege, P. W. J. J. Burgman and A. W. T. Konings, *Exp. Cell Res.*, 1995, **219**, 536–546.

9 H. Li, H. Jin, W. Wan, C. Wu and L. Wei, *Nanomed.*, 2018, **13**, 1639–1656.

10 C. Wu, H. Li, H. Zhao, W. Zhang, Y. Chen, Z. Yue, Q. Lu, Y. Wan, X. Tian and A. Deng, *Nanoscale Res. Lett.*, 2014, **9**, 447.

11 A. E. Caccamo, S. Desenzani, L. Belloni, A. F. Borghetti and S. Bettuzzi, *J. Cell. Physiol.*, 2006, **207**, 208–219.

12 X. Bai, Y. Wang, Z. Song, Y. Feng, Y. Chen, D. Zhang and L. Feng, *Int. J. Mol. Sci.*, 2020, **21**, 2480.

13 A. Andreozzi, L. Brunese, M. Iasiello, C. Tucci and G. P. Vanoli, *Ann. Biomed. Eng.*, 2019, **47**, 676–693.

14 G. Hannon, F. L. Tansi, I. Hilger and A. Prina-Mello, *Adv. Ther.*, 2021, **4**, 2000267.

15 L. Ma, Y. Zhou, Z. Zhang, Y. Liu, D. Zhai, H. Zhuang, Q. Li, J. Yuye, C. Wu and J. Chang, *Sci. Adv.*, 2020, **6**, eabb1311.

17 D. Jaque, L. Martínez Maestro, B. del Rosal, P. Haro-Gonzalez, A. Benayas, J. L. Plaza, E. Martín Rodríguez and J. García Solé, *Nanoscale*, 2014, **6**, 9494–9530.

18 B. C. Wilson and R. A. Weersink, *Photochem. Photobiol.*, 2020, **96**, 219–231.

19 B. V. Harmon, A. M. Corder, R. J. Collins, G. C. Gobé, J. Allen, D. J. Allan and J. F. R. Kerr, *Int. J. Radiat. Biol.*, 1990, **58**, 845–858.

20 Y. K. Kim, E. B. Kang, S. M. Kim, C. P. Park, I. In and S. Y. Park, *ACS Appl. Mater. Interfaces*, 2017, **9**, 3192–3200.

21 G. Guan, K. Y. Win, X. Yao, W. Yang and M. Han, *Adv. Healthc. Mater.*, 2021, **10**, 2001158.

22 U. Stein, B. Rau, P. Wust, W. Walther and P. M. Schlag, *Int. J. Cancer*, 1999, **80**, 5–12.

23 Y. Yang, L. Ma, C. Cheng, Y. Deng, J. Huang, X. Fan, C. Nie, W. Zhao and C. Zhao, *Adv. Funct. Mater.*, 2018, **28**, 1705708.

24 P. Patel, N. V. Patel and S. F. Danish, *J. Neurosurg.*, 2016, **125**, 853–860.

25 M. Gertner, M. Haider and R. Weersink, .

26 X. Qi, Y. Xiang, E. Cai, X. Ge, X. Chen, W. Zhang, Z. Li and J. Shen, *Coord. Chem. Rev.*, 2023, **496**, 215426.

27 R. S. Riley and E. S. Day, *WIREs Nanomedicine Nanobiotechnology*, 2017, **9**, e1449.

28 X. Huang and M. A. El-Sayed, *J. Adv. Res.*, 2010, **1**, 13–28.

29 S. A. Sapareto and W. C. Dewey, *Int. J. Radiat. Oncol.*, 1984, **10**, 787–800.

30 F. Helmchen and W. Denk, *Nat. Methods*, 2005, **2**, 932–940.

31 P. N. Tonolli, C. M. Vera Palomino, H. C. Junqueira and M. S. Baptista, *J. Photochem. Photobiol. B*, 2023, **243**, 112703.

32 M. Overchuk, R. A. Weersink, B. C. Wilson and G. Zheng, *ACS Nano*, 2023, **17**, 7979–8003.

33 Y. Cai, Z. Wei, C. Song, C. Tang, W. Han and X. Dong, *Chem. Soc. Rev.*, 2019, **48**, 22–37.

34 L. O. Svaasand, C. J. Gomer and E. Morinelli, *Lasers Med. Sci.*, 1990, **5**, 121–128.

35 A. Roggan, M. Friebel, K. Dörschel, A. Hahn and G. Müller, *J. Biomed. Opt.*, 1999, **4**, 36.

36 A. Vogel and V. Venugopalan, *Chem. Rev.*, 2003, **103**, 577–644.

37 A. Juzeniene, K. P. Nielsen and J. Moan, *J. Environ. Pathol. Toxicol. Oncol.*, 2006, **25**, 7–28.

38 R. Fernando, J. Downs, D. Maples and A. Ranjan, *Pharm. Res.*, 2013, **30**, 2709–2717.

39 J.-L. Li, B. Tang, B. Yuan, L. Sun and X.-G. Wang, *Biomaterials*, 2013, **34**, 9519–9534.

40 C. Guo, Y. Jin and Z. Dai, *Bioconjug. Chem.*, 2014, **25**, 840–854.

41 T. Curry, R. Kopelman, M. Shilo and R. Popovtzer, *Contrast Media Mol. Imaging*, 2014, **9**, 53–61.

42 H. S. Jung, P. Verwilst, A. Sharma, J. Shin, J. L. Sessler and J. S. Kim, *Chem. Soc. Rev.*, 2018, **47**, 2280–2297.

43 A. S. Karakoti, L. L. Hench and S. Seal, *JOM*, 2006, **58**, 77–82.

44 L. Wang, C. Hu and L. Shao, *Int. J. Nanomedicine*, 2017, **12**, 1227–1249.

45 S. Kamat and M. Kumari, *Front. Microbiol.*, 2023, **14**, 1102615.

46 Y. N. Konan-Kouakou, R. Boch, R. Gurny and E. Allémann, *J. Controlled Release*, 2005, **103**, 83–91.

47 G. Mie, *Ann. Phys.*, 1908, **330**, 377–445.

48 K. L. Kelly, E. Coronado, L. L. Zhao and G. C. Schatz, *J. Phys. Chem. B*, 2003, **107**, 668–677.

49 S. Link, C. Burda, Z. L. Wang and M. A. El-Sayed, *J. Chem. Phys.*, 1999, **111**, 1255–1264.

50 P. K. Jain, X. Huang, I. H. El-Sayed and M. A. El-Sayed, *Acc. Chem. Res.*, 2008, **41**, 1578–1586.

51 C. F. Bohren, *Am. J. Phys.*, 1983, **51**, 323–327.

52 A. O. Govorov and H. H. Richardson, *Nano Today*, 2007, **2**, 30–38.

53 S. Eustis and M. A. El-Sayed, *Chem Soc Rev*, 2006, **35**, 209–217.

54 R. Long, Y. Li, L. Song and Y. Xiong, *Small*, 2015, **11**, 3873–3889.

55 V. P. Chauhan, Z. Popović, O. Chen, J. Cui, D. Fukumura, M. G. Bawendi and R. K. Jain, *Angew. Chem. Int. Ed.*, 2011, **50**, 11417–11420.

56 J.-H. Park, G. Von Maltzahn, L. Zhang, A. M. Derfus, D. Simberg, T. J. Harris, E. Ruoslahti, S. N. Bhatia and M. J. Sailor, *Small*, 2009, **5**, 694–700.

57 J. Penders, M. Stolzoff, D. J. Hickey, M. Andersson and T. J. Webster, *Int. J. Nanomedicine*, 2017, **12**, 2457–2468.

58 X. Gu, Z. Xu, L. Gu, H. Xu, F. Han, B. Chen and X. Pan, *Environ. Chem. Lett.*, 2021, **19**, 167–187.

59 H. Daraee, A. Eatemadi, E. Abbasi, S. Fekri Aval, M. Kouhi and A. Akbarzadeh, *Artif. Cells Nanomedicine Biotechnol.*, 2016, **44**, 410–422.

60 M. A. Dheyab, A. A. Aziz, P. Moradi Khaniabadi, M. S. Jameel, N. Oladzadabbasabadi, S. A. Mohammed, R. S. Abdullah and B. Mehrdel, *Int. J. Mol. Sci.*, 2022, **23**, 7400.

61 S. Link and M. A. El-Sayed, *Int. Rev. Phys. Chem.*, 2000, **19**, 409–453.

62 M. Qi, X. Wang, J. Chen, Y. Liu, Y. Liu, J. Jia, L. Li, T. Yue, L. Gao, B. Yan, B. Zhao and M. Xu, *ACS Nano*, 2023, **17**, 8851–8865.

63 J. Qin, M. Sui, B. Yuan, J. Wang, Z. Yuan and G. Xu, *Sci. Total Environ.*, 2018, **619–620**, 1618–1627.

64 Z. Lv, S. He, Y. Wang and X. Zhu, *Adv. Healthc. Mater.*, 2021, **10**, 2001806.

65 R. Vankayala, A. Sagadevan, P. Vijayaraghavan, C. Kuo and K. C. Hwang, *Angew. Chem. Int. Ed.*, 2011, **50**, 10640–10644.

66 J. J. M. Lamberts, D. R. Schumacher and D. C. Neckers, *J. Am. Chem. Soc.*, 1984, **106**, 5879–5883.

67 Z. Chu, C. Yin, S. Zhang, G. Lin and Q. Li, *Nanoscale*, 2013, **5**, 3406.

68 T. Shang, C. Wang, L. Ren, X. Tian, D. Li, X. Ke, M. Chen and A. Yang, *Nanoscale Res. Lett.*, 2013, **8**, 4.

69 Y. Cheng, A. C. Samia, J. D. Meyers, I. Panagopoulos, B. Fei and C. Burda, *J. Am. Chem. Soc.*, 2008, **130**, 10643–10647.

70 S. Sehgal, J. Kumar, and Nishtha, *Mater. Today Proc.*, 2022, **62**, 6468–6476.

71 S. Link and M. A. El-Sayed, *J. Phys. Chem. B*, 1999, **103**, 4212–4217.

72 X. Yu, Z. Wang, H. Cui, X. Wu, W. Chai, J. Wei, Y. Chen and Z. Zhang, *Molecules*, 2022, **27**, 8766.

73 G. Baffou, R. Quidant and C. Girard, *Appl. Phys. Lett.*, 2009, **94**, 153109.

74 C. F. Bohren and D. R. Huffman, *Absorption and scattering of light by small particles*, Wiley-CH Verlag GmbH & Co KGaA, New York, 2004.

75 N. J. Hogan, A. S. Urban, C. Ayala-Orozco, A. Pimpinelli, P. Nordlander and N. J. Halas, *Nano Lett.*, 2014, **14**, 4640–4645.

76 M. Kumari, A. Mishra, S. Pandey, S. P. Singh, V. Chaudhry, M. K. R. Mudiam, S. Shukla, P. Kakkar and C. S. Nautiyal, *Sci. Rep.*, 2016, **6**, 27575.

77 S. Wacławek, Z. Gončuková, K. Adach, M. Fijałkowski and M. Černík, *Environ. Sci. Pollut. Res.*, 2018, **25**, 24210–24219.

78 C.-G. Yuan, C. Huo, S. Yu and B. Gui, *Phys. E Low-Dimens. Syst. Nanostructures*, 2017, **85**, 19–26.

79 E. Leontidis, K. Kleitou, T. Kyprianidou-Leodidou, V. Bekiari and P. Lianos, *Langmuir*, 2002, **18**, 3659–3668.

80 S. A. AL-Thabaiti, A. Y. Obaid and Z. Khan, *Can. Chem. Trans.*

81 J. E. Ortiz-Castillo, R. C. Gallo-Villanueva, M. J. Madou and V. H. Perez-Gonzalez, *Coord. Chem. Rev.*, 2020, **425**, 213489.

82 N. Li, P. Zhao and D. Astruc, *Angew. Chem. Int. Ed.*, 2014, **53**, 1756–1789.

83 E. J. W. Verwey, .

84 W. Zhang, in *Nanomaterial*, eds D. G. Capco and Y. Chen, Springer Netherlands, Dordrecht, 2014, vol. 811, pp. 19–43.

85 D. Titus, E. James Jebaseelan Samuel and S. M. Roopan, in *Green Synthesis, Characterization and Applications of Nanoparticles*, Elsevier, 2019, pp. 303–319.

86 E. Blanco, H. Shen and M. Ferrari, *Nat. Biotechnol.*, 2015, **33**, 941–951.

87

88 I. Hussain, N. B. Singh, A. Singh, H. Singh and S. C. Singh, *Biotechnol. Lett.*, 2016, **38**, 545–560.

89 A. Gour and N. K. Jain, *Artif. Cells Nanomedicine Biotechnol.*, 2019, **47**, 844–851.

90 P. Zhao, N. Li and D. Astruc, *Coord. Chem. Rev.*, 2013, **257**, 638–665.

91 Z. Zhang, H. Chen, C. Xing, M. Guo, F. Xu, X. Wang, H. J. Gruber, B. Zhang and J. Tang, *Nano Res.*, 2011, **4**, 599–611.

92 P. R. Sajanlal, T. S. Sreeprasad, A. K. Samal and T. Pradeep, *Nano Rev.*, 2011, **2**, 5883.

93 V. K. LaMer and R. H. Dinegar, *J. Am. Chem. Soc.*, 1950, **72**, 4847–4854.

94 W. Ostwald, *Z. Für Phys. Chem.*, 1900, **34U**, 495–503.

95 Ł. Niżnik, M. Noga, D. Kobylarz, A. Frydrych, A. Krośniak, L. Kapka-Skrzypczak and K. Jurowski, *Int. J. Mol. Sci.*, 2024, **25**, 4057.

96 E. E. Connor, J. Mwamuka, A. Gole, C. J. Murphy and M. D. Wyatt, *Small*, 2005, **1**, 325–327.

97 R. G. Rayavarapu, W. Petersen, L. Hartsuiker, P. Chin, H. Janssen, F. W. B. Van Leeuwen, C. Otto, S. Manohar and T. G. Van Leeuwen, *Nanotechnology*, 2010, **21**, 145101.

98 I. Fratoddi, I. Venditti, C. Cametti and M. V. Russo, *Nano Res.*, 2015, **8**, 1771–1799.

99 A. Foti, B. Clépoint, A. Fraix, L. D'Urso, A. De Bonis and C. Satriano, *Front. Mater.*, 2024, **11**, 1381176.

100 W. H. De Jong, W. I. Hagens, P. Krystek, M. C. Burger, A. J. A. M. Sips and R. E. Geertsma, *Biomaterials*, 2008, **29**, 1912–1919.

101 G. Sonavane, K. Tomoda and K. Makino, *Colloids Surf. B Biointerfaces*, 2008, **66**, 274–280.

102 S. M. Amini, T. Emami, M. Rashidi and H. Zrrinnahad, *Food Biosci.*, 2024, **57**, 103446.

103 L. Torrisi and A. Torrisi, *Radiat. Eff. Defects Solids*, 2018, **173**, 729–739.

104 A. Fojtik, M. Giersig and A. Henglein, *Berichte Bunsenges. Für Phys. Chem.*, 1993, **97**, 1493–1496.

105 C. Daruich De Souza, B. Ribeiro Nogueira and M. E. C. M. Rostelato, *J. Alloys Compd.*, 2019, **798**, 714–740.

106 S. Akhtar, S. M. Asiri, F. A. Khan, S. T. Gunday, A. Iqbal, N. Alrushaid, O. A. Labib, G. R. Deen and F. Z. Henari, *Arab. J. Chem.*, 2022, **15**, 103594.

107 K. B. Narayanan and N. Sakthivel, *Adv. Colloid Interface Sci.*, 2011, **169**, 59–79.

108 M. F. Lengke, M. E. Fleet and G. Southam, *Langmuir*, 2006, **22**, 2780–2787.

109 P. Mukherjee, A. Ahmad, D. Mandal, S. Senapati, S. R. Sainkar, M. I. Khan, R. Ramani, R. Parischa, P. V. Ajayakumar, M. Alam, M. Sastry and R. Kumar, *Angew. Chem. Int. Ed.*, 2001, **40**, 3585.

110 A. Andleeb, A. Andleeb, S. Asghar, G. Zaman, M. Tariq, A. Mehmood, M. Nadeem, C. Hano, J. M. Lorenzo and B. H. Abbasi, *Cancers*, 2021, **13**, 2818.

111 G. Marslin, K. Siram, Q. Maqbool, R. Selvakesavan, D. Kruszka, P. Kachlicki and G. Franklin, *Materials*, 2018, **11**, 940.

112 A. Yasmin, K. Ramesh and S. Rajeshkumar, *Nano Converg.*, DOI:10.1186/s40580-014-0012-8.

113 O. Raab, University of Munich, 1900.

114 H. von Tappeiner, *Muench Med Wochenschr*, 1900, **47**, 5–7.

115 S. Lebdai, P. Bigot, P.-A. Leroux, L.-P. Berthelot, P. Maulaz and A.-R. Azzouzi, *J. Urol.*, 2017, **198**, 335–344.

116 M. R. De Souto Medeiros, C. C. Da Silva Barros, A. C. De Macedo Andrade, K. C. De Lima and É. J. D. Da Silveira, *Clin. Oral Investig.*, 2023, **27**, 6471–6482.

117 A. P. Castano, P. Mroz and M. R. Hamblin, *Nat. Rev. Cancer*, 2006, **6**, 535–545.

118 C. S. Foote, *Science*, 1968, **162**, 963–970.

119 C. S. Foote, *Photochem. Photobiol.*, 1991, **54**, 659–659.

120 M. S. Baptista, J. Cadet, P. Di Mascio, A. A. Ghogare, A. Greer, M. R. Hamblin, C. Lorente, S. C. Nunez, M. S. Ribeiro, A. H. Thomas, M. Vignoni and T. M. Yoshimura, *Photochem. Photobiol.*, 2017, **93**, 912–919.

121 M. S. Baptista, J. Cadet, A. Greer and A. H. Thomas, *Photochem. Photobiol.*, 2021, **97**, 1456–1483.

122 H. Ding, H. Yu, Y. Dong, R. Tian, G. Huang, D. A. Boothman, B. D. Sumer and J. Gao, *J. Controlled Release*, 2011, **156**, 276–280.

123 M. Pineiro, A. M. d'A. Rocha Gonsalves, M. M. Pereira, S. J. Formosinho and L. G. Arnaut, *J. Phys. Chem. A*, 2002, **106**, 3787–3795.

124 K. Plaetzer, B. Krammer, J. Berlanda, F. Berr and T. Kiesslich, *Lasers Med. Sci.*, 2009, **24**, 259–268.

125 S. S. Lucky, K. C. Soo and Y. Zhang, *Chem. Rev.*, 2015, **115**, 1990–2042.

126 L. B. Josefsen and R. W. Boyle, *Met.-Based Drugs*, 2008, **2008**, 1–23.

127 M. Lan, S. Zhao, W. Liu, C. Lee, W. Zhang and P. Wang, *Adv. Healthc. Mater.*, 2019, **8**, 1900132.

128 In *Novartis Foundation Symposia*, Wiley, 1st edn., 2007, pp. 4–16.

129 M. Niedre, M. S. Patterson and B. C. Wilson, *Photochem. Photobiol.*, 2002, **75**, 382–391.

130 S. Hatz, J. D. C. Lambert and P. R. Ogilby, *Photochem. Photobiol. Sci.*, 2007, **6**, 1106–1116.

131 P. R. Ogilby, *Chem. Soc. Rev.*, 2010, **39**, 3181.

132 J. H. Correia, J. A. Rodrigues, S. Pimenta, T. Dong and Z. Yang, *Pharmaceutics*, 2021, **13**, 1332.

133 E. Alves, M. A. Faustino, M. G. Neves, A. Cunha, J. Tome and A. Almeida, *Future Med. Chem.*, 2014, **6**, 141–164.

134 H. Schneckenburger, A. Rück, B. Bartos and R. Steiner, *J. Photochem. Photobiol. B*, 1988, **2**, 355–363.

135 D. J. Ball, S. Mayhew, S. R. Wood, J. Griffiths, D. I. Vernon and S. B. Brown, *Photochem. Photobiol.*, 2008, **69**, 390–396.

136 A. Almeida, M. A. Faustino and J. P. Tomé, *Future Med. Chem.*, 2015, **7**, 1221–1224.

137 M. R. Hamblin and T. Hasan, *Photochem. Photobiol. Sci.*, 2004, **3**, 436–450.

138 T. J. Dougherty, C. J. Gomer, B. W. Henderson, G. Jori, D. Kessel, M. Korbelik, J. Moan and Q. Peng, *J. Natl. Cancer Inst.*, 1998, **90**, 889–905.

139 R. Pottier and J. C. Kennedy, *J. Photochem. Photobiol. B*, 1990, **8**, 1–16.

140 D. Dolmans, A. Kadambi, J. Hill, K. Flores, J. Gerber, J. Walker, I. Borel Rinkes, R. Jain and D. Fukurama, *Cancer Res.*, 2002, **62**, 4289–4294.

141 Y. Wang, B. Zhang, L. Zhu, Y. Li, F. Huang, S. Li, Y. Shen and A. Xie, *ACS Appl. Mater. Interfaces*, 2014, **6**, 15000–15006.

142 G. Chang, Y. Wang, B. Gong, Y. Xiao, Y. Chen, S. Wang, S. Li, F. Huang, Y. Shen and A. Xie, *ACS Appl. Mater. Interfaces*, 2015, **7**, 11246–11256.

143 Y. Chen, Y. Gao, Y. Chen, L. Liu, A. Mo and Q. Peng, *J. Controlled Release*, 2020, **328**, 251–262.

144 R. Wang, D. Kim, M. Yang, X. Li and J. Yoon, *ACS Appl. Mater. Interfaces*, 2022, **14**, 7609–7616.

145 L. Li, J. Xie, X. Zhang, J. Chen, Y. Luo, L. Zhang and R. Luo, *Photodiagnosis Photodyn. Ther.*, 2010, **7**, 139–143.

146 X. Li, J. F. Lovell, J. Yoon and X. Chen, *Nat. Rev. Clin. Oncol.*, 2020, **17**, 657–674.

147 A. Villiers, *Chim. Org. - Compte Rendus Séances Académie Sci. Fr.*, 1891, **112**, 435–438.

148 F. Schardinger, *Centrablatt Für Bakteriol. Parasitenkd. Infekt.*, 1911, **29**, 188–197.

149 D. Prochowicz, A. Kornowicz and J. Lewiński, *Chem. Rev.*, 2017, **117**, 13461–13501.

150 S. Li and W. C. Purdy, *Chem. Rev.*, 1992, **92**, 1457–1470.

151 W. Saenger, J. Jacob, K. Gessler, T. Steiner, D. Hoffmann, H. Sanbe, K. Koizumi, S. M. Smith and T. Takaha, .

152 E. López-Tobar, G. P. Blanch, M. L. Ruiz Del Castillo and S. Sanchez-Cortes, *Vib. Spectrosc.*, 2012, **62**, 292–298.

153 H. H. Tønnesen, M. Másson and T. Loftsson, *Int. J. Pharm.*, 2002, **244**, 127–135.

154 J. Szejtli, *Chem. Rev.*, 1998, **98**, 1743–1754.

155 S. Daoud-Mahammed, P. Couvreur, K. Bouchemal, M. Chéron, G. Lebas, C. Amiel and R. Gref, *Biomacromolecules*, 2009, **10**, 547–554.

156 A. W. Coleman, I. Nicolis, N. Keller and J. P. Dalbiez, *J. Incl. Phenom. Mol. Recognit. Chem.*, 1992, **13**, 139–143.

157 E. Renard, A. Deratani, G. Volet and B. Sebille, *Eur Polym J*, 1997, **33**, 47–57.

158 B. Gidwani and A. Vyas, *Colloids Surf. B Biointerfaces*, 2014, **114**, 130–137.

159 G. Mocanu, D. Vizitiu and A. Carpov, *J. Bioact. Compat. Polym.*, 2001, **16**, 315–342.

160 M. Seggio, F. Laneri, A. C. E. Graziano, M. M. Natile, A. Fraix and S. Sortino, *Nanomaterials*, 2022, **12**, 4476.

161 G. Nocito, S. Petralia, M. Malanga, S. Béni, G. Calabrese, R. Parenti, S. Conoci and S. Sortino, *ACS Appl. Nano Mater.*, 2019, **2**, 7916–7923.

162 E. Larrañeta, S. Stewart, M. Ervine, R. Al-Kasasbeh and R. Donnelly, *J. Funct. Biomater.*, 2018, **9**, 13.

163 K. Sen, K. Kowlgi, G. Koper and H. T. Wolterbeek, *Int. J. Nanotechnol. Appl.*, **5**, 173–180.

164 Y. Yagci, M. Sangermano and G. Rizza, *Chem. Commun.*, 2008, 2771.

165 M. R. Langille, M. L. Personick and C. A. Mirkin, *Angew. Chem. Int. Ed.*, 2013, **52**, 13910–13940.

166 Y. Zhai, J. S. DuChene, Y.-C. Wang, J. Qiu, A. C. Johnston-Peck, B. You, W. Guo, B. DiCiaccio, K. Qian, E. W. Zhao, F. Ooi, D. Hu, D. Su, E. A. Stach, Z. Zhu and W. D. Wei, *Nat. Mater.*, 2016, **15**, 889–895.

167 S. Kumar, J. Kuntail, D. K. Sahu, V. S. Yadav and I. Sinha, *Indian J. Phys.*, 2023, **97**, 2727–2733.

168 J. Lv, Y. Yi, G. Wu and W. Liu, *Mater. Lett.*, 2017, **187**, 148–150.

169 V. Amendola and M. Meneghetti, *J. Phys. Chem. C*, 2009, **113**, 4277–4285.

170 V. Filipe, A. Hawe and W. Jiskoot, *Pharm. Res.*, 2010, **27**, 796–810.

171 R. Bellotti, G. B. Picotto and L. Ribotta, *Nanomanufacturing Metrol.*, 2022, **5**, 127–138.

172 P. Anand, A. B. Kunnumakkara, R. A. Newman and B. B. Aggarwal, *Mol. Pharm.*, 2007, **4**, 807–818.

173 O. P. Sharma, *Biochem. Pharmacol.*, 1976, **25**, 1811–1812.

174 A. Giordano and G. Tommonaro, *Nutrients*, 2019, **11**, 2376.

175 M. Nagabhushan and S. V. Bhide, *Nutr. Cancer*, 1986, **8**, 201–210.

176 M.-T. Huang, R. C. Smart, C.-Q. Wong and A. H. Conney, *Cancer Res.*, 1988, **48**, 5941–5946.

177 R. C. Srimal and B. N. Dhawan, *J. Pharm. Pharmacol.*, 2011, **25**, 447–452.

178 Y. Kiso, Y. Suzuki, N. Watanabe, Y. Oshima and H. Hikino, *Planta Med.*, 1983, **49**, 185–187.

179 C. J. Li, L. J. Zhang, B. J. Dezube, C. S. Crumpacker and A. B. Pardee, *Proc. Natl. Acad. Sci.*, 1993, **90**, 1839–1842.

180 Z. Sui, R. Salto, J. Li, C. Craik and P. R. Ortiz de Montellano, *Bioorg. Med. Chem.*, 1993, **1**, 415–422.

181 H. Köhler, *Koehler's Medizinal-Pflanzen in naturgetreuen Abbildungen und kurz erläuterndem*, Germany, 1887, vol. 2.

182 P. Basnet and N. Skalko-Basnet, *Molecules*, 2011, **16**, 4567–4598.

183 F. Ortica and M. A. J. Rodgers, *Photochem. Photobiol.*, 2001, **74**, 745–751.

184 C. Schneider, O. N. Gordon, R. L. Edwards and P. B. Luis, *J. Agric. Food Chem.*, 2015, **63**, 7606–7614.

185 L. Shen and H.-F. Ji, *Spectrochim. Acta. A. Mol. Biomol. Spectrosc.*, 2007, **67**, 619–623.

186 K. I. Priyadarsini, *J. Photochem. Photobiol. C Photochem. Rev.*, 2009, **10**, 81–95.

187 O. N. Gordon and C. Schneider, *Trends Mol. Med.*, 2012, **18**, 361–363.

188 C. S. Mangolim, C. Moriwaki, A. C. Nogueira, F. Sato, M. L. Baesso, A. M. Neto and G. Matioli, *Food Chem.*, 2014, **153**, 361–370.

189 N. S. Jha, S. Mishra, S. K. Jha and A. Surolia, *Electrochimica Acta*, 2015, **151**, 574–583.

190 Y. Sun and Y. Xia, *Anal. Chem.*, 2002, **74**, 5297–5305.

191 J. Jankun, M. Wyganowska-Świątkowska, K. Dettlaff, A. Jelińska, A. Surdacka, D. Wątróbska-Świetlikowska and E. Skrzypczak-Jankun, *Int. J. Mol. Med.*, 2016, **37**, 1151–1158.

192 C. F. Chignell, P. Bilskj, K. J. Reszka, A. G. Motten, R. H. Sik and T. A. Dahl, *Photochem. Photobiol.*, 1994, **59**, 295–302.

193 F. Laneri, C. Conte, C. Parisi, O. Catanzano, A. Fraix, F. Quaglia and S. Sortino, *J. Photochem. Photobiol. B*, 2023, **245**, 112756.

194 E. I. Paramera, S. J. Konteles and V. T. Karathanos, *Food Chem.*, 2011, **125**, 892–902.

195 C. Mohanty, M. Das and S. K. Sahoo, *Expert Opin Drug Deliv*, 2012, **9**, 1347–64.

196 H. Agashe, K. Sahoo, P. Lagisetty and V. Awatshi, *Colloids Surf. B Biointerfaces*, 2011, **84**, 329–337.

197 C. Mohanty, S. Acharya, A. K. Mohanty, F. Dilnawaz and S. K. Sahoo, *Nanomed.*, 2010, **5**, 433–449.

198 E. Shaabani, S. M. Amini, S. Kharrazi and R. Tajerian, *Nanomed J*, 2017, **4**, 115–125.

199 Y. Manolova, V. Deneva, L. Antonov, E. Drakalska, D. Momekova and N. Lambov, *Spectrochim. Acta. A. Mol. Biomol. Spectrosc.*, 2014, **132**, 815–820.

200 M. Ghosh, S. Parida, H. Khatoon, N. Bera, S. Mishra and N. Sarkar, *ChemPhysChem*, 2023, e202300174.

201 S. Hatamie, O. Akhavan, S. K. Sadrnezhaad, M. M. Ahadian, M. M. Shirolkar and H. Q. Wang, *Mater. Sci. Eng. C*, 2015, **55**, 482–489.

202 R. Martin-Trasanco, R. Cao, H. E. Esparza-Ponce, M. E. Montero-Cabrera and R. Arratia-Pérez, *Carbohydr. Polym.*, 2017, **175**, 530–537.

203 D. K. Singh, R. Jagannathan, P. Khandelwal, P. M. Abraham and P. Poddar, *Nanoscale*, 2013, **5**, 1882.

204 A. Adlia, I. Tomagola, S. Damayanti, A. Mulya and H. Rachmawati, *Sci. Pharm.*, 2018, **86**, 41.

205 K. Sindhu, A. Rajaram, K. J. Sreeram and R. Rajaram, *RSC Adv.*, 2014, **4**, 1808–1818.

206 D. Patra and R. El Kurdi, *Green Chem. Lett. Rev.*, 2021, **14**, 474–487.

207 O. Donoso-González, L. Lodeiro, Á. E. Aliaga, M. A. Laguna-Bercero, S. Bollo, M. J. Kogan, N. Yutronic and R. Sierpe, *Pharmaceutics*, 2021, **13**, 261.

208 R. El Kurdi and D. Patra, *Phys. Chem. Chem. Phys.*, 2017, **19**, 5077–5090.

209 F.-Y. Wu, M.-Z. Sun, Y.-L. Xiang, Y.-M. Wu and D.-Q. Tong, *J. Lumin.*, 2010, **130**, 304–308.

210 Z. Pang, R. Raudonis, B. R. Glick, T.-J. Lin and Z. Cheng, *Biotechnol. Adv.*, 2019, **37**, 177–192.

211 N. Sekkat, H. V. D. Bergh, T. Nyokong and N. Lange, *Molecules*, 2011, **17**, 98–144.

212 L. P. Roguin, N. Chiarante, M. C. García Vior and J. Marino, *Int. J. Biochem. Cell Biol.*, 2019, **114**, 105575.

213 S. Lu, A. Wang, Y. J. Ma, H. Y. Xuan, B. Zhao, X. D. Li, J. H. Zhou, L. Zhou and S. H. Wei, *Carbohydr. Polym.*, 2016, **148**, 236–242.

214 C. Schweitzer and R. Schmidt, *Chem. Rev.*, 2003, **103**, 1685–1758.

215 R. Schmidt and E. Afshari, *Berichte Bunsenges. Für Phys. Chem.*, 1992, **96**, 788–794.

216 M. Morisue, S. Ueda, M. Kurasawa, M. Naito and Y. Kuroda, *J. Phys. Chem. A*, 2012, **116**, 5139–5144.

217 A. Ogunsipe, J.-Y. Chen and T. Nyokong, *New J Chem*, 2004, **28**, 822–827.

218 K. C. Das and C. K. Das, *Biochem. Biophys. Res. Commun.*, 2002, **295**, 62–66.

219 E. Baigorria, M. E. Milanesio and E. N. Durantini, *Eur. Polym. J.*, 2020, **134**, 109816.

220 M. Y. Nahabedian, R. A. Cohen, M. F. Contino, T. M. Terem, W. H. Wright and M. W. Berns, .

221 R. Bonnett, D. J. McGarvey, A. Harriman, E. J. Land, T. G. Truscott and U. Winfield, *Photochem. Photobiol.*, 1988, **48**, 271–276.

222 A. Majhi, G. M. Rahman, S. Panchal and J. Das, *Bioorg. Med. Chem.*, 2010, **18**, 1591–1598.

223 J. König, in *Colour Additives for Foods and Beverages*, Elsevier, 2015, pp. 35–60.

224 *Summary of Color Additives for Use in the United States in Foods, Drugs, Cosmetics, and Medical Devices | FDA*, Food and Drug Administration, 2015.

225 *Current approved additives and E numbers in EU*, Food Standards Agency, 2024.

226 S. Ammar, R. Abdelhedi, C. Flox, C. Arias and E. Brillas, *Environ. Chem. Lett.*, 2006, **4**, 229–233.

227 J. F. O'Hara, D. F. Connors, J. Sprung and L. A. Ballard, .

228 T. Harioka, H. Mori and K. Mori, *Anesth Analg*, 1987, **66**, 1049–1060.

229 F. M. Blanco, *Flora de Filipinas [...] Gran edición [...] [Atlas I]*, Manila, Philippines, 1880.

230 R. Christie, *Biotech. Histochem.*, 2007, **82**, 51–56.

231 M. Vautier, C. Guillard and J.-M. Herrmann, *J. Catal.*, 2001, **201**, 46–59.

232 P. P. Roy, J. Shee, E. A. Arsenault, Y. Yoneda, K. Feuling, M. Head-Gordon and G. R. Fleming, *J. Phys. Chem. Lett.*, 2020, **11**, 4156–4162.

233 Y. Kihara, S. Tani, Y. Higashi, T. Teramoto and Y. Nagasawa, *J. Phys. Chem. B*, 2022, **126**, 3539–3550.

234 J. Seixas De Melo, R. Rondao, H. D. Burrows, M. J. Melo, S. Navaratnam, R. Edge and G. Voss, *J. Phys. Chem. A*, 2006, **110**, 13653–13661.

235 J. Seixas De Melo, A. P. Moura and M. J. Melo, *J. Phys. Chem. A*, 2004, **108**, 6975–6981.

236 L. Saikhao, J. Setthayanond, T. Karpkird, T. Bechtold and P. Suwanruji, *J. Clean. Prod.*, 2018, **197**, 106–113.

237 E. L. Roberts, S. Burguieres and I. M. Warner, *Appl. Spectrosc.*, 1998, **52**, 1305–1313.

238 N. Kuramoto and T. Kitao, *J.S.D.C.*, 1979, 257–261.

239 B. Shen, M. Olbrich-Stock, J. Posdorfer and R. N. Schindler, *Z. Für Phys. Chem.*, 1991, 251–255.

240 W. Krieger, J. Lamsfuß, W. Zhang and N. Kockmann, *Chem. Eng. Technol.*, 2017, **40**, 2134–2143.

241 I. Blakey, Z. Merican and K. J. Thurecht, *Langmuir*, 2013, **29**, 8266–8274.

242 P. K. Jain, X. Huang, I. H. El-Sayed and M. A. El-Sayed, *Plasmonics*, 2007, **2**, 107–118.

243 A. Kandelbauer, W. Kessler and R. W. Kessler, *Anal. Bioanal. Chem.*, 2008, **390**, 1303–1315.

244 J. Rocha, C. D. S. Brites and L. D. Carlos, *Chem. – Eur. J.*, 2016, **22**, 14782–14795.

245 Y. Yang, W. Kong, H. Li, J. Liu, M. Yang, H. Huang, Y. Liu, Z. Wang, Z. Wang, T.-K. Sham, J. Zhong, C. Wang, Z. Liu, S.-T. Lee and Z. Kang, *ACS Appl. Mater. Interfaces*, 2015, **7**, 27324–27330.

246 J.-M. Yang, H. Yang and L. Lin, *ACS Nano*, 2011, **5**, 5067–5071.

247 S. Kiyonaka, T. Kajimoto, R. Sakaguchi, D. Shinmi, M. Omatsu-Kanbe, H. Matsuura, H. Imamura, T. Yoshizaki, I. Hamachi, T. Morii and Y. Mori, *Nat. Methods*, 2013, **10**, 1232–1238.

248 G. Ke, C. Wang, Y. Ge, N. Zheng, Z. Zhu and C. J. Yang, *J. Am. Chem. Soc.*, 2012, **134**, 18908–18911.

249 G. Kucsko, P. C. Maurer, N. Y. Yao, M. Kubo, H. J. Noh, P. K. Lo, H. Park and M. D. Lukin, *Nature*, 2013, **500**, 54–58.

250 D. Jaque and F. Vetrone, *Nanoscale*, 2012, **4**, 4301.

251 L. A. Ramolise, S. N. Ogugua, H. C. Swart and D. E. Motaung, *Coord. Chem. Rev.*, 2025, **522**, 216196.

252 Y. Liang, P. F. Moy, J. A. Poole and A. M. Ponte Goncalves, *J. Phys. Chem.*, 1984, **88**, 2451–2455.

253 G. Feng, H. Zhang, X. Zhu, J. Zhang and J. Fang, *Biomater. Sci.*, 2022, **10**, 1855–1882.

254 Z. Huang, N. Li, X. Zhang, C. Wang and Y. Xiao, *Anal. Chem.*, 2018, **90**, 13953–13959.

255 A. von Bayer, in *Berichte der Deutschen chemischen Gesellschaft zu Berlin*, 1871, vol. 4, pp. 555–558.

256 M. Peng, A. M. Kaczmarek and K. Van Hecke, *ACS Appl. Mater. Interfaces*, 2022, **14**, 14367–14379.

257 K. S, B. Sam, L. George, S. Y. N and A. Varghese, *J. Fluoresc.*, 2021, **31**, 1251–1276.

258 L. B. O. Davi, M. S. Silva, R. L. Ferreira, W. Muniz, A. S. Ribeiro, D. J. P. Lima, I. N. De Oliveira and C. D. A. E. S. Barbosa, *Dyes Pigments*, 2021, **194**, 109549.

259 J. Zhou, B. Del Rosal, D. Jaque, S. Uchiyama and D. Jin, *Nat. Methods*, 2020, **17**, 967–980.

260 M. Pongsuchart, C. Danladkaew and T. Khomvarn, .

261 A. M. Alanazi, G. A. E. Mostafa and A. A. Al-Badr, *Unpublished*, 2015, preprint, DOI: 10.13140/RG.2.1.4853.7767.

262 D. E. Jensen, G. K. Belka and G. C. D. Bois, *Biochem. J.*, 1998, **331**, 659–668.

263 I. Hornyak, E. Pankotai, L. Kiss and Z. Lacza, *Curr. Pharm. Biotechnol.*, 2011, **12**, 1368–1374.

264 R. J. P. Williams, *Chem. Soc. Rev.*, 1996, **25**, 77.

265 B. Roy, A. Du Moulinet d'Hardemare and M. Fontecave, *J. Org. Chem.*, 1994, **59**, 7019–7026.

266 S. Sortino, *Chem. Soc. Rev.*, 2010, **39**, 2903.

267 D. A. Wink, K. M. Miranda, M. G. Espey, R. M. Pluta, S. J. Hewett, C. Colton, M. Vitek, M. Feelisch and M. B. Grisham, *Antioxid. Redox Signal.*, 2001, **3**, 203–213.

268 T. J. Martins, C. Parisi, J. Guerra Pinto, I. D. P. Ribeiro Brambilla, M. Malanga, J. Ferreira-Strixino and S. Sortino, *ACS Med. Chem. Lett.*, 2024, **15**, 857–863.

269 F. Laneri, A. C. E. Graziano, M. Seggio, A. Fraix, M. Malanga, S. Béni, G. Longobardi, C. Conte, F. Quaglia and S. Sortino, *Molecules*, 2022, **27**, 1918.

270 S. Korde Choudhari, M. Chaudhary, S. Bagde, A. R. Gadbail and V. Joshi, *World J. Surg. Oncol.*, 2013, **11**, 118.

271 J. S. Stamler, D. J. Singel and J. Loscalzo, *Science*, 1992, **258**, 1898–1902.

272 T. W. Hart, *Tetrahedron Lett.*, 1985, **26**, 2013–2016.

273 D. L. H. WILLIAMS, in *Nitrosation Reactions and the Chemistry of Nitric Oxide*, ed. D. L. H. WILLIAMS, Elsevier Science, Amsterdam, 2004, pp. 137–160.

274 M. Máximo-Canadas, L. Modesto-Costa and I. Borges, *J. Comput. Chem.*, 2024, **45**, 2899–2911.

275 F. Chen, Y. Wang, J. Ma and G. Yang, *Nanoscale Res. Lett.*, 2014, **9**, 220.

276 Z. Zhang, J. Tang, M. Jin, Y. Li, W. Chen, C. Chen, J. Xiang and C. Guo, *Ceram. Int.*, 2023, **49**, 38465–38473.

277 Y. Zhang, H. Zong, C. Zong, Y. Tan, M. Zhang, Y. Zhan and J.-X. Cheng, *J. Am. Chem. Soc.*, 2021, **143**, 11490–11499.

278 M. Malanga, M. Bálint, I. Puskás, K. Tuza, T. Sohajda, L. Jicsinszky, L. Szente and É. Fenyvesi, *Beilstein J. Org. Chem.*, 2014, **10**, 3007–3018.

279 M. Malanga, L. Jicsinszky and É. Fenyvesi, *J. Drug Deliv. Sci. Technol.*, 2012, **22**, 260–265.

Appendix I: Initial synthesis of gold nanoparticles from reduction with curcumin's system C1-L sample, inspired from Seggio and Laneri *et al*. procedure.[160] (Part 4.2.1.)

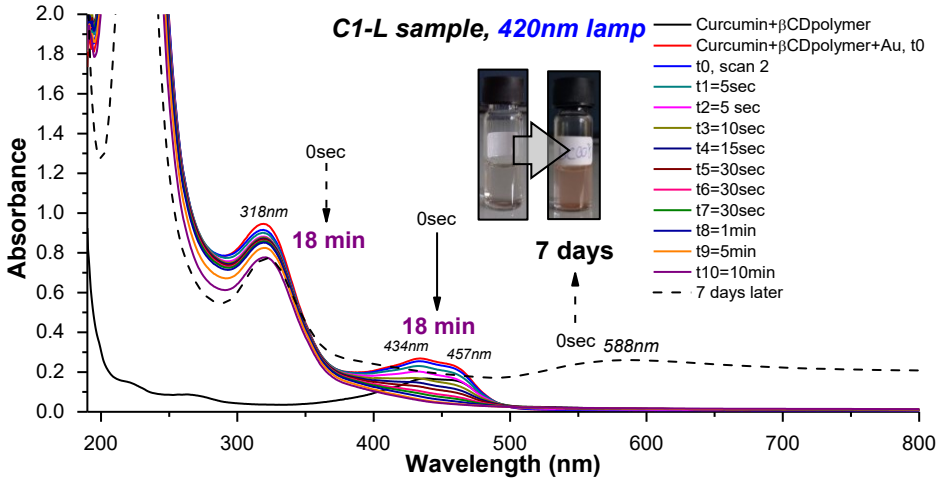

Appendix I: First AuNPs synthesis attempt. Comparison of the absorbance evolution of Curcumin+βCDpolymer+Au (C1-L) by a 420 nm lamp (*ca.* 1 mW.cm^{-1}) and after one week under ambient light (black dotted line). The sample was stirred during the irradiation. The inset show at the left: picture of C1-L after the end of the irradiation, at the right: picture of C1-L one week after the end of the irradiation under ambient light. Measurements were performed in a 1 cm path-length absorbance cuvette using a PerkinElmer UV-Vis spectrophotometer using pure water as the blank. Conditions: [βCDpolymer] = 2.05 mg.mL^{-1}; [$HAuCl_4 \bullet 3H_2O$] = 0.4 mM.

Appendix II: Size measurement from irradiated synthesis of AuNPs from a film preparation of curcumin. C2-L sample (Part 4.2.1.)

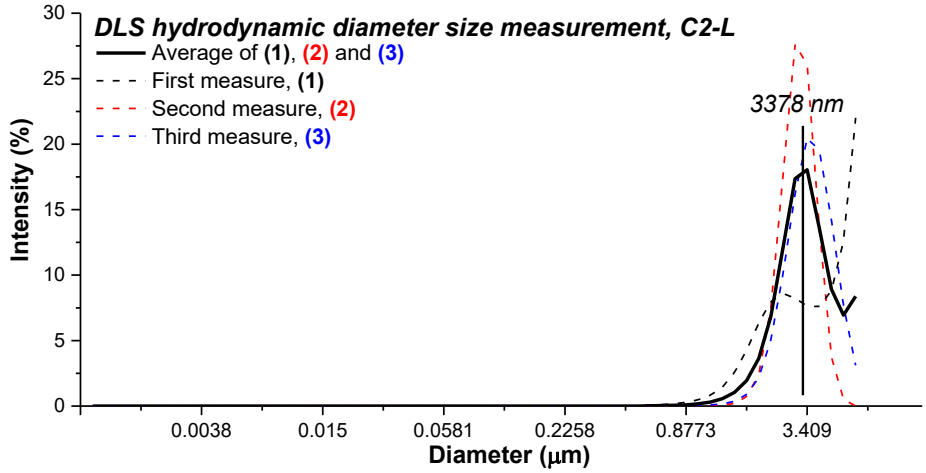

Appendix II: Scattering light intensity distribution (%) of the measure of Curcumin+βCDpolymer+Au (C2-L) over the hydrodynamic diameter (μm). The measurement was performed using a Dynamic Light Scattering HORIBA LB-550, at room temperature (T = 25 °C). Conditions: [Curcumin] = 0.2 mM; [βCDpolymer] = 4.04 mg.mL^{-1}; [$HAuCl_4 \bullet 3H_2O$] = 0.4 mM.

Appendix III: Dark control of AuNPs synthesis with Curcumin/Au ratio (1:20). C3-D sample (Part 4.2.1.)

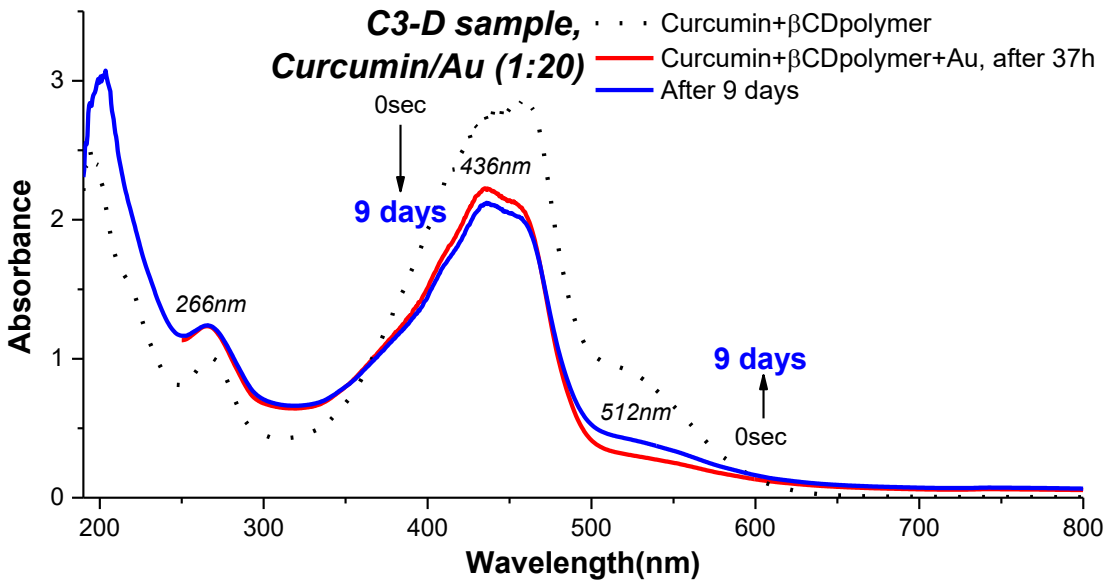

Appendix III: Comparison of the absorbance evolution of Curcumin+βCDpolymer (black dotted line) and dark control of Curcumin+βCDpolymer+Au (C3-D) with Curcumin/Au ratio (1:20) over time. The sample was stirred for thirty-seven hours. Measurements were performed in a 1 cm path-length absorbance cuvette using a PerkinElmer UV-Vis spectrophotometer using pure water as the blank. Conditions: [Curcumin] = 4.99x10^{-5} M; [βCDpolymer] = 2.04 mg.mL^{-1}; [$HAuCl_4 \bullet 3H_2O$] = 0.4 mM.

Appendix IV: Size measurement from irradiated synthesis of AuNPs with Curcumin/Au (1:20). C3-L sample (Part 4.2.1.)

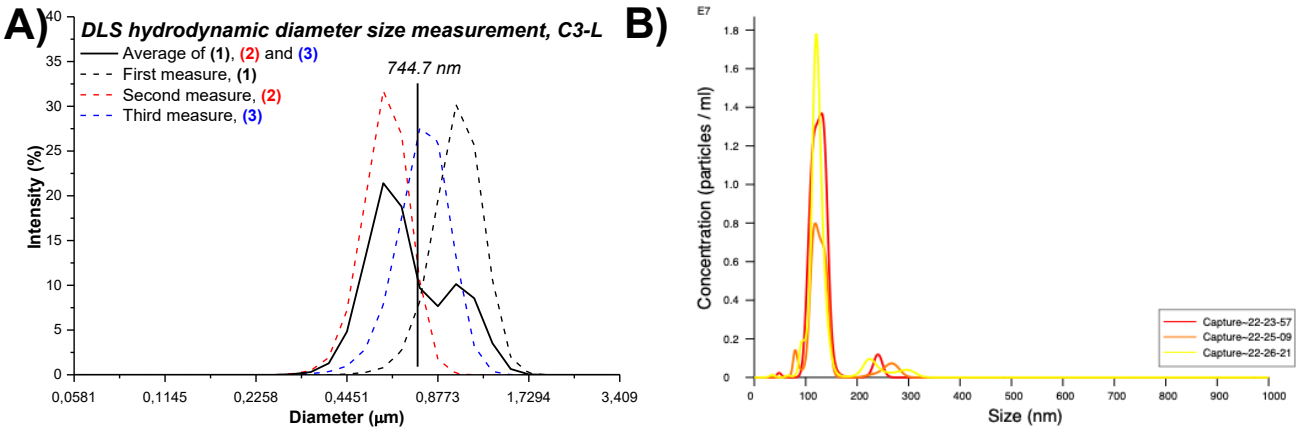

Appendix IV: A) Scattering light intensity distribution (%) of the measure of Curcumin+βCDpolymer+Au (C3-L) over the hydrodynamic diameter (μm). The measurement was performed using a Dynamic Light Scattering HORIBA LB-550, at room temperature (T = 25 °C). B) Evolution of the concentration (particles/mL) of Curcumin+βCDpolymer+Au irradiated (diluted 100 times) over size (nm). The measurement was performed using a NanoSight, at room temperature (T = 25 °C). Conditions: [Curcumin] = 4.99 mM ; [βCDpolymer] = 2.04 mg.mL^{-1} ; [$HAuCl_4 \bullet 3H_2O$] = 0.4 mM.

Appendix V: Dark control, C6-D sample, of AuNPs synthesis with QAβCDPS. (Part 4.2.4.)

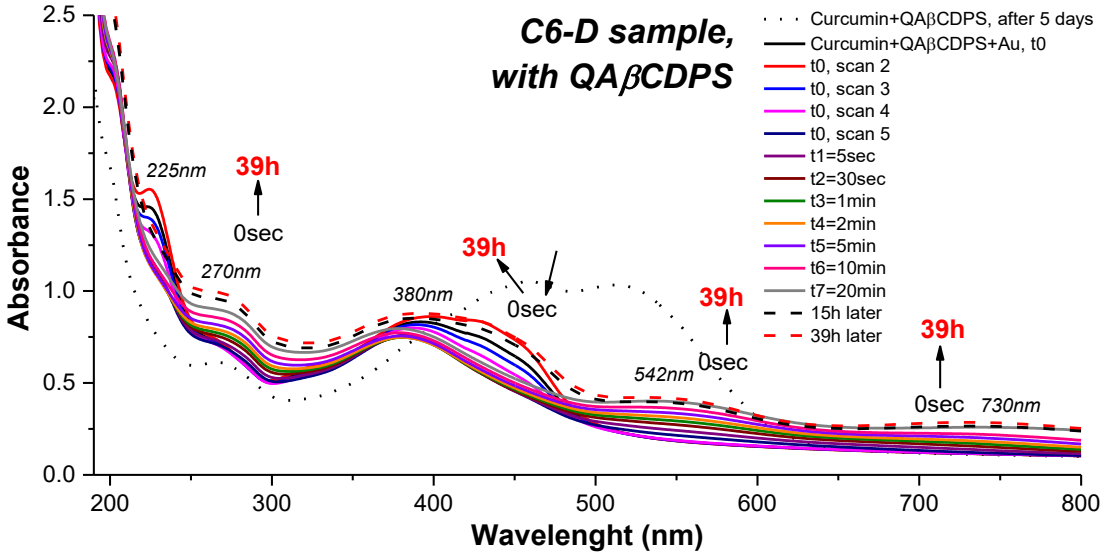

Appendix V: Comparison of the absorbance evolution of Curcumin+QAβCDPS (dark dotted line) and dark control Curcumin+QAβCDPS+Au (C6-D) (plain lines) and after 15h (black dashed line) and 39h (red dashed line) after the synthesis. The stirring was performed in a 1 cm path-length fluorescence cuvette. Measurements were performed in a 1 mm path-length absorbance cuvette using a Jasco V-560 UV-Vis spectrophotometer with air as the blank. Conditions : [Curcumin] = 0.433 mM; [QAβCDPS] = 10.0 mg.mL^{-1}; [$HAuCl_4 \bullet 3H_2O$] = 0.433 mM.

Appendix VI: Dark control, C8-D sample, of AuNPs synthesis with QAβCDPS in PBS. (Part 4.2.5.)

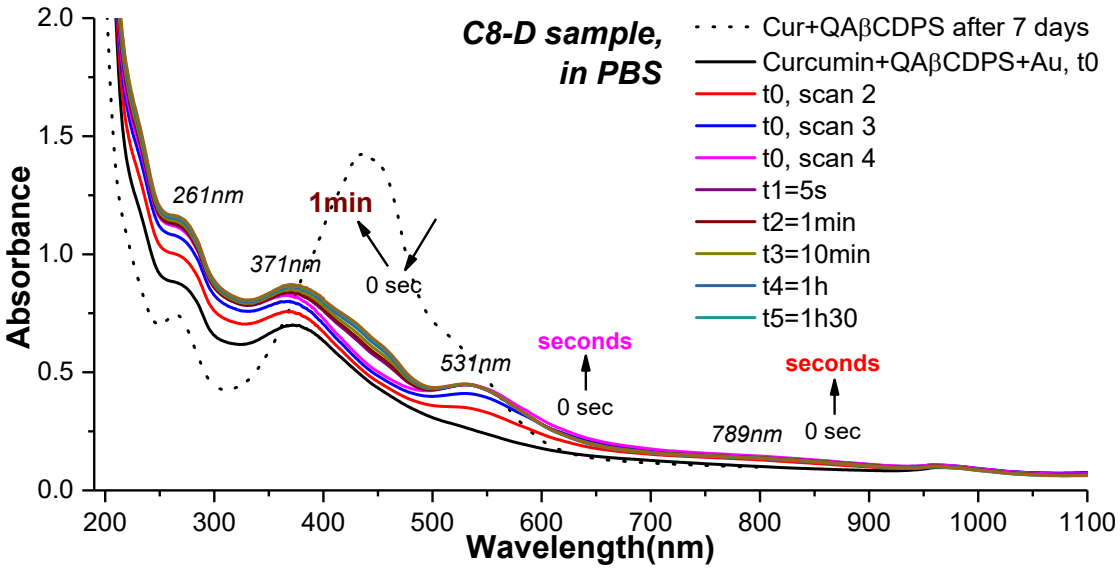

Appendix VI: Comparison of the absorbance evolution of dark control of Curcumin+QAβCDPS+Au (C8-D) in a PBS solution. The sample was stirred in a 1 cm path-length absorbance cuvette. Measurements were performed in a 1 mm path-length absorbance cuvette using a PerkinElmer UV-Vis spectrophotometer with air as the blank. Conditions: [PBS] = 10 mM; [Curcumin] = 0.47 mM; [QAβCDPS] = 10.00 mg.mL^{-1}; [$HAuCl_4 \bullet 3H_2O$] = 0.47 mM.

Appendix VIII: Photothermal study at 750 or 808 nm lasers of irradiated Cur+QAβCDPS+Au. C10-L sample (Part 4.2.6)

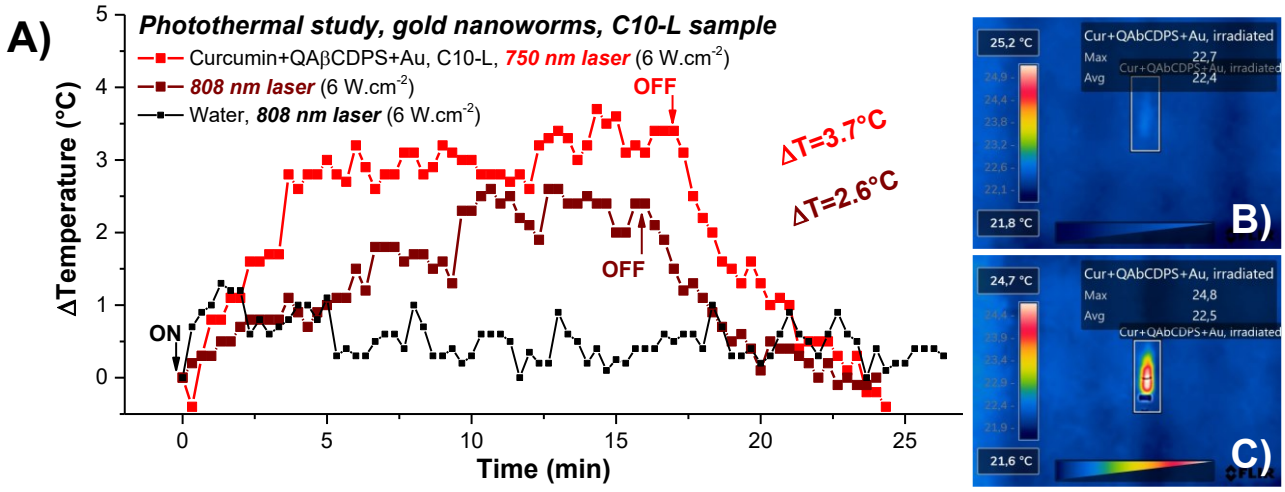

Appendix VII: A) Evolution of temperature over time by laser irradiation at 750 nm (*ca*. 6 W.cm^{-2}) (in red) or at 808 nm (*ca.* 6 W.cm^{-2}) (in dark red) over one cycle of measure of Curcumin+QAβCDPS+Au (C10-I) from the irradiated sample. Comparison with a water sample irradiated in the same conditions (in black); B) Thermal picture taken at the starting point of the irradiation with an 808 nm laser. C) Thermal picture taken at the end of the 808 nm laser irradiation. The temperatures were measured with a FLIR C3 thermal camera.

Appendix VIII: Dark controls of samples with curcumin for antibacterial assays. A) C11a-D and B) C11b-D samples. (Part 4.3.1.)

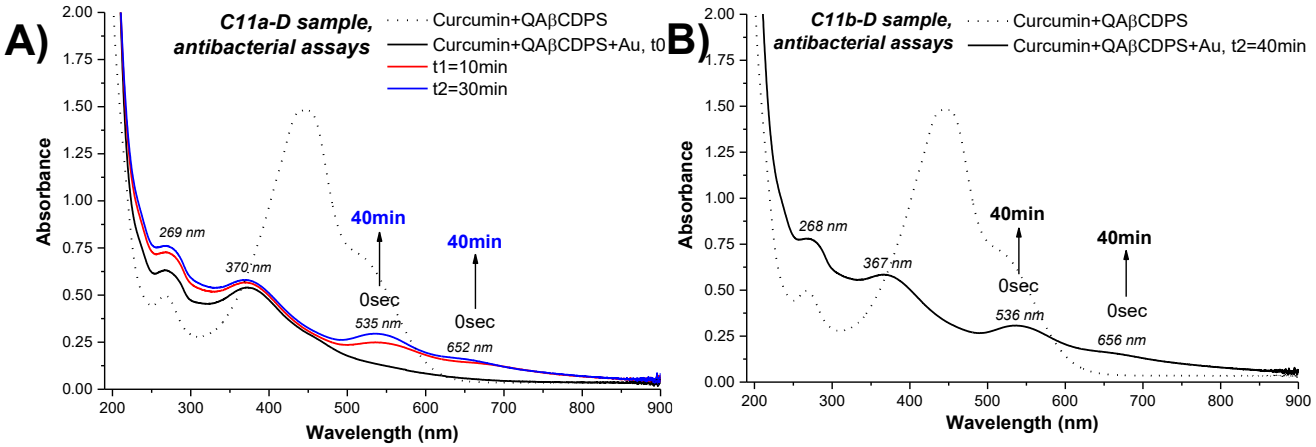

Appendix VIII: Comparison of the absorbance evolution of dark controls of A) first (C11a-D) and B) second (C11b-D) batches of Curcumin+QAβCDPS (black dotted line) and Curcumin+QAβCDPS+Au stirred in a PBS buffer solution after Au addition for antibacterial assays. Measurements were performed in a 1 mm path-length absorbance cuvette using a Jasco V-560 UV-Vis spectrophotometer with air as the blank. Conditions: [PBS] = 10mM; [Curcumin] = 3.14x10^{-4} M; [QAβCDPS] = 10.00 mg.mL^{-1}; [$HAuCl_4 \bullet 3H_2O$] = 4.00x10^{-4} M.

Appendix IX: Growth kinetic of bacteria, with or without photothermia experiment. (Part 4.3.1. and 5.3.1.)

A)

	Light						Dark						
	E. coli			*P. aeruginosa*			*E. coli*			*P. aeruginosa*			
	1	2	3	4	5	6	7	8	9	10	11	12	
A	a	b	c	a	b	c	a	b	S	a	b	S	No compound
B	a	b	c	a	b	c	a	b	c	a	b	c	Neutral polymer
C	a	b	c	a	b	c	a	b	c	a	b	c	No compound
D	a	b	c	a	b	c	a	b	c	a	b	c	Curcumin (irradiated)
E	a	b	c	a	b	c	a	b	*	a	b	*	Curcumin (non-irradiated)
F	a	b	c	a	b	c	a	b	c	a	b	c	Indigo carmine (irradiated)
G	a	b	c	a	b	c	a	b	c	a	b	c	Indigo carmine (non-irradiated)

B)

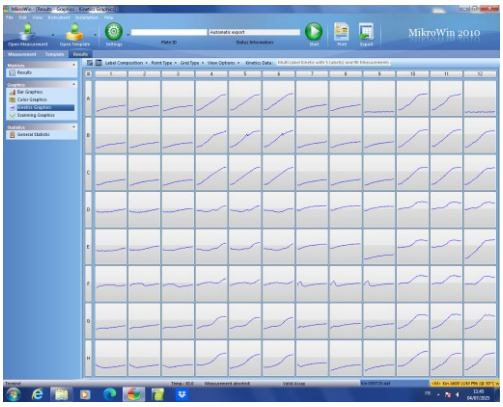

C)

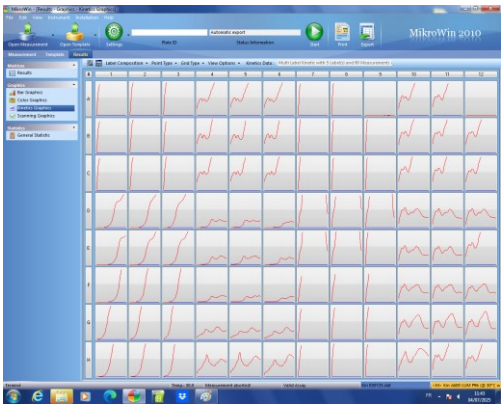

Appendix IX: A) 96-well plate layout. a, b and c correspond to triplicates; * denotes a well with no compound (insufficient volume of formulation); the wellplate area noted “Light” indicate the part of the wellplate that is exposed to laser irradiation; the wellplate area noted “Dark” indicate the part of the wellplate is the dark control, which is protected from laser exposure; S: sterility controls. B) Screenshot of A600 measurements from MikroWin 2010. C) Screenshot of bioluminescence readings after the photothermal experiment.

Appendix X: Irradiated batches for samples with curcumin on cancerous cells assays. A) C12a-L, B) C12b-L and C) C13-L samples (Part 4.3.2.)

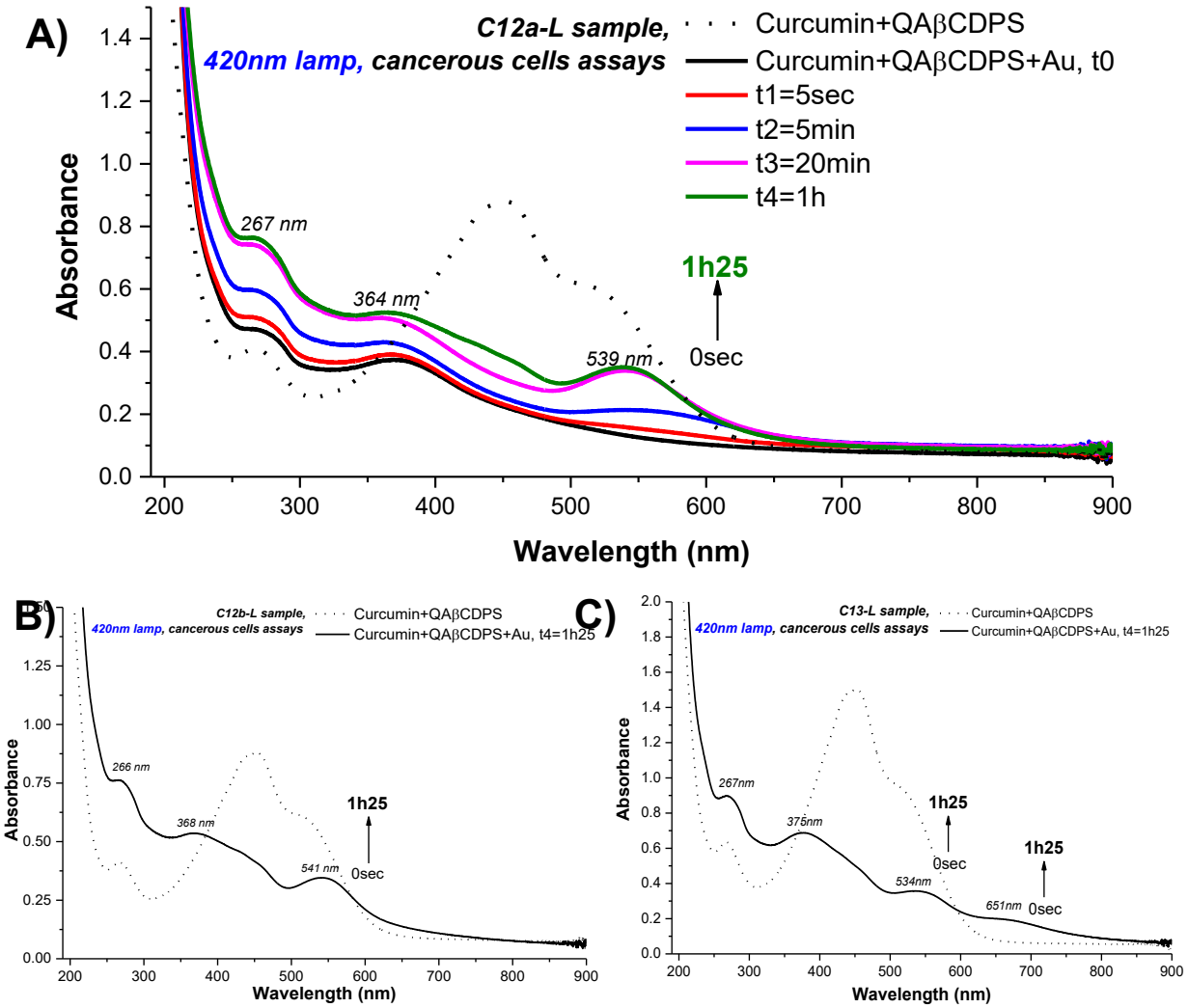

Appendix X: Comparison of the absorbance evolution of A) first (C12a-L), B) second (C12b-L) and C) third (C13-L) batches of Cur+QAβCDPS (black dotted line) and Cur+QAβCDPS+Au (full line) irradiated with a 420 nm lamp (*ca.* 1 mW.cm^{-2}) in a PBS buffer solution after Au addition, with magnetically stirring for cancerous cells assays. Measurements were performed in a 1 mm path-length absorbance cuvette using a Jasco V-560 UV-Vis spectrophotometer with air as the blank. Conditions A) & B): [PBS] = 10mM; [Curcumin] = 4.69x10^{-4} M; [QAβCDPS] = 10.00 mg.mL^{-1}; [$HAuCl_4 \bullet 3H_2O$] = 4.00x10^{-4} M; C): [PBS] = 10mM; [Curcumin] = 4.51x10^{-4} M; [QAβCDPS] = 10.00 mg.mL^{-1}; [$HAuCl_4 \bullet 3H_2O$] = 4.00x10^{-4} M.

Appendix XI: Dark controls for samples with curcumin on cancerous cells assays. A) C12a-D, B) C12b-D and C) C13-D samples (Part 4.3.2.)

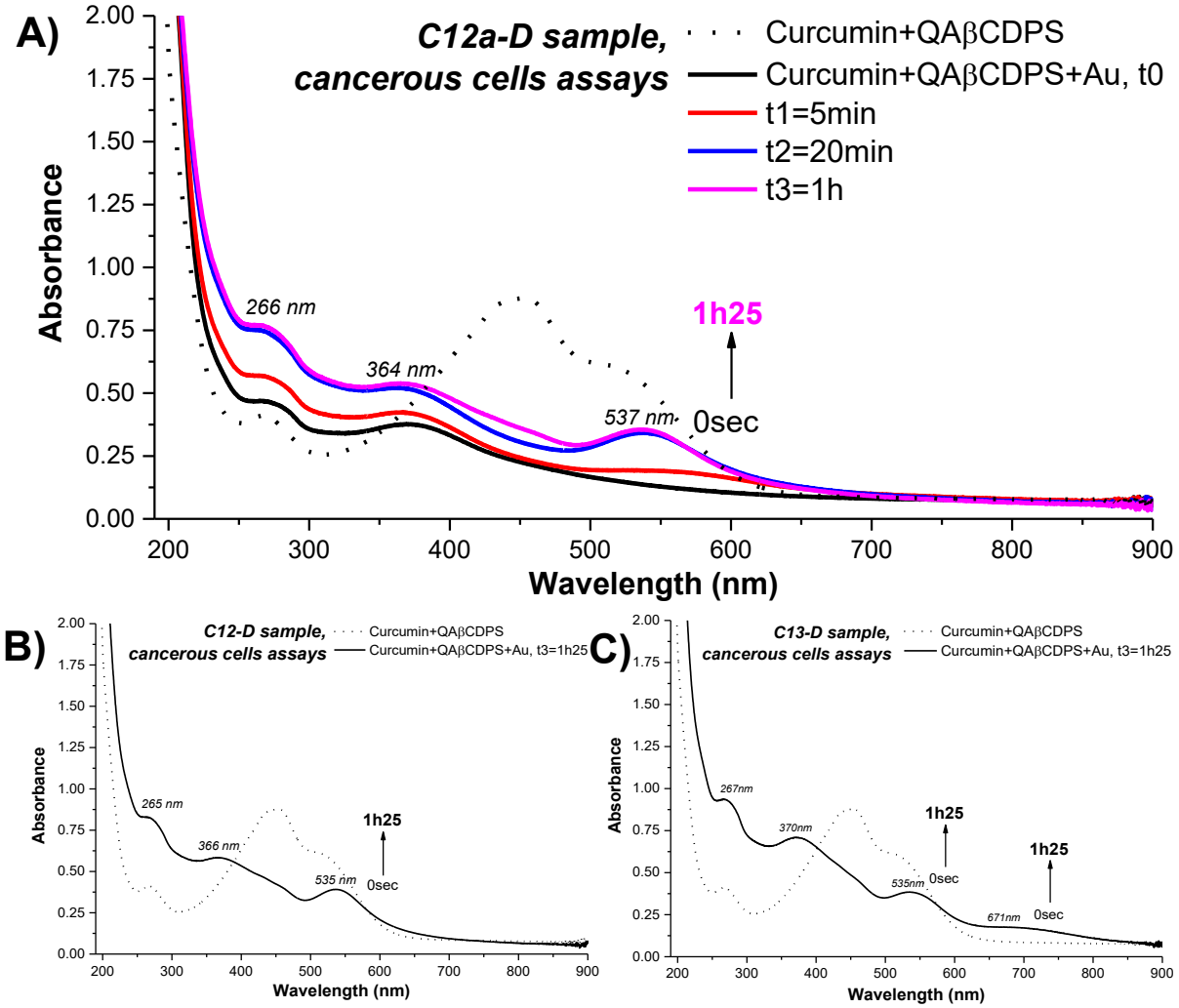

Appendix XI: Comparison of the absorbance evolution of A) first (C12a-D), B) second (C12b-D) and C) third (C13-D) batches of Curcumin+QAβCDPS (black dotted line) and Curcumin+QAβCDPS+Au stirred in a PBS buffer solution after Au addition with magnetic stirring for cancerous cells assays. Measurements were performed in a 1 mm path-length absorbance cuvette using a Jasco V-560 UV-Vis spectrophotometer with PBS as the blank. Conditions A) & B): [PBS] = 10mM; [Curcumin] = 4.69×10^{-4} M; [QAβCDPS] = 10.00 mg.mL^{-1}; [$HAuCl_4 \bullet 3H_2O$] = 4.00×10^{-4} M; C) [PBS] = 10mM; [Curcumin] = 4.51×10^{-4} M; [QAβCDPS] = 10.00 mg.mL^{-1}; [$HAuCl_4 \bullet 3H_2O$] = 4.00×10^{-4} M.

Appendix XII: Phosphorescence of singlet oxygen investigation with Curcumin+QAβCDPS+Au+ZnPc, C14 sample, from ZnPc irradiation. (Part 4.4.1.)

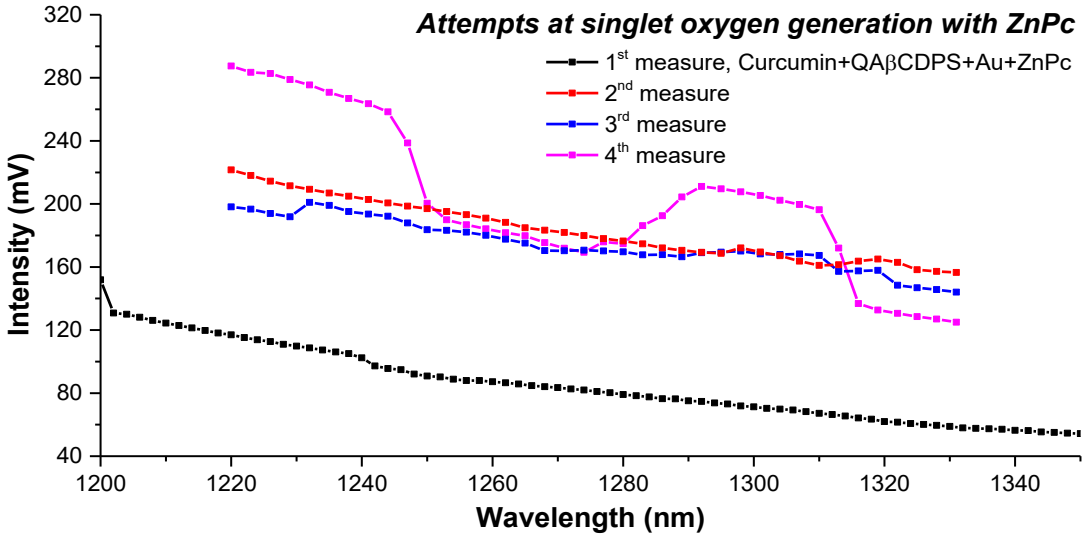

Appendix XII: Evolution of intensity (mV) over wavelength (nm) of phosphorescence of singlet oxygen measured of Curcumin+QAβCDPS+Au+ZnPc (C14) excited using a 671 nm laser (*ca.* 12 $W.cm^{-2}$). Measurements were performed using a Fluorolog-2 spectrofluorometer. Conditions: [Curcumin] = 0.56 mM; [QAβCDPS] = 10.00 $mg.mL^{-1}$; [$HAuCl_4 \bullet 3H_2O$] = 0.56 mM.

Appendix XIII: Absorbance comparison between 1 mm cuvette containing I1-D sample, and gold nanoparticles on empty absorbance cuvette walls after synthesis from indigo carmine's system in dark conditions from I1-D sample. (Part 5.2.1.)

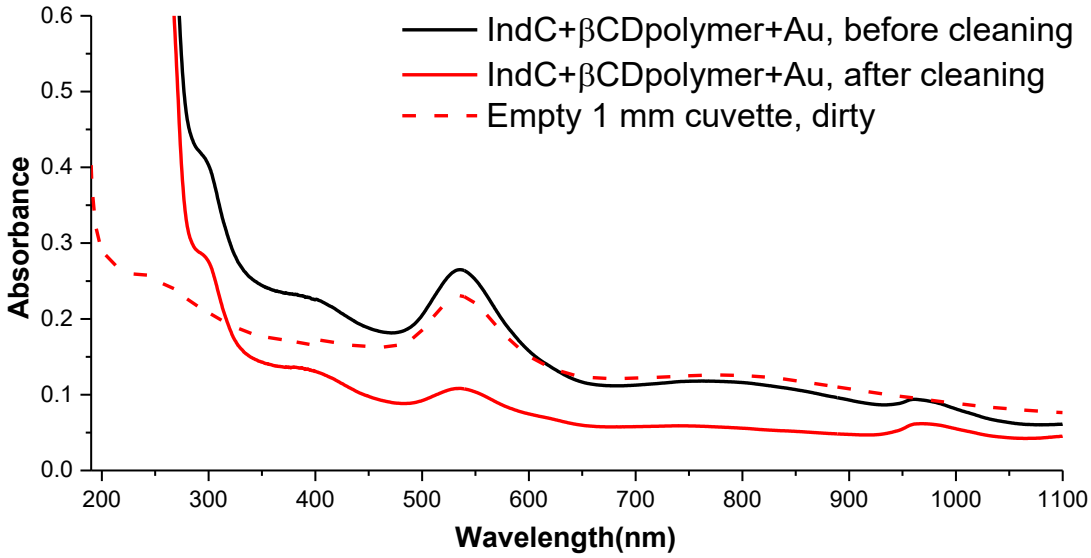

Appendix XIII: Comparison of the absorbance spectra of IndC+βCDpolymer+Au (I1-D) before (black) and after (blue) cleaning of the 1 mm path-length absorbance cuvette. Measurements were performed in a 1 mm path-length absorbance cuvette using a PerkinElmer UV-Vis spectrophotometer with air as the blank. Conditions: [PBS] = 10 mM; [IndC] = 0.349 mM; [βCDpolymer] = 2.58 $mg.mL^{-1}$; [$HAuCl_4 \bullet 3H_2O$] = 0.349 mM.

Appendix XIV: Absorbance evolution of gold nanoparticles synthesis under [N_2] from indigo carmine oxidation, irradiated I3-L sample. (Part 5.2.2.)

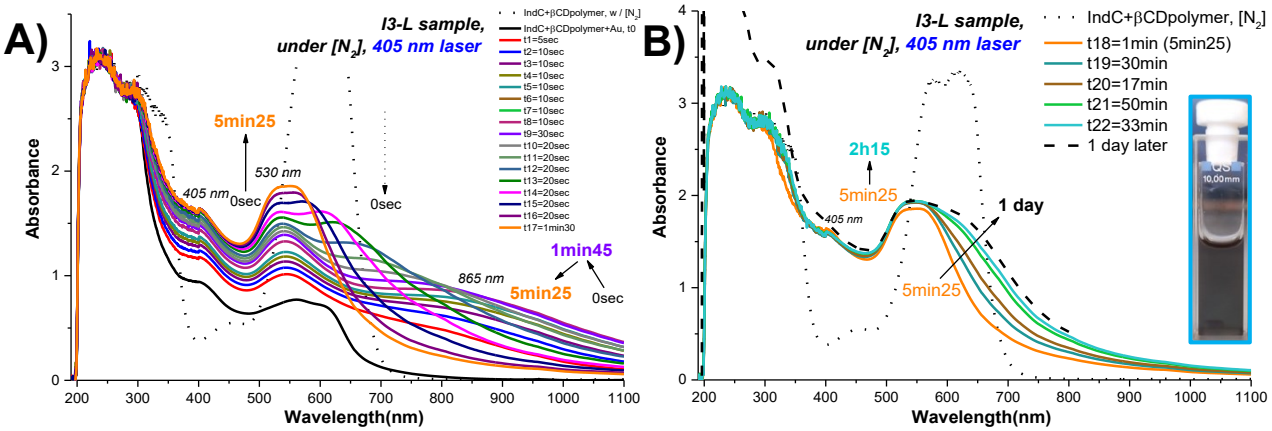

Appendix XIV: Comparison of the absorbance evolution of a second batch of irradiated IndC+βCDpolymer+Au (I3-L) using a 405 nm laser (*ca.* 6 W.cm^{-2}) previously degassed under [N_2], in a PBS solution. A) Irradiation of the system up to 5min25; B) End of irradiation of the system from 5min25 to 2h15. The inset shows a picture at the end of the irradiation. Measurements were performed in a 1 cm path-length absorbance cuvette using a PerkinElmer UV-Vis spectrophotometer with PBS as the blank. Conditions: [PBS] = 10 mM; [IndC] = 0.381 mM; [βCDpolymer] = 2.00 mg.mL^{-1}; [$HAuCl_4 \bullet 3H_2O$] = 0.381 mM.

Appendix XV: Absorbance evolution of gold nanoparticles synthesis under [N_2] from indigo carmine oxidation, dark control I3-D sample. (Part 5.2.2.)

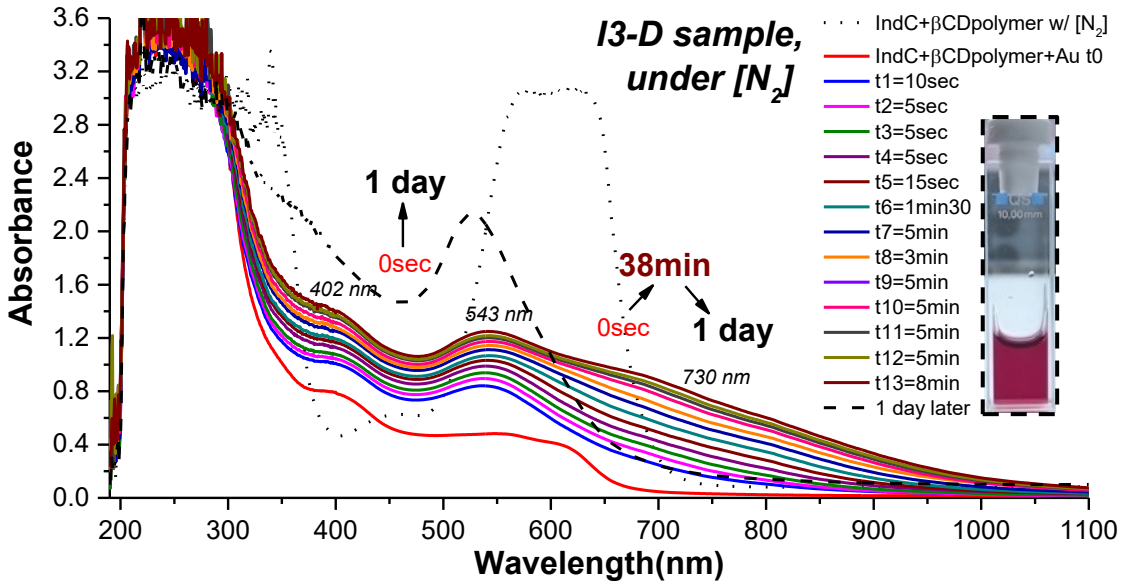

Appendix XV: Comparison of the absorbance evolution of the dark control IndC+βCDpolymer+Au (I3-D) stirred for 38 minutes. The inset shows a picture of the dark control sample under [N_2], 10 days later. Measurements were performed in 1 cm path-length absorbance cuvette using a PerkinElmer UV-Vis spectrophotometer with PBS as the blank. Conditions: [PBS] = 10 mM; [IndC] = 0.391 mM; [βCDpolymer] = 1.59 mg.mL^{-1}; [$HAuCl_4 \bullet 3H_2O$] = 0.391 mM.

Appendix XVI: Absorbance evolution of gold nanoparticles synthesis under [N_2] from indigo carmine oxidation, irradiated with a 405 nm laser (*ca.* 6 W.cm^{-2}) I6-L sample. (Part 5.2.2.)

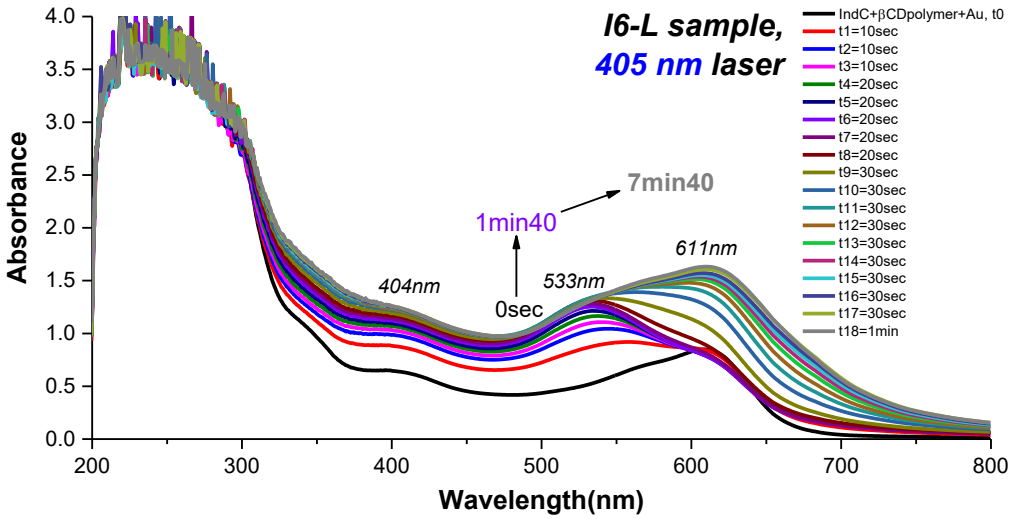

Appendix XVI: Comparison of the absorbance evolution of irradiated IndC+βCDpolymer+Au (I6-L) using a 405 nm laser (*ca.* 6 W.cm^{-2}), in a PBS solution. Measurements were performed in a 1 mm path-length absorbance cuvette using a PerkinElmer UV-Vis spectrophotometer with PBS as the blank. Conditions: [PBS] = 10 mM; [IndC]= 3.87x10^{-4} M; [βCDpolymer] = 2.00 mg.mL^{-1}; [$HAuCl_4 \bullet 3H_2O$]= 3.54x10^{-4} M.

Appendix XVII: Absorbance evolution of gold nanoparticles synthesis from indigo carmine oxidation, for TEM analysis, I7-L sample. (Part 5.2.3.)

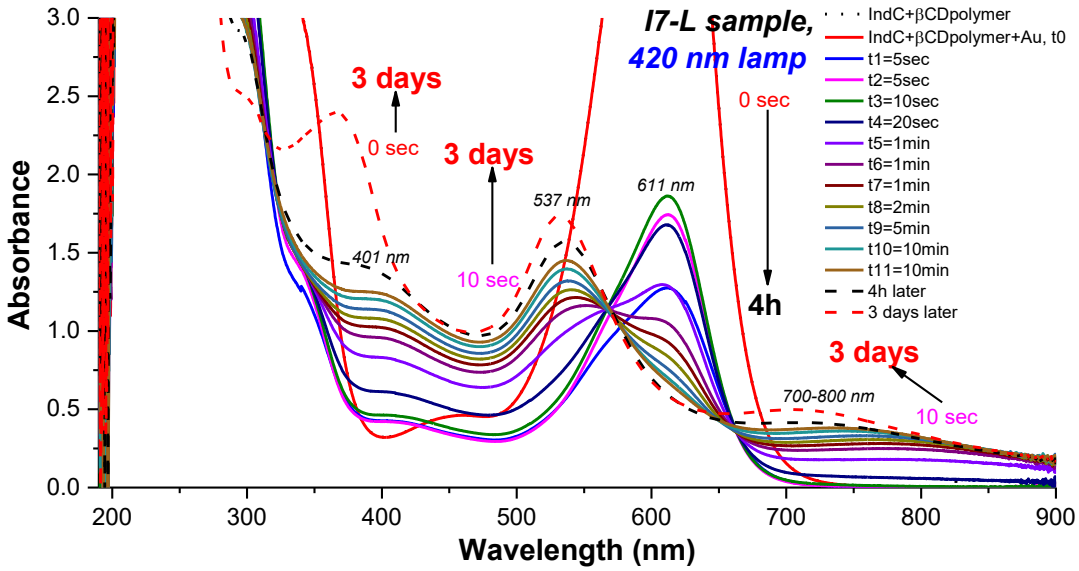

Appendix XVII: Comparison of the absorbance evolution of irradiated IndC+βCDpolymer+Au (I7-L) using a 420 nm lamp (*ca.* 1 mW.cm^{-2}), in a PBS solution. Measurements were performed in a 1 cm path-length absorbance cuvette using a Jasco V-560 UV-Vis spectrophotometer with PBS as the blank. Conditions: [PBS] = 10 mM; [IndC]= 3.66x10^{-4} M; [βCDpolymer] = 2.03 mg.mL^{-1}; [$HAuCl_4 \bullet 3H_2O$]= 4.0x10^{-4} M.

Appendix XVIII: Absorbance evolution of gold nanoparticles synthesis from indigo carmine oxidation, for TEM analysis, I7-D sample. (Part 5.2.3.)

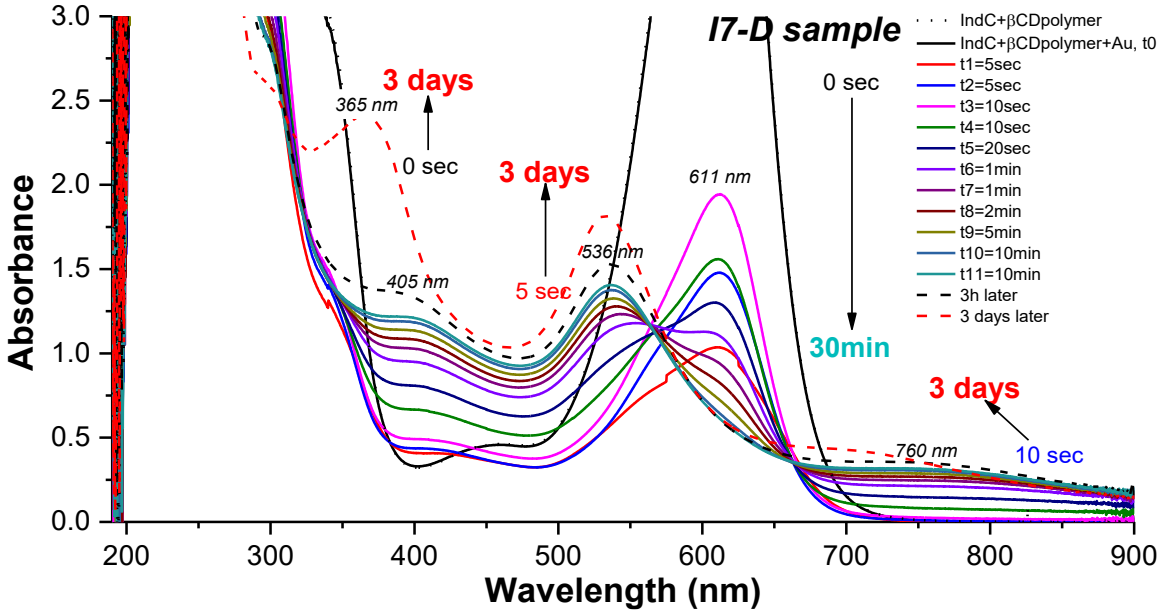

Appendix XVIII: Comparison of the absorbance evolution of the dark control IndC+βCDpolymer+Au (I7-D) stirred for 30 minutes. Measurements were performed in 1 cm path-length absorbance cuvette using a Jasco V-560 UV-Vis spectrophotometer with PBS as the blank. C Conditions: [PBS] = 10 mM; [IndC]= 3.66×10^{-4} M; [βCDpolymer] = 2.03 $mg.mL^{-1}$; [$HAuCl_4 \bullet 3H_2O$]= 4.0×10^{-4} M.

Appendix XIX: Thermal pictures of photothermal studies of IndC+βCDpolymer+Au (I6-L sample) when irradiated at 532 and 671 nm lasers. (Part 5.2.4.)

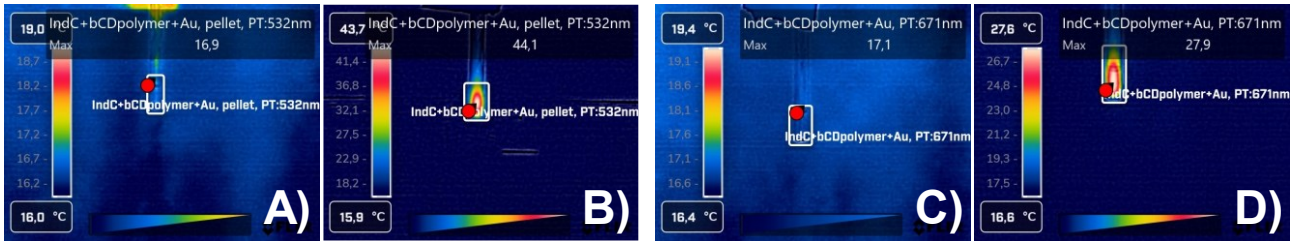

Appendix XIX: A) Thermal picture taken at the starting point and B) thermal picture taken at the end of the 532 nm laser (*ca.* 12 $W.cm^{-2}$) irradiation. C) Thermal picture taken at the starting point and D) thermal picture taken at the end of the 671 nm laser (*ca.* 15 $W.cm^{-2}$) irradiation. The temperatures were measured with a FLIR C3 thermal camera.

Appendix XX: Absorbance evolution of A) irradiated batches (I8a-L, I8b-L, and I8c-L) and B) their respective dark controls (I8a-D, I8b-D, and I8c-D), of gold nanoparticles indigo carmine's system for antibacterial assays. (Part 5.3.1.)

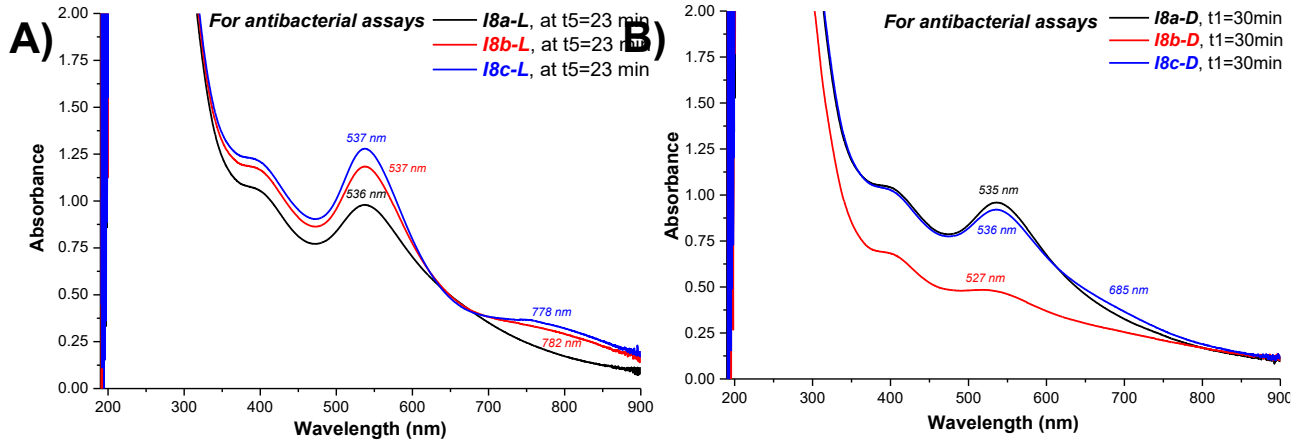

Appendix XX: Comparison of the absorbance of A) irradiated samples (I8a-L, I8b-L and I8c-L), and B) their dark controls (I8a-D, I8b-D and I8c-D) of IndC+βCDpolymer+Au for antibacterial assays. Measurements were performed in a 1 cm path-length fluorescence cuvette, using a Jasco V-560 spectrophotometer, with air as the blank. Conditions: [PBS] = 10mM; [IndC] = 4.29×10^{-4} M; [βCDpolymer] = 2.00 $mg.mL^{-1}$; [$HAuCl_4 \bullet 3H_2O$] = 4.00×10^{-4} M.

Appendix XXI: Absorbance evolution of A) irradiated batches (I9-L and I10-L) and B) their respective dark controls (I9-D and I10-D), of gold nanoparticles indigo carmine's system for cancerous cells assays. (Part 5.3.2.)

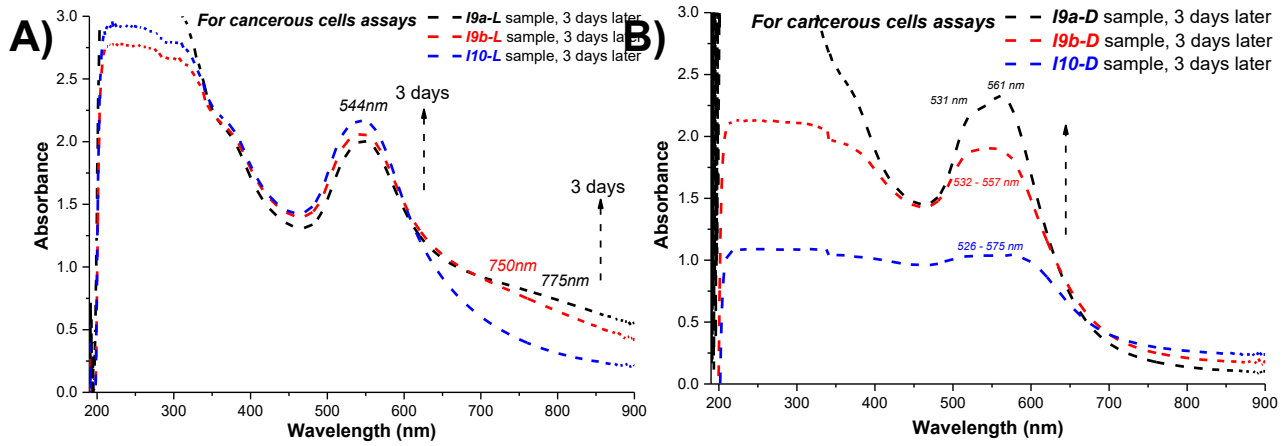

Appendix XXI: Comparison of the absorbance of A) irradiated samples (I9a-L, I9b-L and I10-L), and B) their dark controls (I9a-D, I9b-D and I10-D) of IndC+βCDpolymer+Au for cancerous cells assays. Measurements were performed in a 1 cm path-length fluorescence cuvette, using a Jasco V-560 spectrophotometer, with air as the blank. Conditions: [PBS] = 10mM; [IndC] = 3.76×10^{-4} M; [βCDpolymer] = 2.025 $mg.mL^{-1}$; [$HAuCl_4 \bullet 3H_2O$]= 4.0×10^{-4} M.

Appendix XXII: Absorbance evolution of the synthesis of gold nanoparticles from indigo carmine's system (I11 sample) for the addition of THPP for singlet oxygen investigation. (Part 5.4.)

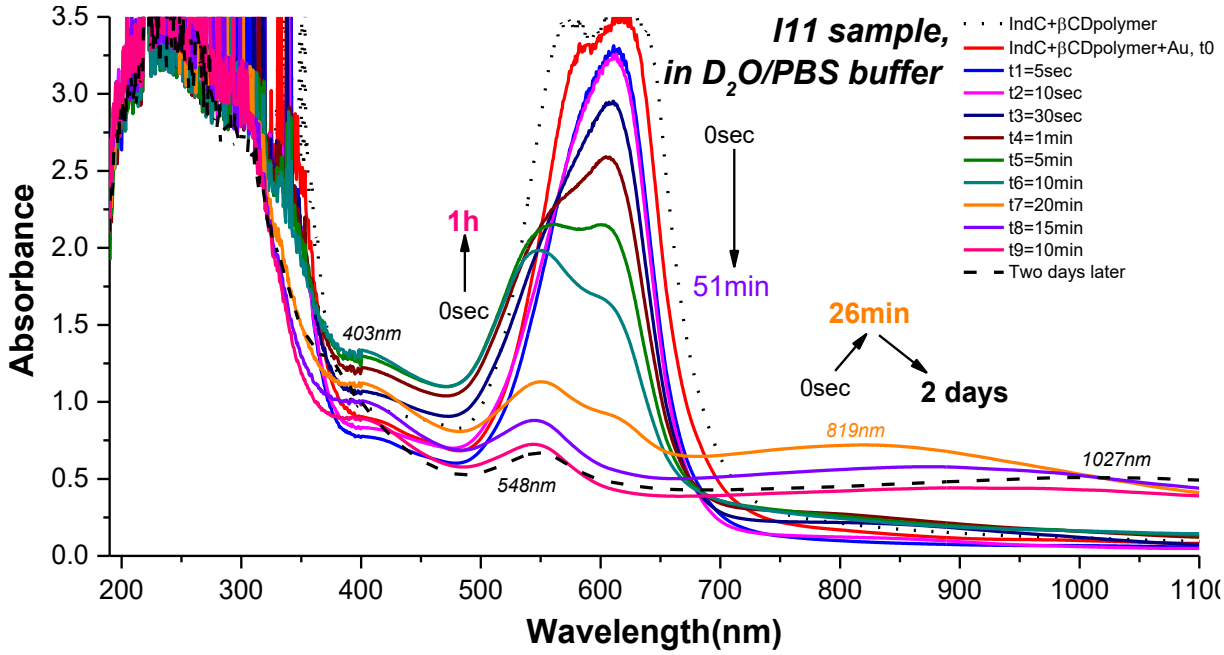

Appendix XXII: Comparison of the absorbance evolution of IndC+βCDpolymer+Au (I11) in a D_2O/PBS solution after Au addition, while irradiated for one hour with 405 nm laser and magnetically stirred. Measurements were performed in 1 cm path-length absorbance cuvette using a PerkinElmer UV-Vis spectrophotometer with PBS as the blank. Conditions: [PBS] = 10 mM; [IndC] = 4.58×10^{-4} M; [βCDpolymer] = 2.03 $mg.mL^{-1}$; [$HAuCl_4 \bullet 3H_2O$] = 4.00×10^{-4} M.

Appendix XXIII: A) Absorbance evolution of the loading of the zinc phthalocyanine in IndC+βCDpolymer+Au and B) Phosphorescence of singlet oxygen investigation with IndC+βCDpolymer+Au+ZnPc. (Part 5.4.)

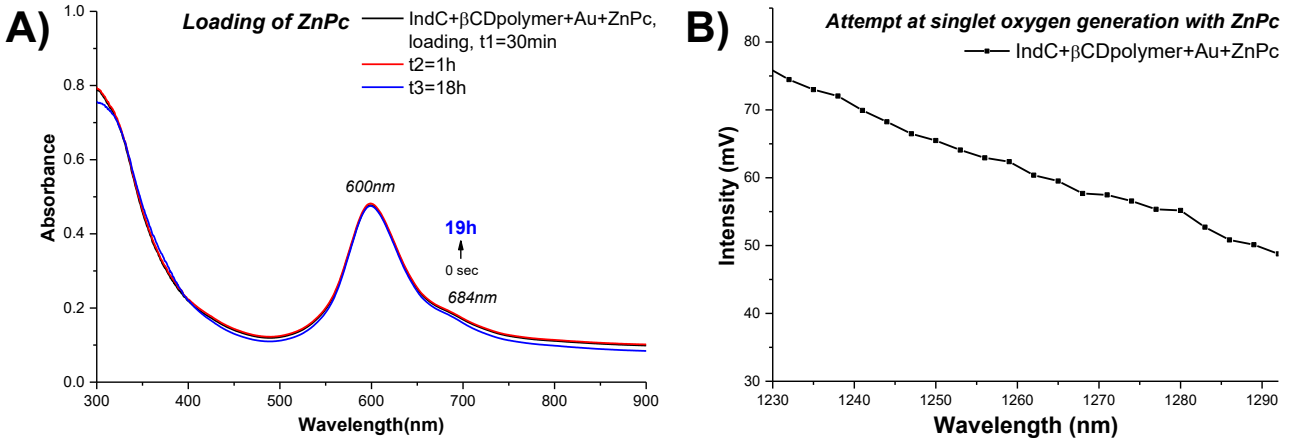

Appendix XXIII: A) Comparison of the absorbance of IndC+βCDpolymer+Au+ZnPc during the loading of ZnPc while magnetically stirred. Measurements were performed in a 1 cm path-length fluorescence cuvette using a PerkinElmer UV-Vis spectrophotometer with air as the blank; B) Evolution of intensity (mV) of phosphorescence of singlet oxygen measured in function of the wavelength (nm) of IndC+βCDpolymer+Au+ZnPc excited using a 671 nm laser (*ca.* 12 W.cm^{-2}). Measurements were performed using a fluorolog-2 spectrofluorometer. Conditions: [PBS] = 10 mM; [IndC] = 0.54 mM; [βCDpolymer] = 2.00 mg.mL^{-1}; [$HAuCl_4 \bullet 3H_2O$] = 0.54 mM.

Appendix XXIV: A) Fluorescence intensity evolution over temperature elevation of RhBITC+FITC βCD polymer in 1:1 ratio, λ_{exc} = 460 nm; and B) evolution of I/Imax over temperature elevation. (Part 6.2.3)

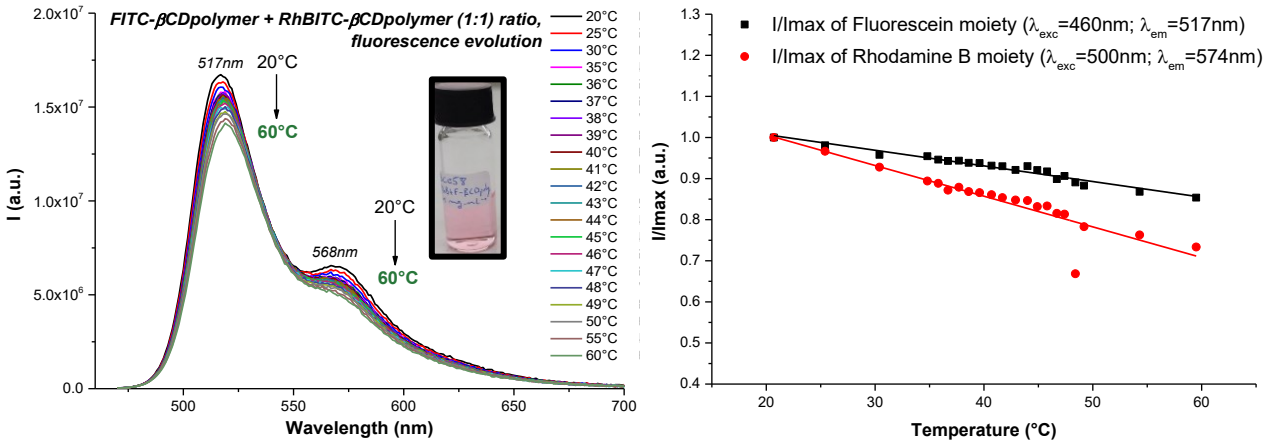

Appendix XXIV: A) Comparison of the fluorescence intensity (arbitrary units) evolution over temperature (°C) of a FITC-βCDpolymer and RhBITC-βCDpolymer mixture (1:1) ratio. λ_{exc} = 460 nm. B) Comparison of I/I_{max} over temperature (°C) evolution of fluorescein and rhodamine B moieties. Measurements were performed in a 1 cm path-length fluorescence cuvette using a fluorolog-2 spectrofluorometer. Conditions: [PBS] = 10 mM; [FITC-βCDpolymer] = 1.00 mg.mL^{-1}; [RhBITC-βCDpolymer] = 1.00 mg.mL^{-1}.

Appendix XXV: Fluorescence intensity evolution over temperature elevation of RhBITC+FITC βCD polymer in 1:1 ratio, A) λ_{exc} = 460 nm, B) λ_{exc} = 500 nm. (Part 6.2.3.)

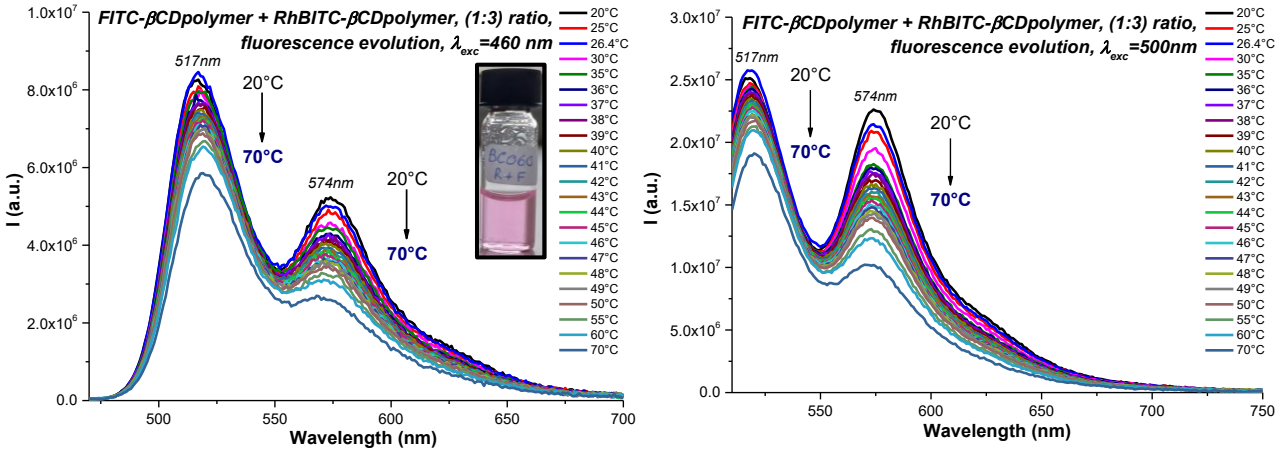

Appendix XXV: A) Comparison of the fluorescence intensity (arbitrary units) evolution over temperature (°C) of a FITC-βCDpolymer and RhBITC-βCDpolymer mixture (1:3) ratio. λ_{exc} = 460 nm. The inset shows a picture of the sample at room temperature. B) Comparison of the fluorescence intensity (arbitrary units) evolution over temperature (°C) of a FITC-βCDpolymer and RhBITC-βCDpolymer mixture (1:3) ratio. λ_{exc} = 500 nm. Measurements were performed in a 1 cm path-length fluorescence cuvette using a fluorolog-2 spectrofluorometer. Conditions: [PBS] = 10 mM; [FITC-βCDpolymer] = 0.50 mg.mL^{-1}; [RhBITC-βCDpolymer] = 1.50 mg.mL^{-1}.

Appendix XXVI: Comparison of absorbance evolution of AuNPs synthesis from GSNO in a PBS solution, dark control, S1-D sample. (Part 6.3.3.)

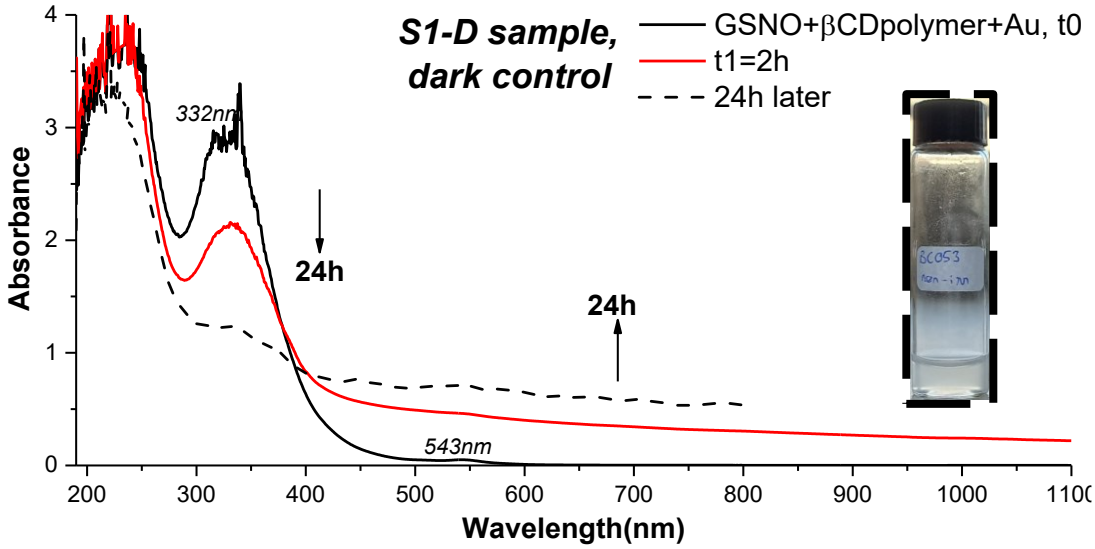

Appendix XXVI: Comparison of the absorbance evolution of GSNO+βCDpolymer+Au (S1-D) during a two-hour-long stirring. The inset shows a picture of the sample at the end of the irradiation. Measurements were performed in a 1 cm path-length fluorescence cuvette using a PerkinElmer UV-Vis spectrophotometer with water as the blank. Conditions: [GSNO] = 1.0 mg.mL^{-1}; [βCDpolymer] = 1.0 mg.mL^{-1}; [$HAuCl_4 \bullet 3H_2O$] = 0.43 mM.

Appendix XXVII: Comparison of absorbance evolution of AuNPs synthesis from GSNO irradiation in a PBS solution, S2-L sample. (Part 6.3.3.)

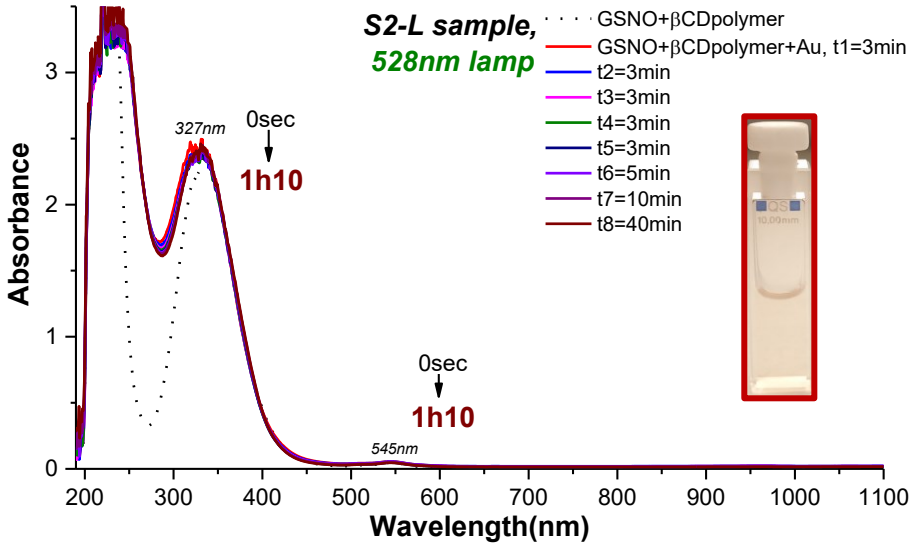

Appendix XXVII: Comparison of the absorbance evolution of GSNO+βCDpolymer+Au (S2-L) during a one hour and ten minutes long irradiation. The irradiation was performed in a 1 cm path-length fluorescence cuvette at 10 cm of the sample using a 528 nm lamp (*ca.* 1 mW.cm^{-2}) while magnetically stirred. The inset shows a picture of the sample at the end of the irradiation. Measurements were performed in a 1 cm path-length fluorescence cuvette using a PerkinElmer UV-Vis spectrophotometer using PBS as the blank. Conditions: [PBS] = 10 mM; [GSNO] = 1.0 mg.mL^{-1}; [βCDpolymer] = 1.0 mg.mL^{-1}; [$HAuCl_4 \bullet 3H_2O$] = 0.5 mM.

Appendix XXVIII: ^{19}F NMR spectrum ($CDCl_3$, 500MHz) of nitroaniline-adamantane. (Part 6.4.1.)

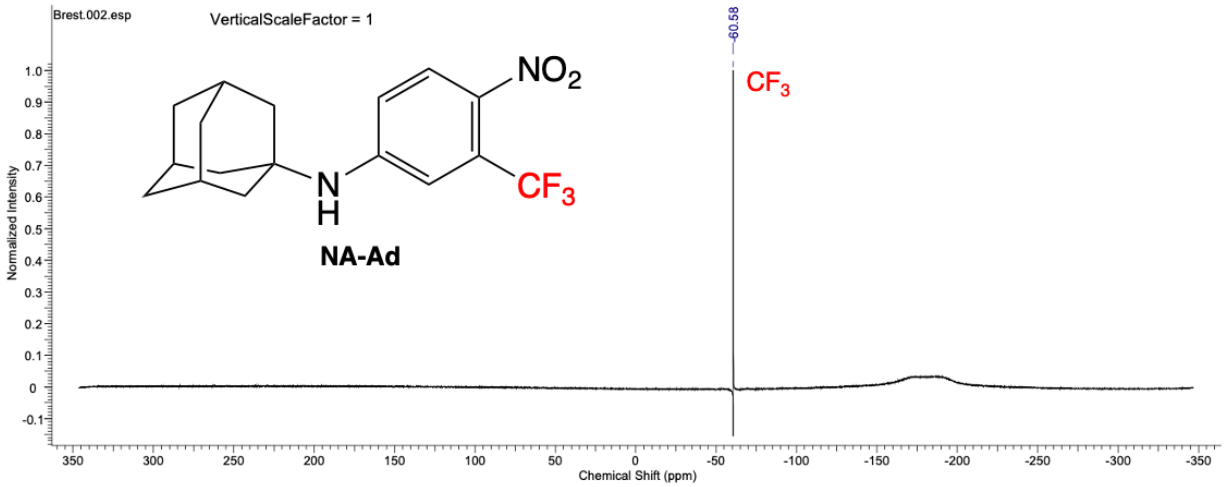

Appendix XXVIII: ^{19}F NMR spectrum of NA-Ad. Data collected using a 500MHz NMR spectrometer in $CDCl_3$, at T = 298 °K.

Appendix XXIX: Synthesis of AuNPs from NA-Ad irradiation, with both RhBITC and FITC βCD polymers, N2-L sample (Part 6.4.2.)

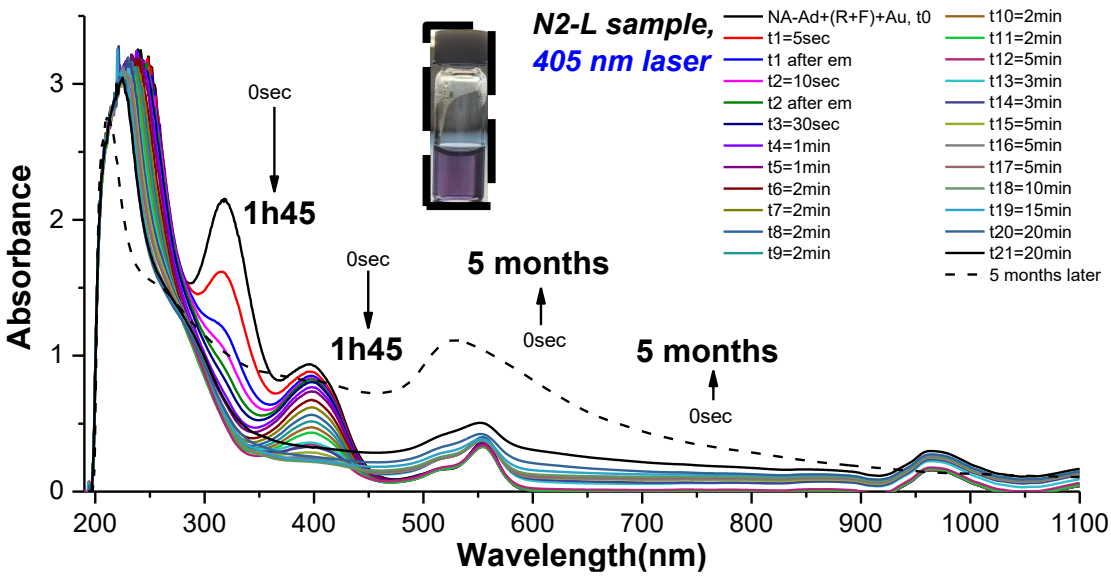

Appendix XXIX: Comparison of the absorbance evolution of NA-Ad+(RhBITC-βCDpolymer+FITC-βCDpolymer)+Au (N2-L) stirred and irradiated with a 405 nm laser (*ca.* 6 W.cm^{-2}) for one hour and forty-five minutes and after five months (dashed line). The inset shows the N2-L sample, five months after the end of the synthesis. Measurements were performed in a 1 cm path-length absorbance cuvette using a PerkinElmer UV-Vis spectrophotometer with PBS as the blank. Conditions: [PBS] = 10 mM; [FITC-βCDpolymer] = 0.50 mg.mL^{-1}; [RhBITC-βCDpolymer] = 1.50 mg.mL^{-1} ; [$HAuCl_4 \bullet 3H_2O$]: 0.5 mM.

Appendix XXX: ^{1}H NMR spectrum (D_2O, 400MHz) of $\beta CD(NH_2)_1$. (Part 6.5.1.)

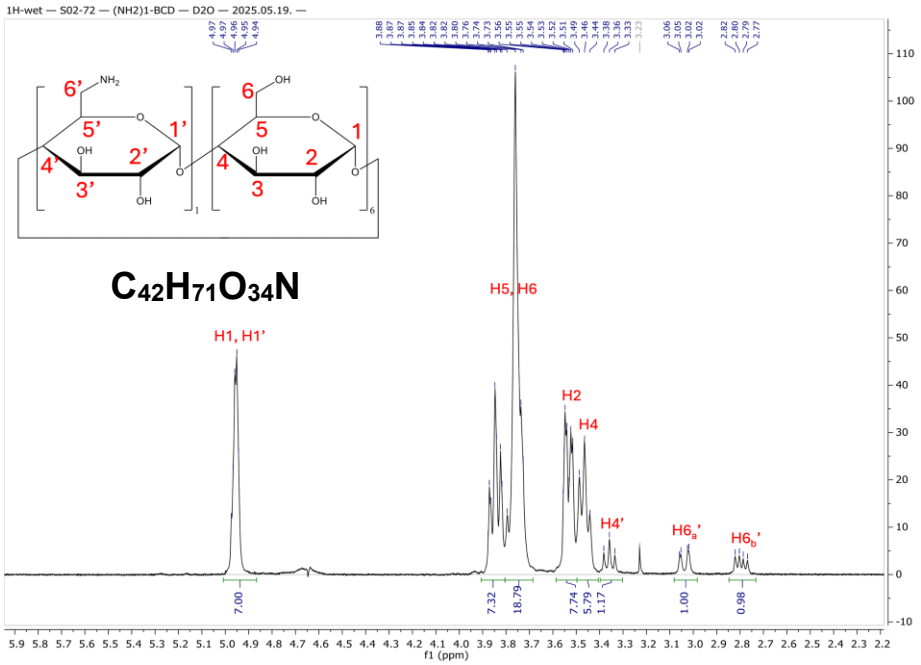

Appendix XXX: ^{1}H NMR spectrum of $\beta CD\text{-}(NH_2)_1$. Data collected using a 400MHz NMR spectrometer, in DMSO-d6, at T = 298 °K.

Appendix XXXI: ^{1}H-^{13}C DEPT HSQC NMR spectrum (DMSO-d6, 400MHz) of βCD$(N_3)_1$, synthesized by CarboHyde. (Part 6.5.1.)

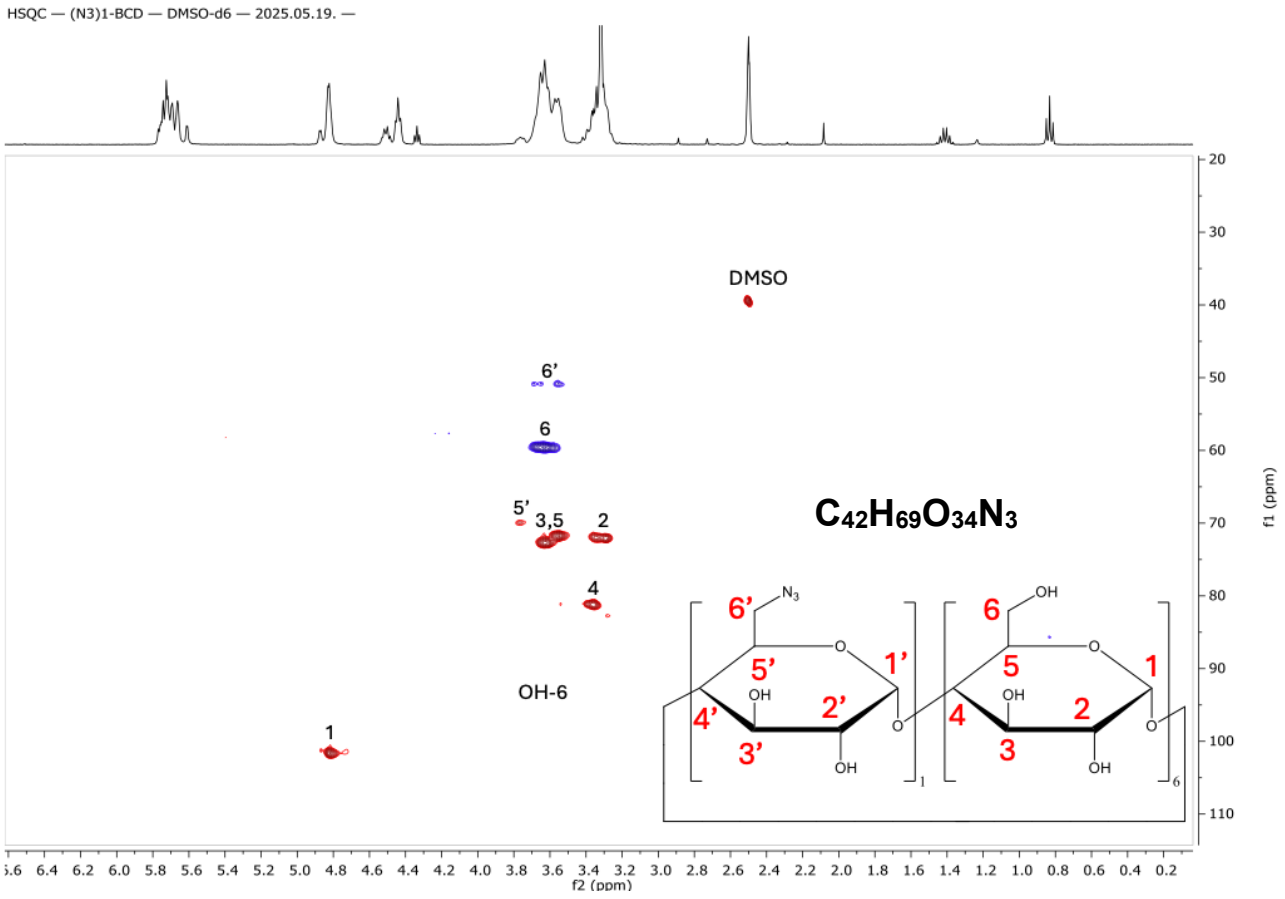

Appendix XXXI: ^{1}H-^{13}C DEPT HSQC NMR spectrum of βCD-$(N_3)_1$, obtained from CarboHyde. Data collected using a 400MHz NMR spectrometer, in DMSO-d6, at T = 298 °K. F2 axis: ^{1}H NMR; F1 axis: ^{13}C DEPT NMR.

Appendix XXXII: ^{1}H NMR spectrum (DMSO-d6, 400MHz) of βCD(FITC)$_1$ from F1 sample (Part 6.5.2.)

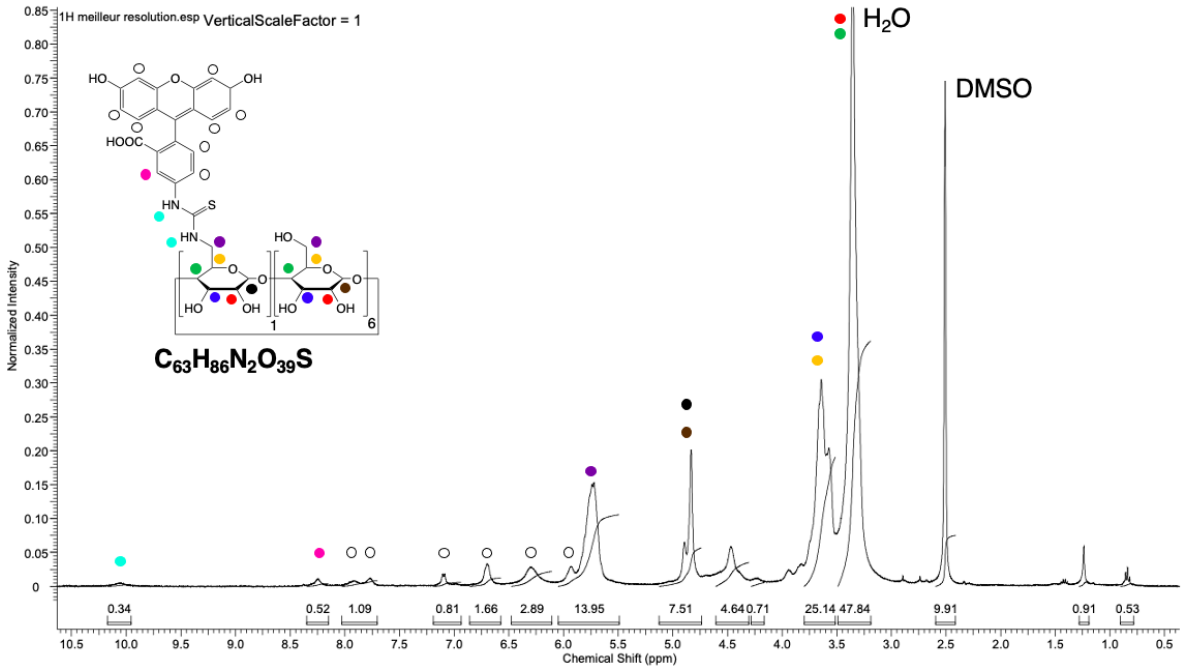

Appendix XXXII: ^{1}H NMR spectrum of βCD-(FITC)$_1$. Data collected using a 400MHz NMR spectrometer, in DMSO-d6, at T = 298 °K.

Appendix XXXIII: ^{1}H NMR spectrum (DMSO-d6, 400MHz) of βCD(DNSA)$_1$ from D4 sample (Part 6.5.2.)

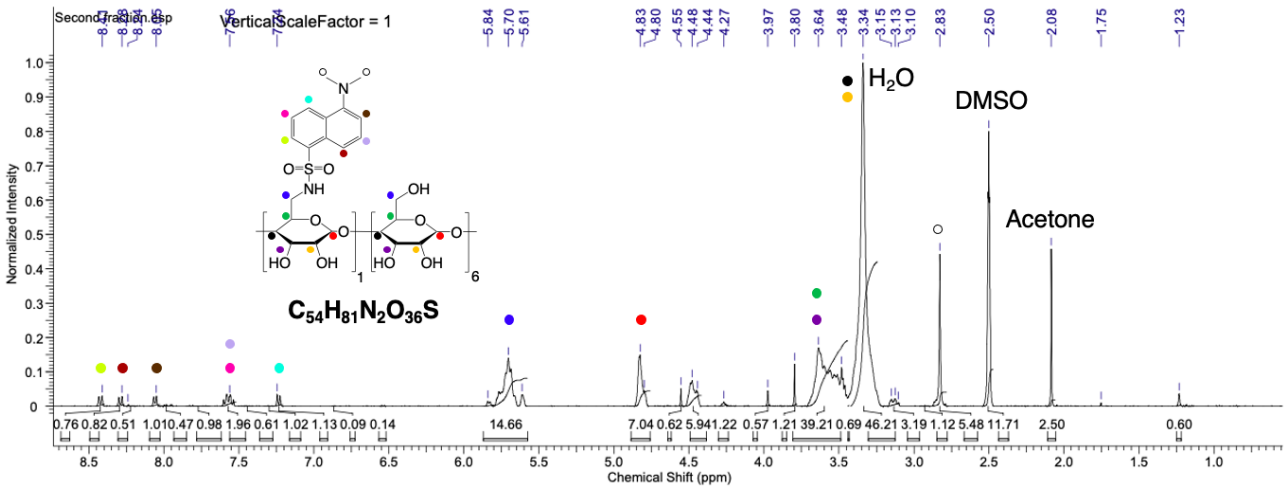

Appendix XXXIII: ^{1}H NMR spectrum of βCD-(DNSA)$_1$ after column chromatography. Data collected using a 400MHz NMR spectrometer, in DMSO-d6, at T = 298 °K.

Outcome of the PhD

Publications:

- « A simple approach for CTAB-free and biofunctionalized gold nanorods to construct photothermal active nanomedicine for potential in vivo applications in cancer cells and scar treatment », A. Foci, B. Clépoint, A. Fraix, L. D'Urso, A. De Bonis, C. Satriano, Front. Mater., 11, 2024, 1381176, https://doi.org/10.3389/fmats.2024.1381176

- « Green synthesis of gold nanoparticles from Curcumin and β-cyclodextrin polymer for application in photothermal therapy. »; B. Clépoint *et al.*; Manuscript in preparation

- « Use of indigo carmine as green reducer for the preparation of gold nanoparticles: synthesis and applications in photothermia. »; B. Clépoint *et al.*; Manuscript in preparation

Secondment:

- CarboHyde, Budapest, Hungary (04/01/2025 – 18/05/2025)

- CEMCA Laboratory, Brest, France (30/05/2025 – 22/07/2025)

Collaborations:

- Dr Marta Maria Natile, University of Padova

- Dr Milo Malanga, CarboHyde

- Prof. Paul-Alain Jaffrès, University of Western Brittany

- Philippe Elies, University of Western Brittany

- Prof. Tristan Montier, Inserm

- Dr Tony Le Gall, Inserm

- Dr Manh Nguyen Quoc, Inserm

Conferences attended:

- Poster presentation, B. Clépoint, A. Fraix, IPM Symposium, Sestri Levante, Italy. December 2023

- Oral presentation, B. Clépoint, A. Fraix, CECP Symposium, Bad Hofgastein, Austria. February 2024

- Flash presentation and poster presentation, B. Clépoint, M. M. Natile, A. Fraix, SIFB Symposium, Messina, Italy, September 2024

- Oral presentation, B. Clépoint, M. M. Natile, A. Fraix, IPM Symposium, Rome, Italy. December 2024

- Oral presentation, B. Clépoint, M. M. Natile, A. Fraix, SIFB Symposium, Online meeting. April 2025

- Poster presentation, B. Clépoint, M. M. Natile, A. Fraix, SP2P Symposium, Toulouse, France. May 2025

Lectures attended:

- Paper-Project writing and Presentation skills, *Prof.ssa Silvia Giordani*, June 2024

- Photochemistry: From Basic Principles to Practical Applications, *Prof. Salvatore Sortino*, October 2024

Summer schools attended:

- X Ciamician Photochemistry School, Photochemical Nanosciences Laboratory, University of Bologna, Italy. June 2025

Acknowledgement

Prof.ssa Aurore Fraix, none of this work would have been possible without you and your hard work. I can only be grateful for the opportunity you offered me. It was not only a thesis but a complete life change; you fulfilled my wish to work on an amazing topic, in amazing countries and meeting amazing and brilliant scientists. Under your guidance, I enjoyed every day, every conversation and every experiment. Your leadership, seriousness, teaching skills, patience and kindness, toward not only me but every student you had, always pushed me forwards, forgetting tiredness, fears, doubts and failures. My only compass was and is your complete satisfaction of this work.

Prof. Salvatore Sortino, I am sure I can't realise how much impact you had on this work and my presence in your group. Your leadership and the positive and optimistic dynamic you disseminate between all of us always amazed me. You are an example for all of us. I am very grateful for your investment into the PhD program and everything else you have done for the group.

Prof. Giuseppe Spoto and *Prof. Salvatore Scirè*, I am very grateful for your investment and everything else you have done to allow the PhD program to run smoothly.

Dr. Milo Malanga, the discipline and the perfection of your work is amazing. You taught me so much, from ridiculous or shameful non-mastered basic stuff to more advanced knowledge of organic synthesis. These months at Budapest were full of lessons. Alongside of you and your team, I got a better understanding of my past failed experiments, and I am sure that all the knowledge learnt at *CarboHyde* will help me for a very very long time.

Prof. Paul-Alain Jaffrès, I am afraid to repeat myself from previous acknowledgment but, once again, let me thank you for opening to me the doors of your research group. Thank you for your leadership, your help, and your precious guidance. A lot of things would not have been possible without you.

Prof. Tristan Montier, *Dr. Tony Le Gall*, *Dr. Manh Nguyen Quoc* thank you for opening me the doors of your laboratory. To be able to see what happen outside of a chemistry lab is always rewarding. I am sure this experience will help me to be better at my job in the future.

Prof.ssa Cristina Parisi, *Dott.ssa Francesca Laneri and Dott.ssa Samantha Sollima*, you have both been too great with me. Always ready to help me in the lab or for any administration

formalities, you have saved my life more than once. You taught me Italian like no one else: in the tears and in the pain. But the patience you demonstrated was a gift and each of my own mistakes you corrected led me a little bit closer to your people and your culture. The day I will leave, I will miss your joys, your songs, and your endless chatting. In all truth, I will miss your Italian soul.

Dr. Tassia Joï Martins, you showed me how far I am, how much I have to achieve to reach my dreams. You are a true example of dedication and perseverance for all of us. Thank you for everything, and for this Brazilian happiness and openness you brought into the lab.

Dr. Thomas Lécuyer, without you and your friends I would have passed these last three years eaten by cats crews or completely burnt by the Sicilian sun, homeless in the streets of Catania. Having another French guy always offering me his assistance and support was a welcoming breath of fresh air. I am way more grateful to you than you can imagine.

At *CarboHyde*, I know I have to thanks everybody I had the opportunity to meet during these 4 months in your lab. *Mihály Balínt, Dr. Kristóf Félegyi, Balázs Kondoros, Daniel Bisericaru, Dr. Tamás Kiss,* thank you for your, how important, strictness and excellence in the lab.

From *CEMCA* lab, it was a great pleasure to see everybody once again. I know which privilege it is to work among the best. Thank you, *Prof. Hélène Couthon*, *Dr. Mathieu Berchel*, *Dr. Chloé Le Roux*, *Wilfried Berthe*, *Olivier Lozach*, *Sylvie Hernot*, *Mariam Simonnin*, *Dr. Loëza Collobert* and *Dr. Alexandra Loubières*.

My parents and grandparents were unconditional supporters. Their sacrifices and their dedication pushed me even higher and farther than where I could ever dream some years ago. And, even from France, my friends reminded me that life is still moving outside of the lab. Their encouragements and joys at each milestone achieved were the greatest fuels.
Déborah, thank you so much for your understanding, your patience and your beautiful support. You helped to make this work even more peaceful and enjoyable.

Finally, I would like to thank all of my professors and teachers I could met before this thesis during these last 20 years of school in France. You have contributed, in one way or another, to the achievement of this dissertation. Absolutely nothing would have been possible without all of your hard work, your hope, and your refusal to give up on my education.